



**HAL**  
open science

# Transport and coupling of ultra-cold atoms to nano-structured surfaces

Jean-Baptiste Gerent

► **To cite this version:**

Jean-Baptiste Gerent. Transport and coupling of ultra-cold atoms to nano-structured surfaces. Physics [physics]. Université de Bordeaux, 2023. English. NNT : 2023BORD0141 . tel-04549505

**HAL Id: tel-04549505**

**<https://theses.hal.science/tel-04549505>**

Submitted on 17 Apr 2024

**HAL** is a multi-disciplinary open access archive for the deposit and dissemination of scientific research documents, whether they are published or not. The documents may come from teaching and research institutions in France or abroad, or from public or private research centers.

L'archive ouverte pluridisciplinaire **HAL**, est destinée au dépôt et à la diffusion de documents scientifiques de niveau recherche, publiés ou non, émanant des établissements d'enseignement et de recherche français ou étrangers, des laboratoires publics ou privés.

THÈSE PRÉSENTÉE  
POUR OBTENIR LE GRADE DE  
**DOCTEUR**  
**DE L'UNIVERSITÉ DE BORDEAUX**  
ECOLE DOCTORALE SCIENCES PHYSIQUES ET DE  
L'INGÉNIEUR  
LASER, MATIERE, NANOSCIENCE

Par **Jean-Baptiste GERENT**

Transport d'atomes ultra-froids et couplage à des surfaces  
nano-structurées.

Transport and coupling of ultra-cold atoms to nano-structured surfaces.

Sous la direction de : **Simon BERNON et Philippe BOUYER**

Soutenue le 6 juin 2023

Membres du jury :

M. Chris Westbrook	DR, LCF, U. Paris-Saclay (FR)	Rapporteur
M. Carlos Garrido Alzar	CR, SYRTE - Observatoire de Paris (FR)	Rapporteur
M. Philippe Tamarat	Pr, LP2N, Université de Bordeaux (FR)	Examineur, Président
M. Naceur Gaaloul	Dr, IQO, Leibniz University Hannover (DE)	Examineur
M. Philippe BOUYER	DR, IOGS (FR) - Quantum Delta (NL)	Directeur de thèse
M. Simon BERNON	Prof. assistant, LP2N, Université de Bordeaux (FR)	Directeur de thèse



---

# Abstract

## English

The entry into the new millennium was marked in the quantum community by the first experimental realizations of the Bose-Einstein condensation of atoms in a vapor, achieved in different research groups. Twenty-five years later, such systems are 'routinely' produced and are the core of many experiments. At the frontier between condensed matter theory, quantum optics, and atomic physics, ultra-cold atoms are subjects of high scientific interest.

An ultra-cold gas can be trapped in optical lattices, giving a realistic way of experimentally realizing a new range of lattice Hamiltonians, that are used to simulate condensed matter systems. In these simulations, ultra-cold atoms are used to mimic the behavior of electrons in a solid-state material and could be used to simulate a wide range of complex condensed matter phenomena, such as the fractional quantum Hall effect, topological insulators, and high-temperature superconductivity.

In order to study such systems, diffraction-limited quantum gas microscopes have emerged as a way to manipulate and detect atoms trapped in lattice potentials. Using far-field interference, experiments have mainly been restricted to a lattice spacing of 500 nm. This limits the speed of dynamics of all physical processes.

Higher energy regimes could be accessed by reducing the lattice spacing. For this purpose, one of the long-term goals of the team is to trap atoms in the near-field of a surface and to make use of the Casimir-Polder forces to shape sub-wavelength potentials. Thanks to nano-fabrication capabilities, the spacing can be reduced to a few tens of nanometers. However, this requires to adapt the imaging techniques to observe cold-atoms with sub-wavelength spatial resolutions.

In this PhD thesis, I report first on the advances toward implementing an atom chip in our experiment, which will serve as an integrated platform to manipulate the quantum gas. I present simulations and study an experimental solution allowing the cloud to be transported to the near-field. The method is based on the interference of a laser radiation in the near field of a rotating surface. It has been fully simulated, and the limitations have been numerically and experimentally assessed. I conclude this part by presenting the first model of chip that has been fabricated.

In a second part, I report on the development of a sub-wavelength imaging method of cold Rubidium 87 atoms which is based on excited state dressing. I detail the concept of this nano-metric spatial resolution method and apply it to super-resolve a single longitudinal atomic density distribution of a cloud trapped in a tight lattice that exhibits a width below 30 nm.

---

## Français

L'entrée dans le nouveau millénaire a été marquée dans la communauté quantique par les premières réalisations expérimentales de la condensation de Bose-Einstein d'atomes dans un gaz, obtenues par différents groupes de recherche. Vingt-cinq années plus tard, de tels systèmes sont produits régulièrement et sont au cœur de nombreuses expériences. À la frontière entre la théorie de la matière condensée, l'optique quantique et la physique atomique, l'étude des atomes ultra-froids est un sujet scientifiquement très prometteur.

Un gaz ultra-froid peut être piégé dans des réseaux optiques, offrant ainsi un moyen réaliste de mettre expérimentalement en place une nouvelle gamme d'Hamiltonien périodiques, utilisés pour simuler la matière condensée. Dans de telles simulations, des atomes ultra-froids imitent le comportement des électrons dans un matériau à l'état solide et pourraient être utilisés pour simuler une large gamme de phénomènes complexes en matière condensée, tels que l'effet Hall quantique fractionnaire, les isolants topologiques et la supraconductivité à température ambiante.

Afin d'étudier de tels systèmes, des microscopes à gaz quantiques, limités par la diffraction, ont émergé comme un moyen de manipuler et de détecter les atomes piégés dans des potentiels périodiques. Utilisant l'interférence en champ lointain, les expériences ont principalement été limitées à des réseaux ayant des périodes proche de 500 nm, ce qui limite la vitesse de la dynamique des processus physiques étudiés. Les régimes d'énergie plus élevés pourraient être atteints en réduisant la période du réseau.

Pour ce faire, l'un des objectifs à long terme de l'équipe est de piéger des atomes dans le champ proche d'une surface et d'utiliser les forces de Casimir-Polder pour façonner des potentiels sub-longueur d'onde. Grâce aux capacités de nano-fabrication, l'espacement entre les sites peut être réduit à quelques dizaines de nanomètres. Cependant, cela nécessite d'adapter les techniques d'imagerie pour observer les atomes avec des résolutions spatiales sub-longueur d'onde.

Dans ce manuscrit de thèse, je rapporte dans un premier temps les avancées vers la mise en place d'une puce atomique sur l'expérience AUFRONS, qui servira de plateforme pour manipuler le gaz quantique. Je présente des simulations numériques et étudie une solution expérimentale permettant de transporter le nuage jusqu'au champ proche. La méthode est basée sur l'interférence d'un rayonnement laser dans le champ proche d'une surface en rotation. Celle-ci a été entièrement simulée et les limites ont été évaluées numériquement et expérimentalement. Je conclus cette partie en présentant le premier modèle de puce qui a été fabriqué.

Dans une seconde partie, je détaille le développement d'une méthode d'imagerie sub-longueur d'onde d'atomes ultra-froids de Rubidium 87 basée sur l'habillage des états excités. J'approfondis le concept de cette méthode atteignant des résolutions spatiales nanométriques et l'applique pour résoudre la distribution de densité d'un atome unique d'une taille inférieure à 30 nm, piégée dans un site unique d'un réseau optique.

---

## Remerciements

Ces quatre années de thèse au sein du LP2N m'ont énormément apporté, et je tiens ici à exprimer mes remerciements à l'ensemble des personnes qui m'ont permis de mener à bien ce projet.

Tout d'abord, je souhaite remercier mon premier co-directeur de thèse, Philippe Bouyer, de m'avoir accueilli dans l'une des équipes du groupe "Atomes Froids" et pour ses précieux conseils, que ce soit en matière de physique au laboratoire ou sur des sujets plus généraux en dehors de celui-ci. Je souhaite également exprimer ma reconnaissance envers les membres du jury pour l'intérêt qu'ils ont porté à mes travaux, notamment Chris Westbrook et Carlos Garrido Alzar en tant que membres rapporteurs, ainsi que Philippe Tamarat et Naceur Gaaloul en tant qu'examineurs.

Je veux remercier chaleureusement l'ensemble des équipes techniques et administratives du laboratoire qui m'ont apporté leur soutien sur de nombreux sujets. Merci à Stéphanie Schultze, Fabien Lehoux et Laurent Porcel pour avoir grandement simplifié les différentes démarches administratives. Je tiens également à exprimer ma gratitude à Jean-Hugues Codarbox et Arnaud Tizon de l'atelier d'électronique pour leurs précieux conseils et pour avoir mis à notre disposition des circuits de hautes performances. Un grand merci à Philippe Teulat de l'atelier mécanique, dont les pièces exceptionnelles ont été indispensables en salle de manip. Enfin, je souhaite remercier Jordan Swietlicki pour nous avoir permis d'utiliser les ressources du FabLab. J'aimerais aussi exprimer ma reconnaissance envers Nicolas Dubreuil et Philippe Lalanne qui m'ont offert la chance d'enseigner aux étudiants en Master de l'Institut d'Optique et de l'Université de Bordeaux, une expérience qui s'est révélée être très enrichissante à la fois sur le plan scientifique et personnel.

Merci à l'ensemble des membres du groupe "Atomes froids" que j'ai eu la chance de rencontrer, que ce soient les permanents et leurs nombreux conseils lors des réunions de groupe, notamment Andrea Bertoldi, Benjamin Canuel et Baptiste Battelier, ainsi que les post-doctorants dont la porte était (presque) toujours ouverte : Dylan, Devang et Vincent Jarlot. Je tiens à remercier également les anciens supop qui ont renforcé les rangs de l'équipe : Célia, Paul, Clément, Geovan, Quentin. Un merci particulier à Luisa, qui a apporté une dose d'énergie et a contribué à instaurer la dynamique actuelle de Cold-Photonics : tu fais maintenant partie des supop pour nous! Enfin, un grand merci à l'ensemble des doctorants de Cold-Photonics pour les bons moments que nous avons passés ensemble et les discussions scientifiques sur des sujets autre que les atomes froids.

Je remercie tout particulièrement les membres de AUFRONS. Romain, merci de m'avoir patiemment enseigné les subtilités de la manip. Travailler à tes côtés a été un véritable plaisir. Vincent, merci pour tes nombreuses explications sur les espaces tensoriels et ton engagement dans les questions théoriques. Guillaume, nous avons passé de nombreuses années ensemble depuis le début de supop, entre les soirées de rédaction interminables, les différentes conférences et tes conseils en FPGA. J'attends avec impatience ta soutenance de thèse pour finir de comprendre

---

ton sujet. Merci à Ruiyang de prendre la suite de la manip, que je sais entre de bonnes mains pour pouvoir conclure les mesures sub-longueurs d'ondes.

Enfin, je souhaite exprimer ma profonde gratitude envers Simon Bernon, qui a été un merveilleux co-directeur de thèse. Je te remercie de m'avoir accueilli dans l'équipe AUFRONS et pour toutes les connaissances à la fois théoriques et pratiques que tu m'as transmises. Ton dévouement en salle d'expérience et ta préoccupation pour le bien-être de tes étudiants m'ont permis de mener à bien ma thèse en m'y investissant pleinement. Tes compétences scientifiques, ton intérêt pour l'entrepreneuriat et tes qualités humaines m'ont très positivement marqué.

Au-delà du cadre académique, l'achèvement de ma thèse a été rendu possible grâce au soutien infaillible de mes amis et de ma famille, que je ne saurais jamais assez remercier.

Merci à mes parents pour l'éducation que vous m'avez offerte, de m'avoir transmis les valeurs que je porte fièrement aujourd'hui, et de m'avoir fourni un environnement dans lequel j'ai pu m'épanouir pleinement. Merci à mes grands-parents, Nicole et Henri, pour tout l'amour que vous me portez, n'oubliez jamais que je pense bien plus souvent à vous que je ne vous appelle. Merci à Josie d'avoir été une grand-mère formidable durant mon enfance, et de m'avoir appris tant de recettes de gâteaux; une part de moi regrette de ne pas avoir pu te connaître une fois adulte. Sache que je conserve précieusement la lettre que tu m'avais adressée le jour de ma naissance. Un grand merci à ma formidable sœur: je suis fier de la relation que nous partageons maintenant que nos crises d'adolescence sont derrière nous.

Merci mille fois à mes amis, les "Cinq Doigts" : Léo, Lynda, Louiza et Mika, pour vos conseils et votre soutien, disponibles 24 heures sur 24. Aux génies de l'Institut, Félix, Etienne et Lucas, merci d'avoir fait sortir le fantôme de supop: les années passées en ingé ont été merveilleuses à vos côtés. Méryl, merci pour tout ce que tu m'as appris sur la psychologie et sur la vie en général. Tu es une amie en or qui m'a fait énormément grandir. Merci à Charlotte ma binôme de colle préférée qui m'a fait survivre à la prépa. Merci à Yannou, mon musicien préféré, de m'avoir expliqué les réseaux de neurones et enmené à l'Opéra Garnier pour notre anniversaire. Merci à Carole de me rappeler qu'il existe un monde en dehors des sciences. Un grand merci à toute l'équipe de Bordeaux, Lisa, Coco, Coclo, Clo. Et surtout, Arnaud, avec qui j'espère partager de nombreuses sessions de surf et de voyages à l'avenir (il est peut-être temps de commencer à réfléchir à cette startup maintenant). Lola, j'aurais aimé te rencontrer plus tôt, mais nous avons bien rattrapé le temps perdu. Enfin, Pauline, tu as été mon pilier lors de la rédaction (merci d'avoir défendue le fait que j'ai le droit de profiter de la vie et de sortir en semaine).

# Contents

<b>1</b>	<b>Experimental apparatus</b>	<b>9</b>
1.1	Overview presentation of the experiment	9
1.1.1	Experimental setup schematics	10
1.1.2	Time and frequency control	10
1.1.3	UHV chamber and 780 laser system	12
1.1.3.1	Vacuum chamber design	12
1.1.3.2	780 nm laser bench	12
1.1.3.3	Dedicated 780 nm laser for sub-wavelength imaging	15
1.2	Imaging Axis	21
1.2.1	Absorption imaging principle	21
1.2.2	Low magnification imaging axis	23
1.2.3	Intermediate magnification imaging	24
1.2.4	Sub-wavelength imaging axis	24
1.3	Hybrid trap and Bose Einstein condensation	28
1.3.1	Atom cloud preparation	28
1.3.2	Magnetic trap and RF evaporation	28
1.3.3	Dipole trap laser at 1064 nm	28
1.3.4	Beam alignment	30
1.3.5	BEC in the hybrid trap	30
1.4	Two ways Accordion lattice	32
1.4.1	Optical setup	32
1.4.2	1529 laser beam properties	34
1.4.3	Optical characterization of the tunable lattice	35
1.4.4	Atomic characterization of the 1529 nm accordion lattice	39
1.4.5	Active common stabilization of the two lattices	40
1.5	Summary	43
<b>2</b>	<b>Sub-wavelength imaging</b>	<b>45</b>
2.1	Super-resolution imaging technique	46
2.1.1	Theoretical model and associated resolution	47
2.1.1.1	Cycling transition	48
2.1.1.2	Repumper transition	49
2.1.2	Experimental results and BAT-curves	51
2.2	Ultra cold atoms in optical lattices	55
2.2.1	Bose atoms trapped in an optical lattice	55

2.2.2	Adiabatic loading of a 1D lattice . . . . .	59
2.2.3	Lattice depth calibration using Kapitza-Dirac scattering method . . . . .	61
2.3	Sub-wavelength manipulation of atoms in a 1D optical lattice . . . . .	62
2.3.1	Double lattice commensurability . . . . .	62
2.3.2	Light shift with the double lattice . . . . .	63
2.3.3	Direct piezo calibration on the atoms . . . . .	65
2.3.4	Second piezo calibration . . . . .	68
2.4	Imaging of a single atom density distribution in a tight 1D optical lattice . . . . .	70
2.4.1	Sub-system preparation: cleaning sequence . . . . .	70
2.4.2	Fine cleaning characterization . . . . .	73
2.4.3	Scan of a single atomic density distribution . . . . .	75
2.4.3.1	Experimental result . . . . .	75
2.4.3.2	Lattices relative phase drift and broadening effects . . . . .	76
2.5	Summary . . . . .	82
<b>3</b>	<b>Atom chip</b> . . . . .	<b>83</b>
3.1	Transport method: rotating chip . . . . .	83
3.1.1	Presentation of the transport scheme . . . . .	84
3.1.2	Derivation of the trapping potential . . . . .	85
3.1.3	Experimental parameters . . . . .	89
3.1.4	Trap dynamic and heating . . . . .	93
3.1.4.1	Theory . . . . .	93
3.1.4.2	Experimental sources of noise . . . . .	99
3.1.4.3	Angle variation . . . . .	103
3.1.5	Study of experimental solutions . . . . .	106
3.1.5.1	New Focus stepper motor . . . . .	106
3.1.5.2	Tekceleo motor . . . . .	110
3.2	Design and setup of an atom chip . . . . .	113
3.2.1	Magnetic trap simulation . . . . .	114
3.2.2	CAD . . . . .	118
3.2.3	Fabrication . . . . .	118
3.2.4	Experimental characterization . . . . .	119
3.2.4.1	Thermal behavior . . . . .	119
3.2.4.2	Rotating arm . . . . .	122
3.3	Summary . . . . .	123
<b>A</b>	<b>Rubidium structure</b> . . . . .	<b>127</b>
<b>B</b>	<b>Electric dipole interaction</b> . . . . .	<b>129</b>
B.1	Far-detuned optical dipole trap . . . . .	129
B.2	Light shift given by second order perturbation theory . . . . .	130
<b>C</b>	<b>Ultra-cold atom trapping</b> . . . . .	<b>133</b>
C.1	Thermal cloud in an hybrid trap . . . . .	133
C.2	Bose Einstein condensate in a 3D harmonic trap . . . . .	134
C.3	Doubly-dressed state formalism . . . . .	137
C.3.1	Total trapping potential . . . . .	137

C.3.2	Presentation of the near-field trap . . . . .	138
<b>D</b>	<b>Experimental setup details</b>	<b>141</b>
D.1	Vacuum quality . . . . .	141
D.2	MOT and RF evaporation . . . . .	142
D.2.1	3DMOT . . . . .	143
D.2.2	OP . . . . .	146
D.3	Alignment of the 1529 nm accordion . . . . .	146
D.4	Lab and coils temperature . . . . .	149
D.4.1	Hybrid trap loading dependency on the MT coils parameters . . . . .	149
D.4.2	Room temperature stabilization . . . . .	152
D.5	General monitoring . . . . .	154
<b>E</b>	<b>Beam position measurement on a photo-diode edge</b>	<b>155</b>



# Introduction

## General context

Over the past century, our understanding of the physical laws governing the world we live in has tremendously improved. The development of the quantum theory has merged the description of both matter and light, in which these two previously distinct concepts now share the same underlying properties. Seventy years after the theoretical prediction by Bose and Einstein in 1924 [1], the first BEC was produced [2]. Like for many field of research, it took time and effort to perform the technological breakthrough that enabled the experiment to catch up with the theoretical prediction. A paradigm example of such research process is the development of the laser [3] that is nowadays a key and enabling technology in many field of research because of its high brightness and coherence properties. As an example, in the field of cold atoms, since the first demonstration of mechanical action of light on atoms [4], laser has been used to trap and cool down atoms [5, 6]. This has been a big leap towards reaching Bose-Einstein condensation in a dilute atomic vapors in 1995 [2].

Since its early development, the quantum theory has successfully described the microscopic world of few-body systems. However, tricky experimental and numerical simulation of larger systems are preventing a full understanding of such N-body correlated systems. The behavior of electrons in solid states crystals is a great example. Bi-dimensional electron gases that consists of electrons moving in a single atomic layer are of a great interest for the quantum physics and condensed matter communities. Behavior of high-Tc superconductors [7] or the properties of edge states in topological insulators [8] are still not perfectly understood and heavily studied. Nevertheless, quantum transport properties like Anderson localization of non interacting particles [9] are well described with the current quantum formalism and successfully extended in describing localization of light in a perturbed 1D [10] or 2D [11] photonic lattice potential.

These examples confirm Feynman idea's [12] that the description of a quantum system can be enlightened by studying another system sharing a similar Hamiltonian. Such systems are called Quantum Simulators (QS) and are developed alongside Quantum Computers (QC) solutions, both implementation sharing similar experimental difficulties. The race toward 'Quantum Supremacy' is launched [13]. Actual application require the ability to tailor at will the Hamiltonian driving the QS, and a good control of the system environment is required. Among the hardware, we can cite superconducting circuits where qubits are based on Josephson junctions which exhibit macroscopic quantum coherence and can behave like neutral atoms [14]. It is a technologically quite advanced solution has demonstrated the implementation of many quantum

optics operations [15]. However, such platforms are built using solid-state nano-fabrication techniques, present most of the time defects and are strongly coupled to their environment leading to a reduction of the coherence time and state randomization [16]. On the opposite side, photonic quantum simulators are based on the manipulation of photons which are weakly coupled to the environment and therefore well protected when they propagate in free space. In general, their manipulation is achieved by tailoring the coupling in cavities or in wave-guide structure [17]. An intermediate candidate are neutral cold atoms based systems. These can be implemented in their ground state in optical lattices or optical tweezers [18] or as arrays of Rydberg atoms [19].

The Quantum field has been rapidly growing and the interest from different investors and public institutions is steadily increasing. While previous results were driven by trying to have an experimental proof of a purely theoretical concept, we are now entering the 21<sup>st</sup> century with a new paradigm. Such quantum systems are now diffusing in the industry : quantum computers and quantum simulators based on neutral atoms are now upcoming products in several companies. Most of the time initiated as deep-tech startups founded by active researchers, such structures are now being integrated in bigger groups and finished products are appearing on the market. Such products offer integrated solutions and target at providing turn-key implementation of complex quantum apparatus.

One close by example is the former SME Muquans, now part of Exail, started in 2011 by Dr. B. Desruelle, Dr. A. Landragin and Dr. P. Bouyer. Their teams has recently demonstrated a Technology Readiness Level (TRL) of 9 for their atomic quantum gravimeter allowing the first detection of mass changes during a volcanic activity [20] by detecting gravity variations at the  $10^{-8}$  m/s<sup>2</sup> level.

Another example is PASQAL, which is based near Paris. It was co-founded by five researcher including the 2022 Nobel prize winner in physics Pr. A. Aspect. PASQAL already showed the ability to simulate 2D Anti-Ferromagnets using N=196 Rydberg atoms [21], pushing toward their goal to develop a Quantum Computer from ordered neutral atoms in 2D and 3D arrays. They also recently achieved defect-free single atom loading of a  $18 \times 18 = 324$  square lattice using optical tweezers, with a probability of 0.37 [22]. All these experimental developments led to the recent release of 'Quantum Discovery', a cloud-based web platform with which users can access PASQAL's quantum emulator with 100 Q-bit.

On the other side of the ocean, ColdQuanta was co-founded by Dr. D. Anderson. One of their open project (CROC program) is to deliver by 2026 to the US Department of Defense 10 prototype <sup>87</sup>Rb based optical clocks at a TRL over 6. They already provide a table-top solution (RuBECi) to produce and manipulate an ultra-cold cloud of <sup>87</sup>Rb . The solution is almost stand-alone and produce BECs of  $10^4$  atoms with a duty cycle of 1 Hz [23] and they started integrating an atom-chip to trap the atoms in a 1D optical lattice [24], demonstrating Landau-Zener tunneling.

Although not exhaustive, this list highlights the high interest for neutral atoms in the development of QC and QS with large private and public investment. Following fundamental research advances, some companies started investing in atom-chip as good candidates to trap and manipulate the cloud in a compact and robust way.

Out of the different candidates, ultra-cold neutral atoms trapped in optical lattices are a good toy-model system to study the quantum properties of matter [25, 26]. Indeed, the atomic interaction can be tuned via Feshbach resonances offering a high tunability while keeping a strong decoupling from the environment, therefore limiting decoherence process. However, the diffraction limit induces two issues for far field optical lattices. First, the scalability is greatly impacted as it impose a fundamental limit on the space requirement for qubits implementation. Also, the accessible energy regime is limited by the lattice recoil energy scale ( $E_R \propto (\text{lattice spacing})^{-2}$ ). For conventional far-field lattices, this prevents to enter deeply into the quantum regime of solid state matter, where the spacing is of the order of the Angstrom.

In my PhD, we have studied another solution that consists in trapping an ultra-cold cloud on an atom-chip where the cloud can be coupled to nanophotonic devices. Despite technical complexity, this approach conserves the long coherence time of neutral atoms, which are well isolated from their environment, while strongly increasing the versatility on the Hamiltonian design. In the section below, we present our solution for implementing such hybrid system.

## PhD framework

The cost of combining two systems is paid by stacking up the constraints and restrictions. In order to properly couple an atomic cloud with a macroscopic device, one should reduce the distance  $d$  between the two. For an evanescent coupling, we expect that the interaction decrease exponentially with the distance. However, in the vicinity of a surface, the Casimir-Polder [27] potential increase as  $1/d^4$  and a fine balance has to be found in order to strongly couple the atoms to the field while still trapping them. In practice this has limited current experiment to the range  $d > 200$  nm.

One solution was proposed in [28] by tailoring the quantum vacuum forces to trap a cloud of atoms close to a dielectric surface. The surface plasmon frequency  $\omega_p$  of the surface is tuned at resonance with an atomic transition. By approximating the surface electromagnetic response with a Drude model, the resonance result in a repulsive Casimir force for the excited state. A 780 nm laser radiation tuned close to resonance will couple the ground and excited states, effectively dressing the ground state. This creates a versatile trap at a position controlled by the 780 nm laser radiation frequency. However, this method requires to match the atomic frequency transition and the plasma frequency which is absolutely not obvious and require proper engineering.

Based on this idea, we implemented a similar solution whose building blocks are presented in Fig. 1 a). The Casimir-Polder (CP) forces act as attractive forces (Fig. 1 b) ). The trap is formed at a distance  $z_t$  by adding an optical repulsive force arising from the AC-Stark interaction with a blue-detuned laser radiation [29] as depicted in Fig. 1 c). This comes from a plasmon excitation of a metallic layer in the multi-layer surface that produces an exponentially decaying spatial profile which dress [30] the excited state.

Recent progress realized in nano-fabrication techniques allows one to design structures of size in the tens of nano-meter range. Applying such structuration on the dielectric surface will modulate the CP interaction and produce an optical lattice with a spacing not constraint by the diffraction limit.

However, this rise the issue of coherence and lifetime of the trap. We have studied the 4

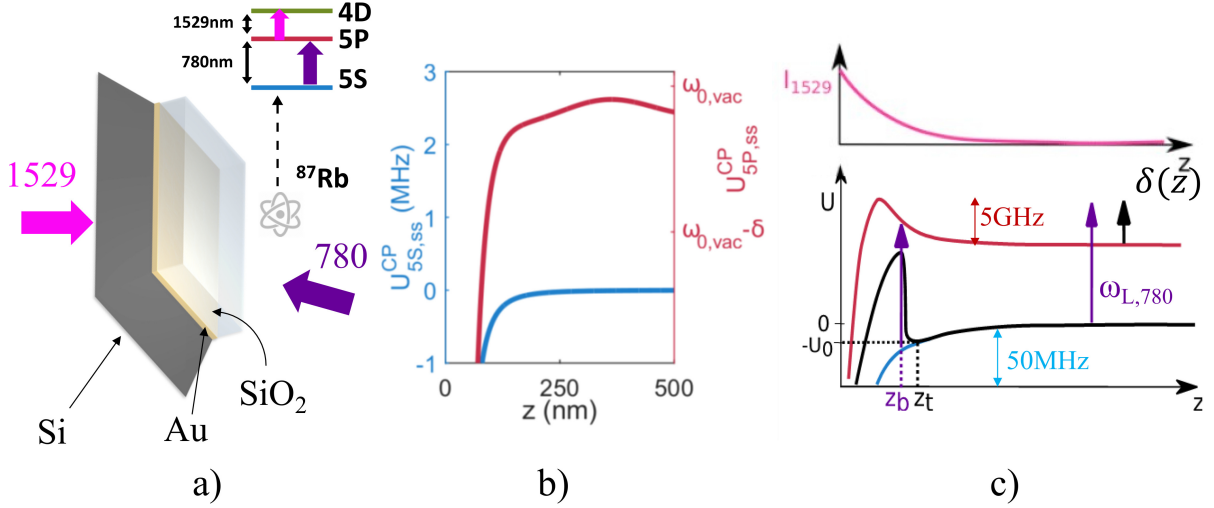


Figure 1: Doubly dressed state (DDS) state trapping scheme. a) Sketch representation of the trapping method including the surface, the dressing lasers and the atoms. b) Casimir-Polder potentials shifting the internal energy levels of <sup>87</sup>Rb atoms as a function of their distance to the surface. c) Exponentially decaying intensity profile of the 1529 nm laser radiation and the resulting potential including CP forces. The DDS trap center  $z_t$  and the resonant position  $z_b$  of the 780 nm laser radiation are not overlapped.

heating mechanism we believe to be dominant in such DDS trap [31]:

- Tunneling effect:  $\tau_t \approx \infty$ . The trap is not the absolute minimum of the potential that diverge in the direction of the surface because of CP forces. Thus, the wave-function can tunnel through the barrier, associated to the loss rate  $1/\tau_t$ .
- Residual scattering[28]:  $\tau_s$ . The trapping position and the resonant position for the 780 nm radiation are only separated by only a few tens of nm. Even tho the strong shift of the excited state reduces the residual scattering rate, it does not entirely cancel it. The rate can range from 400 ms to only 0.1 ms depending on the lattice spacing and on the power of both lasers.
- Transient heating:  $\tau_c = 3.5$  s. After each spontaneous emission event, the coherence term of the density matrix become zero. It is then restored by the 780 nm laser drive with a detuning  $\delta$  over a time  $1/\delta$  during which the wave-function is evolving in another state, which is not trapped and lead to heating.
- Anti-dumping:  $\tau_a = 3$  s. The derivation of the DDS trapping potential is carried is done under the steady state approximation. However, the coherence cannot adapt infinitely fast when the atom move. This leads to correction on the force that correspond to an anti-damping forces and result in heating of the wave-function.

In the end, the trap lifetime is given by the incoherent sum of all these process  $1/\tau = 1/\tau_t + 1/\tau_s + 1/\tau_c + 1/\tau_a$ .

While such trap is not limited by diffraction and can attain sub-wavelength spacing, usual

imaging techniques are. Thankfully, we share this burden with active researchers in the field of biology. They have developed different method that can be divided in two categories: either as super-localization where the center of individual particles are pointed or as super-resolutions where the size of the excited volume is below the diffraction limit set by the wave-length of the laser field driving the interaction. The method we have implemented belong to the second category which can be produced by different physical mechanism.

For example, in Super-Resolution illumination Microscopy [32] (SR-SIM), the illumination is structured. This converts the high frequency pattern of the sample to lower frequencies by Moiré magnification. Using multiple images at different structuration period and directions, and using reconstruction algorithm, one can recover the sub-wavelength details.

Another example is STimulated Emission Depletion [33] (STED) where the fluorescence volume is reduced using stimulated depletion. A spatially homogeneous laser beam excite the samples. A second doughnut-shape laser beam is used to selectively deactivate the fluorescence in the outer regions of the excited area. A non-linear response of the samples at the center of the doughnut-shaped beam dominates, resulting in a sub-wavelength volume. By scanning the two beams across the sample, a high-resolution image can be created.

In the cold-atom community, in-situ imaging techniques resolving each site has been allowed using quantum gas microscope [34]. However, such microscope are restricted to lattice period larger than the PSF of the objective ( $>780/2$  nm). To bypass this limit, the cold atom community has started to implement super-resolution methods.

For example [35] implement both SR-SIM and STED method to optical lattices. They used an optical lattice on a repumper transition to provide bright field absorption images of atoms ground state in a sub-wavelength volume. Using the Moiré effect, they could measure sub-wavelength details at the micrometer scale.

Another technique based on biology method is developed in [36]. They rely on an electromagnetically-induced-transparency scheme with an optical lattice for the control beam intensity. This coherently transfers atoms in a sub-wavelength volume to a bright state that is imaged with a standard imaging system. Their approach is valid for any 3-level system.

In [37], a super-localization method control the spin internal degree of freedom between two hyperfine manifolds. This method requires a focused beam with a diameter smaller than the lattice period and a magic wavelength to shift the level of the upper hyperfine manifold and keep the lower one unchanged.

The method we implemented is related to [35]. Atoms are transferred over sub-wavelength volumes toward an intermediate state via the scattering of only few photons per transferred atoms. The principle of the method, and its spatial resolution are given by a dressing similar to the DDS trapping scheme, detailed in Chapter 2.

The last enabling point to consider is the adiabatic transport of the cloud to the near field of the surface. Indeed, to load the final DDS trap (Fig. 1), the cloud should be trapped at a distance between tens to few hundreds of nanometers. Standard methods prepare clouds

away from the surface before transport [38]. Unfortunately, the transport usually does not reach below  $1 \mu\text{m}$  from the surface.

Neutral atoms have been transported using magnetic or optical traps. Magnetic traps can be displaced over long distances by physically translating a single set of coils out of the vacuum chamber [39, 38] or by successively transferring the atoms through a chain of permanent magnets forming a magnetic conveyor belt [40] or a chain of regular and supra-conducting coils [41]. The same type of conveyor belt scheme can be implemented on atom-chip platforms [42]. Over shorter distances, on-chip transport can be done by varying the current in the conducting wires forming the trap [43, 44].

Optical traps can be used as controllable optical tweezers displacing entire BEC [45] or single atoms [18], or using traveling lattices (optical equivalent of the magnetic conveyor belt) [46, 47]. Continuous transfer between two traps can also be achieved using a guiding laser beam [48]. There are also mixed magneto-optical approaches [49].

For this problematic, we propose a transport method [50] presented in Fig. 2. Atoms are initially trapped in the first fringe of a 1D optical lattice obtained by retro-reflecting on the surface a laser radiation at a high incidence angle (Fig. 2 b ). A rotation of the surface decrease the interfringe and compress the cloud toward the surface (Fig. 2 c ). This transport the atomic cloud from  $5 \mu\text{m}$  to  $250 \text{ nm}$  from the surface (Fig. 2 d ). Current carrying wires are also integrated in the atom-chip to produce a complementary magnetic potential.

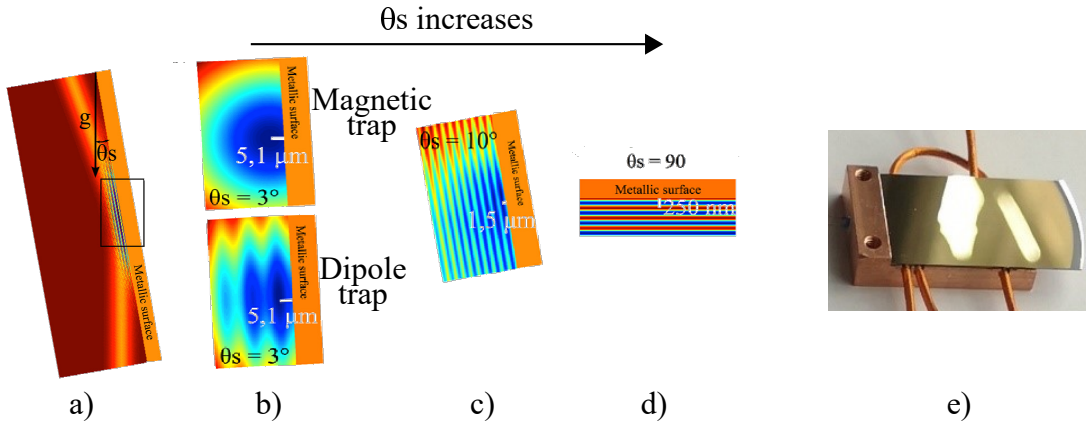


Figure 2: Sketch of the Rotation Transport method. a) Global picture of a laser reflected on a surface with a high incidence angle. b) Insets of a), presenting the magnetic trap generated by current carrying wires implemented in the atom-chip and the dipole trap generated by the laser. The total potential is plotted in c) and d) as the incidence angle decrease ( $\theta_s$  increase). e) Photo of the fabricated atom-chip.

My PhD thesis is a step toward the experimental implementation of such potentials using doubly dressed state traps.

The advances presented in this PhD thesis can be split into two parallel tracks both tackling one of the issue mentioned above. On one hand, the doubly dressed state trapping method is applied in free-space as a sub-wavelength in-situ imaging method. On the other hand, we focus on the implementation of the chip itself. While not presenting nano-structuration yet, experimental progress have been made to fabricate of a functional atom-chip.

The manuscript is organized as follows:

First, we present in chapter 1, the experimental apparatus used to produce and manipulate a free-space doubly dressed  $^{87}\text{Rb}$  BEC. We emphasize on the efforts to improve the experimental conditions stability.

We detail in chapter 2 the experimental implementation of a sub-wavelength imaging method that is an application of the doubly dressed state scheme. Using the dipole force to dress the first excited state of  $^{87}\text{Rb}$  atoms, we are able to address specific part of the cloud with a spatial resolution under 30 nm. This method is used in section 2.4 to super-resolve in-situ individual atomic wave-packets of a cloud trapped in a 1D optical lattice.

Finally, chapter 3 report on the progress made towards the implementation of the atom-chip. A specific transport method allowing to transfer the cloud in the near-field trap is presented and we experimentally study its implementation and the expected behavior of the cloud. Complementary simulations detail the magnetic trapping capabilities of the chip and its expected performance to reach Bose-Einstein condensation and efficient transport. We conclude the chapter by presenting the design, fabrication and experimental characterization of a prototype chip.



# Chapter 1

## Experimental apparatus

We present in this chapter the experimental apparatus (called 'main apparatus') we have developed to produce and study doubly dressed  $^{87}\text{Rb}$  BEC in free space. We start this chapter by recalling in section 1.1 the building-blocks for reaching Bose-Einstein condensation. We present modifications that has been realized in order to increase polarization and power stability of the laser beams and the general atom number repeatability. In section 1.1.3, we discuss vacuum related issues and gives relevant lifetime for the cloud preparation. The 780 nm laser architecture, core of the tools for interacting with a cloud of rubidium, is also detailed there. Imaging axis installed on the experiment are introduced in section 1.2. We detail in section 1.3 the hybrid magnetic and dipolar trap configuration we use to reach the condensation. Then, we present in section 1.4 the two-way accordion lattice installed for the sub-wavelength imaging scheme (see 2.1).

The experiments detailed in Chapter 2 put stringent requirement on the shot-to-shot experimental repeatability. In what follows, we recount many technical aspects of the experimental apparatus for which we try to give immediate relevancy and the reader may have to come back on them while reading Chapter 2.

### 1.1 Overview presentation of the experiment

We begin by listing the fundamental elements of our experimental setup. Further details can be found in previous thesis [51, 52, 53, 54]. The BEC preparation sequence can be divided in three main stages : laser cooling in a MOT, spin-flips evaporation in a magnetic trap, and optical evaporation in an hybrid trap.

A broken glass cell containing Rubidium atoms feeds a 2D Magneto-Optical Trap (2DMOT) in a separate vacuum chamber. A Push beam at 780 nm tuned 2.2  $\Gamma$  below the cycling transition  $|5^2S_{1/2}, F = 2\rangle$  to  $|5^2P_{3/2}, F = 3\rangle$  loads a 3DMOT from the 2DMOT through a 1.5 mm diameter opening between the science chamber and the 2DMOT chamber. This allows for an increase selectivity on the transverse temperature and a differential vacuum between the two chambers. The cloud is then compressed in a Compressed-Magneto-Optical Trap (CMOT) before decreasing

the magnetic trap to perform an optical red Molasses and polarizing the atomic sample with Optical Pumping (OP) steps. The cloud is transferred to a quadrupole Magnetic Trap (MT) and undergo four successive spin-flip evaporation steps. Finally, a far-off-resonance dipole trap (FORT) is added on the MT, realizing an Hybrid Trap in which we perform optical evaporation, up to a pure BEC which is the starting point of the experiments presented in Chapter 2.

### 1.1.1 Experimental setup schematics

An overview schematic of the main apparatus, defining optical axis for the different beams is given Fig. 1.1 showing the  $(x, y)$  plane. We introduce the different optical axis :

- OP : 780 nm optical pumping beams of repumper('OP R') and cooler('OP C'), aligned at  $45^\circ$  in the  $(x; y)$  plane.
- Push : Push beam on the cycling transition at 780 nm to push the atoms from the 2DMOT to the 3DMOT chamber.
- MOT : 780 nm magneto-optical trap collimated beams, both the repumper and cooler are injected in the same fiber.
- Imaging at  $45^\circ$  : imaging axis with a magnification  $\times 0.2$ .
- Imaging along DT1 : imaging axis with a magnification  $\times 2$ .
- DT1 : dipole trap arm 1 at 1064 nm, propagating in the  $\mathbf{y}$  direction with a waist calibrated on the atoms  $w_{DT1}^V = 49.0(1) \mu\text{m}$  for the vertical direction and  $w_{DT1}^H = 51.5(2) \mu\text{m}$  horizontally.
- DT2 : dipole trap arm 2 at 1064 nm, propagating in the  $\mathbf{x}$  direction with a waist calibrated on the atoms  $w_{DT2}^V = 63.1(1) \mu\text{m}$  for the vertical direction and  $w_{DT2}^H = 67.4(4) \mu\text{m}$  horizontally.
- Lattice 1064 : two counter propagating beams at 1064 nm propagating in the  $\mathbf{y}$  direction. The forward beam will be referred to as '1064 lattice forward' and the reflected beam as '1064 lattice RR'. The forward beam waist is calibrated to be  $w_{1064} = 46.8(2) \mu\text{m}$ .
- Lattice 1529 : accordion lattice at 1529 nm with an adjustable angle with a translation stage used to get co-propagating beams (without prism PS991) or counter propagating beams (with prism and when viewed from the top, only the right co-propagating beam) propagating mostly in the  $\mathbf{y}$  direction and interfering on the atoms. The forward beam closest to the fiber collimator is often referred as '1529 Right ', the other one as '1529 Left' and the reflected beam from the right path as '1529 RR'.

### 1.1.2 Time and frequency control

Our control system is based on the software Cicero Word Generator, where analog and digital voltages, frequencies and timings are defined and set via National instrument DAC cards. The

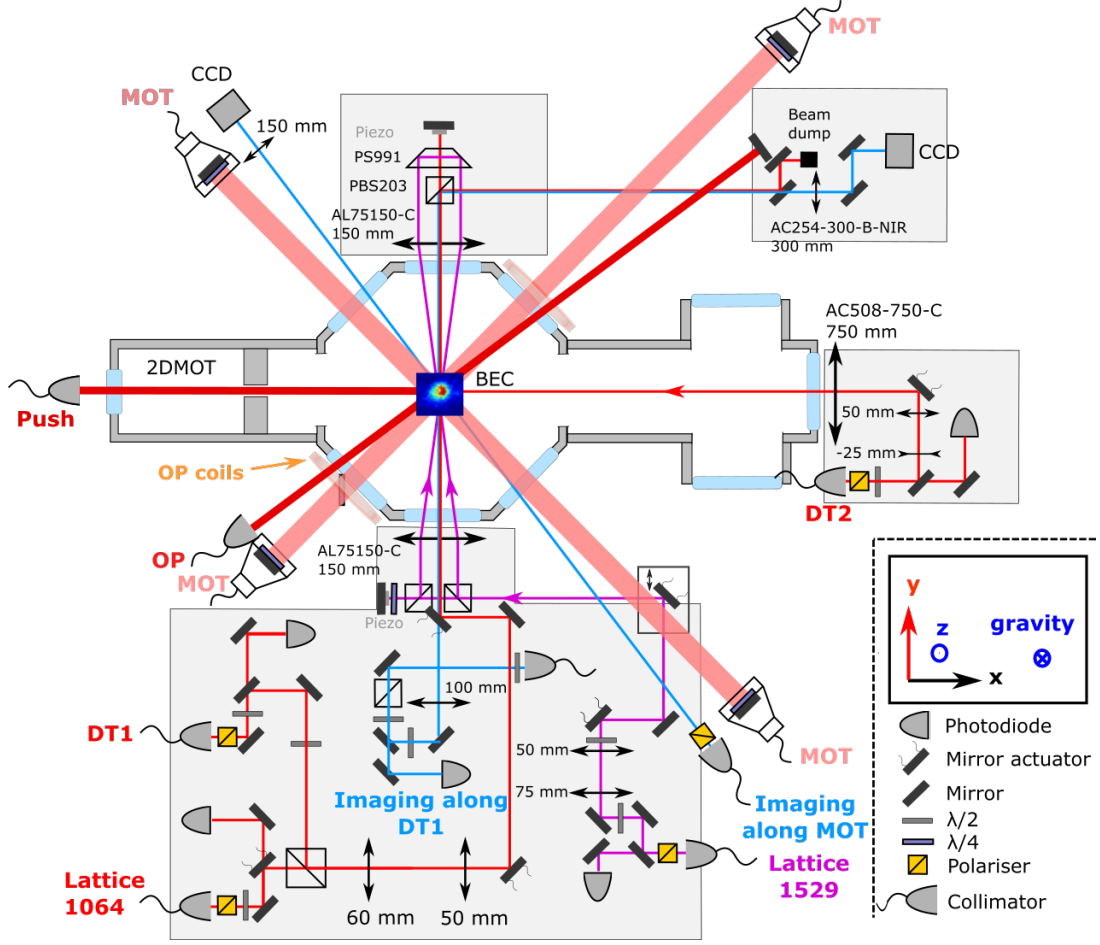


Figure 1.1: Optical schematics of the main experimental setup in the  $(x; y)$  plane. MOT collimators are 2 inches of diameter and have a mounted mirror and quarter wave-plate on top of them. Imaging axis collimator are made with caged lens and fiber plate. The rest of the collimator are mostly PAF from Thorlabs.

output connectors block of the NI cards has been replaced by 'buffer card' circuits developed by the electronics workshop to reduce voltage noise on the output. If needed, further details can be found [54, p.56]. These buffer outputs cards give a linear response<sup>1</sup>. The NI cards are clocked by an FPGA, enabling the separate control of the resolution of every sequence steps, up to  $2 \mu s$ . Timings below this precision can be achieved using different solutions that we present when needed.

Variable frequencies on the experiment are generated by a 4-channel DDS AD9959 from Analog Devices, with 10-bits DACs producing up to 500 MSPS. It is clocked by an amplified O-CMR058IS-NS-R multi frequency reference module from NEL Frequency Controls at 500 MHz. At this output frequency, the crystal phase noise is specified at different frequencies, found in Table 1.1.

<sup>1</sup> $V_{out} = aV_{Cicero} + b$  with both coefficients depending on the buffer channel considered with  $a \approx 0.98$  and  $b \approx 0.25$  mV.

Frequency (Hz)	Typ. SSB Phase noise (dBc/Hz)
10	-111
$10^2$	-118
$10^3$	-149
$10^4$	-163
$10^5$	-166

Table 1.1: Single side band (SSB) phase noise of the 500 MHz NEL frequency reference of the DDS at different frequencies

### 1.1.3 UHV chamber and 780 laser system

Collisions with untrapped fast rubidium atoms or other background gases induce a loss of atoms and can increase the internal energy of the system. Thus, vacuum quality will greatly influence lifetime of trapped atoms. For instance, a good vacuum quality allows in [38] a lifetime in a magnetic trap of more than 180 s, decreasing to only a few seconds where vacuum quality is poor. For pressure below  $10^{-9}$  mbar, measurement of the MOT loading time and dynamic of alkali-metal-atom gives a reasonably accurate pressure gauge[55, 56]. To a certain extend, the MOT lifetime[57] itself can be used as a vacuum pressure measurement with a linear dependency between 3DMOT lifetime and background pressure.

In this section, we present the vacuum chamber we have and pinpoint a poor vacuum quality as being major limiting factor on the production of our BEC.

#### 1.1.3.1 Vacuum chamber design

The science chamber where the 3DMOT (and further traps) is produced is an octogone from Kimball physics with eight CF40 and two DN100CF openings. Two ion pump NEX Torr D100-5 of 100 L/s each, maintain the vacuum in the 3DMOT chamber. Monitoring the ion pump leakage current gives the residual pressure in the chamber, initially near  $10^{-10}$  mbar, which is close to the acceptable limit for ultra-cold atoms experiments [58]. The structure is shown Fig. 1.2. Horizontal viewports have an optical access diameter of 34 mm (5 mm width) and re-entrant vertical ones have an optical access diameter of 75 mm (same width). The inner facet of the re-entrant windows are separated by 20 mm.

In appendix D.1, we give some details on the vacuum quality that has degraded along the PhD. In March 2023, it resulted in a MT lifetime of 3.8 s. In the same appendix, we also give some information on rare gas instability that we have also observed. With such short lifetime, Bose-Einstein Condensation was not reached anymore.

#### 1.1.3.2 780 nm laser bench

A commercial complete laser system for rubidium experiment from Muquans provide the 780 nm lasers used to address the cooler and repumper transition of  $^{87}\text{Rb}$ . More details can be found in [51]. This rack-mounted system is composed of three telecom wavelength laser near 1550 nm, frequency doubled to reach the 780 nm region with linewidth below 100 kHz.

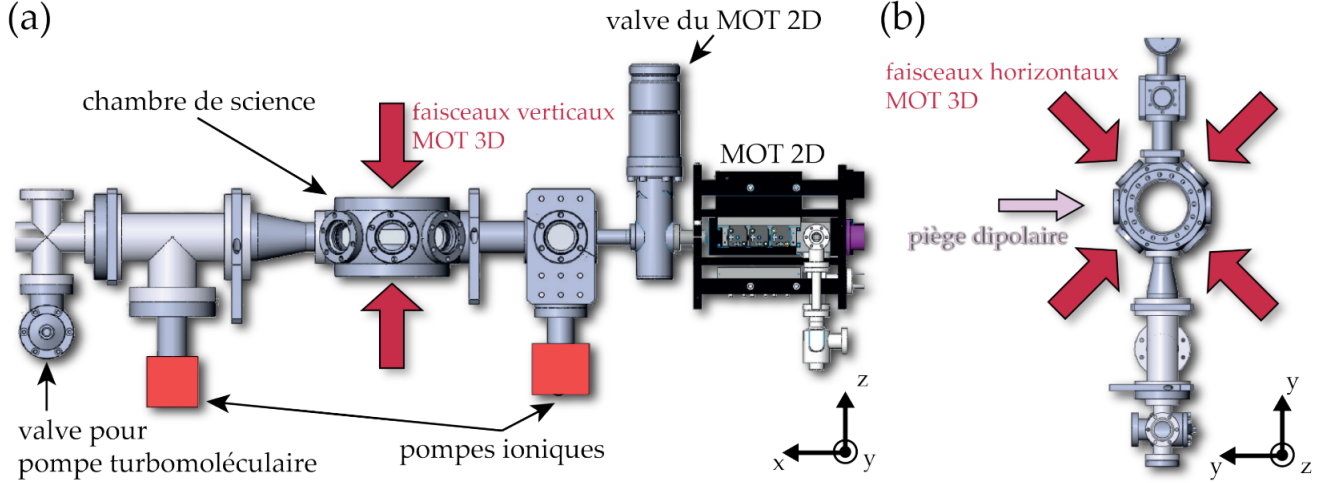


Figure 1.2: CAD of the vacuum chamber. Image from [53].

- Master laser (M). Locked by saturating absorption onto the crossover between the two excited states  $|F_e = 1\rangle$  and  $|F_e = 2\rangle$ . It is used to address repumper transition of the  $^{87}\text{Rb}$  D2-line (see  $^{87}\text{Rb}$  structure in A.1). Once locked, it has a fixed frequency.
- Slave 1 (S1) and Slave 2 (S2). Both lasers are beatnote phase-locked to the Master with an offset to address the cooling transition. The lock point is controlled with a frequency from the DDS, which can be adjusted during the experimental sequence with a tunability up to 4 GHz.

These 3 lasers have a fiber output going to a free space bench where we split up and combine the different laser radiations before injecting fibers going to the main experiment. On this bench, they are split and distributed over different arms, presented Table 1.2. Optical power is controlled with AOM with rise time of 200 ns. Mechanical shutters are used for a perfect extinction with typical response time of 2 ms.

**Master lock offset.** On our bench, the absoluteness of all three wavelengths is given by the saturated absorption lock of the Master. This lock has a tunable offset which drifts in time mainly depending on the room temperature. We monitor and correct these small deviations ( $\simeq 0.2\Gamma$ ) by performing laser spectroscopy on the cycling transition. With such correction, we obtain an absolute frequency at better than  $0.05\Gamma$ . During my PhD, this offset was controlled by a  $4.6\text{ k}\Omega$  trimmer working close to its balance point. The tunability and sensitivity of the trimmer was too high and it has been replaced by a fixed  $2.2\text{ k}\Omega$  resistor, a variable  $100\ \Omega$  and another fixed  $2.2\text{ k}\Omega$ . While with the previous solution, the drift could be  $\pm 0.2\Gamma$  over a month and  $\pm 0.4$  over several months, the new solution allows to reach an absolute precision of  $\pm 0.01\Gamma$  and drifts over 3 months under  $\pm 0.06\Gamma$ . We increased our absolute frequency stability by almost a factor 7. Importance of this parameter will be highlighted throughout the manuscript.

Output fiber	Seeding laser	Transition $ F_g \rightarrow F_e\rangle$	Maximum output power (mW)
MOT2D H C	S1	$ 2 \rightarrow 3'\rangle$	76
MOT2D H R	M	$ 1 \rightarrow 2'\rangle$	15.0
MOT2D V C	S1	$ 2 \rightarrow 3'\rangle$	77
MOT2D V R	M	$ 1 \rightarrow 2'\rangle$	14.2
Push	S1	$ 2 \rightarrow 3'\rangle$	0.580
MOT3D C	S2	$ 2 \rightarrow 3'\rangle$	133
MOT3D R	M	$ 1 \rightarrow 2'\rangle$	21
OP C	S2	$ 2 \rightarrow 2'\rangle$	0.81
OP R	M	$ 1 \rightarrow 1'\rangle$	0.59
Imaging	S2	$ 2 \rightarrow 3'\rangle$	10
Beat-note	M	$ 1 \rightarrow 2'\rangle$	1

Table 1.2: 780 optical free space bench power recap. The maximum powers are measured just before the fiber injection going towards the experiment. Typical fiber injection have an efficiency close to 0.8. 'Beat-note' is used to lock an independent laser '780 R Tunable' presented below.

**Free space power lock** Over time, we have noticed that the performances of the laser rack degraded. The output power is slowly decreasing. To increase the atom number stability in the BEC, we installed a power-lock on the free space output power of each 780 lasers. A photo-diode detect the power on the free space bench<sup>2</sup> and an analog lock circuit act on the power-supply of the 1560 EDFA of each lasers. Monitoring the power on the free space bench shows the stability improvement, presented Fig. 1.3. We give table 1.3 the relative stability with and without the

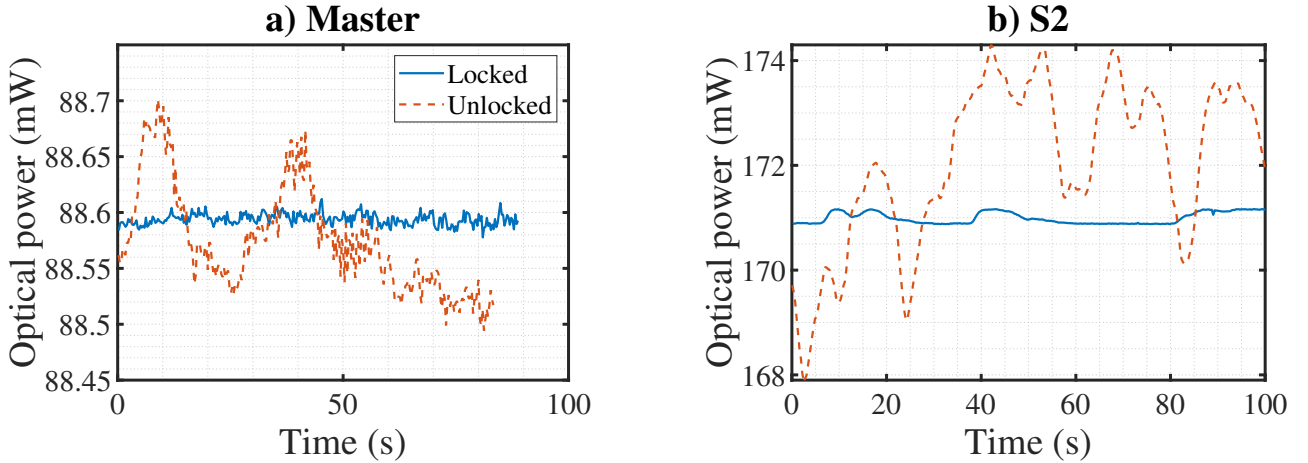


Figure 1.3: Free space optical power measured close to the fiber collimator. On both Master (top) and S2 (bottom), we see that the lock (plain lines) increase the power stability. Data for S1 are not shown but are very similar to S2.

lock for each lasers defined as  $\epsilon_P = std(P)/mean(P)$  where  $P$  is the optical power measured. For each lasers, the stability is improved by an order of magnitude.

**Polarization fluctuations induced by AOM during heat-up.** On the optical bench, we have observed that the heating of AOM was rotating the laser polarization. Indeed, the low

<sup>2</sup>for details on the bench, see [31].

$\epsilon_P$	Master	S1	S2
unlocked	$5.4e-4$	$3.2e-3$	$9.5e-3$
locked	$6.2e-5$	$\emptyset$	$5.7e-4$

Table 1.3: Recap table of the achieved optical power stability on the Muquans free space bench. The lock improve the stability by an order of magnitude for each laser.

power port of polarizing beam splitter cubes working close to the maximum extinction presents high relative polarization fluctuations. Using this drifting polarized beam as an input of an AOM will result in amplified polarization rotation on the diffracted order. The polarization stability can be increased by adding a second PBS to further clean out the incident polarization on the AOM at a cost of reduced optical power. To further reduce this effect, AOM are injected either in CW mode for application requiring long term stability like the MOT, or with comb of pulses for pulsed operation like for the imaging. In Fig. 1.4, we plot the evolution of the output polarization of a free-space AOM by measuring the two ports of a PBS. The polarization rotation has a dramatic effect on the low power port, decreasing the power by 82% and induce a power drift of 7% on the high power port.

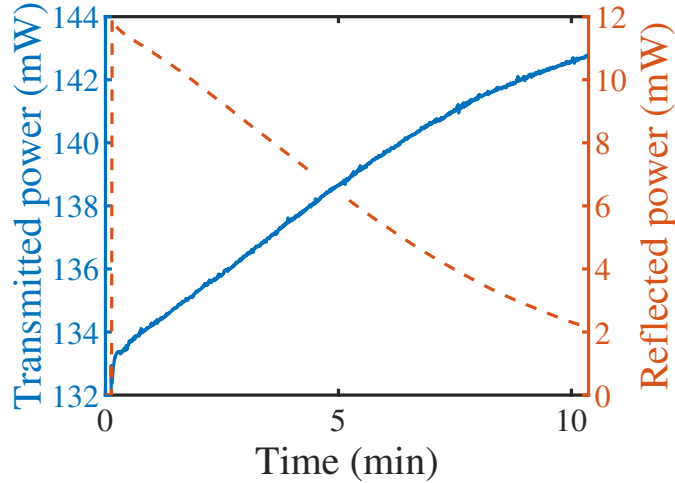


Figure 1.4: Polarization drift at the turn ON of the free space 3DMOT C AOM, monitored by measuring the power balance on both arms of a PBS.

### 1.1.3.3 Dedicated 780 nm laser for sub-wavelength imaging

The method proposed in Chapter 2 to image sub-wavelength volumes require a tunable 780 nm repumper radiation, often referee to as '780 R Tunable'. We describe in this section the laser setup and the solutions implemented to increase both its power and polarization stability. We have settle for a Sacher free-space butterfly laser diode at 780 nm on a separated boxed breadboard. The VBG-780-0818-00124 diode<sup>3</sup> is locked in temperature and driven in current by a Koheron CTL200-1 driver. It can deliver up to 65 mW at 780.24 nm after an optical isolator, and we have 21 mW available after an AOM and fiber injection. Both the free running and

<sup>3</sup>Compared to the setup presented in [54], the diode has been replaced, explaining the difference in the experimental data.

locked laser linewidth has been measured to be less than 100 kHz. The optical setup schematic is given Fig. 1.5. The free-space overlap with 'Master' is collected by a photo-diode and produces a beat-note signal which is converted by a frequency-voltage converter electronic circuit to feedback the laser diode current (0.3 GHz / mA) and lock on the repumper transition. The Sacher laser radiation passes through an AOM driven at 260 MHz and the +1 order is injected into a fiber going to the atoms.

Considering the negative peak of the beat-note, the detuning  $\Delta$  between the tunable repumper and the repumper transition is

$$\begin{aligned}
 \Delta &= \nu_{TR} - \nu_{1 \rightarrow 2'} + \Delta_{AOM} \\
 &= -\nu_B^- + \nu_M - \nu_{1 \rightarrow 2'} + \Delta_{AOM} \\
 &= -\nu_B^- - 156.9/2 + 260.0 \\
 &= -\nu_B^- + 181.5 \text{ MHz}
 \end{aligned} \tag{1.1}$$

where  $\nu_{RT}$  is the output frequency of the 780 R tunable,  $\nu_M$  the one of Master,  $\nu_B^\pm = \pm(\nu_{RT} - \nu_M)$  the positive (resp. negative) frequency component of the beat-note at low frequency and  $\nu_{1 \rightarrow 2'}$  the frequency of the repumper transition  $5S_{1/2} |F = 1\rangle \rightarrow 5P_{3/2} |F = 2'\rangle$ . Thus, to be resonant

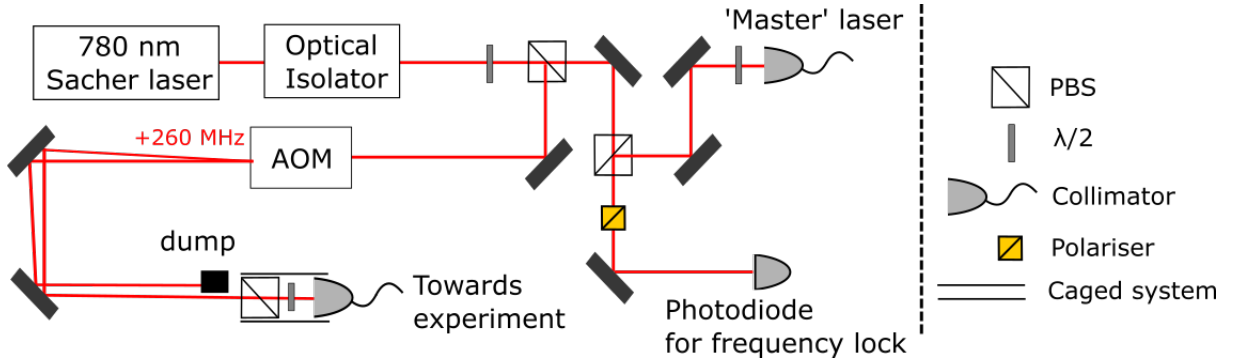


Figure 1.5: Schematics of the 780 Sacher optical bench.

with the repumper transition, the beat-note negative peak should be at 181.5 MHz. In the current configuration, the Sacher laser stays locked over beat-note frequencies ranging from 125 MHz to 600 MHz, corresponding to detuning from the repumper transition from  $-0\Gamma$  to  $+70\Gamma$ . The setpoint is controlled by a voltage generated by a Cicero analog output ( $V_C$ ) according to :  $\nu_B^- (\text{MHz}) = -106.8 \times V_C (V) + 59.04$ .

**Stabilization of the AOM RF chain** The experiments detailed in Chap.2 put stringent requirement on the repumper optical power stability. Pulses duration were too short to implement a power-lock so we have improved the free-running stability.

Recalling the optical setup Fig. 1.5, the laser intensity at the fiber output depends on the AOM response. This AOM (ATM-2001A2 from IntraAction Corp.) is enabled by a TTL generated by Cicero and driven by an RF chain presented Fig. 1.6. In order to produce multiple pulses in a single step and increase the versatility, we are using an analog channel instead of the general TTL output . The minimum timing response of this TTL is then  $2 \mu\text{s}$  followed by

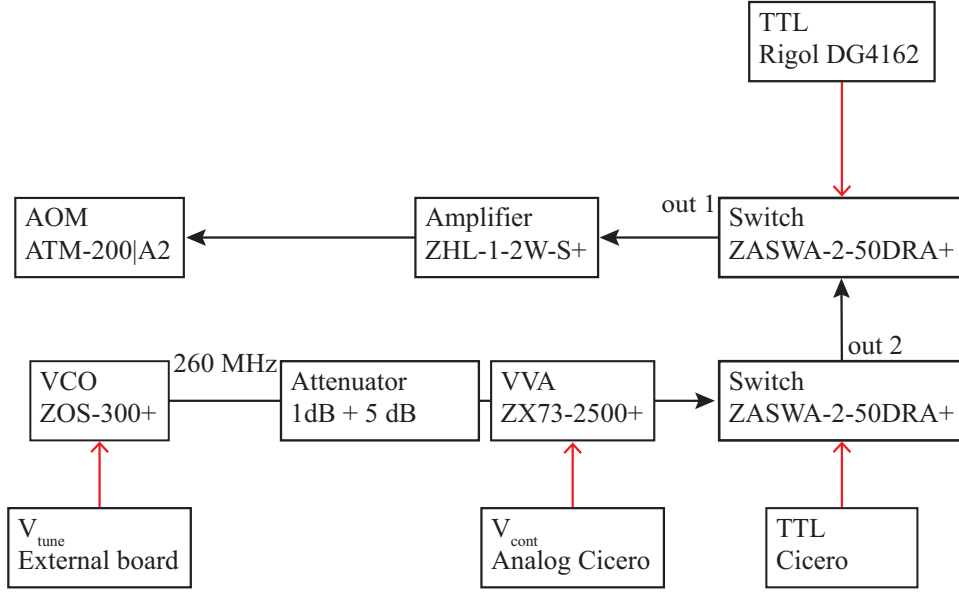


Figure 1.6: Circuit diagram of the RF chain driving the 780 R Tunable AOM. The RF path is represented with black arrow and external controls in red. We use two switch in cascade in order to obtain pulses shorter than  $2 \mu s$ , limited by Cicero. RF will be send to the AOM when the Cicero TTL is HIGH but the DG4162 waveform generator TTL is on LOW, producing pulses as short as  $400 ns$ .

a constant regime. The VVA (mini-circuit, ZX73-2500-S+) has typical (Rise ; Fall) times of  $(14 ; 25) \mu s$  but modifying the setpoint give an important initial overshoot with a relaxation to the target value in  $80 \mu s$  that we can see Fig. 1.7. Since the AOM presented leakage lower than  $10 nW$  when the TTL is OFF, we set the VVA in advance. In order to produce pulses shorter to the  $2 \mu s$  given by the Atticus FPGA, we use two RF switch in series, one being driven by another independent wave-form generator (DG4162) cutting into the effective TTL generated by Cicero. By adjusting the delay between the two TTL, we can produce light pulses as short as  $400 ns$ , limited by the rise and fall time of the AOM on a collimated beam.

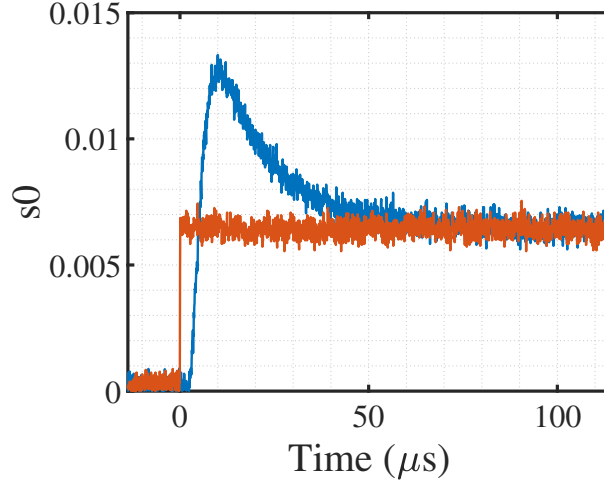


Figure 1.7: 780 R Tune light pulses acquired with the monitoring system during the experiment. The  $x$  axis zero is given by the start trigger of the AOM TTL. On the curve with an overshoot (blue curve), the VVA value is changed at the same time that the TTL switch to high value. We can clearly see the response time of the VCA, with a slower rise of the power and an overshoot, reaching twice the final setpoint value. The other curve (orange) is obtained by changing the VCA setpoint  $200 \mu\text{s}$  before switching the AOM TTL, producing a sharp pulse with no overshoot. The VVA initial rise time seems to be close to  $10 \mu\text{s}$ .

**Optimized setup for limiting polarization fluctuations in fiber injections.** For simplicity, the 780 nm beams are not power-locked before interacting with the atoms. For these beams, polarization and power fluctuations need to be minimized. We have observed that the stability of polarization before the fiber was key to reduce fiber induced polarization fluctuations. For this purpose, we added a polarizer in front of the fiber coupler and use caged system to improve the optical alignment. With the previous scheme, the fiber output ellipticity was around  $3^\circ$ . With the new scheme shown Fig. 1.8, adding a caged PBS, improving optical alignment and optimizing the orientation of the SM1-Z mount holding the lens, reduce the ellipticity down to  $\eta < 0.8^\circ$ . This setup has been installed on the OP and on the 780 R tunable fiber injections. Result of the full characterization of the field polarization<sup>4</sup>. using Thorlabs polar-meter PAX1000-IR1 is presented Fig. 1.9. Typical fluctuations over two hours give the same amplitude than those presented for the fiber under stress. The output polarization is almost purely linear with a residual Ellipticity  $\eta < 0.5^\circ$ . The polarization direction of a linear field can be described in space using the Azimuth angle  $0^\circ < \Theta < 180^\circ$ . In our case, the output polarization rotate in space of  $\pm 0.2^\circ$  only, giving (supposing  $\eta = 0$ ) a relative power balance variation (in intensity) on a PBS of  $10^{-5}$ . In our experiment, such low level of fluctuation was key to stabilize the saturation parameter of the repumper  $s_0^{rep}$  used in Chapter 2. It has been measured on the  $45^\circ$  axis for series of 55 consecutive runs (with the usual experiment cycling time) and we recapitulate table 1.4 the results. We see that the standard deviation  $\sigma$  is increasing with the mean value  $\langle s_0^{rep} \rangle$  of the saturation parameter but the relative variation  $\epsilon = \sigma / \langle s_0^{rep} \rangle$  seems independent.

<sup>4</sup>see PAX manual for definitions of the different quantities at <https://www.thorlabs.com/drawings/36df3d12c4d68979-8D5AE44C-FA11-BD19-C856E1C08BFE0412/PAX1000VIS-Manual.pdf>



Figure 1.8: Picture of the new fiber injection scheme. In the caged system from left to right : PBS; half-wave plate; lens; fiber adapter.

$\langle s_0^{rep} \rangle$	$\sigma$	$\epsilon$
$1.73 \times 10^{-1}$	$1.46 \times 10^{-3}$	0.85 %
$5.72 \times 10^{-2}$	$4.36 \times 10^{-4}$	0.76 %
$9.33 \times 10^{-3}$	$1.48 \times 10^{-4}$	1.59 %

Table 1.4: Stability of the repumper saturation parameter computed with the RedPitaya monitoring system during each experiment. The stabilization of the fiber injection yields a stability close to 1%.

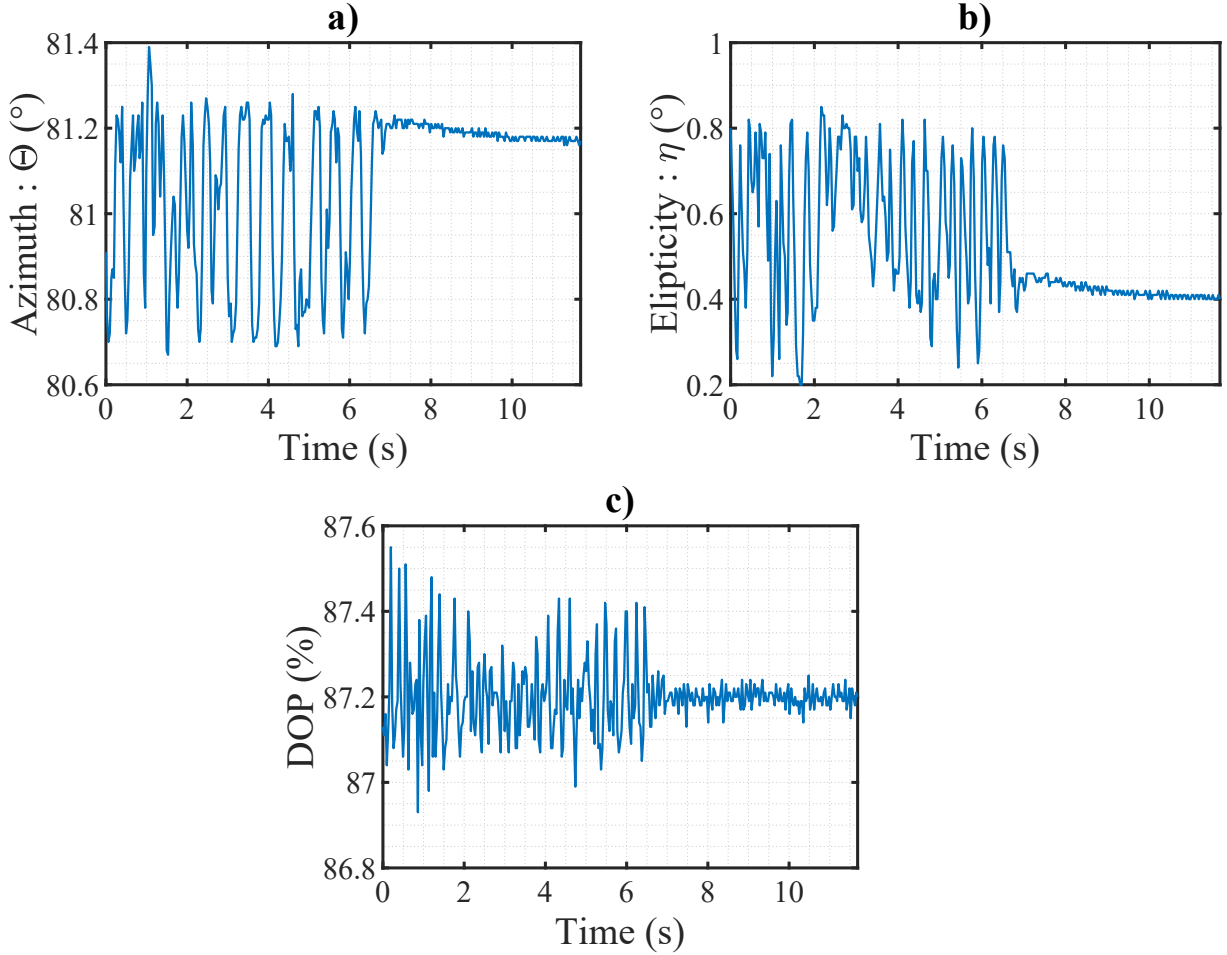


Figure 1.9: Polarization state at the output of a fiber injected with the new scheme. The part with high fluctuations was taken by deliberately stressing the fiber. a) Evolution of the Azimuth parameter describing the polarization direction. We are very close to a linear vertical state, showing fluctuations below 0.3% while being purposefully stressed and fluctuations limited by the detector sensitivity down to  $10^{-4}$  at rest. b) Under stress, the ellipticity vary by  $0.4^{\circ}$ , corresponding to slightly less than 1% compared to  $\eta = 45^{\circ}$  for a circularly polarized beam. At rest, the beam is close to being purely linear, with a residual ellipticity being only  $0.4^{\circ}$ . c) Degree of Polarization (DOP) as a function of time. The fiber output light shows very little un-polarized component with little to no influence of stress on the fiber on the DOP ( $< \pm 0.2\%$ ).

## 1.2 Imaging Axis

Imaging systems are a key component for almost every experiment with a cloud of atoms. We start by quickly recalling the absorption imaging method and briefly present the three imaging axis installed on the main apparatus. We first describe two low numerical aperture (NA) imaging systems with different magnifications, used in the low saturation regime. These two axis are used to get the cloud properties at different experimental stages of the BEC production. Finally we give the main parameters of the high NA imaging system used for the sub-wavelength imaging experiments.

### 1.2.1 Absorption imaging principle

On the experiment, we image the atomic cloud using standard absorption imaging scheme. Measuring the shadow of an interacting light transmitted through a cloud of atoms, gives information on the cloud. The 3D atomic density  $n_{3D}(\mathbf{r})$  is not directly accessible, and we are limited to the column density  $n_{2D}(\mathbf{x}, \mathbf{y})$ , where we have assumed that the light propagation was along  $z$  :

$$n_{2D}(\mathbf{x}, \mathbf{y}) = \int n_{3D}(\mathbf{r}) dz \quad (1.2)$$

The 3D atomic density of a general cloud is given Eq. C.17 and C.20. The transmission  $T(x, y)$  of a probe laser beam of initial intensity  $I_0(x, y)$  is given after interacting with the cloud by :

$$T(x, y) = \frac{I(x, y)}{I_0(x, y)}$$

where  $I(x, y)$  is the light intensity profile after the cloud, collected on the camera.

In the low saturation limit, the optical density profile  $b(x, y)$  is given by the Beer-Lambert law :  $b(x, y) = -\ln(T(x, y))$ . Also, it is related to the on resonant atomic cross section  $\sigma_0$  as :

$$b(x, y) = \sigma_0 n_{2D}(\mathbf{x}, \mathbf{y}) \quad (1.3)$$

Taking into account the saturation of the probe, we have :

$$b(x, y) = -\alpha \ln(T(x, y)) + s_c(1 - T(x, y)), \quad (1.4)$$

Experimentally, the Transmission is computed as  $T = \frac{I_{at} - I_{bkg}}{I_{no} - I_{bkg}}$  where  $I_{at}$  is the intensity transmitted by the cloud interacting with the probe beam,  $I_{no}$  is the intensity profile of the probe transmitted without atoms through the imaging system, and the background  $I_{bkg}$  with no probe<sup>5</sup>. As seen with Eq. 1.5, the saturation parameter  $s_0$  is critical to retrieve the atom number with no systematic error. For that purpose, a monitoring system on all our imaging axis is implemented. A RedPitaya triggered by Cicero record the intensities measured with dedicated calibrated photo-diodes.

---

<sup>5</sup>This appears to still give signal to noise ratio close to unity when working with a low number of atoms due to parts of the imaging beam on the camera with only a few photons. Also, fringes moving between each images due to air fluctuations were a noticed issue. Implementation of [59] or optimizing the fringe remover program could be beneficial in the future

Absorption imaging in the saturating case has been rigorously studied in our group[60] and we showed that the response of an optically dense continuous atomic cloud could be described using a modified Beer-Lambert law and a reduced apparent atomic cross section[61]. We recall here the main result and further details can be found in [54, Chap.D ].

For a circular probe polarization under well-controlled magnetic field orientation and laser detuning, the slope of the correction factor is  $\alpha = 1.17(9) + 0.255(2)b$ .  $\alpha$  is independent of the transverse position in the cloud. The offset  $\alpha_0 = 1.17(9)$  ultimately depends on a fine calibration of the saturation parameter and should be 1 for a perfect  $\sigma$  light. Using Eq. (1.4) and  $d\alpha/db = 0.255(2)$ , we obtain a generalized Beer-Lambert law expression for the optical density that accounts for multiple scattering happening in a dense cloud :

$$b(x, y) = \frac{-\alpha_0 \ln(T(x, y)) + s_0(1 - T(x, y))}{1 + \frac{d\alpha}{db} \ln(T(x, y))}. \quad (1.5)$$

The optical density being an intrinsic cloud quantity, it should be independent of the probe

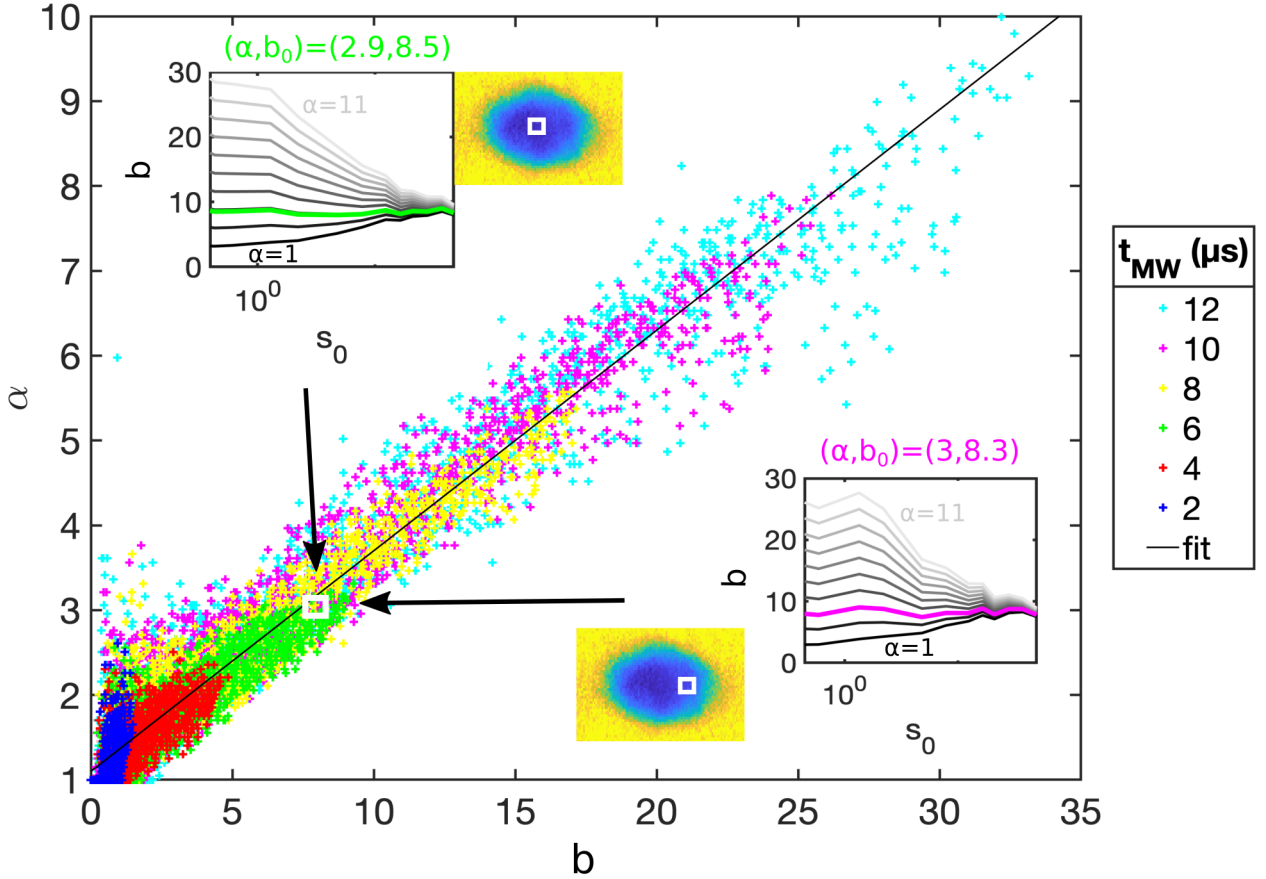


Figure 1.10: Correction factor  $\alpha$  as a function of the optical density. The initial total number of atom is controlled using micro-wave transfer, whose pulse duration  $t_{MW}$  are defined in the legend. Each point corresponds to the analysis of a single pixel and the solid black line is a linear fit giving  $\alpha = 1.17(9) + 0.255(2)b$ .

beam properties. We showed that this is the case by taking into account a correction of  $\alpha$  depending on the optical density. Experimentally, a thermal clouds with different peak atomic density is probed for different saturation parameters at constant number of scattered photons. Analyzing each pixels independently, we extract the couple of parameters  $b(x, y)$  and  $\alpha(x, y)$  giving an optical density independent of the probe saturation. For a circular probe polarization, we plot the resulting curve in Fig. 1.10. Independently of their position in the cloud, equivalent local optical densities lead to the same reduction of the scattering cross section. A linear fit of the entire data-set gives  $\alpha = 1.17(9) + 0.255(2)b$  where the uncertainty is dominated by the uncertainty of the saturation parameter. This offset close to 1 shows that in the limit of low densities the atomic response is well modeled by an ensemble of independent two-level systems (2LS). The value of  $\alpha$  at low atomic density depends both on the probe polarization and magnetic field direction but also linearly depends on the calibration of the saturation intensity as observed by the atomic cloud. The calibration of the offset between probe center and atoms was important in this respect. The dependence of  $\alpha$  on  $b$  shows that it is not solely determined by the probe properties but also depends on the optical density which is a signature of the influence of multiple scattering.

In the following, we describe the different imaging axis implemented, all based on saturated absorption, where we include the correction mentioned above in our image analysis.

### 1.2.2 Low magnification imaging axis

This imaging axis, also called '45° imaging axis', is depicted Fig. 1.1 and is mainly used to image atoms from the MOT to early evaporation in the hybrid trap. Details of the initial installation can be found in the thesis [53]. To measure quantitatively the atom number, we monitor the saturation parameter using a splitter to probe the actual laser power. In 03/2022, a free-space caged splitter has replaced a previously used fiber splitter that was strongly fluctuating under the AC flux. This change reduced the output ellipticity from 3° to  $\eta < 0.5^\circ$ . One port is focused on a detector and monitored with a RedPitaya while the other goes to the atoms. The new collimation optical setup is represented Fig. 1.11. The output polarization of the PM fibers used with this axis are ensured by the stable injection process described above.

The imaging beam is collimated and has a Gaussian waist measured at the entrance of the science chamber of 6.5 mm. We always use a low saturation parameter for this imaging axis. The atomic cloud is imaged on a CCD camera Point Grey Chameleon7 (pixel size 3.45  $\mu\text{m}$ ) by two consecutive lenses with focal lengths of 150 mm (Thorlabs Plano-Convex LA1433-B) and 750 mm (Bi-Convex LB1475-B) positioned at 750 mm from the cloud center. The magnification  $M = 0.198$  has been calibrated by time-of-flight. This allows to image large clouds and/or long time-of-flights. The 780 R tune beam waist has been measured in 05/2022 by knife edge measurement  $w_0^V = 6.09$  mm vertically and  $w_0^H = 7.14$  mm horizontally. The incident 780 power  $P$  in mW on the atoms as a function of the photo-diode response  $V_{out}$  in Volt is given by<sup>6</sup>  $P (mW) = 1.228 \times V_{out} (V) - 2.1e^{-3}$ . This characterization proved to be stable over time. The value acquired by the photo-diode is numerized by the RedPitaya and used to compute the saturation parameter. Fig. 1.12 b) shows the saturation parameter accessible on this axis.

<sup>6</sup>Last characterization with data of the 08/03/2022 and correction from the 1064 offset

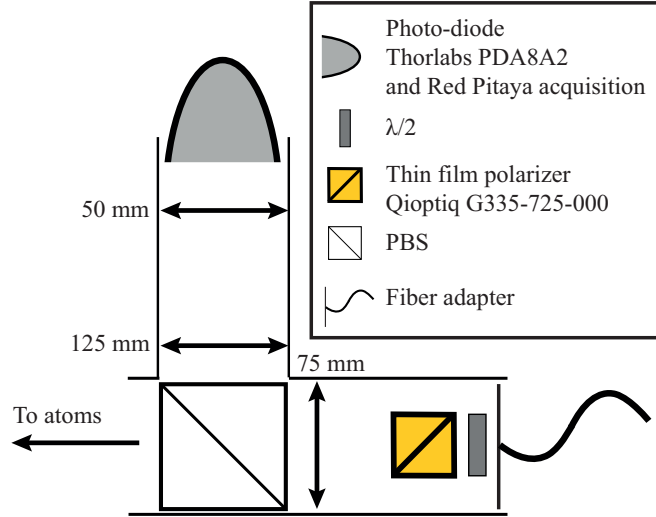


Figure 1.11: Optical schematics of the free-space collimation and detection system of the  $45^\circ$  axis. The lens spacing are not drawn to scale, the fiber head is at the focal point of the first  $f' = 75 \text{ mm}$  lens. The set of two lens  $f' = 125 \text{ mm}$  and  $f' = 50 \text{ mm}$  are focalizing the beam on the photo-diode.

### 1.2.3 Intermediate magnification imaging

This imaging axis also called 'imaging along DT1' has an intermediate magnification of 2. It propagates in the  $y$  direction and is often used to image the cloud in the hybrid trap. This imaging system is well suited to align the different beams (DT, lattice, 1529).

A knife edge measurement done before and after the science chamber give the waist on the atoms to be  $4.8 \text{ mm}$ , with a linear polarization along  $z$ . Using the second  $150 \text{ mm}$  focal aspherical lens, a telescope system is made with an output lens of  $300 \text{ mm}$  focal, that images the cloud on a CCD camera Flir Blackfly BFS-PGE-31S4M. This camera has a matrix of  $(2048 \times 1536)$  pixels with a size of  $3.45 \mu\text{m}$ . All the details are presented in [54, p.71]. The magnification is experimentally calibrated by TOF measurement giving  $M = 1.9$  and the numerical aperture is  $NA = 0.06$ .

### 1.2.4 Sub-wavelength imaging axis

To get the in-situ images of the atomic cloud in the lattice in Chap. 2, we developed a high numerical aperture imaging system. We recall the most important aspect of this imaging system which has been implemented during the previous thesis [54, P.73].

It is composed of a 5-lens home-made microscope objective with a measured numerical aperture of  $NA = 0.3$  on the axis at  $780 \text{ nm}$ . In the lower bound, the Field-Of-View (FOV), defined as the area around the optical axis where the objective is operating in the diffraction-limited regime is  $FOV \approx 200 \mu\text{m}$ . According to the Rayleigh criterion, the resolution is  $d_R = 1.59 \mu\text{m}$ .

This microscope objective image the cloud from below according to the optical setup given in Fig. 1.13 on a low-noise EMCCD Princeton ProEM whose parameters are presented Table 1.5. An intermediate image is created by a  $500 \text{ mm}$  focal lens (AC508-300-B-ML), which is

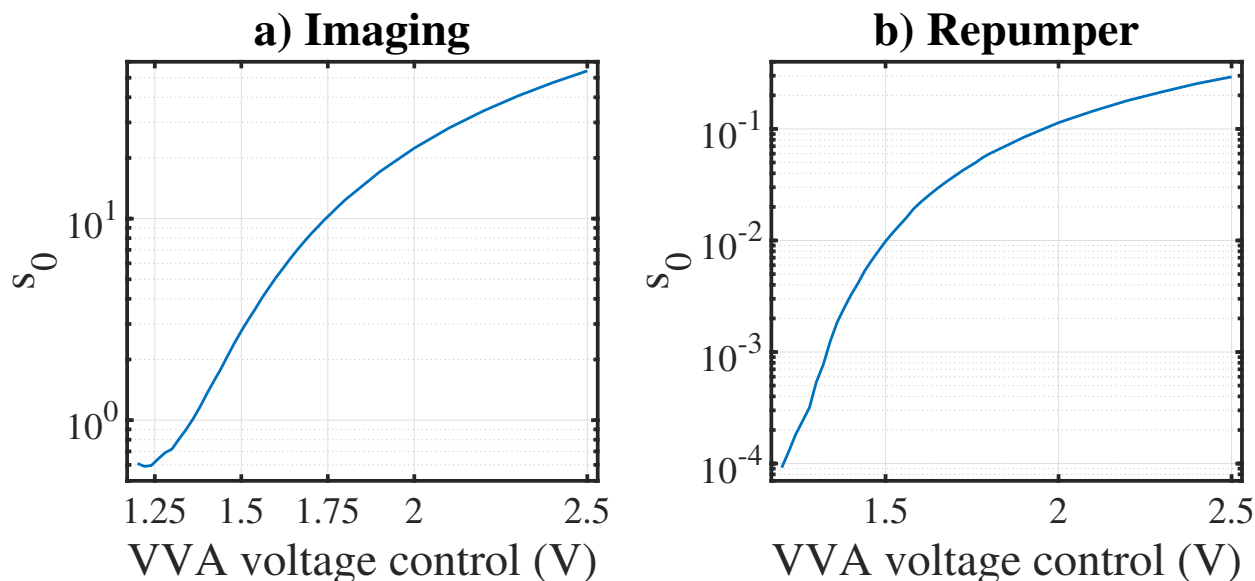


Figure 1.12: Calibration of the saturation parameter depending on the VVA drive. a) imaging on the sub-wavelength axis. b) 780 R tunable on the  $45^\circ$ . These values are computed for a given beam waist, photo-diode calibration and saturation intensity depending on the type of transition.

further imaged on the camera by a telecentric telescope (AC508-150-B, AC508-75-B). All the optics are diffraction limited at the objective NA.

To minimize the time between consecutive image and reduce the noise coming for example from air turbulence on the generated images, the camera is used in frame-transfer (or fast-kinetics) mode. This requires to introduce a razor blade in the intermediate image plane, to hide part of the image plane.

On this axis, the collimated Gaussian beam waist has been measured with a beam profiler and is  $w_0 = 1.1$  mm on the atoms. As depicted on the Fig. 1.13 the imaging beam and the vertical MOT are combined on a PBS with crossed polarization. The power of the imaging beam is monitored by a photo-diode calibrated to  $P$  (mW) =  $2.8389 \times V_{out} + 15.712e - 3$ . The initial focus procedure is detailed [54, p.78]. To fine tune the focus of the imaging system, we move the camera and the telescope instead of the objective. This reduces the sensitivity of the translation stage by  $m^2$  where  $m$  is the transverse magnification. Indeed, let's consider an optical system with two converging lenses of focal  $f_1$  and  $f_2$  separated by a distance  $L$  with a magnification  $m = f_2/f_1$ . The thin-lens equation gives the defocus in the image plane  $dZ$  is given from the defocus in the object plane  $dz$  as  $dZ = m^2 dz / (1 - mdz/f_1 + mLdz/f_1 f_2)$  that can be approximated if  $dz \ll f_1$  as  $dZ \approx m^2 dz$ . Experimentally, with our magnification of  $500/53 * 2 = 18.87$ , a displacement of the camera by  $dZ = 100 \mu\text{m}$  corresponds to a displacement of the object by  $dz = 0.9 \mu\text{m}$  which is below the depth of focus. Experimentally, we adjust the focus by minimizing the size of a small cloud. A good type of cloud is a deeply evaporated BEC, with only a few atoms remaining, loaded in the 1064 lattice compressed at  $1000ER$  (see Chap. 2 for explanations). We then minimize the fitted transverse size of the cloud by displacing the camera and the telescope. Typical image of the cloud and a fit to get the minimum size are presented Fig. 1.14.

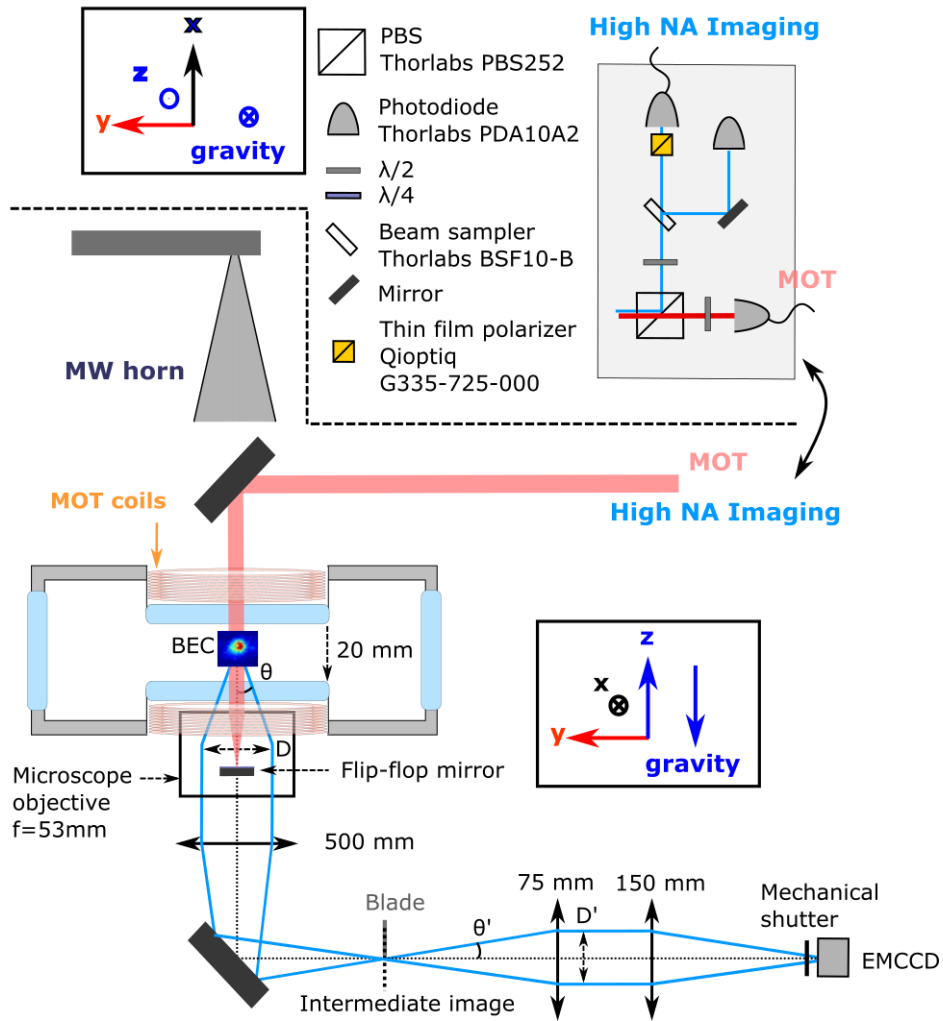


Figure 1.13: Optical schematics of the high NA 'sub-wavelength' imaging axis.

Model	512B eXcelon, coated
Serial number	2502090010
QE (@ 780 nm)	0.85 @ $-70^{\circ}C$ (datasheet)
Active pixels (H)x(V)	2 * (512 $\times$ 512)
Pixel size ( $\mu m$ )	16 $\times$ 16
Digitalisation (bits)	16
Pixel well depth (e-)	141k
Min vertical clock speed ( $\mu s$ )	0.45
Temperature (Air cooled)	Down to $-70^{\circ}C$
Sensitivity, no EM (e-/ADU)	0.75
Readout noise, no EM (e-)	3.15
Dark charge (e-/pixel/s)	0.0066 @ $-70^{\circ}C$
EMCCD gain	[1 : 1000]
Software	Matlab + Lightfield

Table 1.5: Principal characteristics of the EMCCD camera used on the sub-wavelength imaging axis.

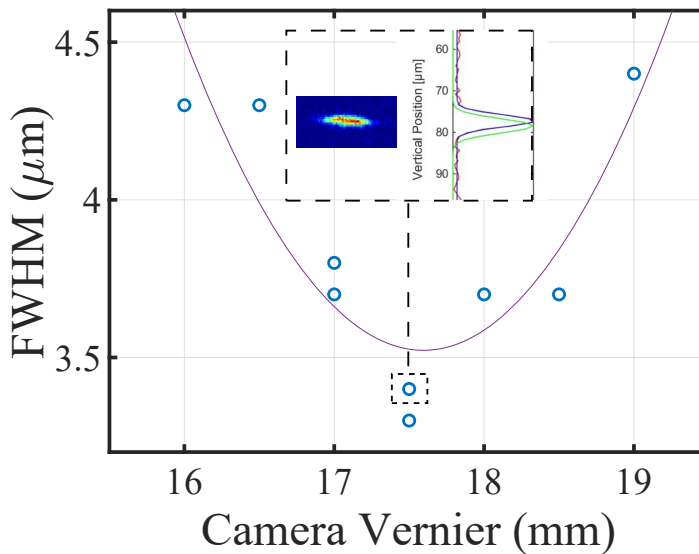


Figure 1.14: Typical data obtained when doing the focus of the ProEM. x-axis given the camera spatial position. Note that the telescope in front is moved accordingly to follow. y-axis is the fitted size given on the Matlab window of the bottom figure. Circles are data point and a quadratic fit (plain line) give the correct focus setting. Out of focus, the cloud seems to be splitting, increasing the fitted size. Most of the time, it will lead to an increase in fitted size but sometimes give an erroneous fit like the one at  $x = 18.5 \text{ mm}$ . The inset is the cloud image and its vertical projection at the correct focus.

## 1.3 Hybrid trap and Bose Einstein condensation

### 1.3.1 Atom cloud preparation

In our experiment, we use a 2DMOT to load a 3DMOT which is further compressed in a CMOT, cooled during a short 6 ms red molasses and Optically Pumped in  $|F_g = 1, m_F = -1\rangle$ . Details of the preparation can be found in Appendix D.2 and in previous thesis [31, 62]. At the end of this preparation, we have approximately  $1.4 \times 10^9$  atoms at 130  $\mu$ K loaded in the Magnetic Trap (MT).

### 1.3.2 Magnetic trap and RF evaporation

The atomic cloud previously polarized in a single mF state is transferred in a magnetic trap. Coils in anti-Helmoltz configuration, with a total resistance  $R_{coils} = 0.45 \Omega$  generate a magnetic gradient up to  $B' = 160$  G/cm at the atom position. The trapping potential for a magnetic moment  $\mu = g_F m_G \mu_B$  is [63] :

$$U_{mag} = \mu B' \sqrt{\frac{x^2 + y^2}{4} + z^2} \quad (1.6)$$

The in-situ MT volume used to compute the phase space density in the trap is the quadrupole trap volume given by :

$$V_0(T) = \frac{32\pi}{\left(1 - \left(\frac{mg}{\mu B'}\right)^2\right)^2} \left(\frac{k_B T}{\mu B'}\right)^3 \quad (1.7)$$

For this step, the magnetic gradient is abruptly ramped up from zero to 50 G/cm and then compressed in 200 ms up to 161.7 G/cm. Then, atoms in the magnetic trap undergo four stages of RF evaporation consisting of linear RF-knife sweeps, 'MTevap 1' to 'MTevap 4'. Duration of each steps and the value of the RF knife are optimized on the resulting phase space density obtained using TOF measurements to get the atom number, temperature and the in-situ volume given by Eq. 1.7. In total, these steps takes one and a half second and gives  $8 \times 10^7$  atoms at 30  $\mu$ K with  $B' = 117.6$  G/cm.

After RF evaporation in the purely magnetic trap, the cloud is transferred in an hybrid trap by adding a dipole trap at 1064 nm. We describe below the laser architecture before developing the transfer procedure and optimization of the number of atoms loaded.

### 1.3.3 Dipole trap laser at 1064 nm

The free space optical bench for the 1064 nm laser is detailed in [51]. The laser source is a solid state laser Mephisto MOPA from Coherent, initially delivering 55 W. The laser is split in free space into three different arms presented Fig. 1.1 : 'DT1', 'DT2' and 'Lattice 1064'. A spatially Gaussian mode is obtained by filtering the mode with a single-mode polarization maintaining fiber. The temporal profile is controlled using an AOM.

To improve the stability and reproducibility of the experiment, all the dipole trap powers are locked. The laser powers are detected after the fiber and the retro-action is carried on the RF

power driving each AOM. These locks have a typical bandwidth of 100 kHz. The power-stability was characterized using a photo-diode with low levels of noise (under -130 dBm/Hz). We compute the RIN and obtain the one-sided power spectrum following equation 3.34. Fig. 1.15 presents a RIN of our dipole trap laser. The noise level of the detection is below the one of the laser, we are therefore not limited by the detection.

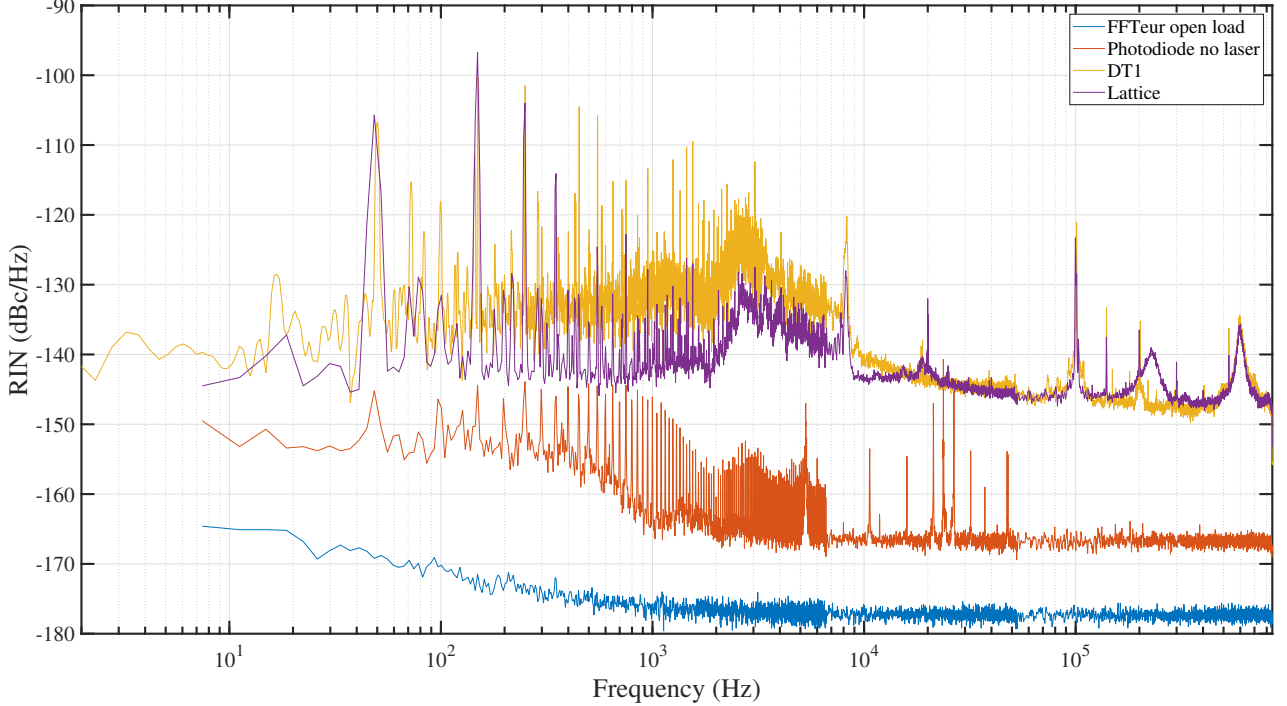


Figure 1.15: Relative Intensity Noise (RIN) of the 1064 nm laser. The power is measured before the lens focalizing our dipole trap beams on the atoms. Noises levels for 'DT1' and 'Lattice' arms are quite similar since they come from the same initial laser and the power control circuits share the same architecture. The laser power is quite stable at low power, with a RIN under -120 dBc/Hz between 1 Hz and 0.85 MHz.

**Dipole trap parameters.** In this section, we present the main characteristics of DT1 and 1064 lattice beams which are combined on a PBS.

For a thermal cloud in the hybrid trap, a sudden increase of the dipole trap power excite breathing-modes [64] and generate center-of-mass oscillations of the cloud. We used this method, called forced oscillations (see [53, p. 65]), to extract the trap frequency  $\nu$ . The measurement were carried on a thermal cloud and not on a BEC which breathing mode frequency are strongly influenced by interatomic collisions [65]. At a given trap power  $P$ , the trapping frequency is computed using the dipole potential given Eq. B.2 and fitted with only the waist  $w_0$  as a free parameter :

$$\nu(P) = \frac{1}{w_0^2} \sqrt{P \frac{12c^2\Gamma}{m\omega_0^3} \left( \frac{1}{\omega_0 - \omega} + \frac{1}{\omega_0 + \omega} \right)} \quad (1.8)$$

Using this method, we evaluated the waist of DT1 to be  $w_0^H = 51.5 \pm 0.2 \mu m$  horizontally and  $w_0^V = 48.96 \pm 0.1 \mu m$  vertically. For '1064 lattice forward', we measured a waist on the atoms of

45  $\mu\text{m}$ , which gives according to ABCD matrix propagation [66] a waist of the reflected beam on the atoms of 75  $\mu\text{m}$ .

The optical power of '1064 lattice' measured before the first aspheric lens is linear with the lock setpoint ( $P_{lattice} (W) = -0.1933V_c^{lattice} + 0.003285$ ) with a maximum power of 1.92 W. For DT1, we have  $P_{DT1} = 0.4152V_c^{DT1} + 0.0201$ , with a maximum power of 3.5 W. Both  $V_c^{lattice}$  and  $V_c^{DT1}$  are the locking voltages set-point (resolution of 0.3 mV, 16-bits output).

### 1.3.4 Beam alignment

The dipole beams positions are finely adjusted on the atoms using Newport AGM100N piezo-actuated mount. We either directly control them with a dedicated software or interface them with Cicero via a Matlab program.

In-situ position of the magnetic trap center measured on the imaging axis along DT1 give the reference position of atoms. Using repumper light instead of 1064 gives a first rough alignment. Due to chromatic aberration, this method is not precise but still good enough to load some atoms in DT1. The fine alignment is done by optimizing the number of atoms loaded. Because of Majorana losses, the optimal loading configuration is obtain when the traps are aligned on the horizontal direction but with MT slightly above DT1 in the vertical direction. The optimum is found for DT1 roughly two waists below the MT zero. The atom number is fairly constant from two to four waists beneath. A good compensation of stray magnetic fields is required to ensure that the magnetic trap center stays fixed while decreasing the magnetic gradient.

The alignment of the 1529, DT2 and 1064 Lattice beams is carried with respect to the position of a small cloud strongly compressed in DT1. They are all aligned in-situ with the imaging axis CCD along DT1, completed when needed by sub-wavelength imaging for the  $y$  direction.

For the 1529, each beams are aligned independently using the light shift induced on an intermediate-sized cloud. Turning ON the 1529 beam and repumping at the top of the light shift give a small cloud in  $|F = 2\rangle$  centered on the beam.

Because of the (many) air-conditioning failure of the lab, this alignment has been carried away many times. In table 1.6, we give the beams displacement as a function of the temperature increase ( $\Delta T$ ) during the AC failure. We additionally measured an event with  $\Delta T = 0.9$  °C where the beam displacement was small enough not to be detrimental to the experiments. Compared to the waist of the 1064 lattice forward beam (60  $\mu\text{m}$ ), theses misalignment are significant and need to be corrected.

### 1.3.5 BEC in the hybrid trap

After loading the hybrid trap, a last stage of optical evaporation is realized by lowering the optical power of DT1. The threshold to reach a pure BEC is relatively stable. The magnetic gradient is linearly ramped from 28.5  $G/cm$  to 24.5  $G/cm$  while the dipole trap power is exponentially

$\Delta T$ ( $^{\circ}\text{C}$ )	$\Delta\text{DT1}$ (H;V) ( $\mu\text{m}$ )	$\Delta\text{Lattice forward}$ (H;V) ( $\mu\text{m}$ )
2.6	(3.84 ; 11.44)	(8.26 ; 7.06)
2.8	(11.8 ; 3.3)	$\emptyset$
>5.7	(22 ; 12.4)	$\emptyset$

Table 1.6: Impact of temperature rise following air conditioning failure on beam alignment.  $\Delta T$  is the maximum temperature increase during the event. We present the displacement in the atomic plane for each directions of two beams, DT1 and 1064 lattice forward. The cloud is imaged on CCD along DT1 imaging axis.

ramped down starting at  $P(t=0) = P_i = 3.0\text{ W}$  down to  $P(t=t_f) = P_f = 35\text{ mW}$  as :

$$P(t) = \frac{P_i + P_f}{1 - e^{-t_f/\tau}} e^{-t/\tau} + \frac{P_f - P_i e^{-t_f/\tau}}{1 - e^{-t_f/\tau}} \quad (1.9)$$

where  $t_f = 3\text{ s}$  and  $\tau = 1/3\text{ s}$  are optimized experimentally to maximize the condensed fraction. With the vacuum getting worst, we observed a decrease of the lifetime in DT1 to 2.5 s. In this configuration, the optimal evaporation time was found to be shifted at  $t_f = 1.5\text{ s}$ , value for which it was still possible to reach a pure BEC.

Experimental demonstration of Bose-Einstein condensation has been done using two methods [67]: sudden optical density increase when lowering the optical power in the dipole trap or the observation of a bi-modal distribution. Evolution of the central optical density with the optical power of DT1 is plotted Fig. 1.16 with two distinct slopes. In Fig. 1.17, we can see on the

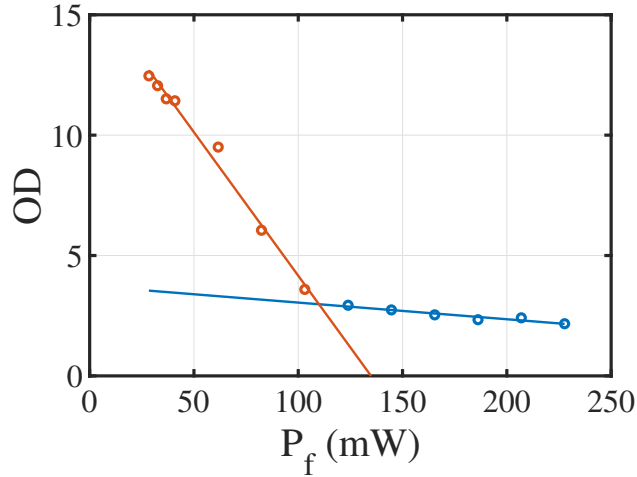


Figure 1.16: Mean optical density over 4 pixels at the cloud center as a function of the power in DT1 at the end of the optical evaporation. Plain lines are the fit over the data of the corresponding colors. The high slope difference is a good indicator that we are reaching Bose-Einstein condensation. The center of the cloud is optically dense but even at the highest computed OD, some photons are transmitted through the cloud and the signal to noise ratio is over 1.17.

central image the thermal and condensed part of the cloud. There, the vertical projection is not well fitted by a Gaussian, since the cloud has a Gaussian outer-shape and a central TF distribution.

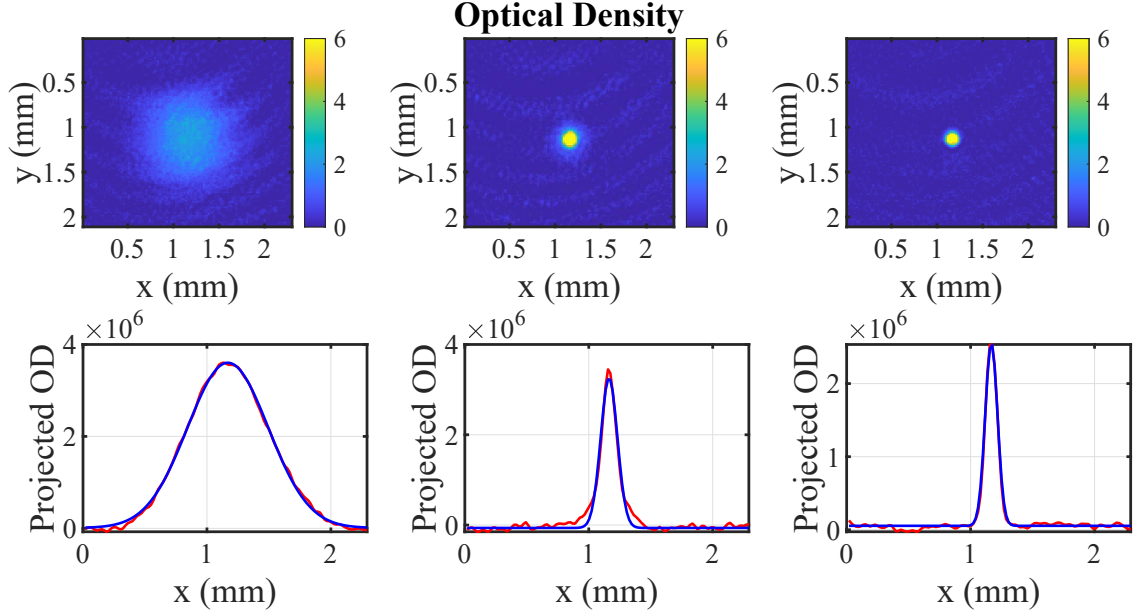


Figure 1.17: Evolution of the cloud after a TOF of 35 *ms* for different power at the end of the optical evaporation in the hybrid trap. Top images are the 2D optical densities, while the bottom images are the corresponding projection along the *y* direction (red) with a Gaussian fit (blue). Left to right are a thermal cloud ( $P_f = 233$  *mW*), a partially condensed cloud ( $P_f = 39$  *mW*) and a pure BEC ( $P_f = 26$  *mW*). Scale of the top images is fixed to clearly see the emergence of the BEC.

This concludes the presentation of the general apparatus producing a  $^{87}\text{Rb}$  BEC. The next section details the experimental implementation of the two-ways Accordion lattice setup used to dress the excited state with an optical lattice at 1529 nm. Characterization of the 1064 trapping optical lattice will be discussed in Chapter 2.

## 1.4 Two ways Accordion lattice

In this section we detail the Accordion lattice setup producing the commensurate lattices at 1529 and 1064, which are the main building block of our sub-wavelength imaging scheme. We now present the experimental setup used to produce an optical lattice at 1529 on the atoms.

### 1.4.1 Optical setup

This setup is inspired from [68, 69], where two incident beams create a 1D optical lattice with tunable periodicity in the focal plane of an aspherical lens. The optical setup depicted in Fig. 1.18 allows to generate either a large lattice interfringe in the co-propagating configuration (a) or small interfringe in the contra-propagating configuration (b).

In the co-propagating configuration, two parallel beams at 1526 nm are reflected from adjacent polarizing beam splitters (PBS) and focused by a single aspherical lens (with an effective focal length  $f' = 150$  mm and outer-diameter  $\phi = 75$  mm) onto the atoms. Translating the beam

along the incident face of PBS-R will effectively modify the incident beams separation on the lens, changing the incidence angle and the resulting lattice periodicity (Translation T1 on the optical schematic in Fig. 1.18).

Comment: A direct translation of the cube is to be avoided since you are then moving mechanical pieces when the interferometer is already opened. This leads to an extreme sensitivity of the center fringe position to vibrations and to the axis of translation. We previously tested this configuration but only present results for the more stable case of moving the incident beam.

Using Fourier optics, the interference pattern of the two beams and the resulting lattice

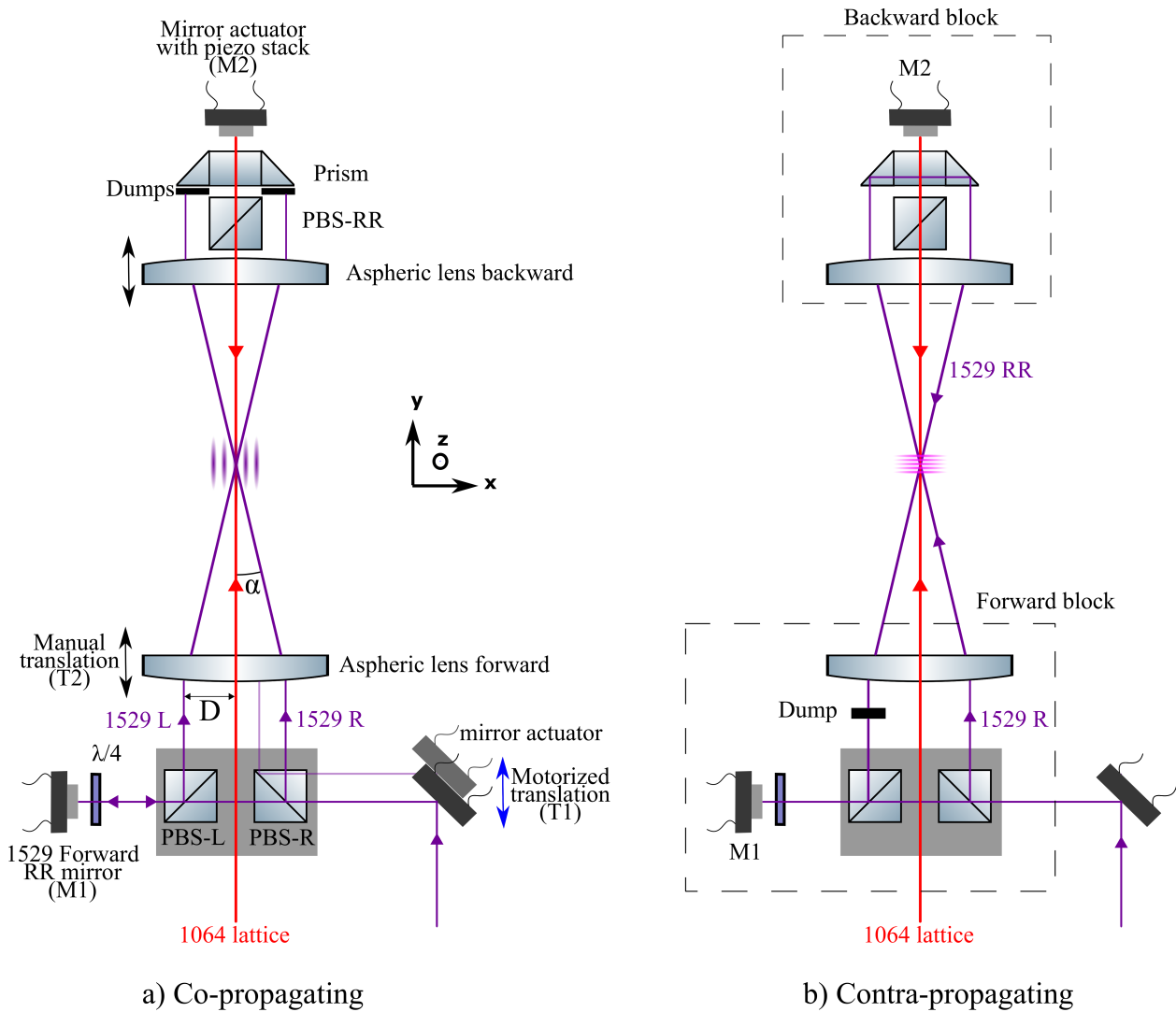


Figure 1.18: Optical schematics of the two ways accordion lattice. In the co-propagating mode (a), '1529 R' and '1529 L' interfere at the atomic position producing fringes along  $x$ . In the contra-propagating case (b) '1529 L' optical path is blocked, and '1529 R' with its reflection by the prism '1529 RR', yielding fringes along  $y$ . The color difference of the fringes emphasizes that the 1064 and 1529 lattices are co-linear in the contra-propagating configuration.

spacing can be calculated precisely. Each lens performs a Fourier-Transform (FT) from an object in the front focal plane to an image in the back focal plane. Noting the field of an

incident laser at the focal plane of the lens  $U(x_1, y_1, -f')$ , the field at the back focal plane is then  $U_0(x, y, f') = FT(U)$ . For an incident Gaussian beam, the resulting intensity distribution is still Gaussian. Using the fact that a translation of a distance  $L$  of the incident beam along the lens, is equivalent to a phase shift of  $e^{i\pi L/\lambda f'}$  of the field in the back focal plane, the total intensity is then :

$$I_0(x, y, f') = 2I_0(x, y, f') \left[ 1 + \cos \left( \frac{4\pi Dx}{\lambda f'} \right) \right] \quad (1.10)$$

with  $D$  the distance between each beam to the optical axis. The resulting interfringe is:

$$i_{1529}^{co} = \frac{\lambda f'}{2D} \quad (1.11)$$

The absolute position of the central fringe is determined by the relative phases of the two beams and is controlled by a piezoelectric stack under the mirror M1. A spatial displacement of the piezo by  $\Delta x_{pz}$  induce a displacement of the central fringe  $\Delta x_0$  according to

$$\Delta x_0 = 2i_{1529}^{co} \frac{\Delta x_{pz}}{\lambda_{1529}} \quad (1.12)$$

The contra-propagating configuration is a repetition of this scheme, where a second aspherical lens is placed symmetrically from the first compared to the atoms, and a prism reflects one PBS axis onto the other.

## 1.4.2 1529 laser beam properties

The sub-wavelength imaging method of Chapter 2 require a precise knowledge of the spatial energy structure of the cloud. Thus, we recall in this section the main characteristics such as the maximum optical power, the optical control scheme and waist at the atomic cloud position of the 1529 nm laser. It is implemented on the accordion lattice setup presented above, to dress the excited state  $5^2P_{3/2}$ .

A distributed-feedback laser (DFB) in a butterfly package from emcore (17821-NM-100-60-FC-PM) gives a maximum output power of 100 mW with a tunable wavelength centered on 1529.56(5) nm. A Koheron current driver (CTL200-2) locks the temperature and current setpoint of the diode. The PM fiber output goes through a polarization maintaining isolator (Advanced Fiber Resources) to a 10/90 polarization maintaining fused coupler (Advanced Fiber Resources). Most of the power goes toward an erbium-doped fiber amplifier. The 33 dBm output goes to a collimator on the experiment with a fiber-coupled 80 MHz AOM (Gooch & Housego) to control the temporal profile of the power. The power detected by a free-space photo-diode is locked using a homemade integrator circuit to feedback the AOM.

The power lock calibration indicate that the optical power  $P_{1529}$  measured before the vacuum chamber is linear with the drive  $V_c$  according to :

$$P(\text{mW}) = 2.2310(7) V_c(\text{V}) \quad (1.13)$$

The laser wavelength can be tuned with the temperature setpoint and has been independently measured to the pico-meter level via the frequency shift induced on a specific hyperfine level of

the excited state and to the femto-meter level directly using a wavelength-meter. The waist of the beam is measured in-situ by performing a tomography [70]. Indeed, the spatial dependency of the 1529 laser intensity shifts the excited state  $|F' = 3\rangle$ . Imaging the cloud in presence of the 1529 light reveal its spatial structure: atoms only absorb photons where the excited state light shift compensate the imaging beam detuning from the bare transition. Images of the spatial atomic distribution on the camera are taken for various 780 nm detuning at constant 1529 power gives a direct image of the 1529 beam. This characterization require a spatially homogeneous cloud over the 1529 beam size and a power small enough to be in the validity domain of the perturbation theory, thus having a linear dependency of the light shift with the 1529 laser intensity. With this method, we measured a waist of  $150 \mu\text{m}$ . Another precise characterization of the light shift induced by the 1529, named 'BAT' curves, does not require an accurate knowledge of the beam waist, and is presented in Chap. 2. In the following, when the excited state is dressed with the 1529, we refer to the repumper being tuned to the maximum light shift as being at the 'top of the modulation' and the case with no light shift as 'bare transition'.

### 1.4.3 Optical characterization of the tunable lattice

In this section, we present the experimental implementation of the forward accordion lattice. We define the available angle range for each configurations and give the beams waist and centroid position stability at the cloud position over the entire displacement of the incident beam. We characterize both the single beam and the resulting interference pattern evolution, and give the fringes dynamic stability.

Albeit the precise alignment of the different optical element, the limiting factor in the stability of the central fringe while changing the angle is the quality of the aspherical lens. Indeed, spherical aberrations increase with the distance to the optical axis which increases as the distance between the beams. The quality of a given lens is evaluated by following the centroid position of the 1529 beams in the focal plane of the lens when the incident beams are close or far from the optical axis in the horizontal plane. In the absence of aberrations, we expect no drift in the horizontal direction. We bought a total of 4 aspherical lenses and noticed differences on the total drift of a few ten microns. The best lens (ALL75-150-S-C from asphericon in standard quality) had been installed as the forward lens on the final apparatus and the second best (AL75150 from Thorlabs) as the backward lens.

**Half-angle extremums value in the co-propagating configuration.** Taking into account the waist of 0.5 mm so the beams are not clipped by the optics, the distance between a beam and the optical axis of the lens is limited in  $[6 ; 24]$  mm. The lower bound corresponds to the spacing between the two PBS, to give an optical access for the 1064. The upper bound is given by the cubes length. This gives  $\alpha$  in  $[2.3 ; 9.2]$  degrees.

**Half-angle extremums value in the contra-propagating configuration.** Here, the distance between a beam and the optical axis of the lens is limited in  $[12.2 ; 20.2]$  mm. In this case, both bounds are given by the prism dimensions. This gives  $\alpha$  in  $[4.7 ; 7.7]$  degrees.

The setup has been characterized on an test-bench (see Fig. ??) independent of the main experiment in co-propagating mode. Using an auxiliary telescope (magnification 200/11), the resulting lattice is imaged on a  $320(H) \times 256(V)$  camera (WiDySWIR 320U from New Imaging Technologies) with  $25\mu\text{m}$  pixel pitch. Pictures are acquired at a 50 Hz rate during the continuous motorized displacement of the beams. A piezo linear stepper actuator (Newfocus : 8321), driven at 2 kHz during the first 9 s push the linear translating stage (T1) on which the mirror mount is placed. This result in a translation of the incident 1529 beam on the right side of PBS1 of  $\Delta D = 11.5\text{ mm}$ , translating the reflected beam further from the optical axis of the lens. The integration time of the camera is short compared to the 0.5 ms drive period of the motor.

Two data set are presented in Fig. 1.20. In Fig. 1.20 (a), both beams are present and we plot

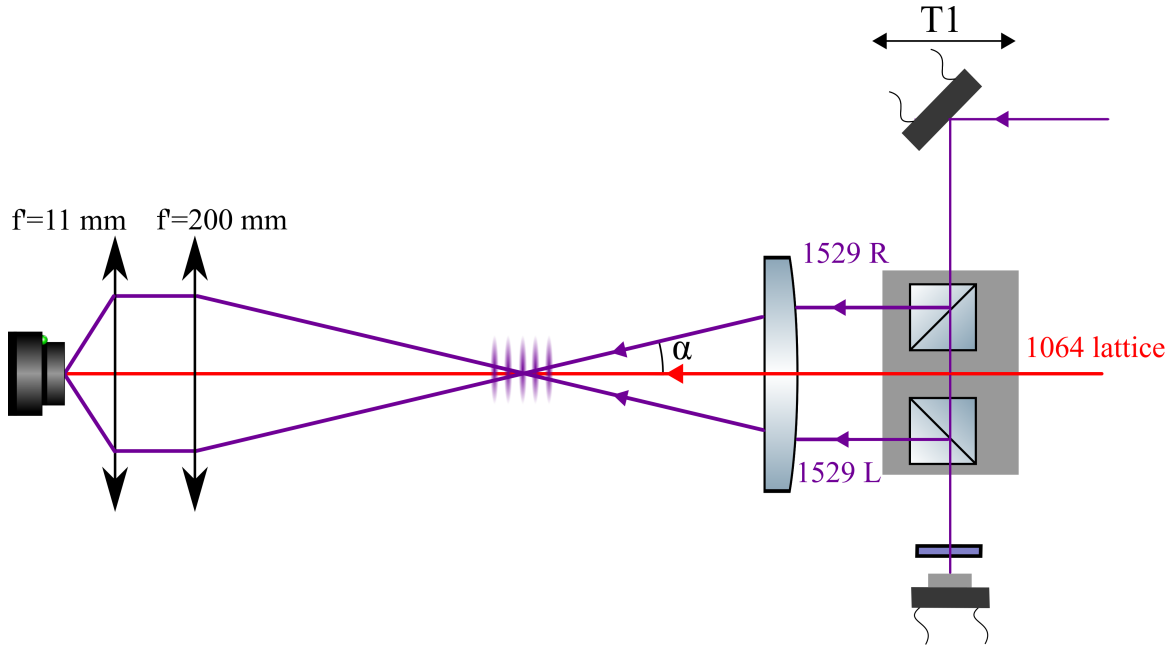


Figure 1.19: Optical setup of the forward accordion lattice test bench.

a 2D image of the fringes by stacking the projection of each acquired images. On this 2D image, there is a single horizontal line at constant intensity corresponding to the central fringe position, which is independent of the half angle. The position of other fringes depend on the interfringe. In Fig. 1.20 (b), we show the standard deviation of the intensity of every lines computed over all the images. It presents a Gaussian envelop corresponding to the two beams overlap and a single dip giving the central fringe position. This central fringe is not necessarily at the center of the Gaussian peak and depend on the optical length difference of the two arms. The half-angle  $\alpha$ , computed using Eq. 1.14, is presented in Fig. 1.20 (c) as a function of the interfringe which is obtained by Fourier analysis.

We now focus on the fitted centroid position and waist of a single beam (Fig. 1.21 a) and c) ) and of the two interfering beams (Fig. 1.21 b) and d) ). For reference, the position of a beam at 1064nm, independent of the translation, has a standard deviation  $\sigma_{1064} = 0.3\mu\text{m}$  for both directions.

On the images, the fringes indicate a  $4^\circ$  angle tilt of the camera. The vertical and horizontal

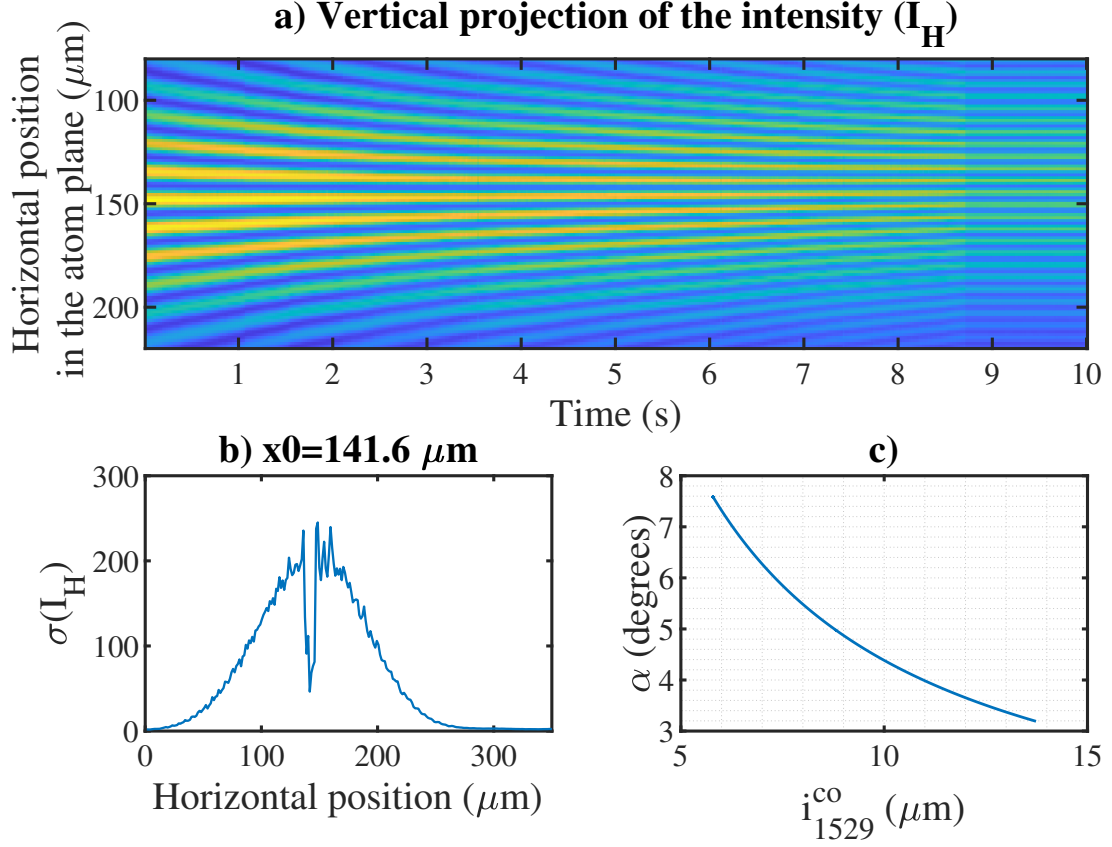


Figure 1.20: Optical characterization of the forward accordion lattice setup. Experimental setup is described in the text. a) 2D stack of the vertical projection of images acquired at 50 Hz while the distance between the 1529 beams is changed. b) Standard deviation of the vertical projection plotted in a) over the 500 images. The title is the horizontal position on the camera  $x_0$  for which  $\sigma$  present a dip. It correspond to the central fringe position, where the intensity is constant with the distance between each beams. c) Half-angle as a function of the interfringe. The interfringe is obtained by fitting the main peak on the FT of each images.  $\alpha$  is computed with the interfringe using Eq. 1.14.

directions then correspond to the lattice axis with an error lower than  $\epsilon = \sin(4^\circ) = 7\%$ , which we neglect in the discussion below.

### Vertical direction

The beam waist ( $w_0 = 84.5 \pm 1.5 \mu\text{m}$ ) presented in Fig. 1.21 c) is fairly constant over the 11.5 mm displacement. However, a sharp transition when the motor stops indicates an effect of the motor usage which is probably due to vibrations.

The position in the atomic plane of '1529 R', (Fig. 1.21 a) ) has a shot to shot stability of  $5 \mu\text{m}$  and drift vertically by  $15 \mu\text{m}$ . A vertical drift caused by a variation of the incident beam angle would correspond to  $6.7 \mu\text{rad}$ . As the same drift can be observed for '1529 L' alone and for the Gaussian envelop of both beams in Fig. 1.21 b), we think that the drift comes from an imperfect flatness of the linear translation stage. This is coherent with the manufacturer website giving a maximum angular deviation of  $250 \mu\text{rad}$  over a 25 mm displacement.

The overlapped beam waist plotted in Fig. 1.21 d) is only increased by 5% compared to the

single beam case, indicating a good alignment.

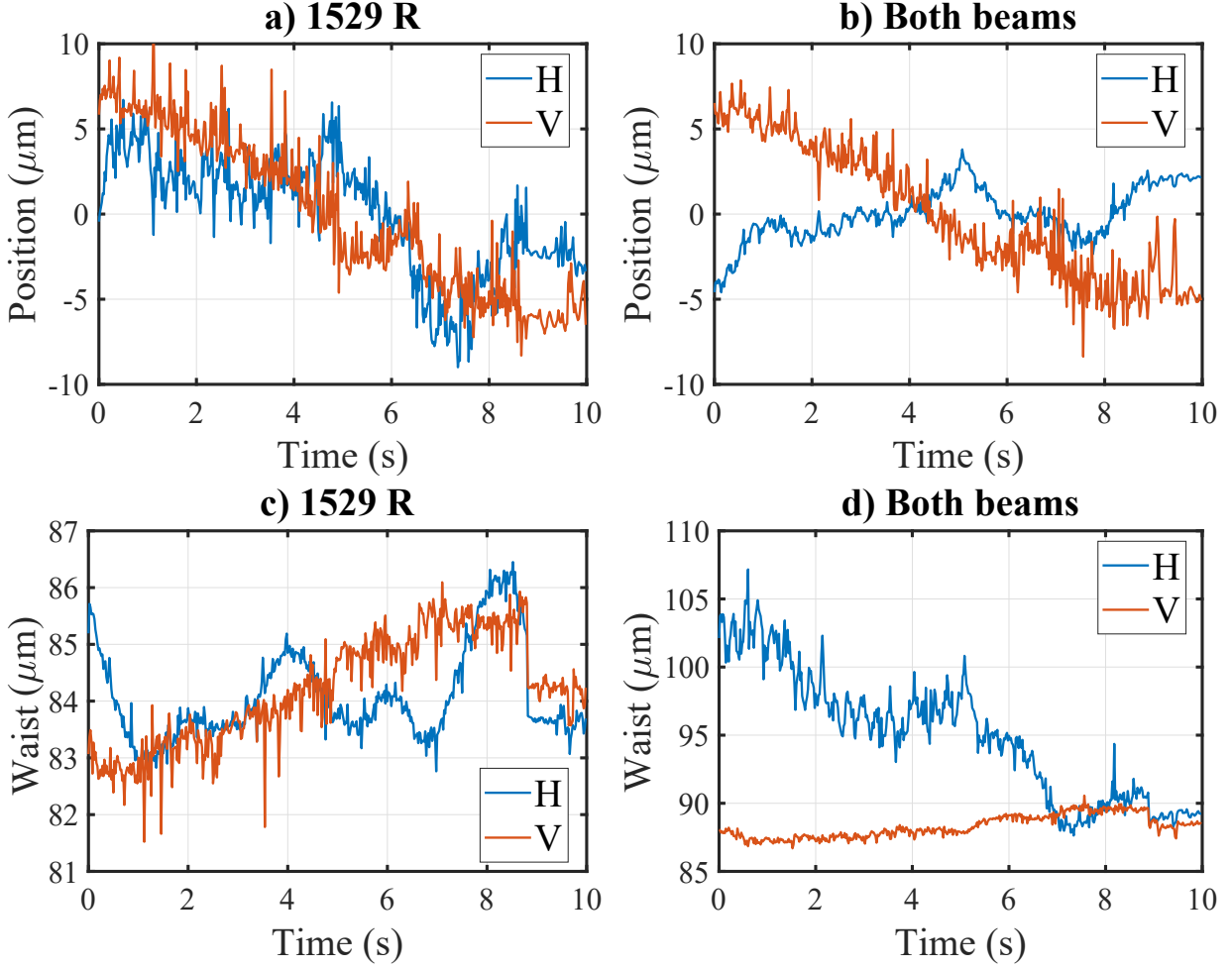


Figure 1.21: Beam position evolution in the atom plane (at the focus of the lens) for the forward accordion lattice setup as beams are moved of  $\Delta D = 11.5$  mm horizontally along the optical axis. a) Evolution of the centroid position for the right beam alone. b) Evolution of the centroid of the Gaussian envelope when both beams are interfering together on the detector. c) and d) Evolution of the fitted waist. The discontinuity near 9 s indicate an effect of the motor on the beam properties. On some images, we observe a residual Etalon effect on the detector front window which could explain the bump at 5 s in (b) and (d).

### Horizontal direction

We see a shot-to-shot stability of the single beam of  $4 \mu\text{m}$  and a drift  $\delta x$  slightly above  $10 \mu\text{m}$ . This drift is in the opposite direction for '1529 L' whereas the Gaussian envelop of the overlapped beams present no significant drift. Also, this is correlated with a decrease of the envelop waist plotted in Fig. 1.21 d), from  $w_0^H = 102 \mu\text{m}$  to  $87 \mu\text{m}$ , still 4% higher than the single beam waist. Thus, we infer that the horizontal beam displacement is mainly due to the camera being out-of-focus by  $\delta x f' / \Delta d = 136 \mu\text{m}$ . Indeed, the focus has been set with a precision of  $100 \mu\text{m}$ . Moving the lens by  $100 \mu\text{m}$  along the focus increase the total beam displacement by  $7 \mu\text{m}$  ( $17 \mu\text{m}$  in total), which correspond to an out-of-focus increasing by  $95 \mu\text{m}$ . Our hypothesis

is strongly supported by the good match between the computed out-of-focus and the actual displacement of the lens using a micro-metric translation stage (10  $\mu\text{m}$  precision).

In conclusion, we have an absolute stability of the beams better than 20  $\mu\text{m}$  over a range of  $5^\circ$  for beams that will have a waist on the atoms of 150  $\mu\text{m}$ . A careful alignment of the focus is required to prevent an horizontal drift that we can expect to be below then 5 $\mu\text{m}$  (maximum deviation to the slope on the horizontal axis). In the next section, we present the measurement of this alignment on the atoms.

The initial installation and alignment procedure of the two-way accordion lattice on our experimental apparatus is detailed in [D.3](#).

#### 1.4.4 Atomic characterization of the 1529 nm accordion lattice

We give below the fringe direction and interfringe that can be experimentally obtained for the two configurations presented on [Fig.1.18](#).

- Co-propagating configuration ( [Fig.1.18 a](#) )  
Blocking the backward path while using both forward beams, '1529 R' and '1529 L', produce an optical lattice at 1529 nm modulated along  $\boldsymbol{x}$ . The interfringe is :

$$i_{1529}^{co} = \frac{\lambda_{1529} f'}{2D} = \frac{\lambda_{1529}}{2 \sin(\alpha)} \quad (1.14)$$

With this setup the resulting interfringe is in  $i_{1529}^{co} \in [5.9 ; 28.7] \mu\text{m}$  which can be resolved by the imaging system (PSF radius of 1.3  $\mu\text{m}$ ).

- Contra-propagating configuration ( [Fig.1.18 b](#) )  
While blocking '1529 L', '1529 R' and its reflection by the prism produce an optical lattice modulated along  $\boldsymbol{y}$  whose interfringe is given by :

$$i_{1529} = \frac{\lambda_{1529}}{2 \cos(\alpha)} \quad (1.15)$$

This resulting interfringe is not resolved by our imaging axis. In this configuration, the incidence angle  $\alpha$  is precisely calibrated using the co-propagating case. The precise characterization of the light shift is carried using the 'BAT' curve method presented in [2.1.2](#).

We present in [Fig. 1.22](#) the half-angle  $\alpha$  calibration realized on the atom in the co-propagating configuration. For this, atoms are repumped at the top of the modulation with an optical lattice at 1529. The interfringe is obtained by Fourier analysis and the half-angle is set at the target angle  $\alpha_{1529} = 5.67^\circ$  (defined in [Chapter 2](#)) using the motorized translation T1.

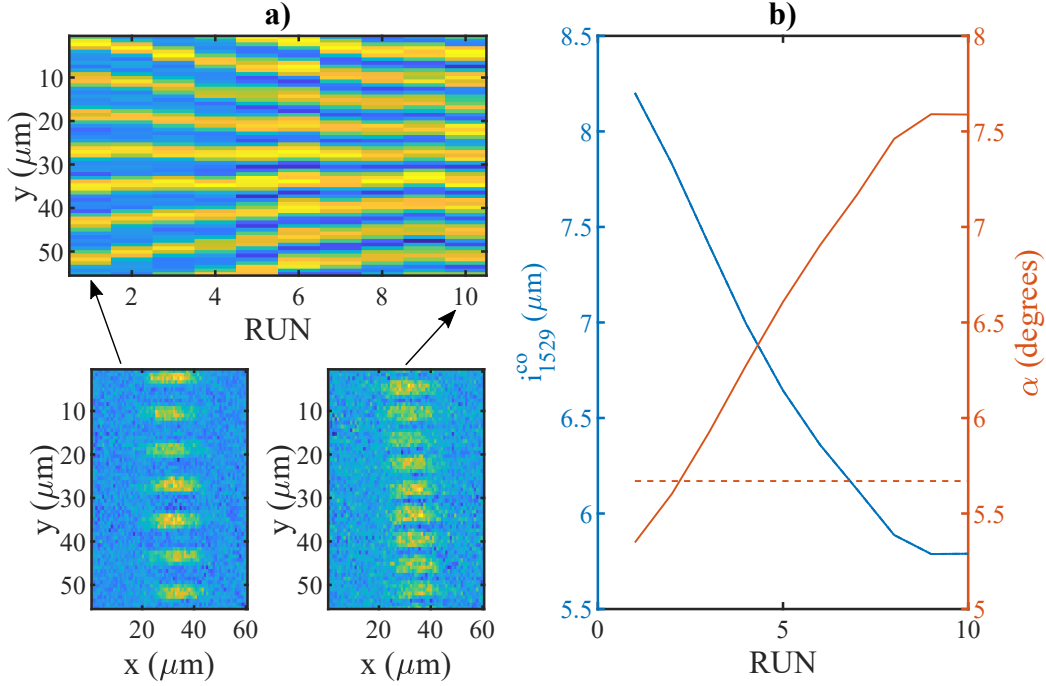


Figure 1.22: Procedure to set the correct half-angle  $\alpha$  on the experiment. Translation T1 is driven in between each RUN. a) 2D stack of the vertical projection of images taken on the sub-wavelength imaging axis with atoms trapped in an hybrid trap in DT2, repumped with 1529 lattice in co-propagating configuration. The phase of '1529 L' is adjusted with the piezo-stack on which '1529 forward RR mirror' is glued so the fixed central fringe is bright. The color map is adjusted to normalize the effect of the atom number differences for clarity. b) Evolution of the lattice period extracted by fitting the FT of the image and the computed half-angle associated. The target angle is represented as a dashed line. T1 is then driven back until the correct interfringe is reached.

### 1.4.5 Active common stabilization of the two lattices

A good control of the relative phases of both lattices is critical for the sub-wavelength experiment. Because of the long optical length ( $L$ ) between the first passage of the light on the atoms and the second, wavelength drift ( $\delta\lambda$ ) can lead to large displacement ( $\Delta x$ ) of the fringes on the cloud. It is however only the relative position of the two lattices that matters and not the absolute position of a given fringe in space. Thus, both lasers have been frequency-locked to a common reference (cavity). This way, both lattices share the same fluctuations, improving their relative fringe position stability on the atoms.

We present in this section both the free-running and locked wavelength stability of the 1064 and 1529 nm lasers.

Both lasers are locked following a Pound-Drevel-Hall scheme [71] on a common Fabry-Perot cavity. The cavity is under vacuum to reduce fluctuations and its temperature is stabilized to 10 mK. We measured at 1064 nm the free-spectral range (FSR)  $\Delta\lambda = 2.90 \pm 0.07$  pm and the transmitted peak Lorentzian FWHM  $\delta\lambda = 0.810 \pm 0.005$  fm. This give a finesse of

$F = \frac{\Delta\lambda}{\delta\lambda} = 3580$ . The optical setup is detailed in a previous thesis [50, p.140]. The wavelength of the two lasers are measured using a HighFinesse WS7-60 wave-meter, giving a precision (measured) of 1 fm. Just after being turned ON, the frequency of the 1064 nm laser take up to 2 hours to stabilize as we see in Fig. 1.23 b).

In Chapter 2, we will try to resolve objects of 30 nm size, and according to Eq. 2.49 the fringe displacement is given by  $\Delta x = i_{1529} L \delta\lambda / \lambda^2$ . On these experiments, there is three different time scale to consider for fringes position fluctuations. The first one,  $\tau_{pz} = 1$  s, is the time in a single experiment over which the atomic cloud will be addressed during the sequence. The second one,  $\tau_{ss} = 90$  s is the time between two consecutive sequences. The last one  $\tau_{wp} = 32$  min is the total time for doing one wave-packet scan (generally 21 sequences). The 1064 wavelength is naturally quite stable as shown in Table 1.7. On the other hand, we see Fig. 1.24 that

Time scale	$\sigma_{1064}$ unlocked (fm)	locked (fm)	$\sigma_{1529}$ unlocked (fm)	locked (fm)
$\tau_{pz} = 1$ s	1.7	0.39	83	0.97
$\tau_{ss} = 90$ s	2.1	0.66	87	1.0
$\tau_{wp} = 32$ min	6.5	3.7	88	5.3

Table 1.7: Typical wavelength stability of the 1064 and 1529 lasers, with and without the PDH cavity lock. The values presented are the standard deviations over the specified timescale, given in femtometer. Data are taken with a HighFinesse WS07-60 wave-meter. The different time scales are defined in the text.

the evolution of the free running 1529 frequency drifts by 0.25 pm on the shortest timescale. These drifts are strongly corrected by the PDH lock whose importance is highlighted Fig. 1.24 b) : without it, the frequency is randomized between two consecutive shots on 0.4 pm. This correspond to a fringe stability of 64 nm higher 30 nm resolution we are aiming for. We show in Fig. 1.24 c) a zoom on the locked case that emphasis the reduced fluctuations. On short time scales, we are down to 5 fm, with some longer time scale (close to an AC cycle) evolution in the 15 fm range, corresponding to a drift of the fringes of 2.4 nm only. Frequencies stability are recapitulated table 1.7.

In conclusion, the PDH lock improved the frequency stability of the 1529 by almost two orders of magnitude, while at least<sup>7</sup> improving by a factor 2 the stability of the 1064. The long term drift could either come from a drift of the wave-meter it-self or from temperature fluctuations of the cavity. Even in this case, it would lead to a common drift of both wavelength and will not impact our measurements<sup>8</sup>.

<sup>7</sup>Given the data, we are really limited by the wave-meter resolution for the data on the locked 1064 laser.

<sup>8</sup>see Chap 2 for details.

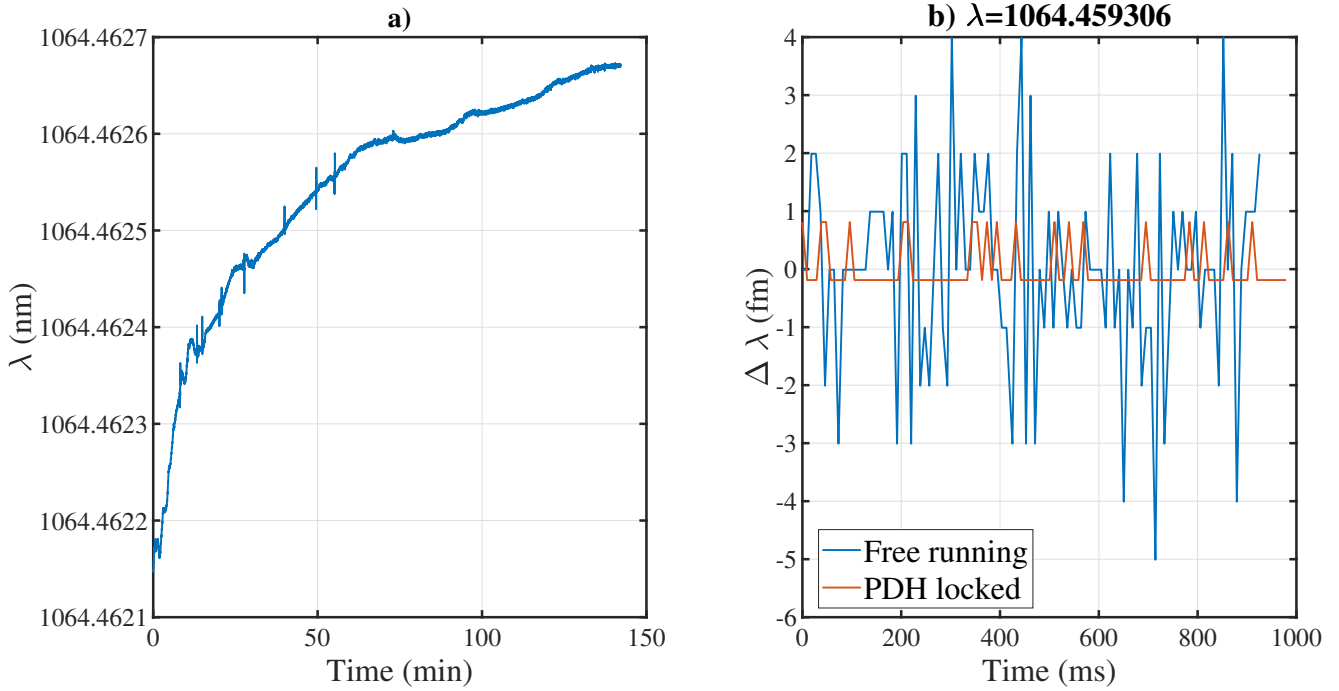


Figure 1.23: Wavelength stability of the 1064. a) Stabilization of the wavelength just after the turn ON. b) Wavelength stabilization using the Pound-Drever-Hall lock. An offset of  $0.1 \text{ pm}$  due to the lock-setpoint has been removed between the free-running and locked case for easiness of read.

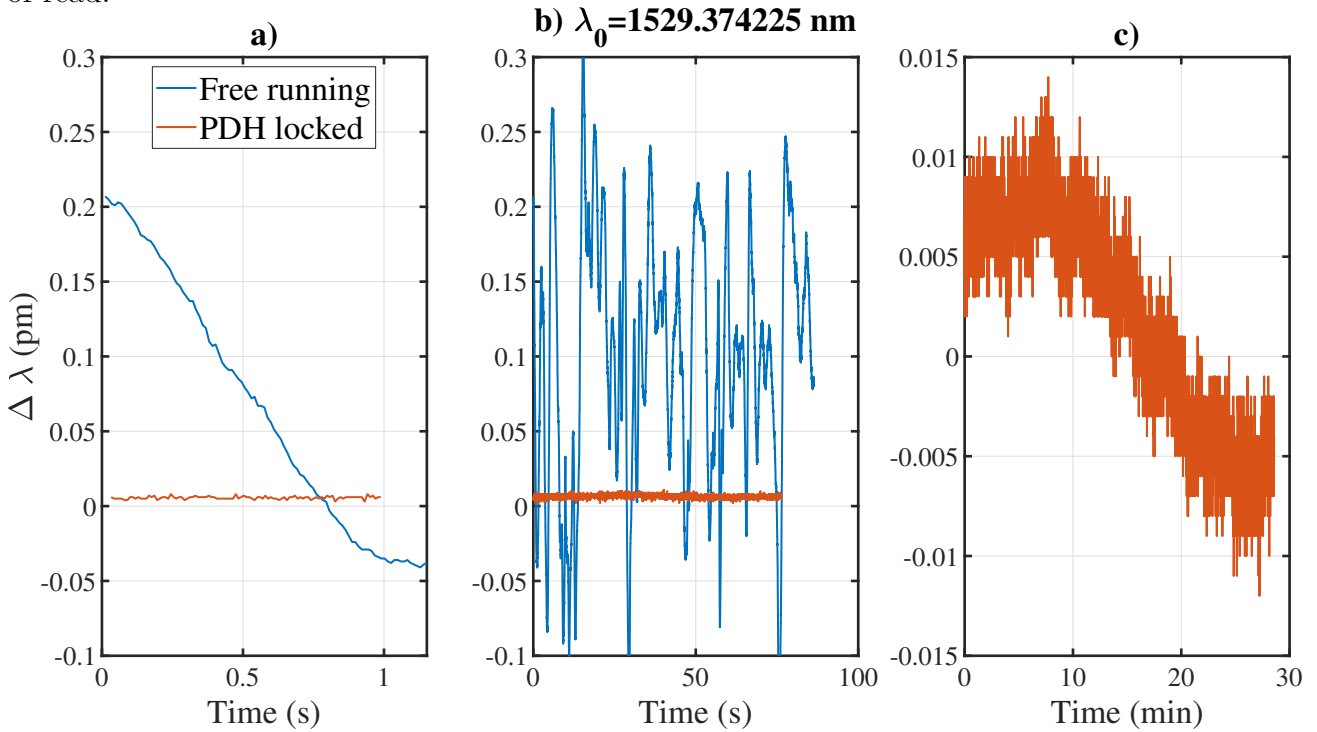


Figure 1.24: Wavelength stability of the 1529. The same data set is used for all the subplots. Notice from left to right the time scale increase, corresponding to the three time-scales mentioned in the text. All three y-axis are in the same unit.

## 1.5 Summary

We gave in this chapter a rapid overview of the experimental apparatus implemented for producing and studying doubly-dressed states in a  $^{87}\text{Rb}$  BEC.

We present in 1.1.3 the vacuum chamber and mention a degrading vacuum quality preventing the realization of Bose-Einstein Condensation. Indeed, the lifetime in our MOT is fluctuating from day to day between 7 to 10 s while the one in our MT is under 4 s. We also introduced the lasers at 780 nm and modifications that we made to increase the power and polarization stability.

Then, we established in 1.2 a reduction factor on the bare scattering cross section for optically dense ensembles as  $\alpha = 1.17(9) + 0.255(2)b$  where  $b$  is the optical density. This correction is used to quantitatively compute the atom number when doing saturated absorption imaging on the three imaging axis presented.

In 1.3, we introduce the 1064 nm laser used for the hybrid dipole and magnetic trapping of the cloud in which we perform optical evaporation until reaching a pure BEC. Thermal considerations on the magnetic trap coils and its impact on the vacuum quality are given in Appendix D.4.1.

Finally, we present in 1.4 the two ways accordion lattice scheme implemented to produce a 1D optical lattice at 1529 nm with tunable periodicity. We also give the optical characterization and alignment procedure of the setup.

This conclude the presentation of the current experimental setup used to produce a pure BEC of  $^{87}\text{Rb}$ . In the next chapter, we describe how it is loaded in a trapping optical lattice allowing to reach spatial resolutions lower than the diffraction limit with a sub-wavelength imaging scheme. For this, shot-to-shot experimental conditions need to be very reproducible, explaining our dedication to detail and to improve the stability of various parameters including laser power and polarization, bulk temperatures, and optical alignments. We saw that the vacuum is now the limiting factor preventing further results to be obtained. Work is in progress to improve the vacuum. In the next chapter, we report on the progress made toward implementing an atom chip under vacuum used to manipulate ultra cold atoms.



# Chapter 2

## Sub-wavelength imaging

Imaging techniques are a key enabling element to understand the world we live in. Experimental confirmation of theories require to observe an object by it's impact on an measurable quantity. As we progress in our knowledge, we need to refine the imaging capabilities and resolutions. A fundamental limit on the resolution of any imaging system is set by the diffraction limit : a point-like EM emitter at wavelength  $\lambda$  will give a spot image always bigger than  $\lambda/2$ .

Instead of using light, one could use electrons as a particle source, presenting a much smaller wavelength than optical photons. Beautiful results have been obtained with the development of electron microscopy since 1931 [72], method overcoming the spatial resolution of light microscopes in 1933 and now entering the atomic regime [73], with resolution smaller than 50 pm. With this indirect imaging method, we are now able to visualize objects at the atomic scale, an amazing result, which is however not always usable. This imaging is for example not possible if the object does not interact with electrons, if objects are too thick (more than a few 100 nm), or studied in-vivo.

For this reason, development of so-called superresolution microscopy techniques have flourished, as ways to beat the diffraction limit in optical microscopes. These techniques were developed in the field of chemistry and biology, giving resolutions at the molecular levels. Image reconstructions based on further image analysis [74] or STEM microscopy, based on the non-linear response of a medium can be used to obtain resolutions lower than the diffraction limit. This type of techniques has been adapted in atomic physics and we can cite for instance imaging of cold atoms trapped in optical lattices with a resolution of 32 nm [35] or exploiting quantum interference in a three-level system, to reach almost 10 nm [36] resolution.

With the trapping scheme presented in 2.2.2, the order of magnitude of the period for the resulting lattice is 100 nm. Super-resolution imaging method are required to study the site correlation of such lattice. The doubly dressed state trap presented in section C.3.2 utilize similar concepts than the selective imaging of a cloud with a spatial resolution better than the diffraction limit that we present below. The quantitative agreement of the imaging method will also serve as an indirect proof of principle of the DDS trap formalism.

In this chapter, we present a super-resolution technique adapted to cold atom experiments in which a laser radiation at 780 nm interact with the cloud only at specific spatial positions. Experimentally, this method is implemented using a 1529 nm laser radiation tuned close to

the  $5P_{3/2} \rightarrow 4D_{5/2}$  transition, which creates an AC-Stark shift with a strong spatial gradient. In this case, the imaging resolution is given by the AC-Stark shift slope and is not limited by diffraction anymore.

The chapter start with a presentation of the method. Then, we recall the theoretical description of an ultra-cold Bose gas trapped in an optical lattice, and present the experimental implementation of a 1D lattice at 1064 nm in which a BEC is adiabatically loaded. We apply our method to selectively image atoms trapped in this lattice with a spacing of 532 nm, below the Point-Spread Function (PSF) width of the imaging system. We conclude the chapter by quantitatively evaluating both experimental and theoretical limits in the lowest resolution and show that it can be used to resolve the single atomic density distribution of a specific site in a deep optical lattice.

## 2.1 Super-resolution imaging technique

In this section, we introduce the super-resolution imaging scheme implemented. A detailed presentation of the method has been given in a previous thesis [54]. We focus here on the experimental implementation and on the results.

Our method is based on the spatial modulation of the excited state, allowing to selectively interact with the cloud over a width depending on the modulation slope. In section 2.1.1, we derive the exact light shift and give the spatial resolution it can attain. Then, we focus in section 2.1.2 the BAT curve method used to experimentally calibrate this light shift. Using it, we quantitatively evaluate the resolution reached on a homogeneous cloud.

According to the internal structure of  $^{87}\text{Rb}$  given in Fig. A.1, the first excited state  $5^2P_{3/2}$  can be dressed [30] with a laser radiation at 1529 nm, tuned close to the  $5^2P_{3/2} \rightarrow 4^2D_{5/2}$  transition. A spatial modulation of the laser intensity get imprinted on the energy level as a spatially dependent energy modulation. To maximize the spatial gradient of the intensity profile, we produce an optical lattice at 1529 nm using the experimental setup presented in 1.4 instead of a highly focused beam. The contra-propagating configuration giving an interfringe under one micron was presented in Fig. 1.18. The 780 nm laser, with detuning  $\Delta_{780} = \omega_{780} - \omega_0$  where  $\omega_0$  is the bare atomic angular frequency of the  $5S_{1/2} \rightarrow 5P_{3/2}$  transition, can be tuned to be resonant at different parts of the modulation. In our case, the slope is maximum at the middle of the modulation, resulting in a very narrow resonant area whose width can be smaller than the diffraction limit. In order to derive this width, we consider the hyperfine structure of the ground state, yielding two different cases when either a repumper or a cooler transition is driven by the 780 laser. The imaging transition correspond to a closed atomic transition where atoms are described as a two-level system (2LS). The repumper transition correspond to an open atomic transition and is described as a three-levels (3LS) or five-levels system (5LS).

- Cycling transition.

The first case, shown Fig. 2.1 a) and b) , is an imaging transition where the full cloud is prepared into the  $5S_{1/2} |F_g = 2, m_F = -2\rangle$  (in our case using a MW transfer), and imaged on the cycling transition  $5S_{1/2} |F_g = 2, m_F = -2\rangle \rightarrow 5P_{3/2} |F_e = 3, m_F = -3\rangle$  with the 1529 laser ON, dressing the excited state. Here, the sub-wavelength resolution emerge directly during the imaging on the cycling transition. This method is very sensitive to

photon recoil during the imaging, that push the imaged atoms away from the imaged volume.

- Repumper transition.

The second case shown in Fig. 2.1 c) and d), corresponds to a repumper transition where the 780 laser is tuned from  $|F_g = 1\rangle$  to  $|F_e = 2\rangle$ . With a few repumper photons, atoms are transferred due to absorption and spontaneous decay in the  $|F_g = 2\rangle$  state. The repumped cloud is then probed with a standard absorption imaging method on the cycling transition, with no 1529 light. Here, the sub-wavelength resolution appears during the repumping process. The reader should keep in mind that during the time between the repumping and the imaging, atoms in this initial sub-wavelength volume will evolve in the trap in the  $|F_g = 2\rangle$  state.

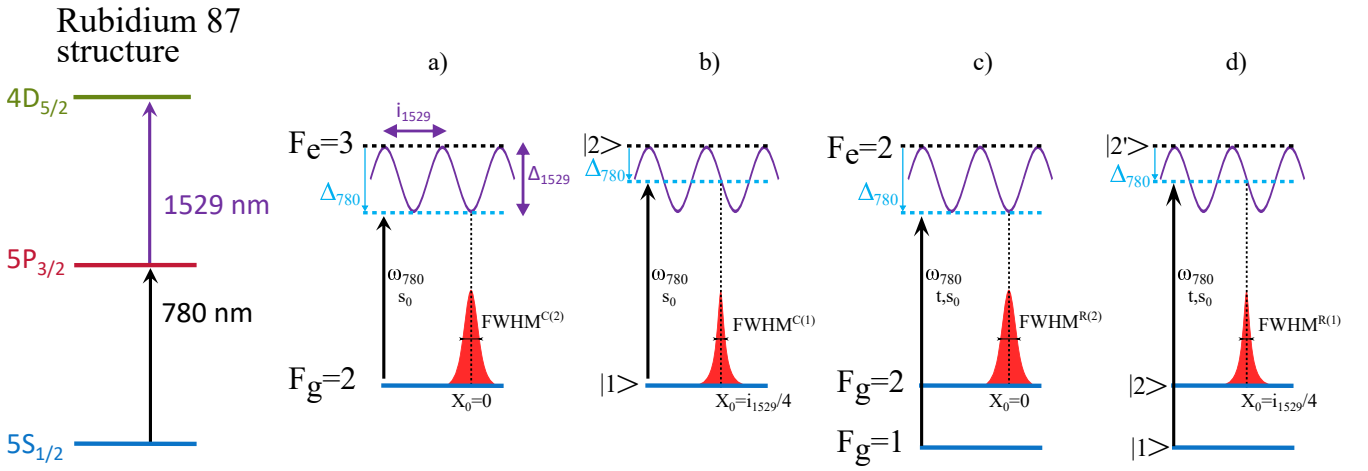


Figure 2.1: Representation of the FWHM achieved with our super-resolution method. On a cycling transition, the system is approximated as 2LS and the detuning is at the bottom of the modulation in a) and at the middle of the modulation in b). For a repumper transition, we consider a 3LS. The 780 nm laser radiation is tuned at the bottom of the modulation in c) and at the middle in d).

### 2.1.1 Theoretical model and associated resolution

In the limit of small energy shifts compared to the hyperfine splitting, second order perturbation theory can be used to compute the energy shifts due to the electric-field dipole interaction as presented in Appendix B. For larger light shift, the exact value is given by the full diagonalisation of the Hamiltonian, including the AC-Stark effect and the Hyperfine splitting. In this work, we consider modulations in the range of 100 MHz, for which the perturbation theory already under-estimate the light shift by 15 % compared to the full diagonalisation [31, 54]. For a better modeling, we apply an hybrid formalism where the maximum light shift is given by the diagonalisation and the shape is linear with the intensity, as given by the perturbation theory. The effect of the 1529 nm laser on the ground state is also evaluated in the perturbation formalism according to Eq. B.5 and gives a light shift of 1.8 kHz, which can be safely neglected for the rest of the chapter.

Reducing our study to one dimension, the space dependent light shift on the excited state can be written as :

$$\Delta_{1529}(x) = \mathcal{F}(I_{1529}(x)) \quad (2.1)$$

where  $\mathcal{F}$  is a functional, given by the exact diagonalisation.

In order to evaluate the resolution, we consider an approximate evaluation of  $\mathcal{F}$ . Thus, an optical lattice at 1529 create a light shift as

$$\Delta_{1529}(x) = \frac{\Delta_{1529}}{2} \left( 1 + \cos \left( 2\pi \frac{x}{i_{1529}} \right) \right) \quad (2.2)$$

where  $\Delta_{1529}$  is the total light shift amplitude in  $\text{rad.s}^{-1}$  evaluated by the full diagonalisation and  $i_{1529}$  the interfringe of the 1529 lattice.

In the following calculation, any ground state shift corresponding for instance to the trapping potential are not included. With the excited state dressing, a 780 nm laser radiation interacting with the cloud will have a detuning

$$\Delta(x) = \Delta_{780} - \Delta_{1529}(x) \quad (2.3)$$

where  $\Delta_{780} = \omega_{780} - \omega_0$  is the laser detuning compared to the bare transition.

With the general expression of the detuning established, we derive the analytic spatial resolution around the fringe bottom and at the middle of the modulation for both a cycling (2LS) and a repumping (3LS) transition. For this, we need to derive the excited state population at steady state which are given by the Optical Bloch Equation (OBE) describing the transfer of atoms from  $|1\rangle$  to  $|2\rangle$  (see Fig 2.1 for state definition). We consider below dynamics over long time scales compared to  $\Gamma$ . Thus, we consider the coherences to be at steady states ( $d\rho_{i,j}/dt = 0$ ). The coherences can be adiabatically eliminated and the OBE in its matrix form reduce to a set of coupled rate equation involving the population only. The complete derivation has been carried within the PhD thesis of R. Veyron [54] and we remind below the main results.

### 2.1.1.1 Cycling transition

For a 2-levels system (2LS), the excited state population at steady state is given by :

$$\rho_{22}(x) = \frac{s_0}{2} \frac{1}{1 + s_0 + 4 \left( \frac{\Delta(x)}{\Gamma} \right)^2} \quad (2.4)$$

with  $s_0$  the saturation parameter of the 780 laser radiation for the cycling transition.

**Bottom of the modulation :** We now expand in series up to the second order the detuning. At the bottom of the modulation, the excited state shift is quadratic and reads :

$$\Delta(x) = \Delta(x_0) - \Gamma \left( \frac{x}{\Gamma x} \right)^2 \quad (2.5)$$

where  $\Gamma_x^{(2)} = \sqrt{\frac{\Gamma}{\Delta_{1529}} \frac{i_{1529}}{\pi}}$ .

At resonance, the excited state population is :

$$\rho_{22}(x) = \frac{s_0}{2} \frac{1}{1 + s_0 + 4\left(\frac{x}{\Gamma_x^{(2)}}\right)^4} \quad (2.6)$$

This distribution is characterized by a full-width at half maximum (FWHM) :

$$FWHM^{C(2)} = \sqrt{2}\Gamma_x^{(2)}(1 + s_0)^{1/4} \xrightarrow{s_0 \rightarrow 0} \sqrt{2}\Gamma_x^{(2)} \quad (2.7)$$

The total excited state population in a single fringe  $f_{22}$  at position  $x_0$  is proportional to the fringe width  $\Gamma_x^{(2)}$  as :

$$f_{22} = \int_{-\infty}^{+\infty} \rho_{ee}(x) dx = \frac{s_0}{2(1 + s_0)^{3/4}} \pi \frac{\Gamma_x^{(2)}}{2} \quad (2.8)$$

**Middle of the modulation :** At the middle of the modulation, corresponding to  $x_0 = i_{1529}/4$ , the light shift is linear in  $x$  and reads :

$$\Delta(x) = \Delta(x_0) - \Gamma \frac{x - i_{1529}/4}{\Gamma_x^{(1)}} \quad (2.9)$$

where  $\Gamma_x^{(1)} = \frac{\Gamma}{\Delta_{1529}} \frac{i_{1529}}{\pi}$  is the excited width of a single fringe.

At resonance, the FWHM for a single fringe at  $x_0$  is :

$$FWHM^{C(1)} = \Gamma_x^{(1)}(1 + s_0)^{1/2} \quad (2.10)$$

Again, we define the total excited state population in a single fringe :

$$f_{22} = \frac{s_0}{2\sqrt{1 + s_0}} \pi \frac{\Gamma_x^{(1)}}{2} \quad (2.11)$$

### 2.1.1.2 Repumper transition

For a repumper transition, atoms can be described as a 3LS, with  $|1\rangle = |F_g = 1, m_F = -1\rangle$ ,  $|2\rangle = |F_g = 2, m_F = -1\rangle$  and  $|2'\rangle = |F_e = 2, m_F = -1\rangle$  as defined in Fig. 2.1 d).

Considering a system in which all states are initially prepared in  $|1\rangle$ , the repumped fraction in state  $|2\rangle$  in the low saturation regime of the pumping laser is :

$$\rho_{22}(x) = 1 - \exp\left(-c_{22'} \Gamma t \frac{s_0}{2} \frac{1}{1 + s_0 + 4(\Delta(x)/\Gamma)^2}\right) \quad (2.12)$$

where  $c_{22'} = 1/2$  is the sum of squared Clebsch-Gordan coefficients from  $|2'\rangle$  to  $|1\rangle$  and  $|2\rangle$  [75].

Under the hypothesis of long pulse duration ( $s_0 \Gamma t \gg 1$ ) assuring the stationary solution

and of well-resolved fringes ( $\Gamma/\Delta_{1529} \ll 1$ ), assuring that only a single fringe of repumper contribute to atoms at a given position, we write the FWHM of the distribution at the bottom of the modulation as:

$$FWHM^{R(2)} = \sqrt{2}\Gamma_x^{(2)} \left( \frac{c_{22'}\Gamma s_0 t}{2 \ln(2)} \right)^{1/4} \quad (2.13)$$

At the middle of the modulation, we have :

$$FWHM^{R(1)} = \Gamma_x^{(1)} \left( \frac{c_{22'}\Gamma s_0 t}{2 \ln(2)} \right)^{1/2} \quad (2.14)$$

These FWHM are similar to the one obtained for the cycling transition with a modified saturation parameter  $s_0^{eff} = 1 - \frac{c_{22'}\Gamma s_0 t}{2 \ln(2)}$ .

This gives a quantitative description of the FWHM of the addressed area, yielding relevant order of magnitude for preparing experiments.

Similarly to the 2LS model, we define the total repumped fraction  $f_{22}$  in one fringe as

$$f_{22} = \int_0^{i_{1529}} \rho_{22}(x) dx \quad (2.15)$$

For the work presented in this manuscript, the sub-wavelength scheme is used on the repumper transition. A correction accounting for the Zeeman splitting of  $|F_g = 1\rangle$  and  $|F_e = 2\rangle$  need to be mentioned. We extend the 3LS by considering a 5-level system (5LS) including the possibility to decay in other ground states  $|F_g = 1, m_F \neq -1\rangle$  effectively reducing the maximum value of the repumped fraction in  $|2\rangle$ . We also include the excited states  $|F_e = 1, m_F \neq -1\rangle$  to which light can couple from the ground state

Exact FWHM computed by numerical diagonalisation of the Hamiltonian and fitting the resulting distribution shows a very good agreement between the 5LS and the 3LS. It also shows that the analytic formulas given in Eq. 2.13 and Eq. 2.14 evaluate the FWHM at both the middle and bottom of the modulation with no error. We note that an evaluation using the analytic formulas for the 2LS tends to under-estimate the FWHM size with a 10 % error compared to the 5LS exact result. These numerical simulations prove that the analytic expressions  $FWHM^{R(1)}$  and  $FWHM^{R(2)}$  give a quantitative result on the repumped volume size for any saturation parameter and light shift up to 40  $\Gamma$ .

We introduce two dimensionless parameters :  $M_{1529} = \Delta_{1529}/\Gamma$  corresponding to the excited state modulation and  $S_{rep} = \Gamma s_0 t$  representing the transition saturation. We plot a 2D map of the achievable resolution depending on these two parameters in Fig. 2.2.

The total repumped fraction  $f_{22}$  defined in Eq. 2.15 is by definition proportional to the total number of atoms transferred in  $|F_g = 2\rangle$ . In the next section, we compare it with atom numbers experimentally measured using absorption imaging. Thus,  $\rho_{22}$  is correctly evaluated if both atom numbers are equal.

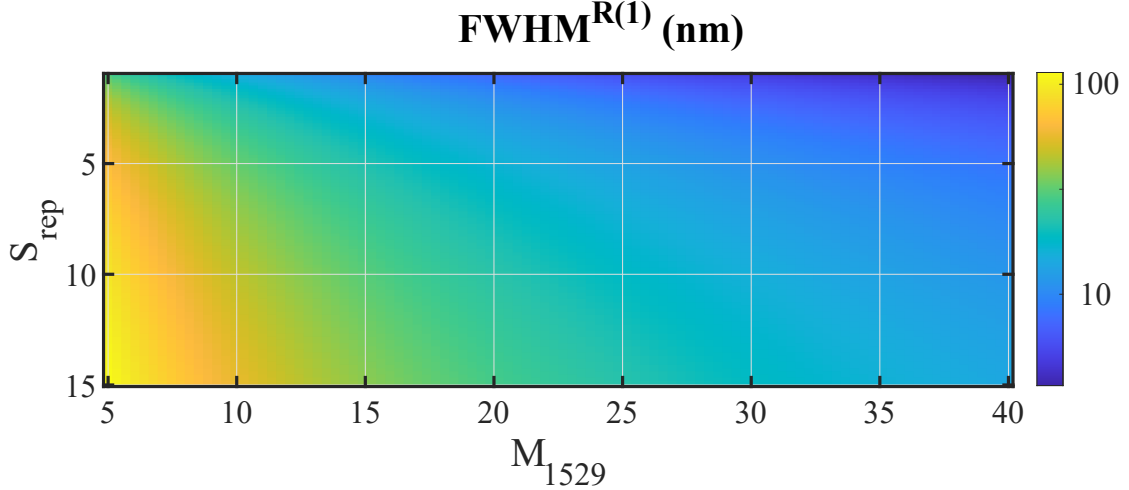


Figure 2.2: Expected Full-width at half maximum of the repumped area computed with Eq. 2.14 for  $i_{1529} = 768$  nm.

### 2.1.2 Experimental results and BAT-curves

Because of the diffraction limit of the imaging objective, the sub-wavelength resolutions width presented above cannot be directly spatially measured. Instead, we measure the number of atoms per fringes. We will demonstrate below that the number of atom per fringe is correctly evaluated by the integrated repumped fraction in a single fringe  $f_{22} = \int \rho_{22} dx$ , which is computed using the Multi-Level system formalism (for a 3LS,  $\rho_{22}$  is given by Eq. 2.12). The experimental proof is presented only in the contra-propagating configuration and more details including the demonstration in the co-propagating case are presented in the previous thesis [62].

Although not detailed here, we have been careful in this work to conjugate the camera with the atom plane and not with a Talbot image [76] that arise when imaging a periodic system.

Before this, we also introduce the calibration method of the excited state light shift, named BAT-curve (related to their shape). We will show that this method provide a quantitative calibration of the excited state lattice depth.

The optical lattice at 1529 nm is generated using the two-way accordion lattice setup represented in 1.4.

#### Excited state calibration : BAT-curves

First, we prove that BAT-curves are a quantitative calibration of the excited state lattice depth. As long as there is no power broadening ( $s_0 t \Gamma \ll 1$ ), we show that the amplitude  $\Delta_{1529}$  can be computed independently of the initial atom number, and repumper parameters. The result presented are obtained in the co-propagating configuration, with an interfringe  $i_{1529}^{co} = 8.30(5) \mu\text{m}$  measured by our high NA imaging system.

A thermal gas is prepared in the cross-dipole trap, elongated along the fringe direction, and the initial atom number is controlled using MW pulses. Acquisition of the repumper pulse ( $\pi$  polarized) during the experiment with an FPGA gives a precise knowledge of the repumper duration  $t$  and saturation parameter  $s_0$ , which has been calibrated in absolute. In this configuration, the 1529 beams waist are measured to be  $w_0^R = 131 \mu\text{m}$  and  $w_0^L = 138 \mu\text{m}$  at

a measured wavelength of  $\lambda_{1529} = 1529.35898(3)$  nm.

Assuming a 3D Gaussian atomic density distribution, the number of atoms repumped in each 1529 fringes is :

$$N_{rep} = \frac{N_0}{\sqrt{2\pi}\sigma_x} \int_0^{i_{1529}} \rho_{22}(x, s_0, t, \Delta_{780}\Delta\omega_{1529})dx \quad (2.16)$$

BAT-curves can be fitted according to Eq. 2.16 with only two free parameters : the initial atom number  $N_0$  and the light shift amplitude of the excited state  $\Delta\omega_{1529}$ . An error on the absolute frequency of the repumper laser radiation can be independently compensated by adding a third free parameter to shift the entire spectroscopy.

There is a good agreement between experimental data giving the atom number as a function of the detuning and the fit using Eq. 2.12 in Eq. 2.16 (shown for the contra-propagating case in Fig. 2.5) so we conclude that BAT-curves are indeed a tomographic spectroscopy of the 1529 lattice. Using this method, we plot the evolution of the computed light shift as a function of the 1529 power in each beam in Fig. 2.3. The measurement is repeated for different initial cloud

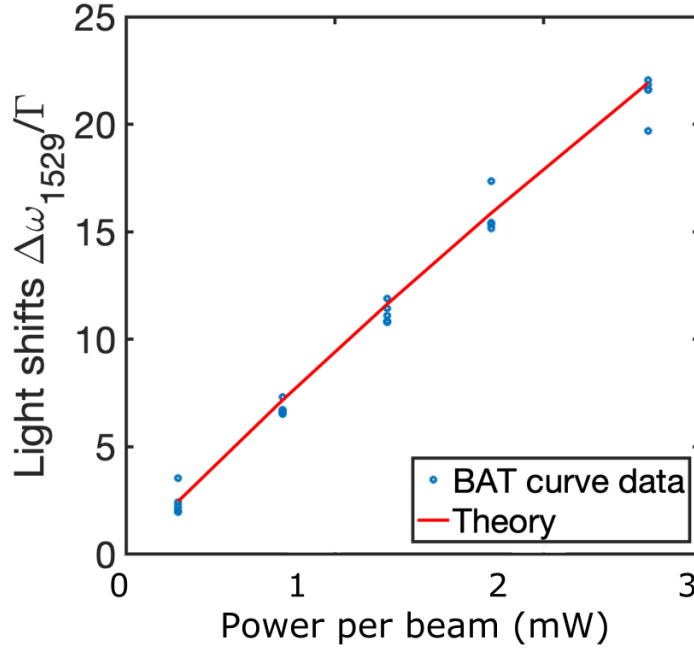


Figure 2.3: Induced light shift on the excited state as a function of the 1529 power. Experimental data fitted with two free parameters according to Eq. 2.16 (blue dots) match with the theoretical expectation (red curve) using no free parameters and full diagonalisation of the 5LS Hamiltonian.

density, saturation parameters  $s_0$  and repumping time  $t_{rep}$ , showing no specific dependency on the computed light shift. The theoretical light shift is obtained by measuring carefully the 1529 lattice parameters (waist of both beams, optical powers) and using the exact diagonalisation of the Hamiltonian for  $\rho_{22}$  in a 5LS to compute  $N_{rep}$  with no free-parameters. Experimental data points match the theoretical light shift which indicate that BAT-curves give a quantitative calibration of the excited state modulation.

## Quantitative repumped fraction in the contra-propagating configuration

In this section, we prove that the total repumped fraction  $f_{22}$  match with the number of atom experimentally measured. The measurement presented here are obtained in the contra-propagating configuration. Using the analytical formulas presented in section 2.1.1 we evaluate the resolution achieved in contra-propagating configuration in which the lattice period is below the diffraction limit of our imaging system. Thus, the light shift and the corresponding width have to be deduced from the number of atoms repumped.

Measuring the interfringe  $i_{1529}^{co} = 7.94(2) \mu\text{m}$  in the co-propagating case gives a precise measurement of the half-angle  $\alpha$  giving  $i_{1529} = 768.4(2) \text{ nm}$  for the contra-propagating configuration according to Eq. 1.15. Because the optical distance from the first passage of '1529 R' on the atoms and its reflection '1529 RR' forming the optical lattice is not negligible compared to the Rayleigh range, the waist of the second beam is hard to predict. This induce an error on the computed light shift so we take the one given by fitting the BAT-curves.

We prepare a thermal cloud in the cross-dipole trap, whose initial atom number is controlled using MW pulses by varying the second pulse length  $t_{MW}$  which brings atoms back in  $|F_g = 1, mF = -1\rangle$  before blasting  $|F_g = 2\rangle$ . The trap is elongated along DT1, in the fringes direction, and is imaged on the high N.A. imaging axis with no frame transfer. Atoms are repumped with the laser tuned at the middle of the modulation. Each measurements are repeated 10 times. The initial atom number is measured with a TOF and averaged 13 times. The optical density is integrated in a square box containing 11 fringes, over which we assume an homogeneous atomic distribution in order to fit the atom number.

We present the normalized atom number per fringe (N) as a function of the light shift in Fig. 2.4. We also plot the expected atom number computed with no free-parameters using Eq. 2.16 where  $\rho_{22}$  is obtained for a 3LS or 5LS model. We see the importance of taking into account the cross-section correction in the high density region to accurately compute the number of atoms. Indeed, the computed number without correction ( $\alpha = 1$  in the legend) gives an under-estimation of the actual atom number. When we include the optical density dependence of the absorption cross section ( $\alpha(OD) = 1.17 + 0.255 OD$ ), we obtain a very quantitative agreement with the model, even at small light shift (large OD).

For the atom number, at the contrary of the light shift computation, significant difference between the 3LS and 5LS model are observed. This can be explained by the reduction of the repumped fraction, which saturate in the 5LS because of the presence of dark states. The measurement shows that  $f_{22}$  obtained with the 5LS model match the experimental data for light shifts up to  $20 \Gamma$ . At  $40 \Gamma$  the discrepancy is probably due to hyperfine states overlap: the resonant condition being fulfilled at another spatial positions for  $|F_e = 3\rangle$  or  $|F_e = 1\rangle$ . At these high light shift, the 5LS model is put in default by assuming that eigenstates are hyperfine states.

In conclusion, the in-situ atom number measured is consistent with the prediction from the total repumped fraction. Thus, the repumped fraction  $\rho_{22}$  is quantitatively evaluated and the corresponding width reach sub-wavelength (compared to 780 nm) spatial resolutions. In the co-propagating configuration, the method achieve a resolution between 100 to 200 nm for light shifts from 20 to  $40\Gamma$  with  $i_{1529}^{co} = 8.3 \mu\text{m}$ . In the contra-propagating configuration where the

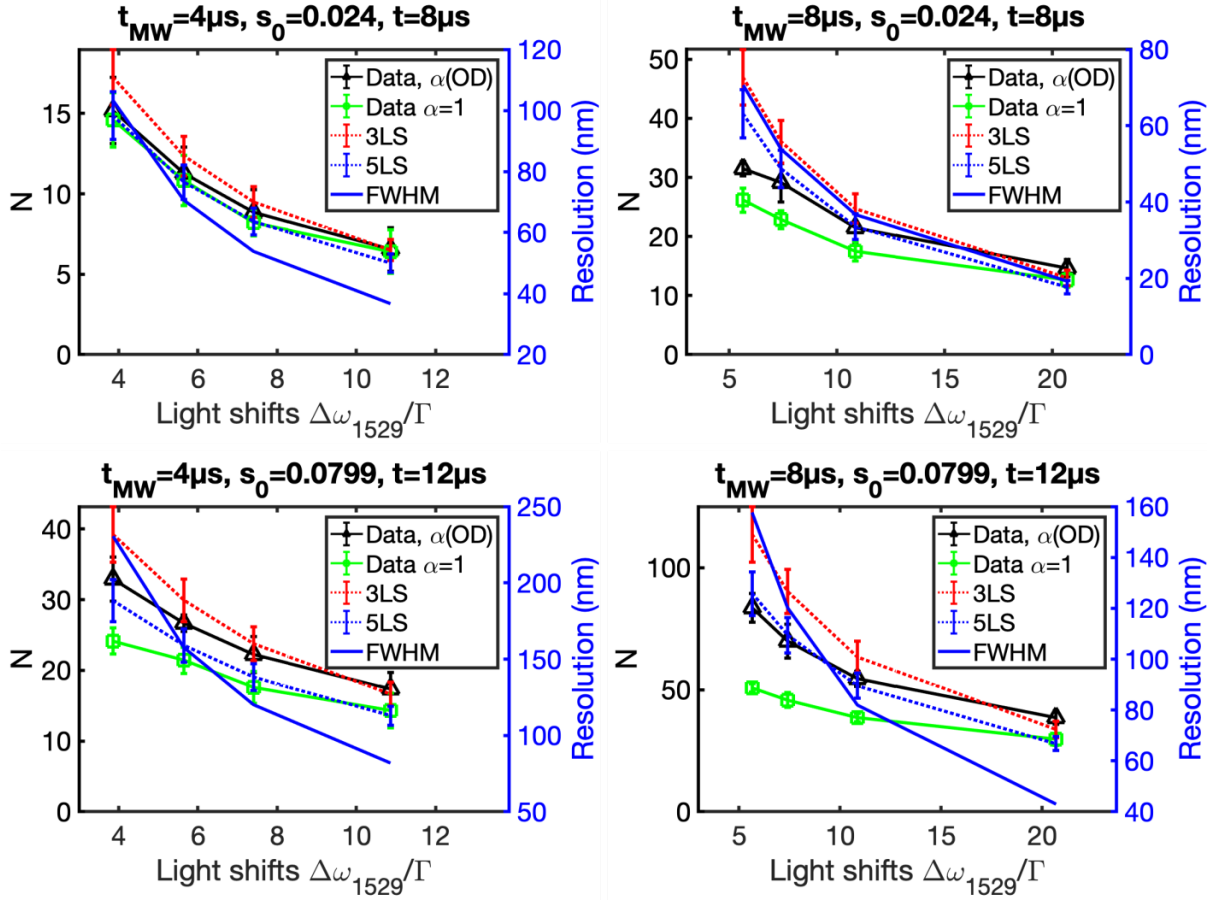


Figure 2.4: Number of atoms at the middle of the modulation integrated in 1 interfringe in the counter-propagating 1529 configuration: experimental data measured with the high NA imaging axis and 3LS and 5LS expectations for the total number of atoms in the cloud based on the total atom number measured by TOF. Error bars are statistical uncertainties. The corresponding resolution given by Eq. 2.14 is plotted on the right y-axis. Reprinted with permission from [54].

period is ten times lower, the resolution is directly divided by 10, reaching a FWHM of 20 nm for a light shift of  $20\Gamma$ .

Experimentally, the exact light shift on the excited state is often calibrated using the BAT curve method. For this, we use a cold cloud in an Hybrid DT1 + magnetic trap. Atoms are repumped in  $|F_g = 2\rangle$  with the '780 R Tunable' laser characterized in section 1.1.3.3, while having the 1529 nm lattice at a variable optical power. We present a spectroscopy on the repumper transition in Fig. 2.5. For small corrections, the light shift increase linearly with the optical power of '1529 R' and we are able to set the light shift with a precision of a few MHz.

In the next section, we will apply this sub-wavelength resolution to image the atomic density distribution of a Bose-Einstein Condensate trapped in a deep 1D optical lattice at 1064 nm with an interfringe of 532 nm. For this purpose, we introduce the formalism and experimental implementation of a BEC trapped in a 1D optical lattice.

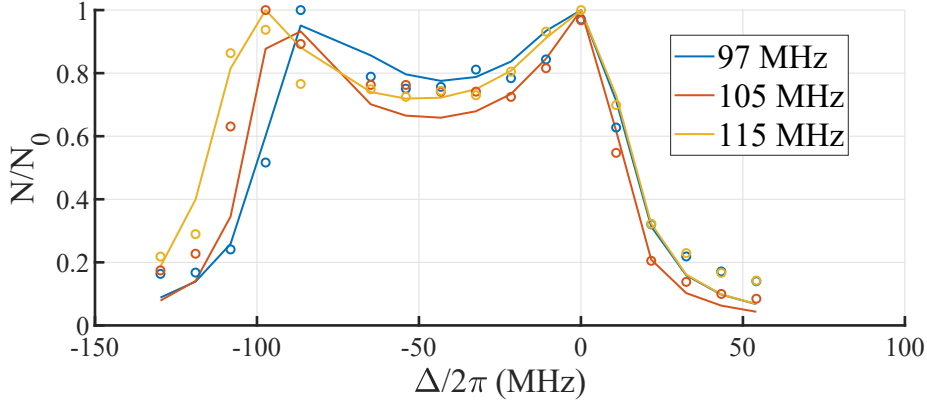


Figure 2.5: Typical BAT curves obtained in the contra-propagating case. We present the data here by normalizing to unity the maximum value of the total number of atom integrated ( $N$ ). The plain lines are fitted over experimental data (circles) using Eq. 2.16. The total atom number and the light shift (given in the legend) are the only free parameters. The optical power of '1529 R' is calibrated to be 6.25 mW (blue curve), 6.69 mW (orange) and 7.36 mW (yellow).

## 2.2 Ultra cold atoms in optical lattices

The same way the 1529 lattice create a spatially dependent light shift on the atom, a cloud can be trapped in a periodic potential when the usual FORT laser radiation present a lattice structure. The simplest lattice is obtained by retro-reflecting the laser. In the case of a 1064 nm laser radiation, it gives a lattice period of 532 nm. As we demonstrate later in this chapter, the method we just introduced will allow to resolve each site of such lattice.

In this section, we describe theoretically the behavior of an ultra-cold cloud of  $^{87}\text{Rb}$  trapped in a 1D optical lattice. Then, we present the experimental apparatus used to adiabatically load a BEC from the hybrid trap into a 1D optical lattice and characterize the trapping potential.

### 2.2.1 Bose atoms trapped in an optical lattice

In this section, we consider a 3D optical potential, with one direction presenting a spatial modulation along  $x$  of period  $i_{latt}$ . The total potential considering the retro-reflection of a laser beam of waist  $w_0$  and optical power  $P_0$  is :

$$V(x, r) = \frac{V_0}{2} e^{-2r^2/w_0^2} \left( 1 + \cos\left(\frac{2\pi x}{i_{latt}}\right) \right) + V_{ext}(x) \quad (2.17)$$

with  $V_0 = 4C_{dip} \frac{2P_0}{\pi w_0^2}$  defined according to Eq. B.5 and  $V_{ext}(x)$  an additional potential along the lattice direction.

We introduce the recoil energy  $E_R = \hbar^2 k^2 / 2m$ , typical energy scale of the system . Using this definition, we write the potential as  $V_0 = sE_r$  with  $s$  a dimensionless parameter, that is negative for a red-detuned lattice.

Albeit the external confinement, the harmonic approximation of the trapping potential along

the lattice gives the trapping angular frequency as :

$$\hbar\omega_{latt} = \sqrt{4V_0 E_r} \quad (2.18)$$

For an harmonic external potential of angular frequency  $\omega_{ext}$ , the total trapping angular frequency is  $\omega_x^2 = \omega_{latt}^2 + \omega_{ext}^2$ .

In the transverse direction, the harmonic approximation gives trapping frequencies as :

$$\nu_t = \frac{1}{2\pi} \sqrt{\frac{4V_0}{m\omega_0^2}} \quad (2.19)$$

## Bloch band

Following the analogy with solid-state physics, the motion of an atom in an optical potential is described by the standard theory of Bloch bands [77]. In the case of a 1D optical lattice, the Hamiltonian of the system is

$$H_{lattice} = \frac{p^2}{2m} + \frac{V_0}{2} \left( 1 + \cos\left(\frac{2\pi x}{i_{latt}}\right) \right) \quad (2.20)$$

According to Bloch's theorem the eigenfunctions of the Hamiltonian above are the so called Bloch functions :

$$\phi_q^{(n)}(x) \equiv e^{iqx} u_q^{(n)}(x) \quad (2.21)$$

with  $u_q^{(n)}$  a periodic function with the same periodicity as the lattice potential. These functions are characterized by three parameters : their band index ( $n$ ), quasimomentum  $q$  and energy eigenvalue  $E_q^{(n)}$ . Atoms occupying the lowest energy band of a relatively deep well are well localized. The Wannier functions, orthogonal to each other, correspond to the limit case of atoms localized in a single site. They are defined in terms of the Bloch functions by [78, 79]:

$$w_n(x - x_j) \equiv \mathcal{N} \sum_q e^{-iq \cdot x_j} \phi_q^n(x) \quad (2.22)$$

where  $\mathcal{N}$  is a normalization constant. This define the Wannier function depending on the Bloch function up to phase terms. However, it was shown [80] that there is a unique choice of phases which optimize the localization in site  $j$ . In this case, the Wannier function  $w_n(x - x_j)$  decays exponentially as  $|x - x_j| \rightarrow \infty$ .

We consider the weakly interacting regime, in which the tunneling rate between neighboring lattice sites is large compared to the interaction energy between two atoms. In this case, the BEC can be described by a macroscopic wave-function, determined using the Gross-Pitaevskii equation. When the chemical potential is small compared to the trap depth, the system can be described using a tight binding model. Therefore, the ground state wave-function of a single site is much smaller than the lattice spacing and the system consist of individual BECs with phases coupled due to the tunneling term.

In the tight binding picture, atoms in the site  $j$  are described by a localized macroscopic wave-function  $\varphi_j(x)$ . For 1D lattices, the confinement in the transverse directions are generally weak compared to the longitudinal one. In this case, the ground state wave-function is broadened

due to the repulsive interaction between the atoms. Thus, an effective width should be found using a variational ansatz.

The localized wave-function, normalized to unity, can be written as [26] :

$$\varphi_j(\mathbf{r}) = w_0(x - x_j)\Theta_y(y)\Theta_z(z) \quad (2.23)$$

We define a macroscopic wave-function describing the total system as a sum of each localized wave-function

$$\Psi(\mathbf{r}) = \sum_j \psi_j \varphi_j(\mathbf{r}) \quad (2.24)$$

where  $\psi_j = \sqrt{\hat{n}_j} e^{i\phi_j}$  is defined for each site  $j$  with a phase  $\phi_j$  and average number of atoms  $\hat{n}_j$ . The total number of atom is given by  $\sum_j |\psi_j|^2 = N$  and the total Hamiltonian is [81] :

$$H = - \sum_{\langle i,j \rangle} J_{i,j} \psi_i^* \psi_j + \sum_j \epsilon_j |\psi_j|^2 + \frac{1}{2} U \sum_j |\psi_j|^4 \quad (2.25)$$

The first term  $J_{i,j}$  corresponds to the hopping between adjacent sites and the summation is carried over first neighbor only. It can be written as :

$$J_{i,j} = J = - \int \left[ w_0^*(x - x_i) \left( \frac{\hbar^2}{2m} \nabla^2 + V_0(x) \right) w_0(x - x_j) \right] dx \quad (2.26)$$

This hopping term is related to the width of the lowest energy band and is given in the Mott-insulator regime by :

$$\frac{J^\alpha}{E_r} = \frac{4}{\alpha \sqrt{\pi}} \left( \frac{V_0}{E_r} \right)^{3/4} e^{-2\sqrt{V_0/E_r}} \quad (2.27)$$

with  $\alpha = 1, 2, 3$  the number of directions presenting a lattice structure.

The second term is due to the external potential confinement, rising the energy of each sites. On site  $j$ , the excess of energy per particle is  $(\epsilon_j - \mu)$ , with  $\mu$  the chemical potential that describe the on-site equilibrium energy of the wave-function.

The third term, is the on-site repulsion due to interaction :

$$U = g^\alpha \int |\varphi_j(\mathbf{r})|^4 d^3\mathbf{r} \quad (2.28)$$

The interaction term  $g^\alpha$  depends on the system dimensionality. For 3D optical lattices, it is  $g^{3D} = \frac{4\pi\hbar^2 a_s}{m}$ , with  $a_s$  the s-wave scattering length. In our case, we have a strong spatial confinement in the lattice direction. If we consider independent sites, the dynamic in each site is the one of a 2D Bose Gas, for which the contact interaction is re-normalized to [82] :

$$g^{2D} = \frac{2\hbar^2 \sqrt{8\pi} a_s}{m a_{QHO,x}} \quad (2.29)$$

where  $a_{QHO,x} = \sqrt{\frac{\hbar}{m\omega_x}}$  is the QHO length obtained in the harmonic approximating of the lattice confinement.

Albeit the external confinement, the transition between the Mott-Insulator (MI) and Super-Fluid (SF) regime is driven by the ratio between the on-site interaction energy and tunneling energy. For 1D lattices, there are strong deviation from the mean-field description, and the transition at large filling ( $\hat{n} \gg 1$ ) occurs at [25]:

$$(U/J)_c = 2.2\hat{n} \quad (2.30)$$

The dynamic of such system is described by a discrete Gross-Pitaevskii equation [83].

### Ground state wave-function

We consider here how the atoms distribute in the lattice for an inhomogeneous system, involving an external confining potential.

In the stationary state, the phases of each wave-functions have to share the same time evolution rate. This impose that the local chemical potential is equal over all the sites. The cloud will then distribute over the sites with a density presenting peaks around the lattice sites and an envelope with a Thomas-Fermi profile. Neglecting the kinetic energy term, the total energy on a single lattice site is :

$$E_j \approx \epsilon_j |\psi_j|^2 + \frac{U}{2} |\psi_j|^4 = \epsilon_j \hat{n}_j + \frac{U}{2} \hat{n}_j^2 \quad (2.31)$$

The chemical potential on site  $j$  is calculated as :

$$\mu_j = \frac{\partial E_j}{\partial n_j} = \epsilon_j + U\hat{n}_j = \text{cst} \quad (2.32)$$

In the experiment presented below, we populate more than 250 lattice sites. Thus, we ignore for the calculation below the lattice discreteness. The density distribution over the lattice is given by the usual Thomas-Fermi parabola [26]:

$$n(x) = \frac{1}{U} \left( \mu - m\omega_{ext}^2 x^2 / 2 \right) \quad (2.33)$$

The corresponding Thomas-Fermi radius is given by the usual equation and the chemical potential depend on the total atom number  $N$  and trapping frequency, given by :

$$\mu = \left( \frac{15 (\lambda/2)^3 m^{3/2} N U \omega_{ext}^3}{16\pi\sqrt{2}} \right)^{2/5} \quad (2.34)$$

This concludes the key theoretical elements required to describe an ultra-cold Bose gas trapped in an optical lattice. We use this formalism to describe our cloud and detail below how we experimentally implemented the trapping of a BEC in a 1D optical lattice.

### 2.2.2 Adiabatic loading of a 1D lattice

Experimentally, the trapping optical lattice is produced using the 1064 nm laser. The forward beam labeled '1064 lattice' shown in Fig. 1.1 is retro-reflected by the mirror M2 represented in Fig. 1.18.

We load a BEC initially prepared in an hybrid dipole ('DT1') and magnetic trap into the 1D optical lattice by slowly ramping up the lattice potential. An adiabatic transfer allows the BEC to remain in the many body ground state of the system. For such adiabaticity, one needs to fulfill two timescales criteria:

#### Single atom band population dynamic

We consider here the single particle motion, where a sudden change in the lattice potential could excite the cloud by populating higher energy bands. The time scale for adiabaticity is determined by the energy difference between the levels. Considering the adiabaticity criterion for the transfer from the lowest into the  $n$ -th energy band of a non interacting gas, reduced to quasi-momentum  $q \sim 0$ , away from the border of the Brillouin zone, we have [84, 85]

$$|\dot{s}| = \left| \frac{d}{dt} V_0 / E_r \right| \ll 16 E_r / \hbar = 204 \text{ kHz} \quad (2.35)$$

where the recoil energy for  $^{87}\text{Rb}$  at  $\lambda_{1064} = 1064.46(1) \text{ nm}$  is  $E_r / \hbar = 2\pi \times 2.02606(3) \text{ kHz}$ . The expression established above holds even at low trap depth  $V_0 \leq E_r$  where the adiabaticity is harder to fulfill since the level spacing increases with the potential depth.

#### N body dynamic and non linear processes

We now consider the many-body physics within the lowest Bloch band [86].

For a given set of lattice depth and external confinement potential, the many body ground state has a Thomas-Fermi like density profile defined in Eq. 2.33. When the trap parameters change, atoms redistribute over the lattice sites through tunneling in order to maintain a constant chemical potential.

This defines a second time scale  $\tau_{NL}$  for adiabaticity depending on the hopping energy. We define an adiabaticity criteria as [87]

$$\mathcal{A} = \max_{t \leq \tau_{ramp}} \left( \frac{\hbar |j|}{J^2} \right) \quad (2.36)$$

where  $\tau_{ramp}$  is the time to ramp up (or down) the lattice potential.  $\mathcal{A} \ll 1$  ensures an adiabatic evolution.

We consider a last time scale associated to the diffraction time [88]

$$\tau_{DF} = 2mr_{TF}^2 / \hbar \quad (2.37)$$

with  $r_{TF}$  the outer Thomas-Fermi shape of the cloud defined with Eq. 2.33. In most BEC systems, we have  $\tau_{NL} \gg \tau_{DF}$  thus fulfilling the adiabaticity criteria of Eq. 2.36 is sufficient to be adiabatic compared to the second and third timescale.

### S-Shape lattice ramp up

Inspired by [87], the 1D optical lattice power is ramped up from  $V_0(t = 0) = V_i$  to  $V_0(\tau_{ramp}) = V_f$  with an S-shape time dependency defined by

$$V_0(t) = \frac{V_1}{1 + e^{-\alpha(t-t_0)}} + V_2 \quad (2.38)$$

with

$$V_1 = \frac{V_i - V_f}{(1 + e^{\alpha t_0})^{-1} + (1 + e^{-\alpha(\tau_{ramp}-t_0)})^{-1}} \quad (2.39)$$

$$V_2 = V_i - \frac{V_1}{1 + e^{\alpha t_0}}$$

The loading is optimized compared to adiabaticity by changing  $\alpha$ ,  $t_0$  and  $\tau_{ramp}$ , with  $V_i = 0E_r$  and  $V_f = -40E_r$ . The inverse S-shape is used to return to the initial trap depth and we assess the BEC thermal fraction of the cloud using TOF measurement. We found that the initial BEC can be recovered for  $\tau_{ramp} \geq 200$  ms, with  $\alpha = 9/\tau_{ramp}$  and  $t_0 = \tau_{ramp}/2$ . Using the S-shape ramp defined in Eq. 2.38, we numerically evaluate the adiabaticity criterion mentioned above for 5 values of  $V_f$  as a function of  $\tau_{ramp}$ . In Fig 2.6 a), we see that we are well adiabatic compared to the criteria defined in Eq. 2.35. The criteria defined in Eq. 2.36 is plotted in Fig. 2.6 b) and gives the expected ramp time which should be implemented. Experimentally, we choose  $V_f = -40E_r$  and  $\tau_{ramp} = 300$ , and we are very adiabatic concerning the second criteria with  $\mathcal{A} = 0.07$ .

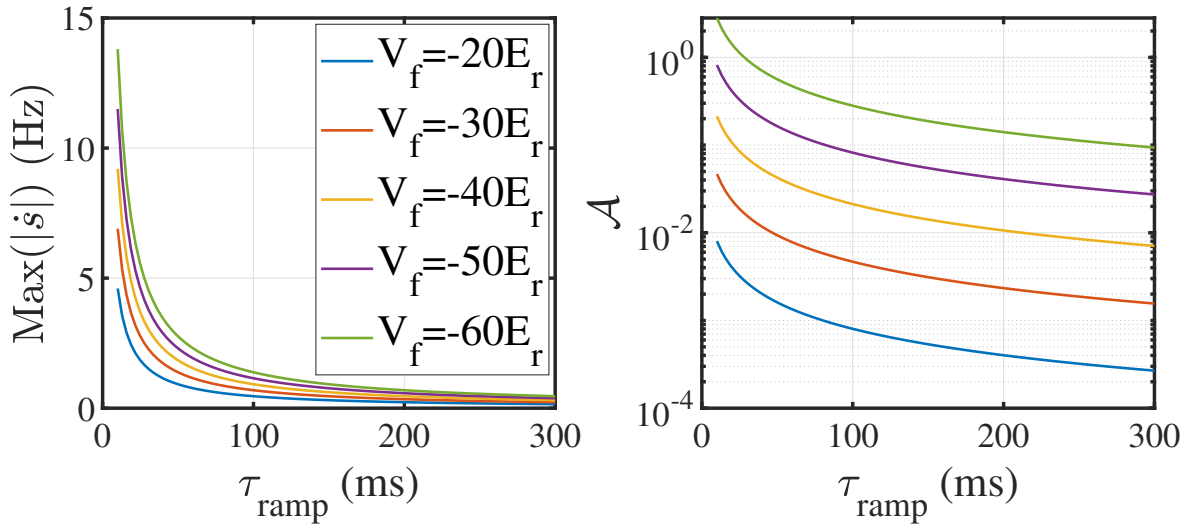


Figure 2.6: Numerical evaluation of the adiabaticity of the lattice loading for different final trap depth  $V_f$  with  $\alpha = 9/\tau_{ramp}$  and  $t_0 = \tau_{ramp}/2$ . a) Evaluation of the maximum value of the left part of Eq. 2.35 over the entire ramp up a function of the total ramping time. b) Evaluation of the criteria defined in Eq. 2.36 as a function of  $\tau_{ramp}$ .

A more quantitative approach is to measure the momentum component of the cloud in the lattice. A sudden turn off of the potential project the ground state  $\Psi_0$  on the plane wave basis. A TOF measurement should give [85] 65 % in  $0\hbar k$  and 17 % (in each)  $\pm 2\hbar k$ .

Experimentally, we find a good agreement up to  $V_0 = -4E_r$ , after which the images are too blurred to accurately compute the momentum distribution (data not shown).

Comparison of both method mentioned above with the theory rely on the accurate knowledge of the trap depth. Thus, we present below how it is precisely calibrated.

### 2.2.3 Lattice depth calibration using Kapitza-Dirac scattering method

Many aspects of the lattice dynamics are driven by the trap depth. We present in this section how the final depth is calibrated as a function of the forward beam power, independently of other experimental parameters.

Theoretically, the trap depth can be derived from the beams waist, optical powers and alignment of '1064 lattice ' and '1064 lattice RR' using Eq. 2.17. However, the exact knowledge of '1064 lattice RR' beam waist is not straightforward. Using ABCD matrix propagation formalism [66], we compute it to be  $75 \mu\text{m}$ , while the forward beam waist is calibrated at  $45 \mu\text{m}$ . Thus, we use an absolute calibration of the lattice depth which is based on the atoms dynamic in the lattice, using Kapitza-Dirac scattering. This method actually measures the oscillation frequency between the lattice bands [85, 89].

For the measurement, the lattice is suddenly turned ON at  $V_f$ , kept constant for a variable time  $\tau$ , and abruptly turned OFF. This correspond to a Mach-Zehnder interferometer, where the initial cloud in the plane wave basis get projected on the Bloch wave basis, in which it evolve for a time  $\tau$  before each components are projected back on the plane wave basis. The resulting momentum distribution as a function of  $\tau$  is an analytical expression which is fitted over experimental data obtained by a TOF measurement, with the lattice depth as the only free parameter.

Details of the measurement were already presented in [54] and we give only the final calibration in Fig. 2.7. The lattice depth is  $V_0/E_r = -0.73(1) \times P$ , with P the locked optical power of the single forward beam in mW. The linear dependency is in good agreement with equation 2.17.

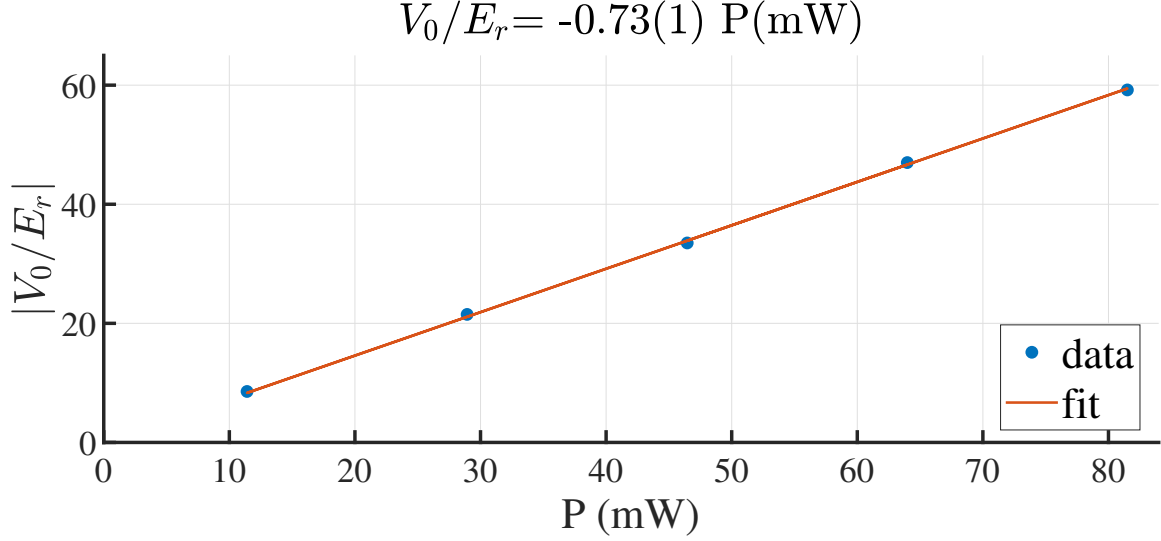


Figure 2.7: Calibration of the trap depth as a function of the optical power of '1064 lattice' power using Kapitza-Dirac scattering analysis. The statistical error in the title correspond to the fit uncertainty.

## 2.3 Sub-wavelength manipulation of atoms in a 1D optical lattice

We use the method introduced in the first section to interact with an ultra-cold cloud on spatial distances under the PSF of our imaging system.

We start by presenting in section 2.3.1 the two lattices configuration, one dressing the excited state, and one trapping the atoms in their ground state. In section 2.3.2, after deriving the total light shift induced on the atoms, we present numerical simulations to establish a clear picture of the repumping process. Finally, we present two absolute calibrations method of the piezo-stacks displacing the lattices fringes.

### 2.3.1 Double lattice commensurability

Superposing two periodic lattice of different interfringe  $i_{1064}$  and  $i_{1529}$  can produce a super-lattice configuration whose period is defined by the commensurability of the combined lattices.

We define two integer  $m_{1064}$  and  $m_{1529}$  as to have  $m_{1064} i_{1064} = m_{1529} i_{1529}$ . In the experimentally available range of angles  $\alpha \in [3.5; 8]^\circ$ , we chose the smallest  $m_{1529}$  possible. Thus, we have  $m_{1064} = 13$  and  $m_{1529} = 9$ , associated with  $i_{1064} = 532.23$  nm and  $i_{1529} = 768.78$  nm. According to Eq. 1.15 it correspond to an angle<sup>1</sup>  $\alpha = 5.9158^\circ$ . The super-lattice period is then  $6.9190 \mu\text{m}$ , which is resolved by our imaging system.

The half-angle is precisely deduced by measuring the lattice interfringe in the co-propagating configuration (see Fig. 1.22). The interfringe is extracted by Fourier analysis, with an error at 68% of  $0.1 \mu\text{m}$ . This correspond to an error on the contra-propagating interfringe of  $0.1$  nm. Over one super-lattice period, the calibration error of  $9 \times 0.1 = 0.9$  nm can be neglected

<sup>1</sup>Note that this value differ from what has been used in the previous thesis due to an error on the dipole trap wavelength.

compared to the expected ground state size of several tenths of nanometers.

For convenience, we label each sites in one super-lattice period. The sites of the 1064 using Arabic numbers from site 0 to site 12. For the 1529 lattice, we precise if we are at the bottom or the top of the modulation and label each extremum using Roman numerals from Site I to site IX as depicted in Fig. 2.9.

Before going into details, we can get a mind picture of the repumping process in the double lattice configuration to clarify the effect of a relative phase  $\Phi$  sweep. We start at  $\Phi = 0$ , with both lattice aligned and the repumper radiation is tuned at the bottom of the modulation. As site 0 and Site I are aligned, atoms are efficiently transferred in  $5^2S_{1/2} |F = 2, m_F = -1\rangle$ . Increasing the phase difference as depicted in Fig. 2.9, spatially move the trapping lattice to the left. The next combination of site which will be aligned are (3, III). Indeed, 3 has moved in space while III remained fixed. The order giving the combination of resonant sites is : (0,I), (3,III), (6,V), (9,VII), (12,IX), (2,II), (5,IV), (8,VI), (11,VIII) and then (1,I) etc...

In this second passage by Site I, the trapping lattice would have move by exactly one interfringe, the site 1 being at the end at the spatial position where the site 0 was initially.

With this picture in mind, we now study the exact light shift which is imprinted on the atoms.

### 2.3.2 Light shift with the double lattice

We derive in this section an expression of the total light shift in the double lattice configuration. We consider the contra-propagating case, with 1D lattices along  $\mathbf{y}$ . We write the total light shift due to theses lattices as

$$\begin{aligned}\Delta_{1064}(y) &= \frac{V_0}{2} \left( 1 + \cos \left( 2\pi \frac{y}{i_{1064}} + \Phi \right) \right) \\ \Delta_{1529}(y) &= \frac{\Delta_{1529}}{2} \left( 1 + \cos \left( 2\pi \frac{y}{i_{1529}} \right) \right)\end{aligned}\tag{2.40}$$

where  $\Phi$  is the relative phase of the two lattices.

As we detailed in section 2.1.1, the 1529 lattice create a light shift on  $5P_{3/2}$ . It is red-detuned and dresses the energy level downwards. The modulation amplitude of the 1529 lattice  $\Delta_{1529}$  in  $\text{rad.s}^{-1}$  is experimentally calibrated using the BAT method presented in section 2.1.2.

Each contribution can be computed independently and the global detuning from the bare transition is given by

$$\Delta(y) = \Delta_{780} - \frac{U_{5P}(y) - U_{5S}(y)}{\hbar} = \Delta_{780} - \Delta_{1529}(y) + \Delta_{1064}(y)\tag{2.41}$$

with  $\Delta_{780} = \omega_0 - \omega_{780}$  the detuning of the laser radiation at angular frequency  $\omega_{780}$  from the bare transition of angular frequency  $\omega_0$ , and  $U_{5P}$  (resp.  $U_{5S}$ ) the total excited state (resp ground state) potential generated by the dressing lasers.

1064 Polarization	Repumper (MHz)		Cooler (MHz)	
Linear along $\mathbf{z}$	5,466551927	0.901 $\Gamma$	3.80	0.626 $\Gamma$
Linear perp. to $\mathbf{z}$	5,466577717	0.901 $\Gamma$	6.30	1.04 $\Gamma$

Table 2.1: Total light shifts of  $^{87}\text{Rb}$  for a lattice depth of  $s = -1000$  at 1064 nm for the repumper transition  $|F_g = 1, m_F = -1\rangle$  to  $|F_e = 2, m_F = -1\rangle$  and cooler transition  $|F_g = 2, m_F = -2\rangle$  to  $|F_e = 3, m_F = -3\rangle$

## High power FORT

At high power, the dressing of the excited state by a far-off resonance laser need to be included. Given that we are far detuned from the bare transition, one cannot apply the rotating wave approximation. However, both rotating terms are well independent and their induced light shifts can be computed separately and summed.

The exact light shift can be calculated [54] using Eq. B.7. We present in table 2.1 the total induced light shift for a linearly polarized lattice of depth  $V_0 = -1000E_r$  on the repumper and cooler transition. We consider the case were the polarization is either linear along the quantization axis ( $\mathbf{z}$ ), corresponding to a  $\pi$ -polarization or linear along a direction perpendicular to the quantization axis such that the shift is the sum of half the one of a  $\sigma_-$  plus half the one of a  $\sigma_+$ .

Experimentally, a spectroscopy on the cooler transition gives a light-shift induced by 'Lattice' (polarized along  $\mathbf{x}$ ) at  $-1000E_r$  of  $0.995 \pm 0.025\Gamma$ . These type of scan are sensitive to the initial atom number drift that can induce a shift of the fitted resonance by  $\pm 0.02\Gamma$ , which could explain the slight deviation from the theoretical value given in table 2.1. A spectroscopy on the repumper transition gives a shift of  $0.95(8)\Gamma$ , in good agreement with the value presented table 2.1. Fig. 2.8 present the different spectroscopy for the imaging transition where the reference is given by a cloud imaged during a TOF. The lattice imaged in-situ at low power ( $-40 E_r$ ) shows no shift (the expected shift is  $0.04\Gamma$ ) whereas we can see the effect of the lattice shift at  $-1000E_r$ .

This light shift is relevant for all large power dipole trap and should be accounted for in order to properly compute the atom number and manipulate the atoms.

In conclusion, the light shift amplitude for the 1064 lattice, defined in Eq. 2.40, should be replaced by

$$\tilde{V}_0 = V_0/E_r \times 2\pi \times 5.47 \text{ kHz} \quad (2.42)$$

## Numerical simulation

Now that we have established the total light shift with respect to the bare transition, we use simple numerical simulations to evaluate the spatial profile of the cloud.

We consider that atoms are initially in the ground state  $5^2S_{1/2} |F = 1, m_F = -1\rangle$ , in the double lattice configuration.

For large trap depth, clouds in each lattice sites are independent wave-packets without long-range correlation. We can define the atomic density in the well  $j$  as  $n_0^j(y)$ , given by 1D-QHO ground

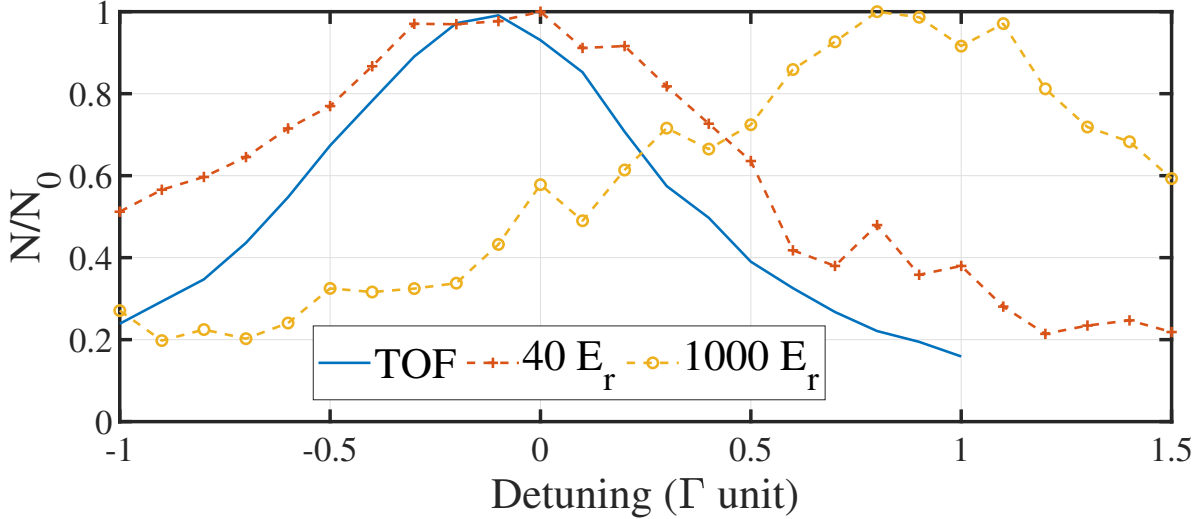


Figure 2.8: Spectroscopy on the imaging transition. The atom number shown in the y-axis is normalized to unity for direct comparison. Plain lines is a reference curve giving the bare transition resonance. It is shifted from 0 due to a drift of the error signal of the Master lock, as discussed in section 1.1.3.2. Dashed curves correspond to the lattice being imaged in-situ, where we can see the light-shift induced by a FORT at high power.

state given by Eq. C.17. The repumped fraction  $f$  is given by :

$$f = \int_{-\infty}^{+\infty} \rho_R(y) dy \quad (2.43)$$

where  $\rho_R(y) = \rho_{22}(y)n_0(y)$  is introduced as the repumped population with  $\rho_{22}$  the repumped population of a 3LS defined in Eq. 2.12. We plot in Fig. 2.9 the light shift induced by the 1064 nm lattice  $\Delta_{1064}(y)$  and by the 1529 nm dressing  $\Delta_{1529}(y)$ . The x axis is in unit of the trapping lattice site number  $i_{1064}$ .

Imaging such a system gives the convolution of the repumped population with the PSF of the imaging system :  $\rho_R(y) * PSF(y)$ . We plot in Fig. 2.10 the resulting sub-system (plain lines) when repumping at the bottom of the modulation and the image obtained after convolution with the PSF (dashed lines) for a lattice depth of  $V_0 = 40E_r$  and  $V_0 = 1000E_r$ . These two case are plotted for  $\Phi = 0$  and  $\Phi = \pi/2$ . Here, different sites of the super-lattice get repumped. Even by compressing tightly the wave-functions in a deep trapping lattice, we are not able to resolve directly individual sites. The signal is indeed perturbed by residual excitation of neighboring sites (mostly  $\pm 3$ ).

### 2.3.3 Direct piezo calibration on the atoms

In the previous section, we established that a perfect commensurability could be achieved, giving a super-lattice with an interfringe of  $i_{SL} = 6.92 \mu\text{m}$ , resolved with the high-NA imaging axis. During my PhD, the relative phase of the lattices  $\Phi$  was controlled using two different piezo-stacks, whose displacement was moving the 1064 lattice spatially. The change was made in March 2022, and we present in this section the calibration of the first piezo used. This piezo

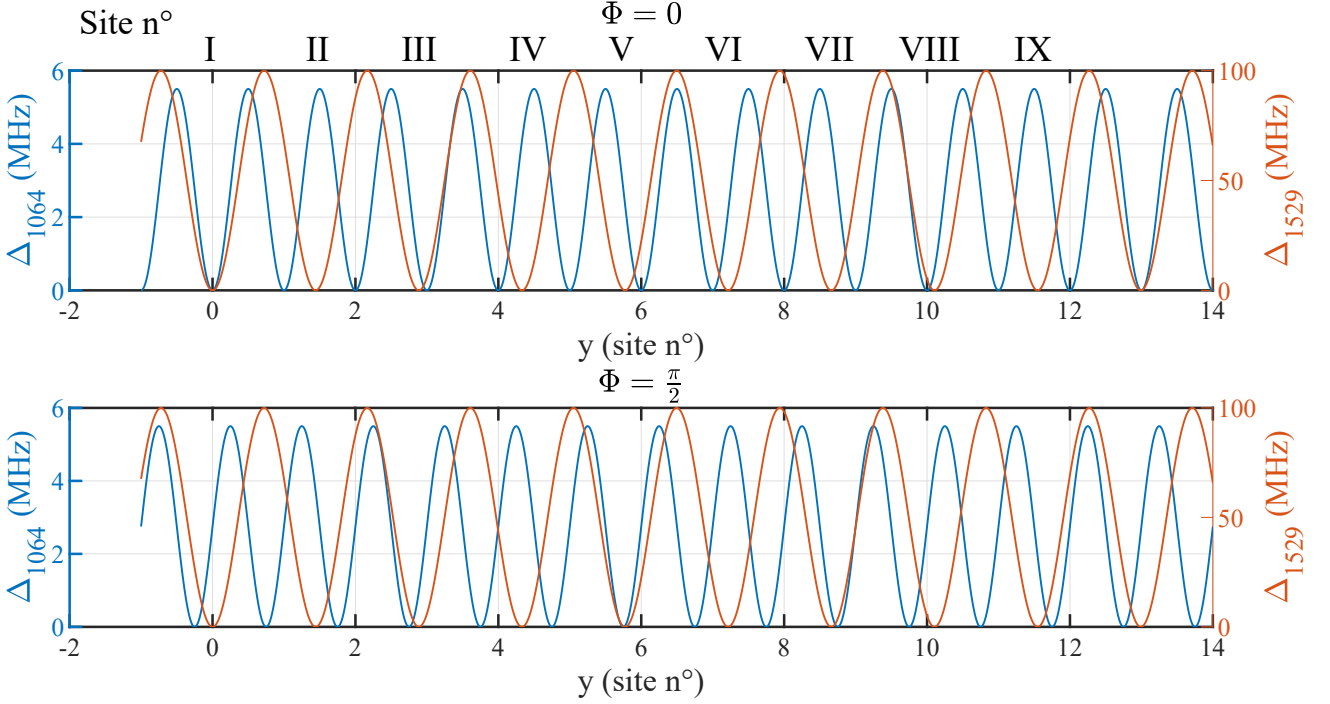


Figure 2.9: Spatial representation of the light shift induced by the two lattices for two relative phases  $\Phi$ . In the simulations, the x axis is fixed and given in unit of  $i_{1064}$ . Changing  $\Phi$  shifts the 1064 lattice. We mention that the y-axis are frequencies unlike the angular frequency defined in Eq. 2.40.

was driven in open loop and its calibration has been carried using the atoms.

A pure BEC is prepared in  $5^2S_{1/2} |F = 1, m_F = -1\rangle$  and adiabatically loaded in the trapping optical lattice of depth  $V_0 = -1000E_r$ . Repumping at the bottom of the modulation creates a subsystem in  $5^2S_{1/2} |F = 2, m_F = -1\rangle$  which is imaged on the cycling transition without modulation on the excited state. The relative phase of the two lattices is scanned by acting on the 1064 piezo-stack mentioned above.

Starting with a phase  $\Phi_0$ , we label each sites in the 1064 lattice separated by  $i_{1064}$ . We consider the site 0 at position  $y_0$  in the imaging plane of the camera. A displacement of the piezo by  $i_{1064}$  spatially move the trapping lattice, equivalent to a phase shift of  $2\pi$ , so the site +1 (or -1 depending on the drive direction) is now at  $y_0$ , and both images will be the same. However, when the lattice is moved by  $\pi$ , the 1529 lattice is perfectly in the middle of site 0 and +1, and the center of the distribution  $\rho_R(y) * PSF(y)$  will also be at  $y_0$ . This is illustrated in Fig. 2.11 b) with numerical simulations of the experimental situation, using a PSF of  $1.3 \mu\text{m}$ . In the imaging plane, the spacing between each distribution is the super-lattice interfringe  $i_{SL}$ . Furthermore, the fringe displacement on the image  $\Delta y_{SL}$  is linear with the lattice displacement  $\Delta y_0$  as

$$\Delta y_{SL} = 2 \frac{i_{SL}}{i_{1064}} \Delta y_0 = 25.9(8) \Delta L_{pz} \quad (2.44)$$

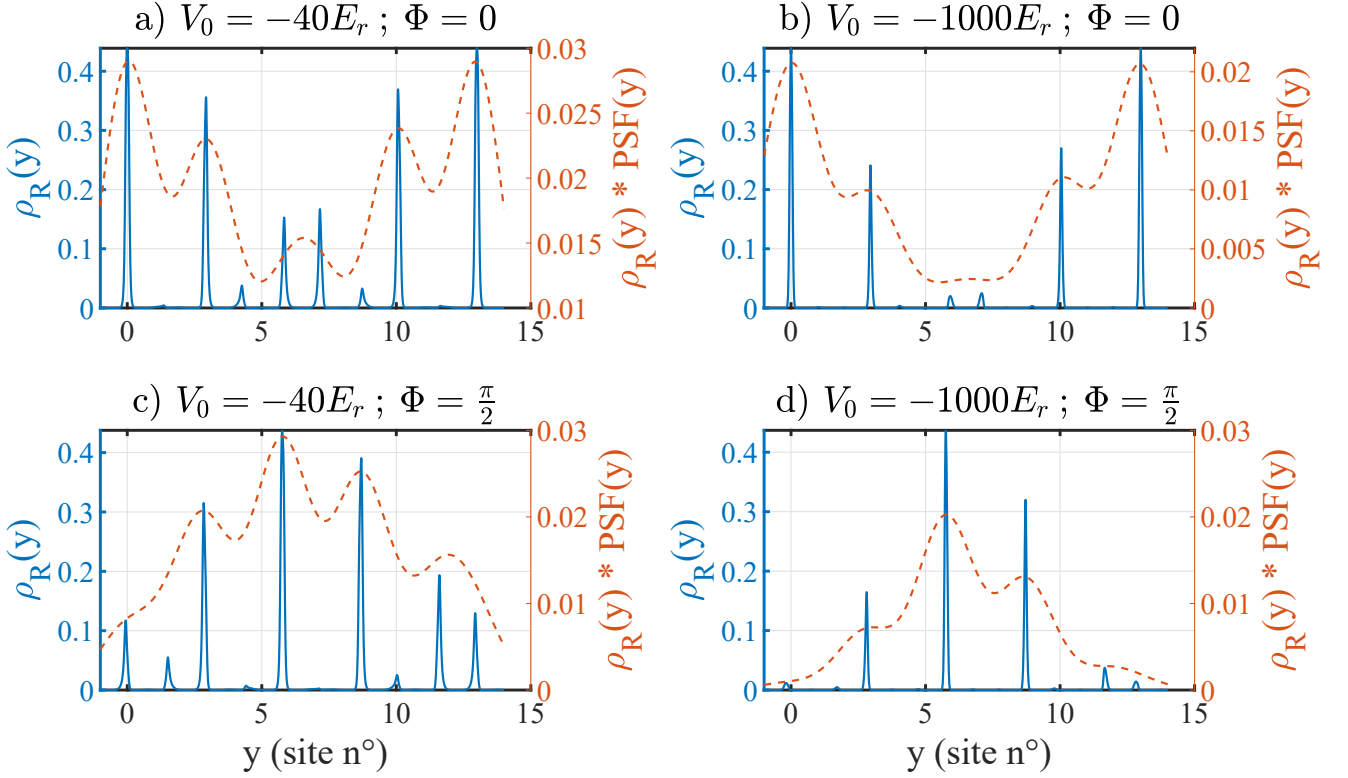


Figure 2.10: Numerical simulation of the repumping and imaging process using the double lattice configuration. We plot on the left y-axis the repumped fraction  $\rho_R(y)$  as plain lines and on the right y-axis the convolution of the repumped fraction with the imaging system PSF as dashed lines. All x-axis are the same, giving the spatial position in unit of  $i_{1064}$ .

where  $\Delta L_{pz} = \Delta y_0$  is the piezo displacement.

To bypass the magnification uncertainty of the imaging system, we fit the super-lattice interfringe, whose statistical error gives the slope uncertainty. We scan the relative phases of the two lattices by changing the piezo-stack drive voltage from 0 to 8 V. The measurement is repeated four times and one out of two experimental realizations are done with the piezo driven at 0V to reject long term phase drifts.

We plot in Fig. 2.11 a) 2D stacks of the horizontal projections in the atomic plane. The structure along a bright fringe expected from the numerical simulation is not resolved, which could mean that the imaging PSF is higher than  $1.3 \mu\text{m}$  or that we are not repumping perfectly at the bottom of the modulation. This discrepancy could also be due to the fact that we did not include pixelisation in our simulation. We present in Fig. 2.11 c) the calibration of the piezo displacement  $\Delta L_{pz}$  obtained with Eq. 2.44 as a function of the drive  $V_c$  in V. Fitting the data points with a second order polynomial function yields :

$$\Delta L_{pz}(\text{nm}) = 2.54 V_c^2 + 101.1 V_c$$

Using this calibration, we find a piezo voltage of 4.67 V to shift the 1064 lattice by  $i_{1064}$ . Using

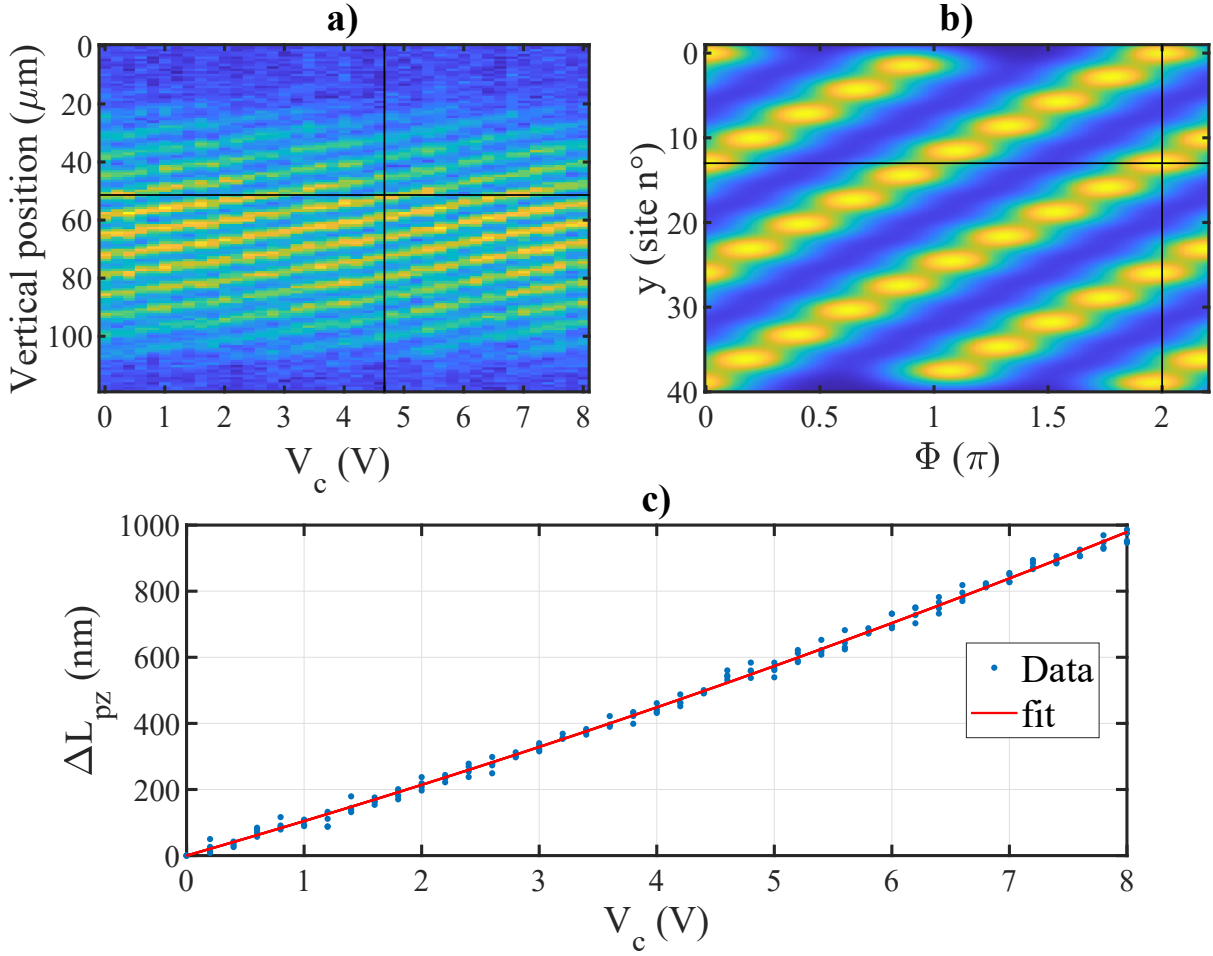


Figure 2.11: Calibration of the piezo displacement using the atoms. a) 2D stacks of the cloud projected along the horizontal direction. The black lines are added as visual guide. The vertical line at  $V_c=4.67$  V correspond to a piezo displacement of  $\Delta L_{pz} = i_{1064}$ . b) Numerical simulation of a). c) Piezo-stack displacement as a function of the driving voltage. Experimental piezo displacement data points are fitted with :  $\Delta L_{pz}$  (nm) =  $2.54 V_c^2 + 101.1 V_c$ .  $V_c$  is the driving voltage of the piezo-stack (in V).

the black lines in a) as visual guide, we confirm that we cross two bright fringes as expected.

### 2.3.4 Second piezo calibration

Around march 2022, we changed the piezo-stack under M2 for a P2K2FMC2 controlled in closed-loop operation with a pre-amp circuit (AMP002) and a dedicated driver (BCP301). Before the installation, the piezo displacement is calibrated using an interferometer setup like the forward accordion lattice. An achromatic doublet (AC508-750-B) of focal  $f' = 750$  mm produce fringes on an EMCCD camera (Andor Luca R - DL 604M VP) with  $1004 \times 1002$  pixels of  $8 \mu\text{m}$  pitch.

During each run, one image is taken with the piezo at the zero position and another one

after a given displacement. This reject long term position drift due to temperature, measured over 10 minutes to be a bit above 100 nm. Indeed, we simultaneously measured air temperature variations of 200 mK. The two cubes are placed next to each other so the interfringe can be approximated by  $\lambda/2$ . Using Eq. 1.12, we get the central fringe displacement as a function of the displacement of the reflective mirror M1 :  $\Delta x_0 = \Delta x_{pz}$ . Using the linear thermal expansion coefficient (CTE) for steel, of  $11 \mu\text{m}/\text{K}/\text{m}$ , over the 5 cm length between the cubes and M1, we expect a shift of the first fringe of 110 nm.

The piezo displacement is characterized at low drive, over only 2V out of the maximum 75V. The calibration obtained depend neither on the time between the two consecutive images from 250 ms to 650 ms nor on the pause time between each run from one second to one minute. Each data set consist of 8 points repeated 20 times. The images are projected along the fringes direction. We fit independently the Gaussian envelop and the phase of the sinusoidal modulation, from which we extract the fringe displacement, plotted as a function of the driving voltage in Fig. 2.12. Contrary to typical piezo operation, that present hysteresis and drive uncertainty up to 30%, the piezo-stack displacement in close loop-operation is linear with the drive with a coefficient  $c_{pz} = 773(3) \text{ nm}/\text{V}$ . The uncertainty on the slope is the standard deviation obtained by repeating the calibration 10 times over 3 consecutive days. The standard-deviation of the displacement for each repetitions, lower than 6 nm, is independent of the drive and indicate a numerical error on the fitted displacement. Although the position of the central fringe at zero displacement is well correlated with temperature fluctuations, temperature dependency of the slope is not. The manufacturer website indicate  $0.24 \text{ nm}/\text{V}/\text{K}$  and typical fluctuations of the lab room temperature is under 0.5 K, giving a slope error of  $0.12 \text{ nm}/\text{V}$  which doesn't explain the statistical uncertainty of  $c_{pz}$ . The calibration proved to be quite robust even when taking

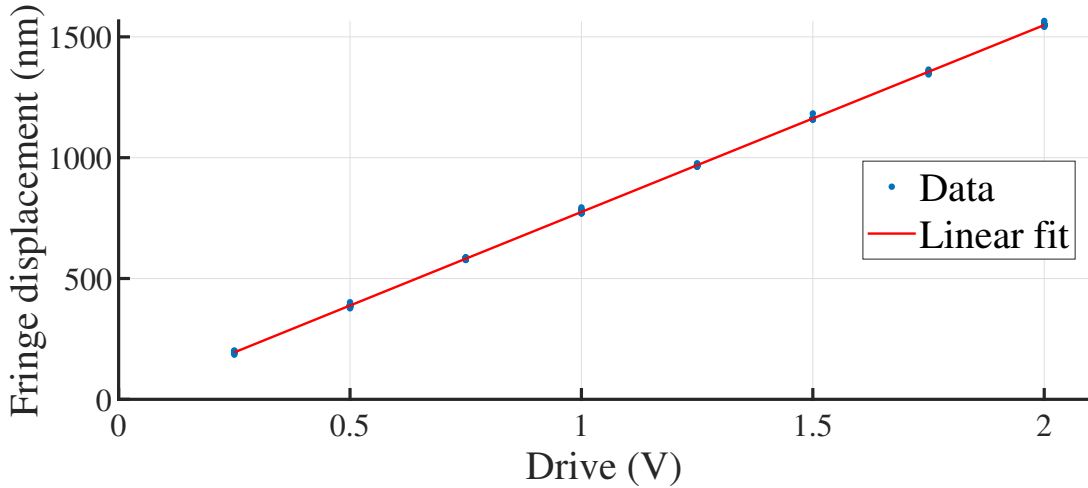


Figure 2.12: Optical calibration of the piezo-stack giving the displacement of the trapping lattice fringes with the driving voltage.

out and placing back the mirror and piezo in their mount.

In this section, we demonstrated that the method can be used to image different sites in an optical lattice by varying th relative phase between each lattices. In order to be more

quantitative on the atom number and resolution, we study in the next section how to prepare a wave-function in a single site before imaging the associated density distribution.

## 2.4 Imaging of a single atom density distribution in a tight 1D optical lattice

In this section, we aim at preparing a sub-system where 12 out of 13 of the 1064 nm lattice site are depleted and the last site is imaged with sub-wavelength resolution. Indeed, we will take advantage of our method to selectively clean the lattice leaving well separated wave-functions with the super-lattice periodicity. In section 2.4.1, we present the depletion sequence we have engineered. The depletion process is quantitatively compared with numerical simulations. In section 2.4.2, we present results where we resolve the atomic density distribution with the 780 nm laser tuned at the middle of the 1529 modulation. We evaluate experimental limitations leading to an apparent broadening of the distributions in 2.4.3.2 and present in section 2.4.3.1 the final resolution we obtained.

### 2.4.1 Sub-system preparation: cleaning sequence

We start by presenting the depletion sequence we have developed. Using our the method in a repumper configuration, atoms are pumped into  $5S_{1/2} |F_g = 2\rangle$ . We use a total of 5 step during which the relative phase  $\Phi$  and the 780 nm repumper detuning are adapted to successively excite on resonance different sites. Once the atoms have been transferred to  $|F_g = 2\rangle$ , another 780 nm laser tuned on the cycling transition is used to blast these atoms, leaving only the ones still in  $5S_{1/2} |F_g = 1\rangle$  trapped in the 1064 nm lattice.

Experimentally, we adiabatically load a BEC with  $2 \times 10^5$  atoms in the 1064 nm lattice as described in section 2.2.2. The magnetic trap is turned OFF, and a magnetic field bias of 500 mG along  $z$  is applied, which set the quantization axis. The lattice potential is linearly ramped up in 100 ms from  $V_0 = -40E_r$  to  $V_0 = -1000E_r$ . After this, DT1 is turned OFF by ramping down the optical power.

Using the labeling defined in Fig. 2.9, we aim at keeping the site 0. Each of the 5 steps are defined using their respective duration. We refer to the detuning value using a dimensionless parameter  $d \in [0, 1]$  where  $d = 0$  corresponds to the bottom of the modulation, and to  $d = 1$  corresponds to the 780 nm laser radiation tuned at the top of the modulation.

First, we detail the coarse cleaning (CC) steps which clean all sites except 0, 3 and -3 (equivalent of site 10 because of the super-lattice periodicity).

- $t_1$  : Site 0 is at the bottom of the modulation and the initial phase define  $\Phi = 0$ . The 780 nm laser radiation tuned at the top ( $d=1$ ) of the modulation clean sites 2, 5, 8, and 11.

The 1064 nm lattice is moved in 350 ms by displacing the 1064 nm lattice by  $i_{1529}/4$ . The relative phase is now  $\Phi = \pi/2$  and site 0 is tuned at the middle of the modulation, where the

excited state slope is the strongest.

- $t_2$  : The detuning slightly change to  $d=0.97$  clean this time sites 1, 4 and 7.
- $t_5$  : The detuning is changed to the bottom of the modulation,  $d = 0.03$  and the light pulse cleans the sites 6, 9 and 12.

We show in Fig.2.13 raw images obtained with the coarse cleaning steps alone (no further super-resolution method).

The entire lattice is imaged in a), but the structure cannot be resolved. Local decrease of optical density in the cloud are due to high density effects. As we increase the cleaning time  $t_{CC} = t_1 = t_2 = t_5$  in b), fringes start to appear. Finally, with enough cleaning, we resolve in c) fringes corresponding to the sites 0, 3 and -3. Fringes obtained by projecting c) along the horizontal direction (not shown) have a visibility close to 1. Trying to further increase  $t_{CC}$  will only decrease the signal and the width of the fringes will stay constant. The coarse cleaning steps mentioned above are not adapted to clean sites  $\pm 3$  while keeping atoms in site 0.

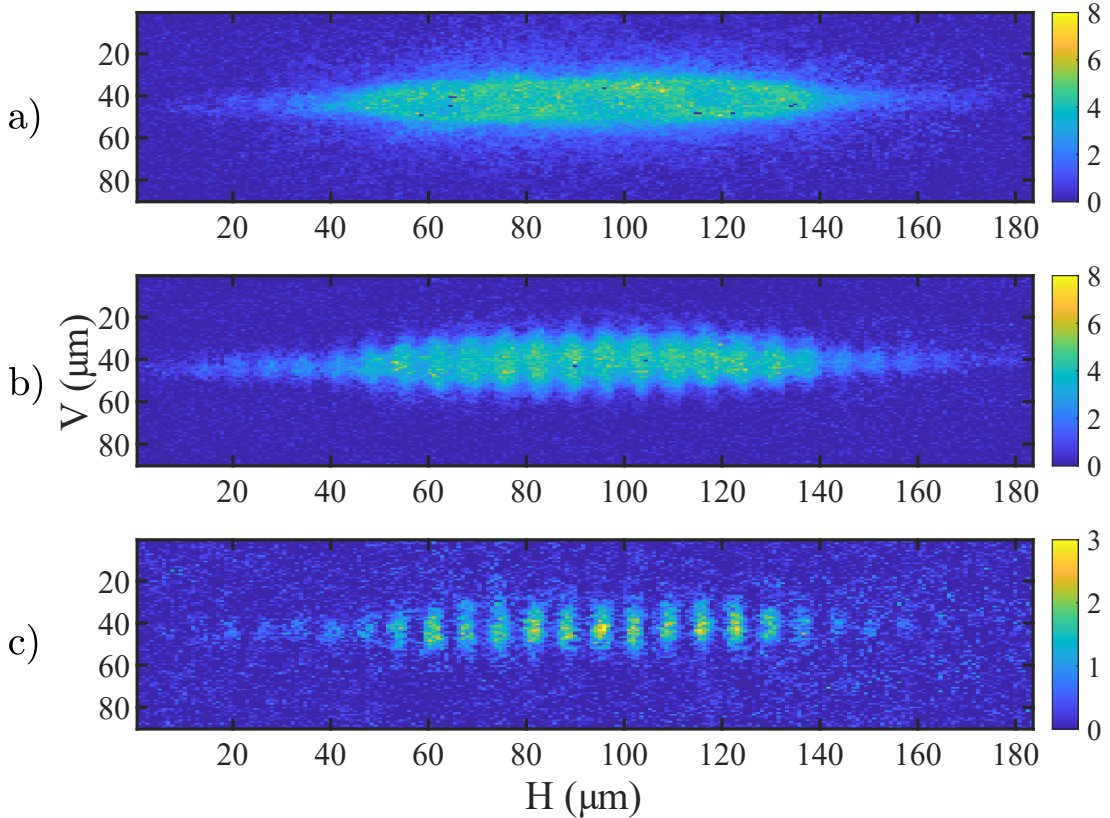


Figure 2.13: 2D images of the in-situ optical densities of atoms in the 1064 lattice. Images are taken on the high N.A. imaging axis with a bare excited state during the repumping and imaging process. a) Entire system with no cleaning. b) The lattice structure start to appear when we implement the 3 coarse cleaning steps mentioned above. c) The cleaning time  $t_{CC}$  is increased until obtaining the maximum visibility.

Given the double periodicity we could experimentally implement, sites  $\pm 3$  are difficult to clean without affecting the site 0. Indeed, with site 0 at the middle of the modulation,  $\pm 3$  sites have the same detuning as if they were physically only at 59 nm from site 0 as represented in Fig. 2.14. We recall that the ground state width at  $V_0 = -1000E_r$  is 30 nm. The high longitudinal trap frequency is 128 kHz corresponding to an oscillation period of the atoms in the trap of 8  $\mu$ s. On longer pulse duration, the depleted density distribution of site  $\pm 3$  will keep redistributing such that the equilibrium wave-function stay unchanged. We call this process the fine cleaning stage. Repumping on the side of the density  $|\Psi_{\pm 3}(y)|^2$  will still deplete these sites, while almost not affecting site 0. The key idea here is that we will deplete these sites on the wings of the distribution, where the density distribution of site 0 is exponentially suppressed.

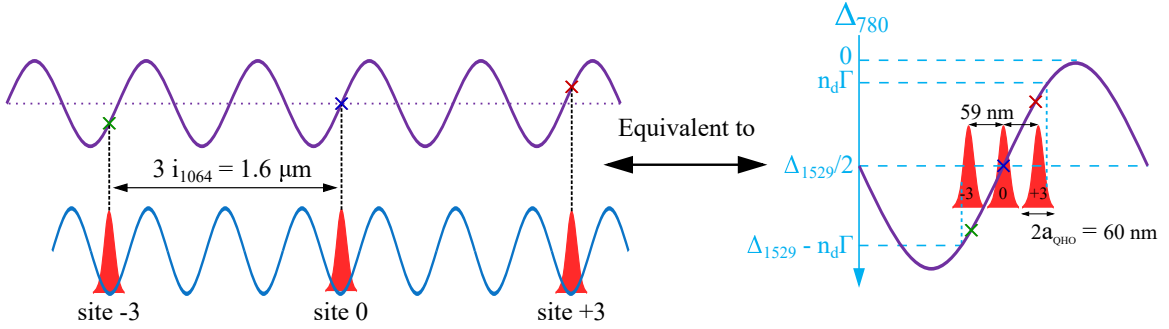


Figure 2.14: Schematic of the equivalent situation considering site 0 and  $\pm 3$ . The atomic densities are spatially  $1.596 \mu\text{m}$  apart but in term of light shift difference it is equivalent as wave-functions separated by only 59 nm.

For the fine cleaning (FC), we implement two more steps, symmetric compared to site 0:

- $t_3$  : The detuning is changed to  $d = (1 - n_d) \Gamma / \Delta_{1529} = 0.82$  and clean the site -3 (or 10) from the side.
- $t_4$  : The detuning is changed to  $d = n_d \Gamma / \Delta_{1529} = 0.18$ , to clean site +3.

The cleaning sequence defined above is numerically optimized on a figure-of-merit (FOM) built on two quantities.

The total population in site  $j$  is written  $N_{(j)}$  and initially normalized to unity. The final purity of the system is defined as

$$\eta = \frac{N_{(0)}}{\sum_j N_{(j)}} \quad (2.45)$$

The FOM is defined as

$$\text{FOM} = N_{(0)} \times \eta \quad (2.46)$$

The optimization parameters are the repumping times  $t_k$  and detunings. The relevant quantity to consider for cleaning each sites is the number of photon scattered. Thus, the repumper saturation parameter  $s_0^{rep}$  and repumper duration  $t_{rep}$  are at first order equivalent and we set  $s_0^{rep} = 0.012$  to avoid power broadening. Furthermore, we limit the number of parameter to optimize by imposing that the coarse cleaning step duration are equal  $t_1 = t_2 = t_5$  and the same for the fine cleaning steps  $t_3 = t_4$ . The relative phase of the lattices  $\Phi$  and the detuning  $d$  are fixed during the sequence, at their values given above.

We present the optimization as a function of  $t_1$  in Fig. 2.15 a). We focus here on the 1D plot where the repumping time ratio  $t_3/t_1 = 1.833$  is at the optimum value. The optimization yields  $t_1 = 70 \mu\text{s}$ , corresponding to  $\eta = 0.89$  and  $N_{(0)} = 2/3$ . The number of photon scattered by each site for this sequence is plotted in Fig. 2.15 b) and is for each site, at least 10 times the one of site 0.

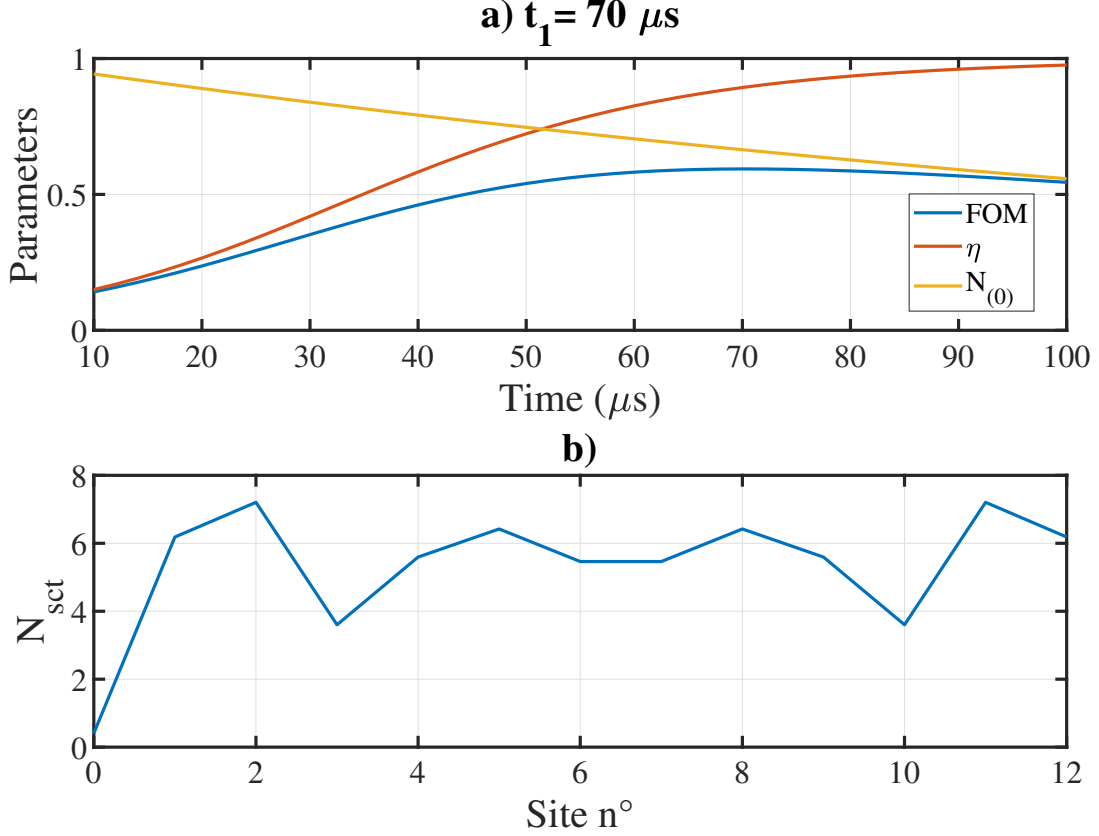


Figure 2.15: Numerical optimization of the cleaning process. a) Evolution of the optimization parameters defined in the text as a function of the repumping time  $t_1$ . The optimum is obtained at  $t_{\text{opti}} = 70 \mu\text{s}$ . b) Corresponding mean number of scattered photons  $N_{\text{sct}}$  for each sites. Site 0 scatter on average 0.4 photons.

Using this cleaning sequence, we should be able to prepare individual wave-functions trapped in the 1064 nm lattice and separated by the super-lattice periodicity.

## 2.4.2 Fine cleaning characterization

We present in this section an application of the super-resolution scheme by resolving spatially the atomic density distribution of single 1064 lattice sites, separated by the super-lattice period. For this, we need to implement the cleaning sequence detailed above.

The coarse cleaning steps are optimized experimentally starting from the numerical simulations presented in Fig. 2.15.

When applying the super-resolution method during the repump process, we saw previously

that the site  $\pm 3$  will lead to an apparent broadening of the density distribution. Thus, the fine cleaning steps are optimized by minimizing the final density distribution width.

Experimentally, at the end of the cleaning sequence, we tune the '780 R Tunable' laser to be resonant at the middle of the modulation, to have the highest spatial selectivity, given by Eq. 2.14. Then, we act on the piezo-stack to move the relative phase  $\Phi$  between the 1529 dressing lattice and the 1064 trapping lattice. This scans the atomic density. In fact this corresponds to a spectroscopy of the transition where the resonant condition depend on  $\Phi$ . The final repumping step of duration  $t_{rep}$  at saturation  $s_0^{rep}$  pump atoms in  $|F_g = 2\rangle$ . We then turn off the excited state modulation and image the sub-system on the bare cycling transition using the high N.A. imaging axis.

Images are projected along the vertical direction, perpendicular to the fringe direction, and we compute the total atom number over the entire cloud, corresponding to approximately 20 super-lattice sites.

The total atom number is fitted by a Gaussian function with four parameters as:

$$N = N_0 e^{-\frac{(y-y_0)^2}{2\sigma^2}} + N_{off} \quad (2.47)$$

### Unbalanced cleaning

First, we implement each step of fine cleaning separately. As we deplete only  $+3$  (resp.  $-3$ ), there is a displacement of the wave-function toward the other direction. Cleaning with  $t_4$  only is shown in Fig. 2.16 and with  $t_3$  only in Fig. 2.17. The data presented were taken with  $t_{CC} = 180 \mu\text{s}$ , at a saturation parameter of  $s_0^{rep} = 10^{-2}$ , a bit above the optimal value find previously to ensure that no residual sites other than 0 and  $\pm 3$  are populated. The FC is done at  $s_0^{rep} = 2 \times 10^{-2}$ .

For each case, we expect a displacement of the wave-function by a maximum of  $59/2=29.5$  nm when one of the  $\pm 3$  sites are emptied.

In Fig. 2.16, the displacement is of 24(4) nm, while it is of 32(4) nm for the symmetric situation of Fig. 2.17. The difference between the two could be due to the initial relative phase value  $\Phi$ , breaking the symmetry compared to site 0 or simply due to a long term drift since the second atomic density distribution of Fig. 2.17 is taken 75 minutes after the first one.

### Balanced cleaning

Now, we implement the fine cleaning steps in a balanced way, with  $t_{FC} = t_3 = t_4$ . We expect the central position  $y_0$  to remain constant when increasing the cleaning while the width decrease. We plot in Fig. 2.18 the atomic densities spectroscopy for increasing cleaning time. The coarse cleaning steps were all equal to  $t_{CC} = 300 \mu\text{s}$ . Experimentally,  $y_0$  shows no particular drift but seems to fluctuate over 10 nm. The same spectroscopy is done for  $t_{CC} = 200 \mu\text{s}$  and we compared the evolution of the width as a function of the fine cleaning time. We start with a higher initial width for  $t_{CC} = 200 \mu\text{s}$ , indicating that other residual sites have not been cleaned entirely. This point out to sites 6 and 12, which the fine cleaning steps finish to deplete. Both case converge towards the same slope for long  $t_{FC}$ , and the final width is in both case of 40 nm. This is larger than what we expect and we detail bellow some causes of broadening.

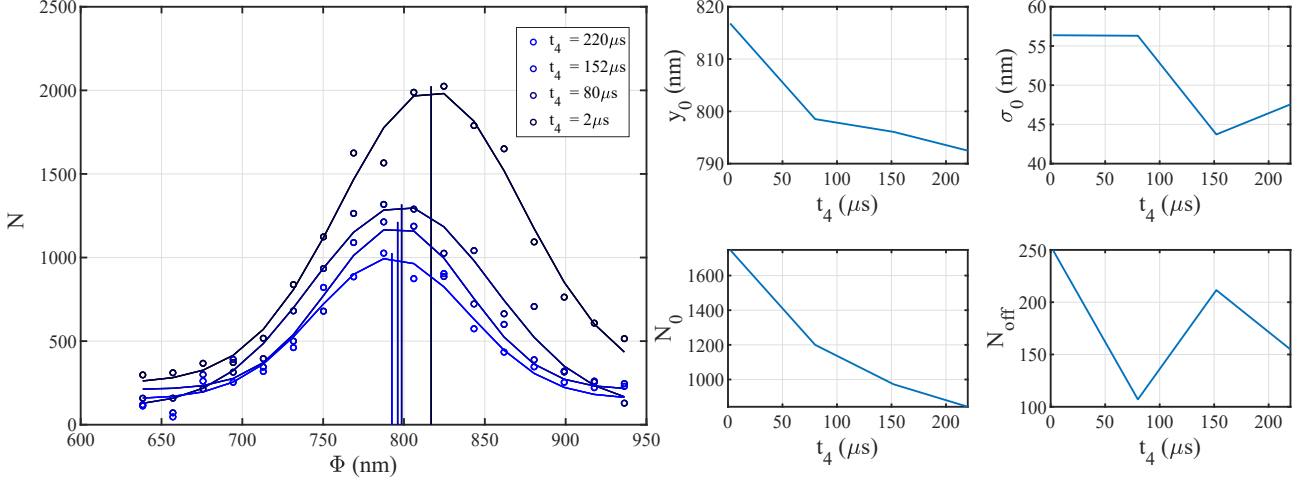


Figure 2.16: Spectroscopy of the atomic density distribution. The fine cleaning is done on one side only, with duration given in the legend. The lattice depth is  $V_0 = -1000E_r$  and the light shift is calibrated using a BAT at 102 MHz. Plain lines are fitted over the data point (circles) using Eq. 2.47. Each wave packet fitted center  $y_0$  is indicated by the vertical lines. The x-axis give the relative phase converted in a spatial displacement of the 1064 nm lattice. All the fitted parameters are plotted on the side as a function of the FC time.

## 2.4.3 Scan of a single atomic density distribution

### 2.4.3.1 Experimental result

We present in this section a measurement of the width of the density distribution of atoms trapped in a super-lattice after cleaning following the scheme detailed above.

For this scan, the half-angle has been set to  $\alpha = 5.67^\circ$ , which gives  $i_{1529} = 768.44$  nm. The displacement of the piezo-stack has been calibrated in terms of absoluteness and accuracy by scanning the density distribution over few 1529 nm lattices fringes ( $\sim 1 \mu\text{m}$  displacement). The interfringe is then measured to be  $\Delta y = 385 \pm 3$  nm where we expect  $i_{1529}/2 = 384.22$  nm. This gives the error on the relative phase displacement of 0.2%. This calibrate the piezo-stack displacement. A slight asymmetry of 3 nm from each side of the central peak was also observed and indicate that the last repumping step, was not exactly at the middle of the modulation. It corresponds to an error of 0.8 MHz. This is to be compared to  $\Delta_{1529} = 2\pi \times 101$  MHz which has been measured with the BAT method whose resolution is of the same order of magnitude. We emphasis that both the commensurability mismatch and repumping at  $d \neq 0.5$  do not lead to a measurable broadening of the density distribution.

A BEC of  $N_{tot} = 2 \times 10^5$  atoms is adiabatically transferred in the 1064 nm lattice at  $V_0 = -1000E_r$ , over approximately 250 sites. We repeat 5 spectroscopy of 21 points, with  $t_{CC} = 180 \mu\text{s}$  at  $s_0^{rep} = 0.01$  and  $t_3 = t_4 = 220 \mu\text{s}$  at  $s_0^{rep} = 0.02$ . Using Eq. 2.14, the final repumping gives  $FWHM^{R(1)} = 28$  nm. The expected width for the atomic density is then  $\sigma = \sqrt{(FWHM^{R(1)}/2.35)^2 + \sigma_{QHO}^2} = 24$  nm. An independent fit of each of the 5 distributions indicates a mean central position of  $y_0 = 830(7)$  nm. We reject the long term drift by displacing

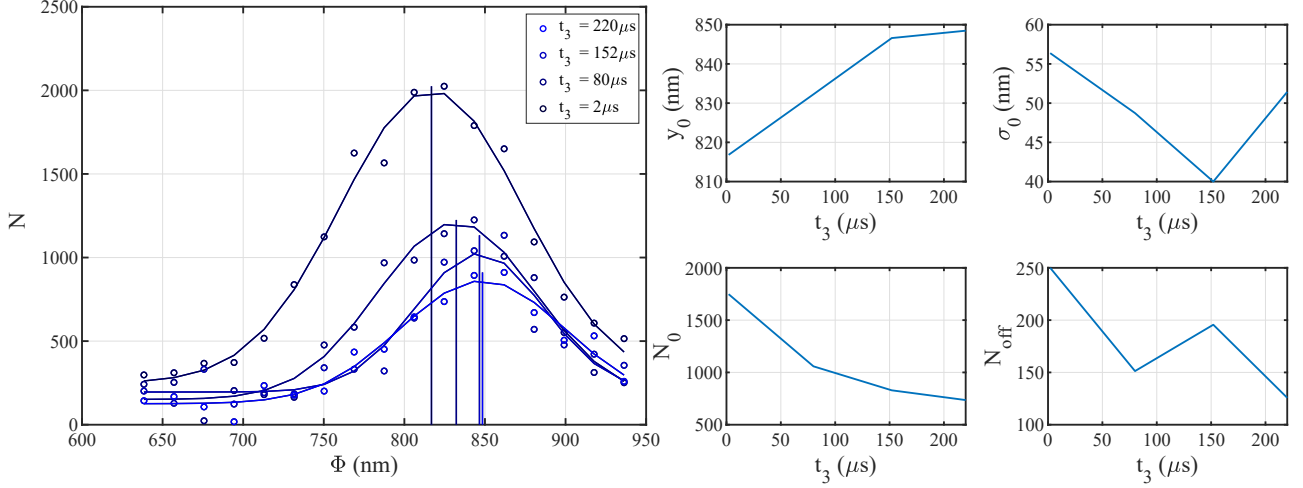


Figure 2.17: Spectroscopy of the atomic density distribution when the FC is done on the other site compared to Fig. 2.16.

each atomic densities by their respective center and fit the entire data set to obtain the averaged width, plotted in Fig. 2.19. This result in a width  $\sigma = 38(8)$  nm, 1.6 times larger than expected.

Different broadening factors are studied below and in [54]. In our experiment, the signal to noise ratio with only a total of 500 atoms per image is close to unity which is a limiting factor. Improvement of the data analysis<sup>2</sup> has been necessary to attain the result we presented here. For the data presented above, the numerical error on the number of atoms integrated in the entire image is on average  $\pm 115$  with little to no dependency on the value of  $N$ . Each cleaning steps is long compared to the trap oscillation period. We suspect that the residual atomic motion could be a reason for the broadened width. This increase of the width could also be due ton an incomplete cleaning but is very unlikely given the estimated number of photon scattered. In the current status of the experiment, we are limited by our poor SNR ( $\sim 4$ ) and we cannot further investigate this issue.

### 2.4.3.2 Lattices relative phase drift and broadening effects

In this section, we account for the experimental factors leading to a relative phase shift of the two lattices and evaluate the resulting broadening. First we numerically evaluate how the initial relative phase plays a significant role in the final width.

#### Initial relative phase

Up to now, we assumed that there was an initial alignment of the lattices and that we could define a proper site 0. However, it is never truly the case and we evaluate the effect of a variation of the relative phase. The two lattices are initially perfectly aligned when one bright fringe of each lattices are spatially overlapped. We define the distance between peaks of each lattice by

<sup>2</sup>low noise readout, frame transfer, fringe removal, imaging power stability and homogeneity. More details are presented in chapter 1.

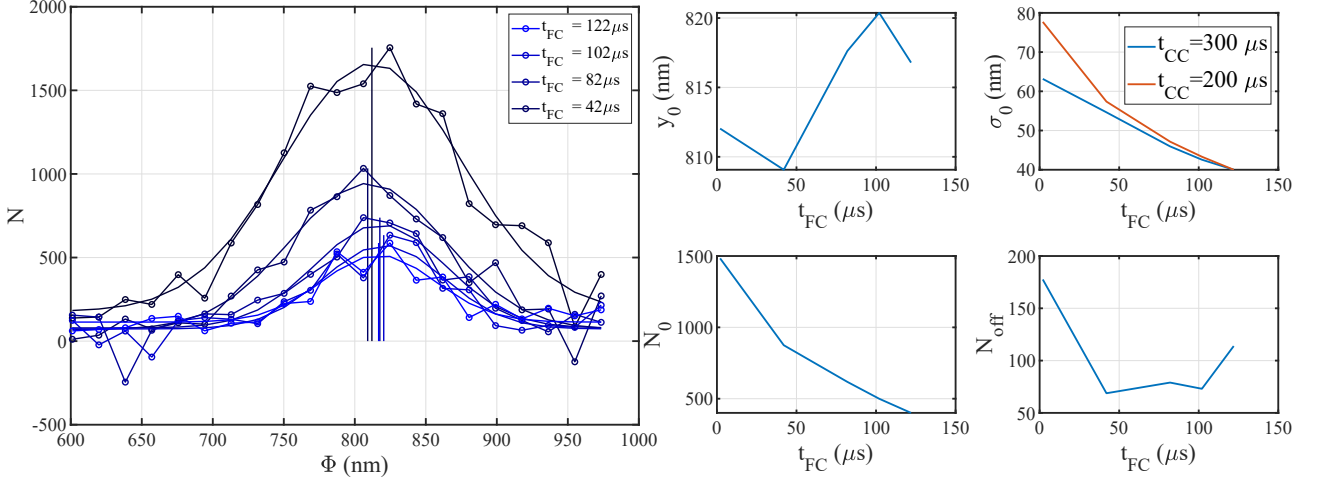


Figure 2.18: Spectroscopy of the atomic density distribution with a symmetric fine cleaning,  $t_{FC} = t_3 = t_4$ . We plot the different densities (plain lines with circles) and their fit (plain lines). The coarse cleaning time is  $t_{CC} = 300 \mu\text{s}$ . In addition, we plot the evolution of the width for  $t_{CC} = 200 \mu\text{s}$  (rest of the data not shown).

$dy = y_0^{1064} - y_0^{1529}$ , given by :

$$dy = i_{1064} k - i_{1529} m + i_{1064} \frac{\Phi}{2\pi} \quad (2.48)$$

where  $k$  and  $m$  are integers.

The shortest distance between the bottom of the 1064 nm lattice and the 1529 one is obtained by computing the minimal value of  $dy$  over all  $k$  and  $m$  possible values. We plot in Fig. 2.20  $dy$  as a function of  $\Phi$ , indicating that every 59 nm, a different site is fully resonant. The worst case correspond to having a 1529 nm bottom aligned in between site 1 and 2 (see the inset of the figure for site labeling), where the final configuration present two peaks, in site 0 and 3. This is obtain for a shift of 30 nm and would increase the measurable width to 47 nm. This is one of the different possibility for final broadening and we evaluate below the relative phase stability as to conclude if this is a limiting factor.

### Wavelength drift

We evaluate here the impact of wavelength drift, presented with the Pound-Drever-Hall cavity lock in 1.4.5.

For both lattices, the drift at the atomic position is given by :

$$\delta\Phi = 2\pi \times L \frac{\delta\lambda}{\lambda^2} \quad (2.49)$$

with  $L_{1064} = 486$  mm and  $L_{1529} = 505$  mm, the optical lengths between the first and second passage on the atomic cloud, neglecting the lens thickness.

For the 1529, we measured a drift up to 0.4 pm over the time scale of the second. The resulting fringe displacement is thus given by  $\delta y = \delta\Phi / 2\pi \times i_{1529} = 64$  nm. At 1000  $E_r$ , the harmonic

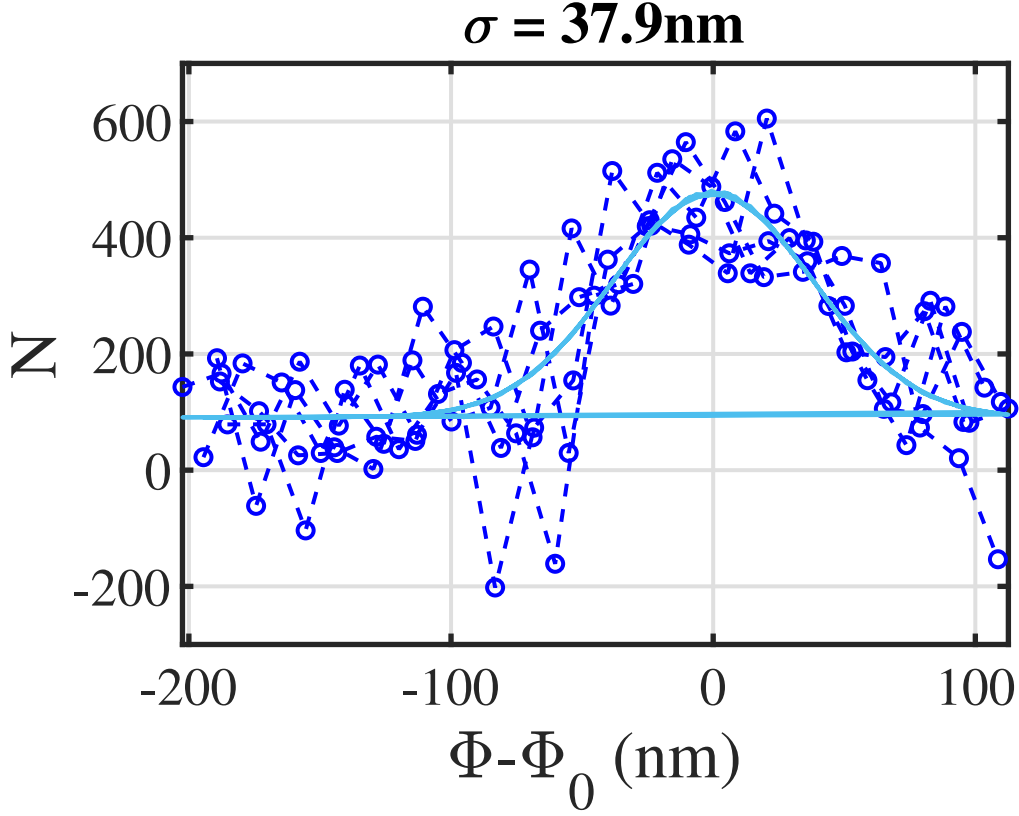


Figure 2.19: Spectroscopy in the cleaned super-lattice. 5 set of 21 points are repeated consecutively. The x-axis indicate that each set of densities are displaced by their own fitted center. The resulting displaced data points (dashed lines with circles) are fitted using Eq. 2.47 with  $y_0 = 0$  fixed. The resulting width is given in the title.

oscillator ground state is  $a_{HO} = 30.1$  nm, so the previous displacement happening on time scale of the experiment is not negligible. Locking the 1529 on the cavity reduces the short term drift to 5 fm, corresponding to a shift  $\delta y = 0.8$  nm. When both lasers are locked on the cavity whose length is  $L_{cavity} = 194.46$  mm, they share a common phase reference each  $2L_{cavity}$ . Thus, when computing the relative phase fluctuations, the optical distance in Eq. 2.49 can be reduced to  $\tilde{L} = L - 2mL_{cavity}$ , with  $m$  an single integer. The closest reference is in our case  $m=1$  giving  $\tilde{L}_{1064} = 97$  mm and  $\tilde{L}_{1529} = 116$  mm, effectively reducing the shift of the 1529 to 0.2 nm only. The lock bandwidth is typically few kHz. Given the arguments presented above, we can neglect relative lattice mismatch due to wavelength drifts in our experiments.

### Backward accordion block temperature stabilization

In this section we study a spatial drift of the super-lattice fringes due to the magnetic trap coils thermalisation over long experimental cycles. This issue is solved by locking the temperature of the backward accordion lattice block. Indeed, the block is placed on a separated 30 cm long aluminum bread-board, above the sub-wavelength imaging axis telescope, whose temperature is correlated with the magnetic gradient coils heating up.

The experimental preparation has been presented in section 2.3.3 where a BEC is loaded

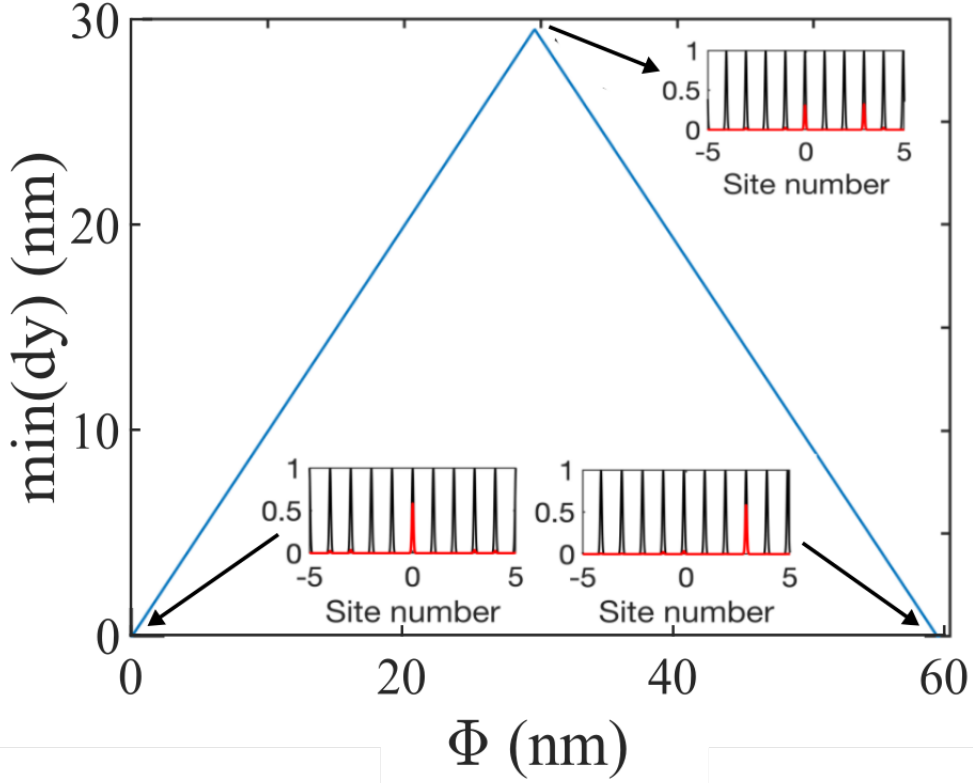


Figure 2.20: Minimal distance between an alignment of the two lattices as a function of  $\Phi$  (expressed in nm). The insets show the normalized lattice site populations before the cleaning (black) and after the cleaning (red).

in the 1064 lattice at  $s=-1000$ . The excited state is dressed with the 1529 lattice (100 MHz) and atoms are repumped at the bottom of the modulation. The super-lattice sub-system is imaged on the high N.A. imaging axis.

We present an initial data set in Fig. 2.21 a) consisting of repetitions at constant relative phase of the two lattices. We plot 2D images by stacking the horizontal projections of consecutive experimental realizations. In the atomic plane, the fringes drift spatially by  $16 \mu\text{m}$  due to the backward block heating up with the coils temperature increasing by 2.5 K. After 150 RUN, a new thermal equilibrium is reached and the fringes stabilize. To understand this effect, a thermistance is clamped to the breadboard and monitor the temperature evolution during another scan. Both temperatures are plotted together in b) which highlight the correlation.

To solve the issue, a temperature controller (Wavelength Electronics PTC2.5K-CH) drives a TEC placed underneath the breadboard, locking the temperature with a precision better<sup>3</sup> than 10 mK. We plot in Fig. 2.21 c) the stabilized fringes, with a residual drift of  $2 \mu\text{m}$  correlated with the room temperature, showing mean value variation of 60 mK over the experiment duration. In this data set, the cloud also drift vertically by  $2.5 \mu\text{m}$ . We speculate on a thermal effect on

<sup>3</sup>This value is limited by the digitization of the acquisition system while the temperature controller precision is indicated at 1 mK.

the imaging axis alignment.

For the data presented in a), we infer the breadboard temperature to increase by 233 mK. Given the Linear temperature expansion coefficient of the aluminum[90] of  $22 \mu\text{m}/\text{K}/\text{m}$ , we expect a variation of the relative optical length distances  $\Delta L = 0.233 \times 22 \times 0.01 = 51$  nm. Using Eq. 2.44, this correspond to a fringe displacement in the atomic plane of  $1.3 \mu\text{m}$ , which is not in quantitative agreement with the  $16 \mu\text{m}$  measured. However, it is quite difficult to correctly asses the drift given the complex system with multiple constraints and different materials.

In conclusion, locking the backward accordion lattice block reduced the drift of the super-lattice fringes by a factor 8. The residual drift happen over 250 experimental realization, with a cycling time of 90 s. We believe the residual drift displace both lattices together, which has no impact. If not, we note that during a single experimental shot, the phase need be controlled only over 1 s. Applying a reduction factor of  $250 \times 90$ , this estimate the shot-to-shot shift at  $0.09 \mu\text{m}$ . During a single sequence, the relative phase would still be stable but what is labeled as site zero may not be constant during a scan.

## 2.4. IMAGING OF A SINGLE ATOM DENSITY DISTRIBUTION IN A TIGHT 1D OPTICAL LATTICE

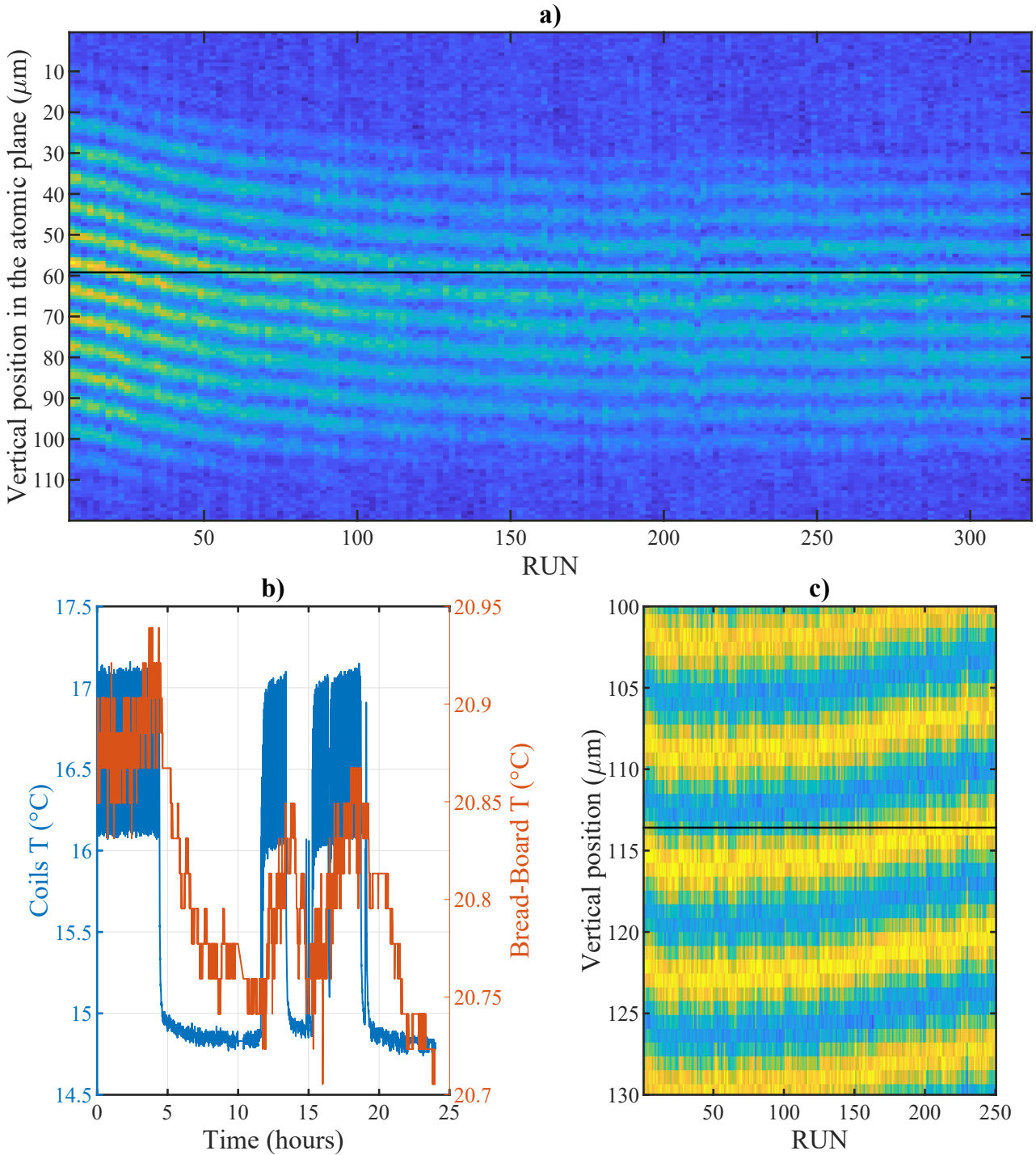


Figure 2.21: Spatial stabilization of the atomic cloud on the high N.A. imaging axis. a) With no temperature lock. Stacked horizontal projection with normalized atom number at a constant relative phase between the two lattices for consecutive experimental realizations. Over consecutive experiment sequences, we observe a spatial drift of the fringes over  $16 \mu\text{m}$  in the atomic plane. b) Temperature correlation of the coils copper plate (left axis) and the bread-board holding the backward accordion lattice block (right axis). c) Same as a) but the temperature is locked at better than  $10 \text{ mK}$ . The black horizontal lines in a) and c) are visual guides.

## 2.5 Summary

In this chapter, we detailed a super-resolution method developed in the team based on a spatial selectivity arising from the excited state modulation.

First, we recall the method in section 2.1 and give the theoretical resolutions it can reach depending on the type of transition considered. We implement it experimentally with the BAT curve scheme, and demonstrate that the resolution can be as low as 20 nm.

Then, we introduced in section 2.2 the theoretical concept describing ultra-cold Bosons trapped in optical lattices and presented the experimental implementation of a retro-reflected 1D lattice at 1064 nm. The lattice depth has been characterized using the diffraction of the BEC on the 1D grating produced by the lattice.

In section 2.3, we introduce the super-lattice scheme obtained when considering both lattices. The total light shift is carefully evaluated and we calibrate with two different methods the relative phase control of the lattices.

Finally, the super-resolution method is applied to image on our high NA imaging axis the single atom density distribution of a unique lattice site. We demonstrated that we were able to resolve an on-site density with a width of 38 nm, much smaller than the diffraction limit. We explored possible broadening effects on the sample size.

Further investigation on the matter are now on hold as we are working on the vacuum quality of the science chamber. We are also considering the implementation of a much simpler situation by changing the trapping lattice wavelength to 1022 nm. It would allow to have a super-lattice commensurability of 3 and 2, and would eliminate the clutter of having to clean the site as carefully as we are now.

# Chapter 3

## Atom chip

Ultra cold atoms trapped in optically or magnetically shaped potentials are the building blocks of the emerging field of atomtronics [91]. For this purpose, controlling atoms in the near vicinity of surfaces is a real opportunity to reach strong atom light coupling in a configurable environment where nano-fabrication capabilities can be used at best. The reduced size increase the energy scale up to the proper quantum regimes where magnetic quantum correlations or strongly correlated phases could be observed.

Our project aims at reducing the spacing of an optical lattice. For this purpose, we develop an hybrid quantum system of Bose and Fermi quantum gas in close proximity of a nano-structured surface based on the implementation of an atom chip [92, 93, 94]. Among standard tools, our design include magnetic fields generated by wires carrying few amps and a reflective surface that allows magneto-optical trapping.

In this chapter, we detail the initial simulations, design and characterization of the chip that will later be used on the experiment.

First, we synthesize the specificity of our atom chip platform, presenting the different traps, allowing to transport atoms from the far-field to the close vicinity of the surface [53]. In 3.1, we present the transport method [50] for transferring the atomic cloud from 5  $\mu\text{m}$  to 250 nm from the surface and introduce the theoretical formalism that describe non adiabatic mechanism. We apply this formalism to compute the heating rate of various experimental sources of noises. Then, we present in section 3.2 our progress regarding the atom-chip simulations, CAD and realization of a first prototype. Finally, we present the experimental characterization of this chip in section 3.2.4.

### 3.1 Transport method: rotating chip

A key ingredient to reach an exhaustive control of states and dynamics of cold atoms and ions is their efficient transport by moving the confining trap. Transport should ideally be lossless, fast and coherently lead to a well defined final state. In the case of an adiabatic transport, there should only be an evolution of the basis states but no redistribution over higher energy states. Efficient atom transport is a major goal for many applications such as quantum information

processing in multiplexed trap array [95, 96], controlled translation from the production chamber to the manipulation chamber [45, 97, 49], and velocity control to launch [98] or stop atoms [99]. In quantum gas experiment, adiabatic transport is generally realized by "slowly" displacing the center of a non-dissipative trap. This slowness criteria will be defined latter in 3.1.4.1. Usual transport method include moving the atoms in a magnetic trap [43, 44], using a moving dipole trap or controllable optical tweezers [45, 18]. In our work, we intend to reach the near field of surfaces where strong coupling to evanescent field can be reached. Magnetic traps are weakly confining limiting the transport of atoms to no-less than few  $\mu\text{m}$  from the surface. Indeed, for lower distances, the attractive Casimir force will dominate over the repulsive magnetic barrier, leading to a crash of atoms on the surface. As for optical tweezers, trapping is limited by the transverse Gaussian profile of the beam that does not allows to reach distances under the micro-meter from a macroscopic surface. The doubly dressed state trapping scheme developed in the team [29] allows to trap atoms even down to few tens of nanometers but it requires the cloud to be already at a few hundreds of nanometers from the surface.

### 3.1.1 Presentation of the transport scheme

To bridge the gap from few  $\mu\text{m}$  to few hundreds of nanometers , we now introduce a novel transport method named rotating chip transport. It uses the interference of a continuous laser radiation at 1064 nm and its reflection by the surface to generate a trapping optical lattice. Starting with a high angle of incidence, atoms are transferred into the first fringe, producing a large dipole trap volume at a few microns of the surface. The incidence angle is then decreased by rotating the surface up to the normal incidence. During this rotation, the first fringe is compressed and transported toward the reflective surface (Fig. 3.1 a) ). We detail in section 3.2 how a complementary magnetic potential generated by wires below the chip can compensate for gravity during the rotation transport (Fig. 3.1 b) ). Thereby, we consider in this section only the optical dipole trap generated by the laser and its reflection.

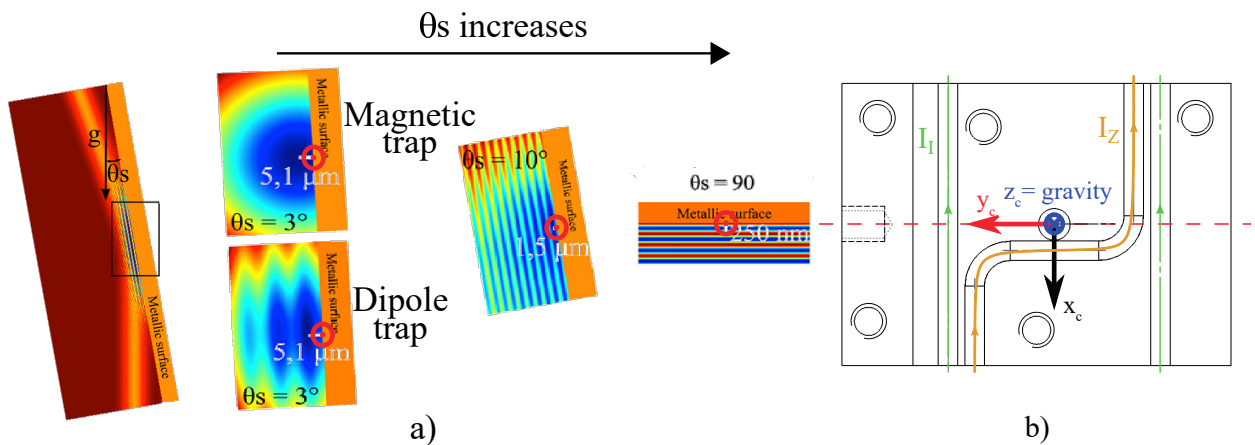


Figure 3.1: Sketch of the Rotation Transport method. a) Hybrid optical dipole and magnetic trap. b) CAD of the chip defining the current in the wires  $I_I$  and  $I_Z$ . The rotation axis (dashed red line) correspond to the red circles in a).

### 3.1.2 Derivation of the trapping potential

We start this section with analytical calculations of the trapping potential and numerical evaluation of the error made using a Quantum Harmonic Oscillator (QHO) approximation.

In the following, we consider the reflection of a Gaussian beam onto a plane surface. To stay general, the surface that could be metallic is described with a complex index of refraction. We first derive the total intensity profile in the vicinity of the surface which creates a 1D lattice structure.

All the notations used in this section are defined in Fig. 3.2. We use the frame of reference associated with the chip in which the reflective surface is at rest. In the lab frame, the chip rotates around  $\mathbf{y}$ . For any field  $\mathbf{E}_\alpha$ ,  $r_\alpha$  denote the radial distance to the propagation axis and  $d_\alpha$  the longitudinal distance to the focus.

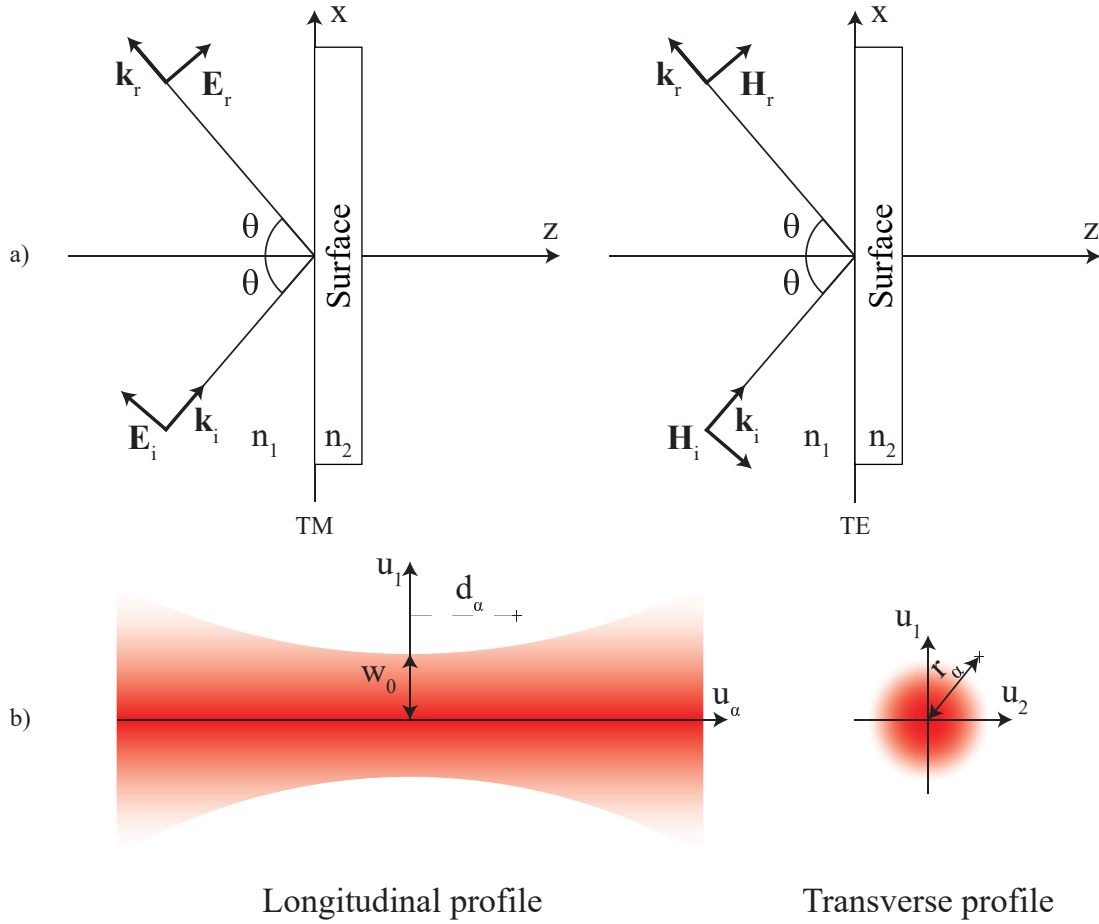


Figure 3.2: a) Oblique incidence of TM and TE polarized waves on a planar surface. For TM polarization, the electric field lie on the plane of incidence. For TE polarization, the electric field is perpendicular to the plane of incidence. b) Cartoon picture of the propagation of a Gaussian beam. For a field  $\mathbf{E}_\alpha$  propagating along  $\mathbf{u}_\alpha$ ,  $r_\alpha$  denote the radial distance to the propagation axis and  $d_\alpha$  the longitudinal distance to the focus.

Following [100], we split the field into two component : transverse electric (TE or s-wave) and transverse magnetic (TM or p-wave). We write the electric Gaussian field of waist  $w_0$

propagating along  $\mathbf{u}_i$  taken at point  $\mathbf{r} = (x; y; z)$  of space :

$$\mathbf{E}_i(r_i, d_i, \mathbf{r}, t) = \tilde{E}_0(t) \left( A_{TM}^+ (\cos(\theta)\mathbf{u}_x - \sin(\theta)\mathbf{u}_z) + A_{TE}^+ \mathbf{u}_y \right) \frac{w_0}{w(d_i)} e^{-r_i^2/w^2(d_i)} e^{-i \left( \mathbf{k}_i \cdot \mathbf{r} + k_i \frac{r_i^2}{2R_i(d_i)} - \psi_i(d_i) \right)} \quad (3.1)$$

Where  $\mathbf{k}_i = \frac{2\pi}{\lambda_0} (\sin(\theta)\mathbf{u}_x + \cos(\theta)\mathbf{u}_z)$  is the k-vector of the incident beam ,  $\tilde{E}_0(t) = E_0 e^{i\frac{2\pi c}{\lambda_0} t}$  the amplitude and time dependent phase factor,  $R_i(d_i)$  the radius of curvature of the wavefront and  $\psi_i(d_i)$  the Gouy phase. We have  $r_i^2 = (x \cos(\theta) - z \sin(\theta))^2 + y^2$ .

The contribution of the TE and TM components in the incident field are weighted respectively by the coefficient  $A_{TE}^+$  and  $A_{TM}^+$  that are both real positive numbers, verifying  $(A_{TM}^+)^2 + (A_{TE}^+)^2 = 1$ . Note that the dependence of the field on the spatial variables is redundant. It nevertheless stress the different contributions and help the numerical implementation.

The reflected field can be written as :

$$\mathbf{E}_r(r_r, d_r, \mathbf{r}, t) = \tilde{E}_0(t) \left( A_{TM}^- (\cos(\theta)\mathbf{u}_x + \sin(\theta)\mathbf{u}_z) + A_{TE}^- \mathbf{u}_y \right) \frac{w_0}{w(d_r)} e^{-r_r^2/w^2(d_r)} e^{-i \left( \mathbf{k}_r \cdot \mathbf{r} + k_r \frac{r_r^2}{2R_r(d_r)} - \psi_r(d_r) \right)} \quad (3.2)$$

with  $\mathbf{k}_r = \frac{2\pi}{\lambda_0} (\sin(\theta)\mathbf{u}_x - \cos(\theta)\mathbf{u}_z)$  and  $r_r^2 = (x \cos(\theta) + z \sin(\theta))^2 + y^2$ .

We introduce the generalized complexes Fresnel coefficients :

$$\begin{aligned} \rho_{TE} &= |\rho_{TE}| e^{i\phi_{TE}} = \frac{A_{TE}^-}{A_{TE}^+} \\ \rho_{TM} &= |\rho_{TM}| e^{i\phi_{TM}} = \frac{A_{TM}^-}{A_{TM}^+} \end{aligned} \quad (3.3)$$

Considering an interface between two medium of complex indexes of refraction ( $n_1 = 1$  and  $n_2 = \tilde{n} - i\kappa$ ), we can write the Fresnel coefficients as [100, p.249]:

$$\begin{aligned} \rho_{TE} &= \frac{\cos(\theta) - \sqrt{\left(\frac{n_2}{n_1}\right)^2 - \sin^2(\theta)}}{\cos(\theta) + \sqrt{\left(\frac{n_2}{n_1}\right)^2 - \sin^2(\theta)}} \\ \rho_{TM} &= \frac{\sqrt{\left(\frac{n_2}{n_1}\right)^2 - \sin^2(\theta)} - \left(\frac{n_2}{n_1}\right)^2 \cos(\theta)}{\sqrt{\left(\frac{n_2}{n_1}\right)^2 - \sin^2(\theta)} + \left(\frac{n_2}{n_1}\right)^2 \cos(\theta)} \end{aligned} \quad (3.4)$$

where we generalized the square root function to the complex plane.

Given some realistic approximations, the expression above can be further simplified, yielding an analytic formula for the total intensity profile in the vicinity of the surface. Indeed, we are here studying the field only at a few microns from the surface. The lasers used in the experiment typically have a wavelength of 1064 nm, with a waist  $w_0 = 100 \mu\text{m}$ , propagating in the vacuum. The Rayleigh range  $z_R = \pi w_0^2 / \lambda_0 = 30 \text{ mm}$  being large compared to the typical distances under study, we neglect the change of the beam radius, wavefront curvature, and the Gouy phase

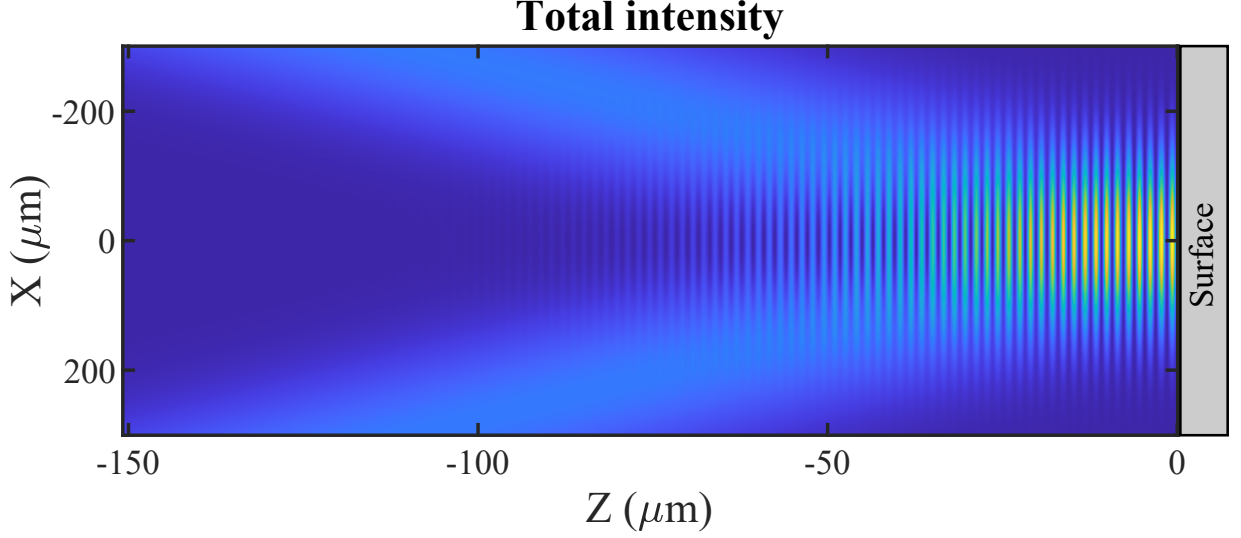


Figure 3.3: Total intensity spatial distribution in the incidence plane numerically computed with the exact Gaussian profiles. The incident beam is polarized along  $\mathbf{u}_y$  (TE) with an incidence angle  $\theta = 70^\circ$ .

along the propagation. For both fields, we then have :

$$\forall d_\alpha : \frac{w_0}{w(d_\alpha)} = 1; \quad k_\alpha \frac{r_i^2}{2R_\alpha(d_\alpha)} = 0; \quad \psi_\alpha(d_\alpha) = 0$$

Recalling the definition of the Intensity  $I = \epsilon_0 c \langle |\mathbf{E}_t|^2 \rangle = \frac{\epsilon_0 c}{2} \mathbf{E}_t \mathbf{E}_t^\dagger$  with  $\mathbf{E}_t = \mathbf{E}_i + \mathbf{E}_r$ , we separate the total intensity in three contributions, each corresponding to a component of polarization of the total field:

$$I_t(\mathbf{r}) = \frac{\epsilon_0 c}{2} |E_0|^2 \left( (C_+ - C_-) |A_{TM}^+|^2 + C_y |A_{TE}^+|^2 \right) \quad (3.5)$$

where :

$$\begin{aligned} C_+(\mathbf{r}) &= e^{-2r_i^2/w_0^2} + |\rho_{TM}|^2 e^{-2r_r^2/w_0^2} \\ C_-(\mathbf{r}) &= 2e^{-(r_i^2+r_r^2)/w_0^2} |\rho_{TM}| \cos(2\theta) \cos\left(\frac{2\pi}{\lambda_0} 2 \cos(\theta)z + \phi_{TM}\right) \\ C_y(\mathbf{r}) &= e^{-2r_i^2/w_0^2} + |\rho_{TE}|^2 e^{-2r_r^2/w_0^2} + 2e^{-(r_i^2+r_r^2)/w_0^2} |\rho_{TE}| \cos\left(\frac{2\pi}{\lambda_0} 2 \cos(\theta)z + \phi_{TE}\right) \end{aligned} \quad (3.6)$$

We have  $r_i^2 + r_r^2 = 2(x^2 \cos^2(\theta) + y^2 + z^2 \sin^2(\theta))$ .

For the sake of simplicity and to focus the discussion on meaningful physics, we restrict the analytics below to the case of a TE incident polarization :  $A_{TE}^+ = 1$ . Nevertheless, the numerics are performed on the general case of incident polarization. Simulation of  $I_t$  for the case of a TE incident polarization is presented in Fig. 3.3.

The generated dipolar potential given by Eq. B.2 is proportional to the total intensity and will be approximated along each of the three directions of space as a one dimension quantum harmonic oscillator (1D-QHO). This approximation is numerically validated with a maximum

relative difference over the theoretical TF distribution (see Eq. C.22 with  $N = 10^5$  atoms) by less than 2%. Around the trap center, the potential can be considered as separable. Each direction is given by

$$U_\alpha(\alpha) = \frac{1}{2}M\omega_\alpha^2(\alpha - \alpha_0)^2 \quad (3.7)$$

In the case of a red-detuned FORT, the trap center is situated at a maximum of intensity. In the direction perpendicular to the surface, we consider the trap formed by the bright fringe the closest to the surface. We therefore develop the QHO form around this trap center which is at  $z = d_0 < 5 \mu\text{m}$ . At this distance from the surface, the two Gaussian beams are still well overlapped. In the transverse direction, the total intensity profile only present one maximum. Neglecting gravity, the trap center is situated at  $(x_0 = 0; y_0 = 0)$ . The evolution of the trap position in the  $z$ -direction is given by :

$$d_0(\theta) = -\frac{\phi_{TE}\lambda_0}{4\pi \cos(\theta)} \quad (3.8)$$

and the trap frequencies are given by

$$\begin{aligned} \omega_x^2 &= \omega_y^2 \cos^2(\theta) \\ \omega_y^2 &= -C_{dip} \frac{2P_0}{\pi w_0^2} \frac{4}{Mw_0^2} \left(1 + |\rho_{TE}|^2 + 2|\rho_{TE}|\right) \\ \omega_z^2 &= -C_{dip} \frac{2P_0}{\pi w_0^2} \frac{|\rho_{TE}| 32\pi^2 \cos^2(\theta)}{\lambda_0^2 M} \end{aligned} \quad (3.9)$$

with  $C_{dip}$  introduced in eq. B.5 and  $P_0 = I_0\pi w_0^2/2$  the incident beam total power.

The exact potential, with no approximations, is given by :

$$U_{tot}(\mathbf{r}) + U_0 = C_{dip} \frac{\epsilon_0 c}{2} |\mathbf{E}_i + \mathbf{E}_r|^2 \quad (3.10)$$

We illustrate the previous part with numerical simulation and present in Fig. 3.3 the exact intensity profile in the incident plane. For these simulations, we used the complex refractive index  $(n + ik)$  of a thin layer ( $53 \mu\text{m}$ ) of gold<sup>1</sup> at 1064 nm [101] : refractive index  $n = 0.24789$  and extinction coefficient  $k = 7.3057$ . The sign convention is taken so that the dielectric constant is given by  $\epsilon = n^2 - k^2 + 2ink$ . A slightly different value for bulk gold has been reported in [102] but the difference seen in the numerical simulation was negligible. We present in Fig. 3.4 the important results of the numerical simulations. As expected with the dependency of the trapping frequency with the square root of the incident power (Eq. 3.9), all frequencies are increasing with the optical power. The trapping frequency in the direction normal to the surface which is driven by the lattice structure of the overlapped beams is 3 orders of magnitude larger than frequencies which are driven by the Gaussian nature of the beams. In Fig. 3.4 b),  $\epsilon_\alpha$  is calculated as the relative error of the exact potential and the approximation by separable QHO at a distance  $\alpha_{TF}$ , defined as the Thomas Fermi radius of a trapped interacting BEC with  $N = 10^5$  atoms. In Fig. 3.4 d), we compare the trap frequency as numerically fitted on the exact potential (dashed) and the result of Eq. 3.9. It shows that the approximation of the

---

<sup>1</sup>This value correspond to the mirror we used for the chip, presented in 3.2.3

potential by separable QHO is good to better than 2%. Interestingly, the ratio  $\nu_z/\nu_x = 252(2)$  is almost independent of the incidence angle (residual dependence through  $|\rho_{TE}|^2$ ).

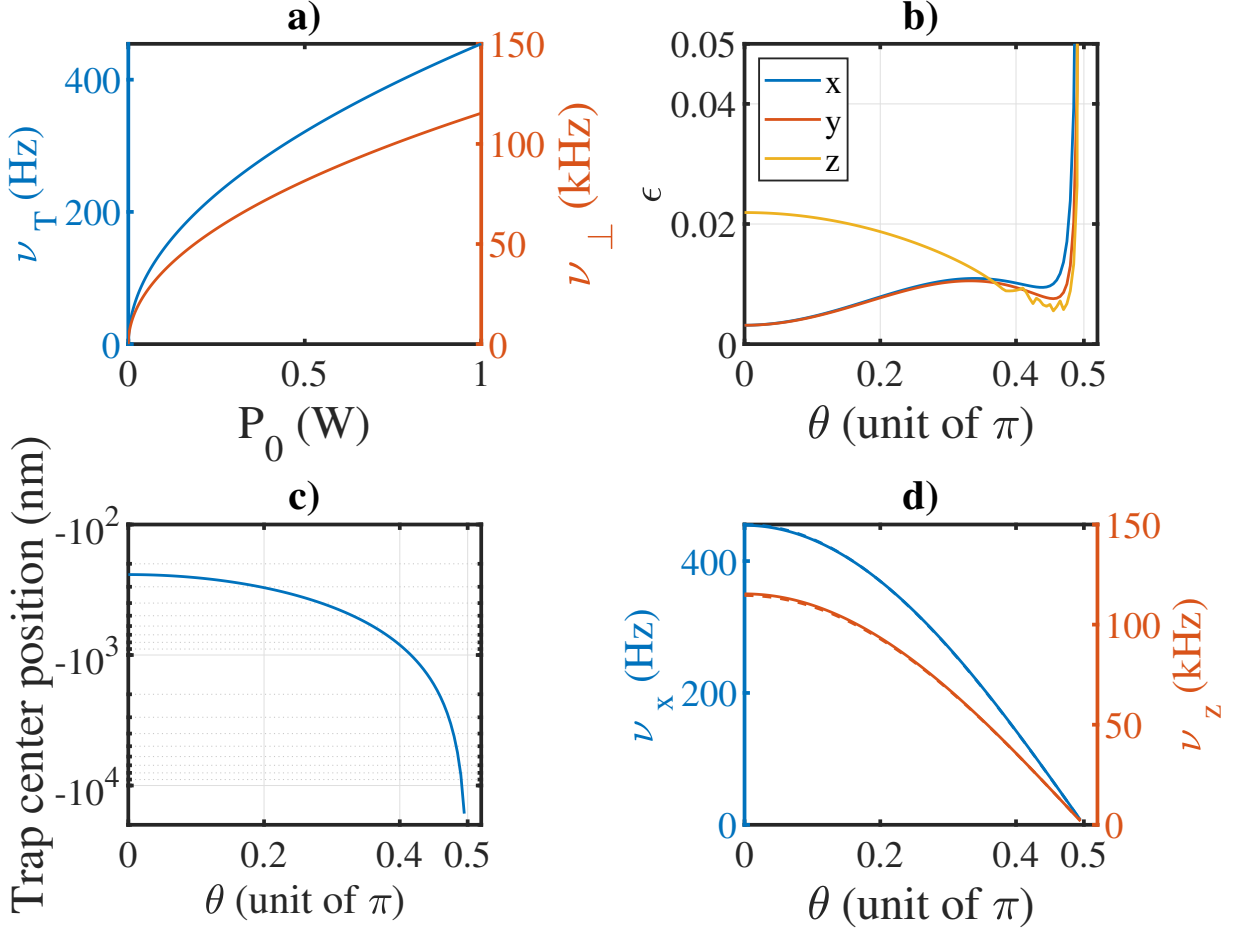


Figure 3.4: a) Evolution of the trapping frequencies with the power of the incident beam for an incidence angle  $\theta = 0$ . At normal incidence, the frequencies along the transverse direction are equal ( $\nu_x = \nu_y = \nu_T$ ).  $\nu_\perp$  is the trapping frequency along the normal direction ( $\mathbf{u}_z$ ). The other curves are computed with an incident power of 1 W. b) Evolution of the relative error  $\epsilon_\alpha = \frac{|U_{tot} - U_\alpha|}{U_{tot}}$ , made with the harmonic approximation given in Eq. 3.7, with the incidence angle. This error value is computed at a distance  $\alpha_{TF}$  from the trap center for each direction. c) Trap center position along the normal direction as a function of the incidence angle. d) Trap frequencies as a function of the incidence angle.  $\nu_y = 458(4)$  Hz is slightly increasing with the angle. Dashed lines are the fitted frequency over two TF radius of the exact potential and plain lines are the approximations given in Eq. 3.9.

### 3.1.3 Experimental parameters

We define now a first guess experimental sequence where the trap frequencies evolution are optimized over the transport to minimize heating. The optimization is carried by changing simultaneously the optical power and the incidence angle.

As mentioned earlier, gravity is compensated by a magnetic potential (see 3.2.1). Both

are therefore neglected for now.

We present in Fig. 3.5 a) the variation of power and angle over time, and the related trap frequencies in b).

We aim at producing an optical lattice with a depth close to  $40E_R$  in the longitudinal direction while keeping the transverse direction relatively loose to prevent 3-bodies collisions. The initial low trapping frequency along  $\boldsymbol{x}$  at high incidence angle need to be compensated by a high optical power. Starting at  $\nu_x = 50$  Hz, it defines an optical power of 4.5 W for a beam waist of  $100 \mu\text{m}$ . We begin the chip rotation at the lowest initial speed of the motor (Tekceleo motor presented in 3.1.5.2). This allows to be as adiabatic as possible. After 100 ms at the lowest speed,  $\nu_x$  has reached 100 Hz and we modify the speed with constant acceleration and deceleration (linear velocity change). The optical power is decreased as  $1/\cos^2(\theta)$  so the frequency along the transverse direction will stay constant until the end of the rotation.

Starting and stopping at the lowest rotation speed is intuitively the easiest way to limit cloud heating by having the smallest instantaneous acceleration<sup>2</sup>.

The ground state energy of the system for each set of trapping frequencies has been computed by solving numerically the stationary solution of the Gross-Pitaevskii equation and is plotted as a function of time in Fig. 3.6. Be aware that this is not the actual evolution in time of the energy of the system but simply the 3D ground state energy of the trap at a given time. According to our simulations, the ground state energy is well approximated (the maximum relative error is 10%) by considering that the longitudinal direction is a 1D-QHO with  $N$  non-interacting particles in the ground state of the harmonic oscillator and that both longitudinal directions are in the Thomas-Fermi regime. For the presented trap, this is the approximation giving the lowest errors compared to three independent 1D-QHO or a cloud fully in the TF regime.

---

<sup>2</sup>An optimization on the speed driving compared to this simple linear increase could be the implementation of an S-shape on the acceleration, similarly to the initial ramp up of the lattice presented in section 2.2.2.

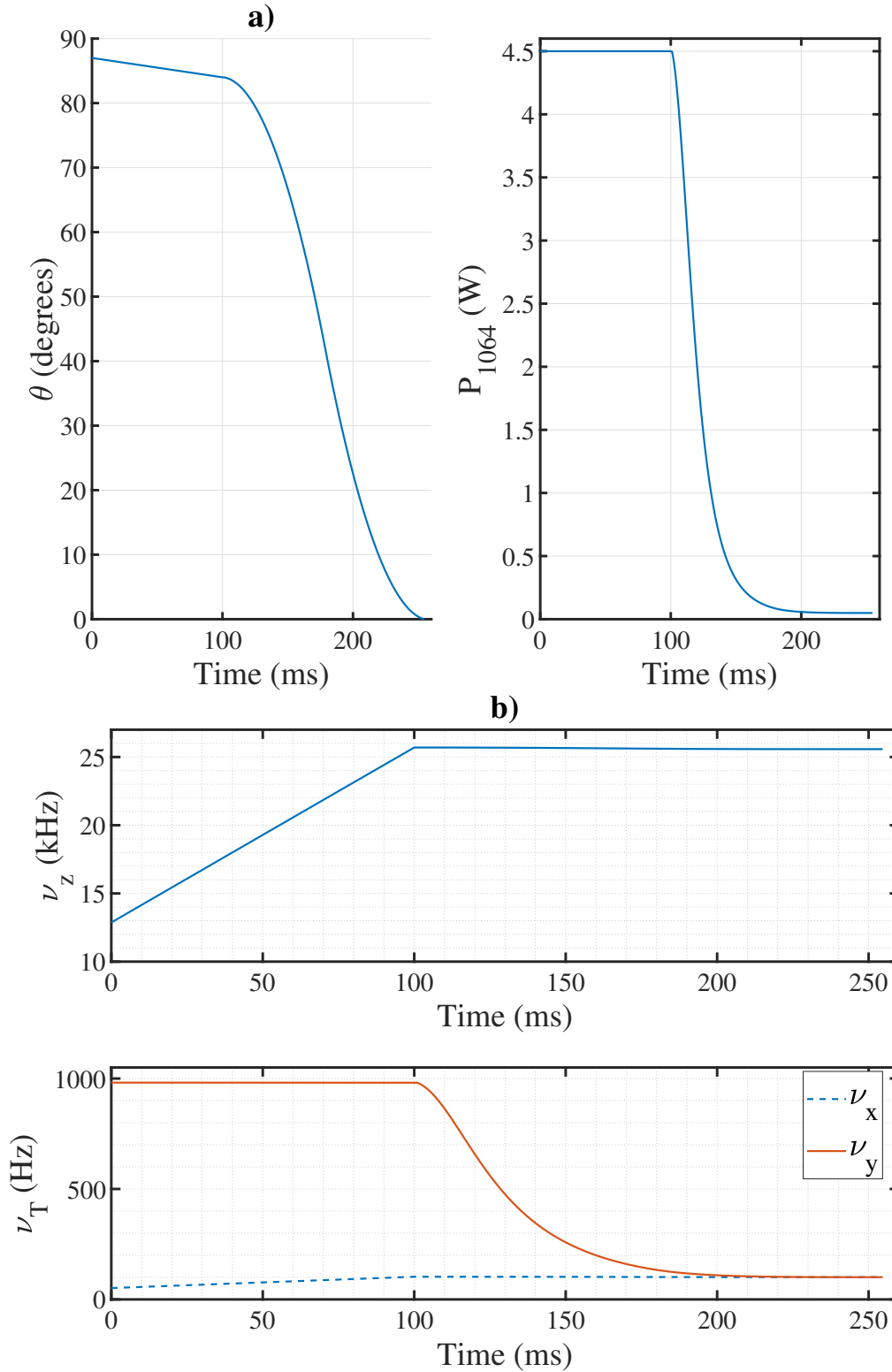


Figure 3.5: Proposed experimental sequence for the rotation transport. a) Evolution of the drive variables. During the rotation of the chip, the optical power is adapted so the longitudinal trap frequency is constant during the second part of the transport, from 100 ms to 255 ms. b) Evolution of the resulting trap parameters, the longitudinal trapping frequency increase from  $\nu_z = 12.9$  kHz to 25.6 kHz. During the first 100 ms, the chip is rotated at the lowest speed to compress the trap from  $\nu_x = 50$  Hz to 100 Hz. The power decrease then allows a decompression along the last direction from  $\nu_y = 1$  kHz to 100 Hz.

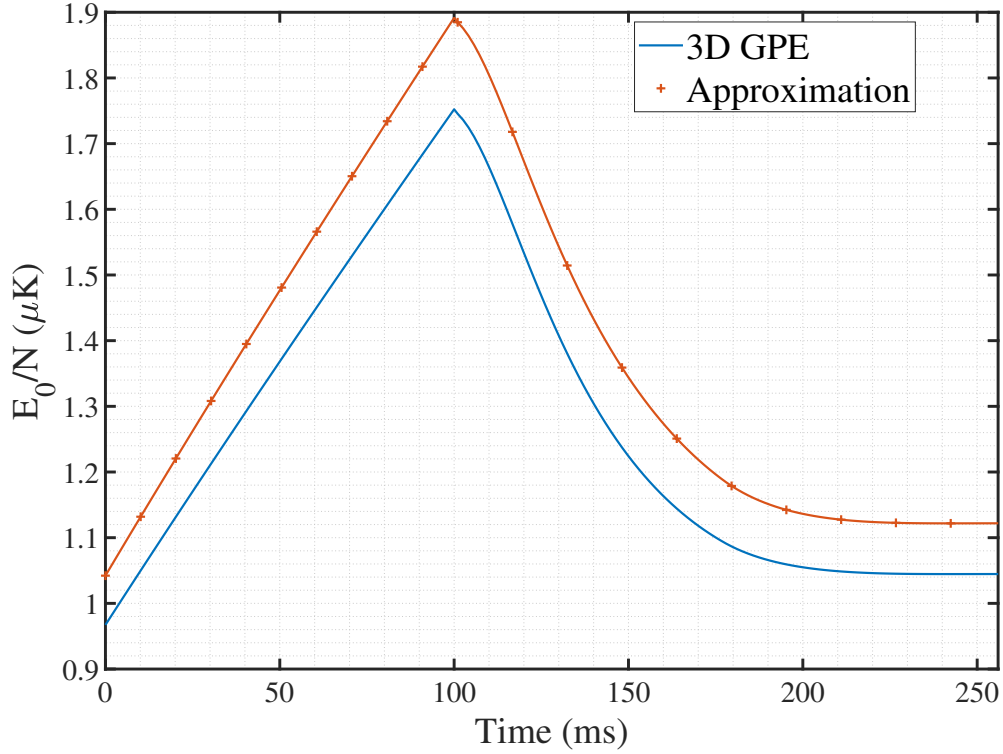


Figure 3.6: Ground state energy per particles for the trap presented above at different time of the rotation. The plain line is the stationary solution of the 3D-GPE solved numerically. The plain line with crosses is the approximated energy  $E = 2E_{TF}/3 + E_{QHO}/3$  considering the transverse directions to be in the Thomas-Fermi regime and the longitudinal direction as a 1D-QHO at frequency  $\nu_z$ .  $E_{TF}$  is computed using the given set of trap frequencies according to Eq. C.23 and  $E_{QHO}$  according to Eq. C.19. The relative error between the two energies is fairly constant, between 8 and 10%.

### 3.1.4 Trap dynamic and heating

In the literature related to the transport of cold atoms cloud, the term "heating" has different definitions. In an harmonic potential, center-of-mass oscillation (or mode) is the only motion-excited mode. Non-harmonic terms in the Hamiltonian and interactions between the atoms couple this sloshing mode with higher order modes which lead to an increase of temperature [103]. In [39, 42] the velocity distribution difference at the beginning and the end of the transport is measured. By extracting the global temperature of the cloud with usual TOF expansion method, the heating can be defined as a statistical temperature increase. [104] define the heating of the cloud by looking at the energy distribution over the QHO vibrational states. This way, it defines an average energy for the cloud and heating result from transitions to higher excited states of the oscillator. A sudden displacement of the trap cloud lead to excitation to higher excited states when projecting the wave-packet on the newly formed basis. The trap center thus need to evolve slowly so the atoms can adiabatically follow it's trajectory. However, the reader should note that the heating is considered on the final sate. Hence, transients excitation in the instantaneous basis at intermediate time are not synonymous of heating as they can be coherently retrieved.

Following the transport method presented in 3.1.1, the rotation of the surface will compress the first fringe towards the surface. For this rotation, we have considered two types of motors inducing distinct type of motions.

The first was a stepper motor ([New focus picomotor 8321](#)) which exists in a UHV compatible version. Each steps abruptly change the trap center position and is followed by a resting time during which the atoms evolve in the translated trap. During this resting time, residual motion such as damped oscillations or fluctuations in the angular position are observed (see Fig. 3.13). The second was a continuous rotation motor ([Tekceleo WLG-75](#)), driven by ultrasonic waves. It produces a linear evolution of the incidence angle with a controllable speed between 5 and 175 rotation per minute (rpm).

We model the displacement of the trap by a QHO Hamiltonian (Eq. 3.9) with time dependent parameters. Evolution under a time dependent resting force has been well studied in the classical treatment of parametric excitation [105] where it was shown that specific sinusoidal modulations can lead to an exponential heating of the cloud. In the following, the evolution of the trap parameters in time are discussed according to adiabaticity criterion. Moreover, we study the behavior of  $N$  atoms evolving in a constant trap with randomly fluctuating parameters according to [104, 106]. We first derive the general theoretical formalism then adapt it for each motors and present the expected heating induced on the transported cloud.

#### 3.1.4.1 Theory

We consider at first a 1D problem. Extension to higher dimensions is explained afterwards. In the case of uncorrelated variations, time dependence of the QHO parameters can be treated independently, as separate perturbations Hamiltonian. We will discuss the treatment of correlated variation after presenting the formalism for each separate cases. We derive below the theoretical evolution of the system for specific time dependent parameters.

### Linear sweep of the restoring force.

As we previously saw, trapping frequencies of the different directions are in quite different regimes and we derive relevant adiabaticity criterion for each of them. The experimental conditions for this study are the one presented in 3.1.3.

We consider first the longitudinal direction, along  $z$  which corresponds to atoms trapped in a 1D optical lattice. Thus, variations of the longitudinal trapping frequency can be viewed as compression or decompression of the optical lattice. We consider the same adiabaticity criterion as for loading atoms in a lattice for which two timescales are relevant :

- Adiabaticity with respect to the band population.

Changing the lattice potential too fast will populate higher energy bands. The level spacing gives the adiabaticity timescale. Considering the adiabaticity criterion for the transfer from the lowest into the  $n$ -th energy band of a non interacting gas, reduced to quasi-momentum  $q \sim 0$  and away from the border of the Brillouin zone, we have [84, 85]:

$$\frac{d}{dt}V_0/E_r \ll 16Er/\hbar = 204 \text{ kHz} \quad (3.11)$$

where the recoil energy for  $^{87}\text{Rb}$  at 1064 nm is  $E_r/h = 2.0323 \text{ kHz}$ . This condition is more easily fulfilled for larger potential depths since the level spacing increases.

Evaluating this condition at the beginning of the rotation, when the longitudinal direction is linearly compressed from  $s = 10$  to  $s = 40$  in 100 ms gives  $\frac{d}{dt}V_0/E_r = 300 \text{ Hz}$  so we are largely in the adiabatic regime.

- Adiabaticity compared to many body dynamics [86, 87].

A second time scale appears in the evolution of the system where, due to many body interactions, atoms redistribute over the lattice sites through tunneling in order to adapt the system size to the instantaneous Thomas-Fermi shape. In our case, we want atoms to remain in the first fringe of the optical lattice. At the initial loading, with  $s = 10$ , the hopping time  $\hbar/J$  is under 30 ms, which then should be compensated by adding an energy gradient in the transverse direction. This should be considered once having the final rotation sequence.

Along  $y$ , the trap is decompressed from 1 kHz to around 100 Hz. Given a time reversal argument and following the same criterion as stated for the longitudinal direction with respect to the band population<sup>3</sup>, we have :

$$\mathcal{A}_y = \left| \frac{\partial \omega_y}{\partial t} \right| / (2\omega_y)^2 \ll 1 \quad (3.12)$$

which is verified numerically as  $\mathcal{A}_y < 5 \times 10^{-3}$ .

Lastly, the  $x$  direction is well described throughout the whole displacement by the TF approximation.

### Linear sweep of the trap center.

In the laboratory frame of reference, the trap center evolution is a curve given by the evolution of the distance to the surface along the longitudinal direction and the rotation of the chip. Along

---

<sup>3</sup>If we can adiabatically load a lattice under this criterion, we should be able to adiabatically decompress a lattice back into the TF regime.

$\mathbf{x}$ , the density distribution is quite close to the TF distribution (Eq. C.22). In this direction, the density profile experience a compression from  $r_{TF}^x = 40 \mu\text{m}$  to  $30 \mu\text{m}$ . Thus, even taking an upper bound for the displacement to be of  $5 \mu\text{m} = r_{TF}^x/8$  indicates a negligible effect of the trap-center variation.

We restrict the study to a linear translation of the cloud toward the surface and neglect the effect of the chip rotation. In this case, only need to consider the linear compression of a 1D-QHO.

When transferring a BEC to a single Bloch state  $|n, q\rangle$  of an optical lattice, the usual adiabaticity criterion reads [85] :

$$\left| \left\langle i, q \left| \frac{\partial H}{\partial t} \right| 0, q \right\rangle \right| \ll \Delta E^2(q, t)/\hbar \quad (3.13)$$

where  $\Delta E$  is the energy difference between the ground state and the first excitable state  $|i\rangle$ . We establish an adiabaticity criterion  $\mathcal{A}$  at  $q = 0$ . Given that  $\frac{\partial \hat{x}}{\partial t} = 0$  in the case of a constant trapping frequency but time dependent trap center given by Eq. 3.8, the criteria reads

$$\mathcal{A} = \frac{\partial d_0}{\partial t} \frac{1}{2\sqrt{2}\pi\nu_z a_{HO}^z} \ll 1 \quad (3.14)$$

where  $a_{HO}^z = \sqrt{\hbar/m\omega_z}$  is the 1D-QHO length.

In Fig. 3.7, we show the numerical evolution of the criteria along the rotation sequence, which

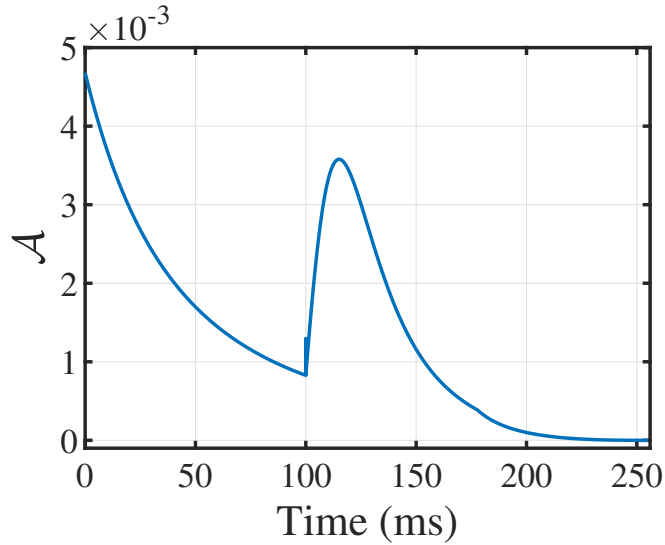


Figure 3.7: Adiabaticity criterion evolution during the experimental sequence proposed in 3.1.3. The time evolution of the trap center has been evaluated by numerical differentiation.  $\mathcal{A}$  is negligible compared to unity at all time, indicating an adiabatic process.

indicate an adiabatic process.

#### $\epsilon_k$ : noise on the spring constant.

In this paragraph, we study the impact of noise, or random time-fluctuations, on the trapping

frequency [104]. We consider here the model Hamiltonian :

$$H = \frac{p^2}{2m} + \frac{1}{2}m\omega_x^2(1 + \epsilon_k)x^2 \quad (3.15)$$

The effect of  $\epsilon_k$  can be studied using first-order time-dependent perturbation theory. The perturbation Hamiltonian is :

$$H'_k(t) = \frac{1}{2}m\omega_x^2x^2\epsilon_k(t) \quad (3.16)$$

Considering an atom initially in the state  $|n\rangle$ , the average rate to make a transition to a state  $|m \neq n\rangle$  in the time interval  $T$  is given by :

$$R_{m \leftarrow n} = \left(\frac{m\omega_x^2}{2\hbar}\right)^2 \int_{-\infty}^{+\infty} e^{i\omega_{mn}\tau} \langle \epsilon(t)\epsilon(t+\tau) \rangle \left| \langle m|x^2|n \rangle \right|^2 d\tau \quad (3.17)$$

where we introduced the correlation function for fractional fluctuation :

$$\langle \epsilon(t)\epsilon(t+\tau) \rangle \doteq \frac{1}{T} \int_0^T \epsilon(t)\epsilon(t+\tau) dt$$

Here we assumed that the averaging time  $T$  is short compared to the time scale over which the populations vary, but large compared to the correlation time of the fluctuations. We thus used an extended Wiener-Khintchine theorem in its time-average form (see [107, p.63]). For this definition to hold, we had to suppose that the average trap angular frequency  $\omega_x$  was constant over the averaging time. We discuss this assumption after deriving the main result. We define  $S_k(\omega)$  the one-sided power spectrum of the fractional fluctuation in the spring constant :

$$S_k(\omega) \doteq \frac{2}{\pi} \int_0^{+\infty} \cos(\omega\tau) \langle \epsilon(t)\epsilon(t+\tau) \rangle d\tau \quad (3.18)$$

This spectrum should be normalized so that

$$\int_0^{\infty} S_k(\omega) d\omega = \int_0^{\infty} S_k(\nu) d\nu = \epsilon_{0k}^2$$

where  $\epsilon_{0k}$  is the root-mean-square fractional fluctuation in the spring constant and  $\nu = \omega/2\pi$  the associated frequency. We have used:  $S_k(\nu) = 2\pi \times S_k(\omega)$ .

Using the transition matrix elements of  $x^2$  and  $\omega_{n\pm 2,n} = \pm 2\omega_x$ , we have

$$R_{n\pm 2,n} = \frac{\pi\omega_x^2}{16} S_k(2\omega_x) (n+1 \pm 1) (n \pm 1) \quad (3.19)$$

The average energy can be defined with  $P(n, t)$  the probability that a trapped atom occupy a state  $|n\rangle$  at time  $t$  as

$$\langle E_x(t) \rangle = \sum_n P(n, t) (n + 1/2) \hbar\omega_x \quad (3.20)$$

The evolution of the average energy is then given by:

$$\langle \dot{E}_x \rangle = \Gamma_x^k \langle E_x \rangle \quad (3.21)$$

General solutions of this equation are an exponential increase with a rate constant  $\Gamma_x^k$  :

$$\Gamma_x^k = \pi^2 \nu_x^2 S_k(2\nu_x) \quad (3.22)$$

where  $\nu_x$  is the trap oscillation frequency in Hz . We define the energy e-folding time  $T_x^k = 1/\Gamma_x^k$ , as the time to increase the average energy  $\langle E_x \rangle$  of a factor  $e$ .

To treat more than one dimension, we should suppose that the energy is equally distributed, and that the system is at thermal equilibrium at all times. This is verified if collisions processes happens on time scales shorter than the heating process of each directions, redistributing the energy and leading to a 3D trap always at thermodynamic equilibrium. In this case, we can define an average heating rate of the mean energy as the arithmetic mean of each 1D heating rates.

Along the 2 transverse directions, we use the TF approximation that gives a total energy closer to the 3D-GPE stationary solution than the 1D-QHO approximation. The longitudinal direction is way more compressed and can be treated as a 1D-QHO without interaction and can be treated independently.

The heating time scale, was averaged over  $T$ . As mentioned above,  $T$  need to be sufficiently long to resolve the spectrum of the fluctuation  $\epsilon$ . Eq. 3.17 is valid for constant angular trap frequency  $\omega_x$  which are in the kHz range. To use this formalism, we will consider the trap frequency to be constant over a time  $T = \frac{10}{2\nu_x}$ . We consider the assumption valid if  $T_x^k \gg T$ , which indicates that  $T$  is small enough to well discretize the trajectory.

#### $\epsilon_x$ : noise on the trap center.

In this section, we study the impact of noise on the trap center[106]. Here, the effective Hamiltonian take the form :

$$H(t) = \frac{1}{2} m \omega_x^2 (x - \epsilon_x(t))^2 \quad (3.23)$$

Fluctuations in any additive, spatially constant potential do not cause transitions. The term in  $\epsilon_x^2(t)$  in the Hamiltonian can thus be neglected.

The perturbation Hamiltonian is

$$H'_x(t) = m \omega_x^2 x \epsilon_x(t) \quad (3.24)$$

The transition rate is given by

$$R_{n \pm 1 \leftarrow n} = \frac{\pi}{2\hbar} m \omega_x^3 S_x(\omega_x) (n + 1/2 \pm 1/2) \quad (3.25)$$

with  $S_x$  the one-sided power spectrum of the position fluctuation normalized so that

$$\int_0^\infty S_x(\omega) d\omega = \int_0^\infty S_x(\nu) d\nu = \epsilon_x^2 \quad (3.26)$$

with  $\epsilon_x$  the mean square variation in the trap center position.

The evolution of the average energy is given by :

$$\langle \dot{E}_x \rangle = \dot{Q}_x = \frac{\pi}{2} m \omega_x^4 S_x(\omega_x) = 4m\pi^4 \nu_x^4 S_x(\nu_x) \quad (3.27)$$

This leads to an heating rate that is independent of the trap energy. We define an energy doubling time  $T_x^x$ , as the time needed to double the initial average energy :

$$\langle \dot{E}_x \rangle = \frac{\langle E_x(t=0) \rangle}{T_x^x} \quad (3.28)$$

The evaluation of the initial energy depend on the direction considered. In the chip frame of reference, transverses directions are in the Thomas-Fermi regime. Whereas the longitudinal direction, with a higher trapping frequency, is some-time in between the two extreme cases. For the transverses directions, we use the TF approximation in which the total initial energy of the 3D cloud is given by Eq. C.23 and assume that the energy is equally distributed over the three directions. For the longitudinal direction, we study the worst case, corresponding to no interactions. Supposing that the atoms are initially in the ground state, the initial energy is :  $\langle E_z(t=0) \rangle = N\hbar\omega_z/2$ . For precise numerical applications, we instead use the steady-state ground-state energy of the Gross-Pitaevskii equation with  $N$  atoms. We recall that this approximation has been already checked for the specific experimental sequence described in section 3.1.3.

### 3D generalization and correlated noises.

Some experimental variations can affect both the trap center and the trap constant, yielding a correlated time-dependence of these two parameters.

For such case, the total Hamiltonian is :

$$H(t) = \frac{1}{2}m\omega_x^2(1 + \epsilon_k)(x - \epsilon_x(t))^2 \quad (3.29)$$

Using Eq. 3.16 and 3.24, we write :

$$H(t) = \frac{1}{2}m\omega_x^2x^2 + H'_x(t) + H'_k(t) - 2x\epsilon_k(t)\epsilon_x(t) + H_{offset}(t) \quad (3.30)$$

Since  $\epsilon_k(t) \ll 1$ , the term  $2x\epsilon_k(t)\epsilon_x(t)$  is negligible compared to  $H'_x(t)$ . Also,  $H_{offset}(t)$  encapsulate terms with no dependence on the position operator. It therefore cannot drive transitions between states and does not induce heating.

In equation 3.30,  $H'_x$  and  $H'_k$  have different polynomial dependency on the position operator  $\hat{x}$  which prevent to directly compare them. However, the two heating rate  $T_x$  and  $T_k$  can be compared. If they are separated by several order of magnitude, the initial independence treatment is valid since both Hamiltonian act on a different time scale.

For the case of a three-dimensional trap, we introduce an average heating rate for the trap constant :

$$\Gamma^k = \frac{\Gamma_x^k + \Gamma_y^k + \Gamma_z^k}{3} \quad (3.31)$$

and an average heating term for the trap position :

$$\dot{Q} = \frac{\dot{Q}_x + \dot{Q}_y + \dot{Q}_z}{3} \quad (3.32)$$

A Fokker-Planck equation for the energy distribution in the three-dimensional trap can be

derived[106], and give the evolution of the total energy  $E$  under sufficient ergodicity as :

$$\dot{E} = \Gamma^k E + \dot{Q}N \quad (3.33)$$

where  $N$  is the total number of particles. With this formulation, the competition between the two different source of heating is clear and both terms can be compared using the initial energy distribution. In the following we treat each direction separately.

### 3.1.4.2 Experimental sources of noise

The QHO trap of Eq. 3.7 depends on experimental parameters related to the laser properties (intensity, pointing, polarization) as well as the surface orientation whose evolution can be treated with the formalism introduced in the previous section. Below, we study the effect of noise on each of these parameters independently.

#### Laser intensity fluctuations

We consider here absolute intensity fluctuations  $\delta I(t)$ . The instantaneous intensity  $I_i(t) = I_0 + \delta I(t)$  affects the spring constant (3.15). To match the formalism introduced in the previous section, we have :

$$\epsilon_k = \delta I / I_0 \quad (3.34)$$

We introduce the one sided power spectrum of the fractional intensity noise :

$$S_k = \frac{2}{\pi} \int_0^\infty \cos(\omega\tau) \langle \epsilon_k(t) \epsilon_k(t + \tau) \rangle d\tau$$

In the laser metrology community, this notation corresponds to the usual definition of the Relative Intensity Noise (RIN) :  $RIN = \frac{\delta I}{I_0}$ . With this definition, the one-sided power density  $S_I$  is the Fourier transform of the auto-correlation function of the normalized power fluctuations (Wiener-Khintchine theorem).

Using the RIN of our dipole trap laser (Fig. 1.15), we obtain the one-sided power spectrum. Injecting this result in Eq. 3.15, we obtain the heating rate generated by this instability. The energy e-folding time (defined in Eq. 3.22) is plotted in Fig. 3.8. As shown in Eq.3.22, the heating rate is only sensitive to the double of the trap frequency which lies in the range [0; 300] kHz (see Fig. 3.4). We conclude that the laser intensity noise effect can be neglected during the rotation transport. A more general conclusion can be drawn given the time scale presented that are above  $10^5$  s for any frequency below 30 kHz : our dipole trap lifetime is not limited by laser intensity noise.

#### Laser polarization fluctuations

With the full dipole potential derived in 3.1.2, we simulate the effect of slight variation of the incident field polarization on the QHO parameters. Starting with a fully TE polarized incident field, we introduce a perturbation  $\epsilon_P$  as :

$$\left| A_{TM}^+ \right|^2 = \epsilon_P \quad (3.35)$$

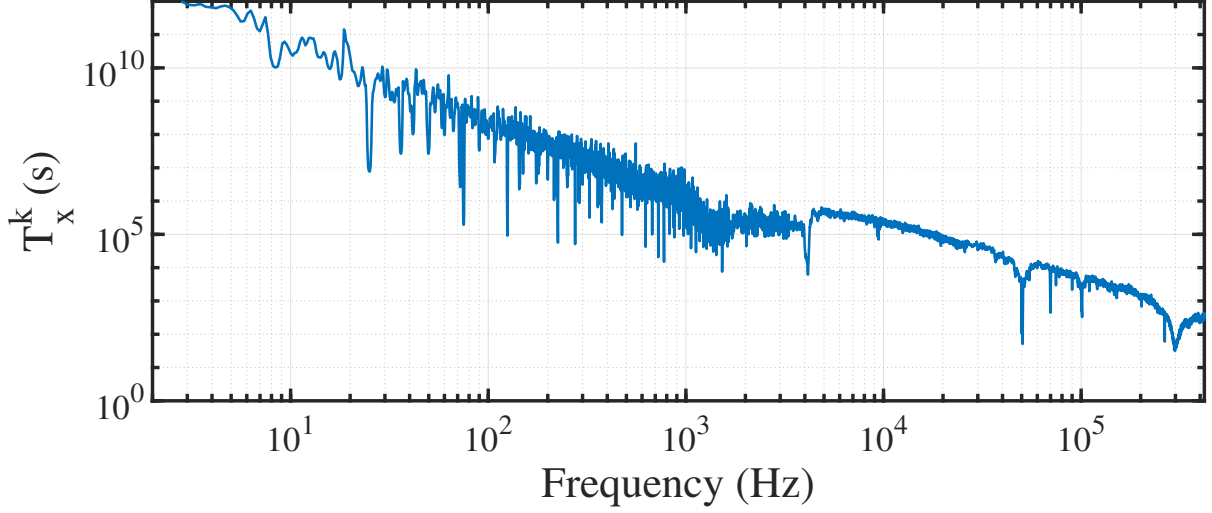


Figure 3.8: Expected heating time scale due to laser intensity noise plotted in log-log. The energy e-folding time is decreasing with the trapping frequency. Even in the worst case of stopping the final trap configuration on the peak at 50 kHz (corresponding to half the lock bandwidth), we would still have a lifetime of 50 s, which is long enough to transfer to the near-field trap.

For a TE (resp TM) polarization, the constant phase in the cosine function of Eq. 3.6,  $\phi_{TE}$  (resp  $\phi_{TM}$ ), gives the trap center position in the longitudinal direction. As we see in Fig. 3.9, these terms are close for normal incidence but strongly differ for higher angles. A mix between TE and TM polarization will thus shift the trap center in the longitudinal direction. It is less intuitive for the trapping frequency but numerical simulations also indicate a dependency on the polarization depending on the incidence angle. Physically, this can be understood by the dependence of the penetrating depth for the TM polarized case, which is more pronounced for higher incidence angles. In the transverse direction, as the Rayleigh range is large, the incident polarization will have very little effect. By numerically fitting the exact potential with three independent 1D-QHO, we extract the fluctuation on the trap pulsation as :

$$\epsilon_P^k = \left| 1 - \left( \frac{\nu_z(\epsilon_P)}{\nu_z(TE)} \right)^2 \right| \quad (3.36)$$

where  $\nu(\epsilon_P)$  is the fitted 1D-QHO trap frequency for an incident polarization with a component  $|A_{TM}^+|^2 = \epsilon_P$  and  $\nu(TE)$  the one for a fully TE incident polarization. Fluctuations on the trap center  $z_0$  are obtained similarly as

$$\epsilon_P^z = |z_0(\epsilon_P) - z_0(TE)| \quad (3.37)$$

These variations are compared in amplitude in Fig. 3.10 with the data that will later be detailed in section 3.1.5.1. Data for fluctuations on the trap center position are not presented here as there are several order of magnitude below the one induced by angle variations.

We observe in Fig. 3.10 that the polarization fluctuations of a fiber system ( $PER \approx 20\text{dB} \Leftrightarrow |A_{TM}^+|^2 = 10^{-2}$ ) are critical and will dominate over angle fluctuations. Therefore, the polarization need to be filtered.

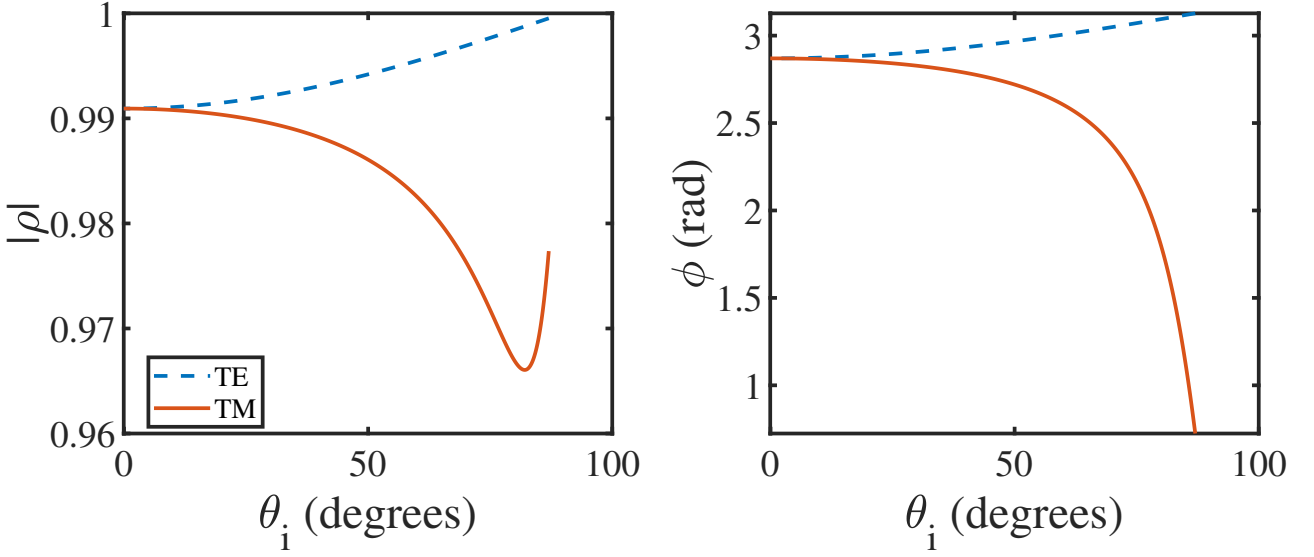


Figure 3.9: Evolution of the amplitude and phase of the generalized Fresnel coefficients.  $\phi_{TE}$  is fairly constant with the incidence angle because the electric field, oscillating parallel to the surface will always be reflected the same way. The strong dependence of  $\phi_{TM}$  can be explained by the evolution of the penetrating length of the electric field with a component perpendicular to the surface.

Typical PBS from Thorlabs are indicated to have an extinction ratio<sup>4</sup> of  $3 \times 10^4$  and Glan-Thompson polarizers of  $10^5$ . Assuming a similar spectral distribution of the fluctuations of polarization and angle variation, filtering with a Glan-Thompson polarizer will be enough to neglect the effect of polarization fluctuations compared to angle fluctuations.

### Absolute position of the chip

In the transverse direction, displacement of the chip will not affect the trap. However, fluctuations of the position of the chip along the fringes direction will lead to fluctuations in the trap center position. Noting  $\delta_d$  the fluctuations of the surface position along the fringe direction, we have :

$$\epsilon_x = \delta_d \quad (3.38)$$

We measured the rotation arm stability using a 4-quadrant photo-detector. This detector has a bandwidth of 250 kHz with a measured stability<sup>5</sup> of  $\sigma = 0.21 \mu\text{m}$  on the optical table. The measured stability on the rotation arm presents fluctuations similar to the reference configuration which are both certainly limited by electronic detection noise. Using this over-estimation of the stability, we computed a lifetime above 1 s for trapping frequencies up to 15 kHz.

<sup>4</sup>The Extinction Ratio (ER) is defined as  $ER = T_{max}/T_{min}$  where  $T_{max}$  is the maximum transmission when the polarizer's axis are aligned with the incident field proper axis and  $T_{min}$  is the minimum transmission. These values are given in intensity and the output polarized beam will have a maximum residual TM polarized component of  $\epsilon_P = \frac{1}{1+ER} \approx 1/ER$

<sup>5</sup>We define a standard deviation based on the acquisition of the detector signal over a few milliseconds for a stable configuration.

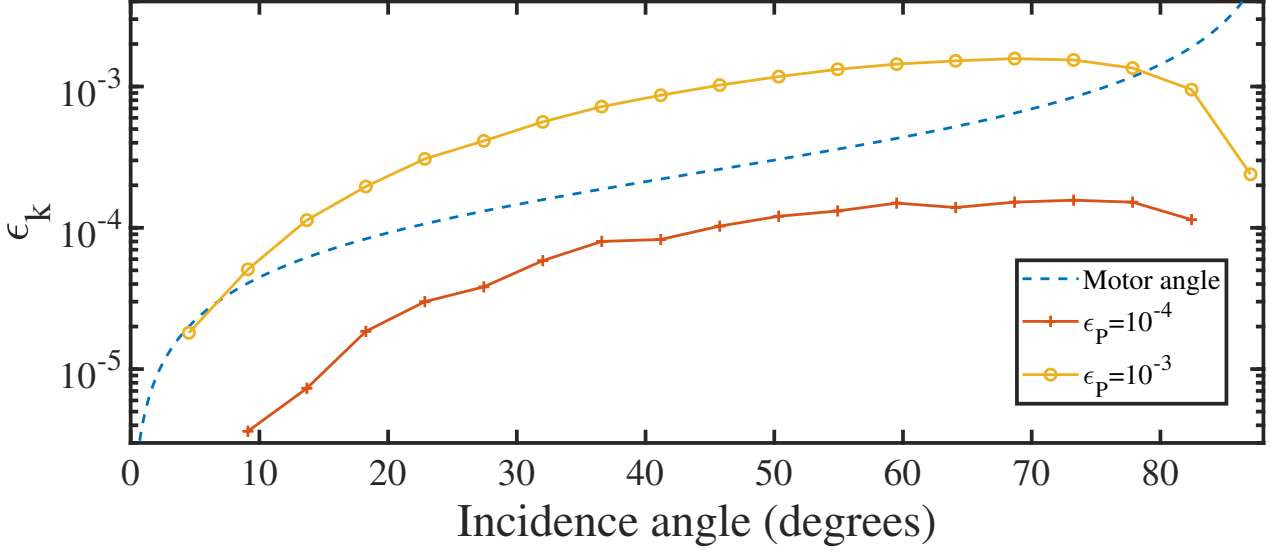


Figure 3.10: Comparison between fluctuations on the trap constant for different experimental sources of noise, depending on the incidence angle  $\theta_i$ . Dashed line : Standard deviation of the reconstructed  $\epsilon_z^k$  for data presented in 3.1.5.1, representative of typical fluctuations induced by noise on the reflective surface angular position during the rotation transport. Plain lines: difference  $\epsilon_P^k$  introduced in Eq. 3.1.4.2 for an incident electric field with a TM component of amplitude  $|A_{TM}^+|^2 = 10^{-4}$  (red crosses),  $|A_{TM}^+|^2 = 10^{-3}$  (yellow circles).

The chip stability can also be inferred from the sub-wavelength measurement presented in the previous chapter. In these measurement, the reflecting surface was out of the vacuum and we measured shot to shot stability over 400 ms giving  $\sigma = 6$  nm and a maximal shift of 15 nm. Using this measurement to re-normalize the four-quadrant ones give a lifetime over 1 s up to 120 kHz. With our current scheme, we are trapping a BEC in an optical lattice with longitudinal frequency of 128 kHz and manipulating the cloud for at least 800 ms with no specific sign of heating.

### Beam pointing stability

Beam pointing is independent of the surface. It can be studied either during the rotation transport or at rest and has two distinct effects. It first change the incidence angle leading both to fluctuations in the spring constant, and in the trap center position. In our present dipole trap configuration, we measure in-situ shot to shot fluctuations of the trap center around  $1 \mu\text{m}$  as measured with atoms trapped in DT1 (see section 1.1 for experimental setup). DT1 was aligned with the optical axis of a 150 mm focal lens. If we attribute the position fluctuation at the focus to angle fluctuations of the beam, we get a upper bound on the beam pointing stability of  $7 \mu\text{rad}$ . This is negligible compared to the values typically measured for motor angle instabilities of 0.34 mrad shown in Fig. 3.13. We therefore expect that beam pointing will not affect the spring constant during the rotation transport.

The second effect is a displacement of the beam in the transverse direction, for which the displacement of the trap center is directly proportional to a displacement of the beam. Being independent, the two directions can be treated separately. With  $\delta_x$  the beam displacement along

$x$ , we have:

$$\epsilon_x = \delta_x \quad (3.39)$$

The PSD of the beam pointing fluctuations are measured with the 4-quadrant photo-detector fixed on the optical table. The associated heating time computed using Eq. 3.27 is plotted in Fig. 3.11. Both vertical and horizontal directions are analogous. The heating time scale is above the minute so we can neglect the effect of beam pointing fluctuations in the transverse direction.

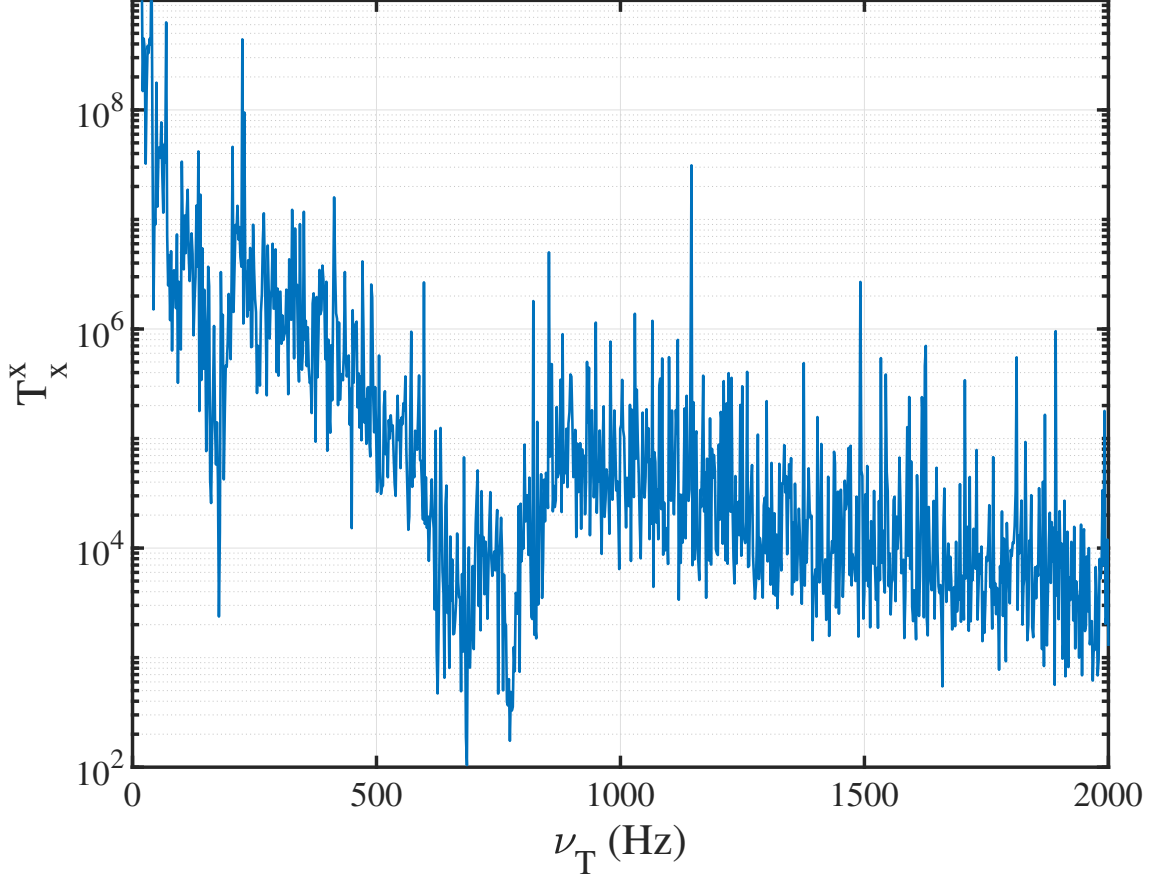


Figure 3.11: Heating time as a function of the trapping frequency induced by fluctuations in the beam transverse position. Frequencies of the x-axis are typical values obtained during the transport scheme. We took a worst case scenario of  $\langle E_x(t=0) \rangle / N = 0.33 \mu\text{K}$ .

### 3.1.4.3 Angle variation

We detail here the evolution of the QHO during the rotation of the chip. The angle evolution can be separated in two part : the desired trajectory  $\bar{\theta}(t)$  and residual fluctuations  $\delta\theta(t)$ . Assuming a constant rotation speed  $\Omega_m$ , the angular evolution starting from  $\theta_0$  at  $t_0$  is :

$$\theta(t) = \bar{\theta}(t) + \delta\theta(t) = \theta_0 + \Omega_m (t - t_0) + \delta\theta(t) \quad (3.40)$$

Non adiabaticity induced by  $\bar{\theta}(t)$  has been studied in 3.1.4.1. We focus now on the effect of the residual angular fluctuations. For a perfectly stable incident beam, slight fluctuations of the motor angular position impact the incidence angle of the beam on the surface. We write the

angle of the surface as  $\bar{\theta} + \delta\theta$  and obtain the form of 3.23 with

$$\epsilon_x = \delta\theta d_0(\bar{\theta}) \tan(\bar{\theta}). \quad (3.41)$$

where  $d_0(\bar{\theta})$  is the trap center position without fluctuations defined Eq. 3.8.

This, additionally leads, to fluctuations in the spring constant of the trap as :

$$\epsilon_k = -2\delta\theta \tan(\bar{\theta}) \quad (3.42)$$

The fluctuation of the chip ( $\delta\theta$ ) were obtained by measuring the beam pointing stability fluctuation of a reflected beam using either power fluctuations at the edge of a photo-diode (method 1) or a 4-quadrant photo-diode (method 2). We give below the main formula giving the angle fluctuations for each method. Detailed derivation is given in appendix (E).

- Method 1 : Photo-diode edge measurement

We use here a single photo-diode (PD), illuminated by a Gaussian beam centered on the edge of the detector. Any fluctuations in the beam position is converted by the detector as power variations. Obviously the measurement is affected by the intrinsic laser power instability. It is valid only if the laser power instability can be neglected. A schematic of the experimental setup is given in Fig. 3.12 a).

The angular fluctuations are given by

$$\delta\theta(t) = \frac{V_{PD}(t) - V(\bar{\theta}(t))}{\frac{dV}{d\theta}(\bar{\theta}(t))} \quad (3.43)$$

where  $V_{PD}(t)$  is the measured photo-diode signal and the derivation is given by (see section E)

$$\frac{dV}{d\theta}(\theta) = \alpha_{PD} \frac{\sqrt{2}}{w_0} \frac{2}{\cos^2(2(\theta - \theta_0))} \frac{2D}{\sqrt{\pi}} \left( e^{-\frac{2}{w_0^2}(p_x + D \tan(2(\theta - \theta_0)))^2} - e^{-\frac{2}{w_0^2}(D \tan(2(\theta - \theta_0)))^2} \right)$$

With this method, the frequency range that we have for  $S_x$  is limited on the lower bound by the total acquisition time of the signal. We acquire the signal with a RedPitaya with 14 effective memory buffer. The highest decimation factor give a total buffer length of 8.590 s, corresponding to a lowest frequency of 116.4 mHz. The highest frequency is limited by the detector sampling rate of 12 MHz.

The detection of angle fluctuation is mainly limited by the noise coming from the detector. By accounting for the detector expected response function, we need to carefully look at edges effect and noises. Close to each edges,  $\frac{dV}{d\theta}$  tends to zero and the computation of  $\delta\theta$  diverge. The photo-diode typically present an offset of 12 mV and has noise levels (computed by integrating the NEP over the whole bandwidth) close to 100  $\mu$ V. The RedPitaya acquiring  $\pm 1$ V on 14 bits yield a digitization noise of 0.12 mV. We evaluate experimentally the resulting noise during a photo-diode scan. As the beam waist is multiple time smaller than the pixel size, we extract of the flat hat part the noise from

the acquisition system (including the Red-Pitaya digitization, detector noise, and laser power fluctuations). Usual data gives a standard-deviation around  $\sigma_{noise} = 0.3$  mV.

Angle fluctuations due to the motor should not depend on the position on the detector. We can then define  $\delta\theta_{mot}$  as an amplitude of the signal we measure and a Signal to Noise Ratio (SNR) given by :  $SNR = \delta\theta_{mot}/\delta\theta_{noise}$  . This give a criteria on usable data, with  $SNR > 1$ . In practice, edge effect are also important and we restrict this criteria to  $SNR > 25$ .

- Method 2 : 4-Quadrant Photo-detector

Here, we use a 4-quadrant photo-detector(Koheron PD4Q) that measure the beam position. The face of the detector is represented on the insert of Fig. 3.12 b). It is composed of four photo-diodes each producing a current  $I_\alpha$  ,  $\alpha = \{A; B; C; D\}$  when receiving light. Three outputs are generated, completely giving the beam position in each direction and the total integrated intensity. The position in each of the direction is given with  $V_x = (I_A + I_D) - (I_B + I_C)$  and  $V_y = (I_A + I_B) - (I_C + I_D)$ . The constructor precise a beam position resolution of 20 nm in a 10 kHz bandwidth for a beam waist  $w_0 = 2$  mm and optical power of 30  $\mu$ W. Even over the whole detector bandwidth this beam position resolution is several order of magnitudes smaller than the measured fluctuations, so we can safely neglect it.

In the following, we neglect the projection effect due to having a linear detector with a circular beam motion. Indeed the resulting tilt of the beam compared to the plane detector surface would be  $\alpha = 51.2$  mrad. Projecting a Gaussian beam on a planar surface has the effect of contracting one direction by a factor  $\cos(\alpha)$ . This correspond to a relative error of the waist of  $3 * 10^{-4}$  for one direction with respect to the other.

We consider a movement along  $x$  and we drop the index for this direction. When the beam is fully on the detector, there is a bijection between the output voltage  $V(t)$  and the position of the center of the beam  $x(t)$ . Thus we work directly with the position as our signal (converting intrinsic noises from the detector and acquisition stage to negligible position noise) and following the formalism presented in method 1, we have :

$$x_{sig}(t) = x_{sig}(\bar{\theta}(t) + \delta\theta(t)) = x(\bar{\theta}(t)) + \frac{dx}{d\theta}(\bar{\theta})\delta\theta(t) \quad (3.44)$$

with  $x$  the beam position with no fluctuations defined in equation E.3 and we have :

$$\frac{dx}{d\theta} = D \frac{2}{\cos^2(2(\theta - \theta_0))} \quad (3.45)$$

This yields the following formula for the angle fluctuations :

$$\delta\theta(t) = \frac{x_{sig}(t) - x(\bar{\theta}(t))}{\frac{dx}{d\theta}(\bar{\theta}(t))} \quad (3.46)$$

Imperfect 1D sweep is corrected by measuring  $V_y$  and adjusting  $V_x$  if we detect a slope on the other direction.

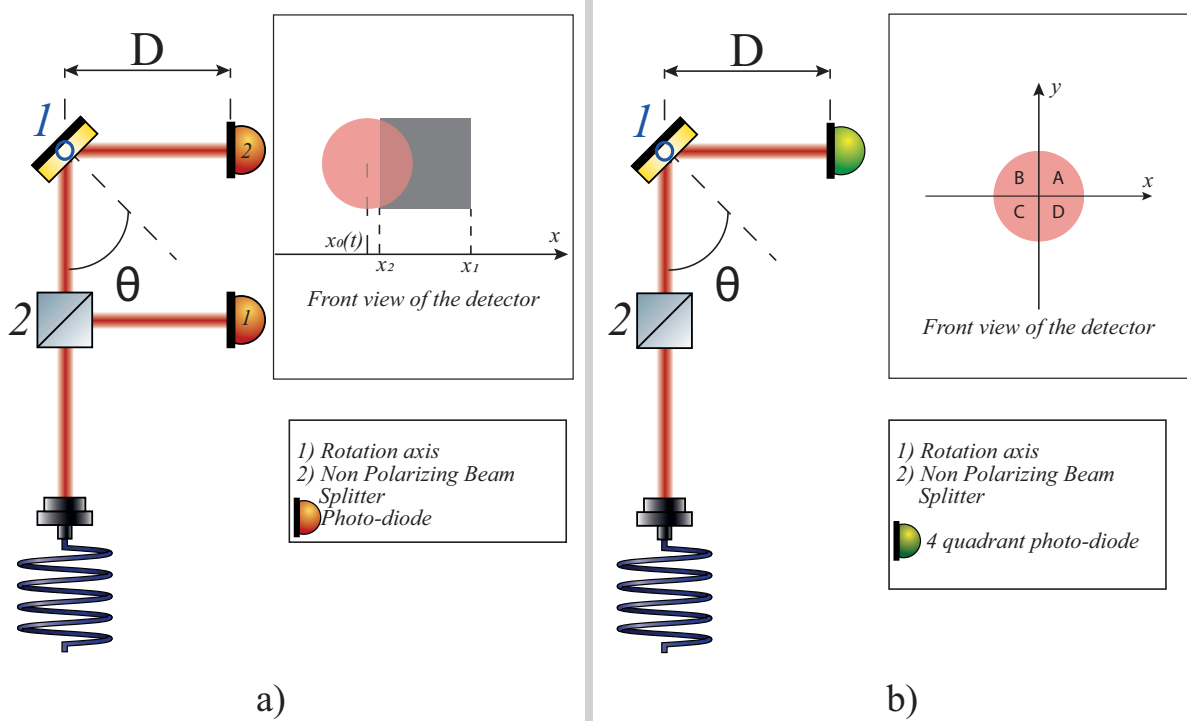


Figure 3.12: Experimental setup for detecting the fluctuations in the angular positioning of the chip by measuring the beam position using the edge of a photo-diode ( Method 1: a ) or with a 4-quadrant photo-diode ( Method 2: b ).

### 3.1.5 Study of experimental solutions

The design and the implementation of the atom-chip require to develop a UHV-compatible chip [38] but also to be able to replace the chip in the science chamber without having to bake and pump the whole chamber. Therefore, we planned on mechanically moving the atom chip in the vacuum chamber with an extendable arm. As we found limited solutions of UHV-compatible motors, we decided to use a rotating transfer-arm with the motor outside the vacuum. The arm will extend from two areas under-vacuum with differential pressure in between. One side will be under low vacuum ( $P \approx 10^{-8}$  mbar) with a fast-lock window to change the chip. A valve allows to keep the low pressure chamber under vacuum while changing the chip. The arm will extend up to a physical block-stop that guarantees a precise end positioning of the chip.

The transport scheme presented in section 3.1.1 require a span of rotation angle of at least  $\pi/2$ , with enough torque to drive the transfer-arm axis loaded with the chip. The amount of acceptable PSD of the rotation angle is constrained by the heating rate that has been evaluated in section 3.1.4.3. Using the experimental setups presented in section 3.1.4.3, we will now infer the expected heating during the rotation transport of an atomic cloud using two different motors.

#### 3.1.5.1 New Focus stepper motor

As a first solution, we have characterized a piezo linear stepper actuator (Newfocus model : 8321). This stepper motor can be driven at a repetition rate up to 2 kHz and has a step size of 0.78 mrad. In the following, we discuss : the heating induced by imperfect surface rotation,

vibrations induced by the motor and the operational easiness.

### Noise induced heating

Data taken using the Photo-diode edge measurement experimental setup described in 3.1.4.3,

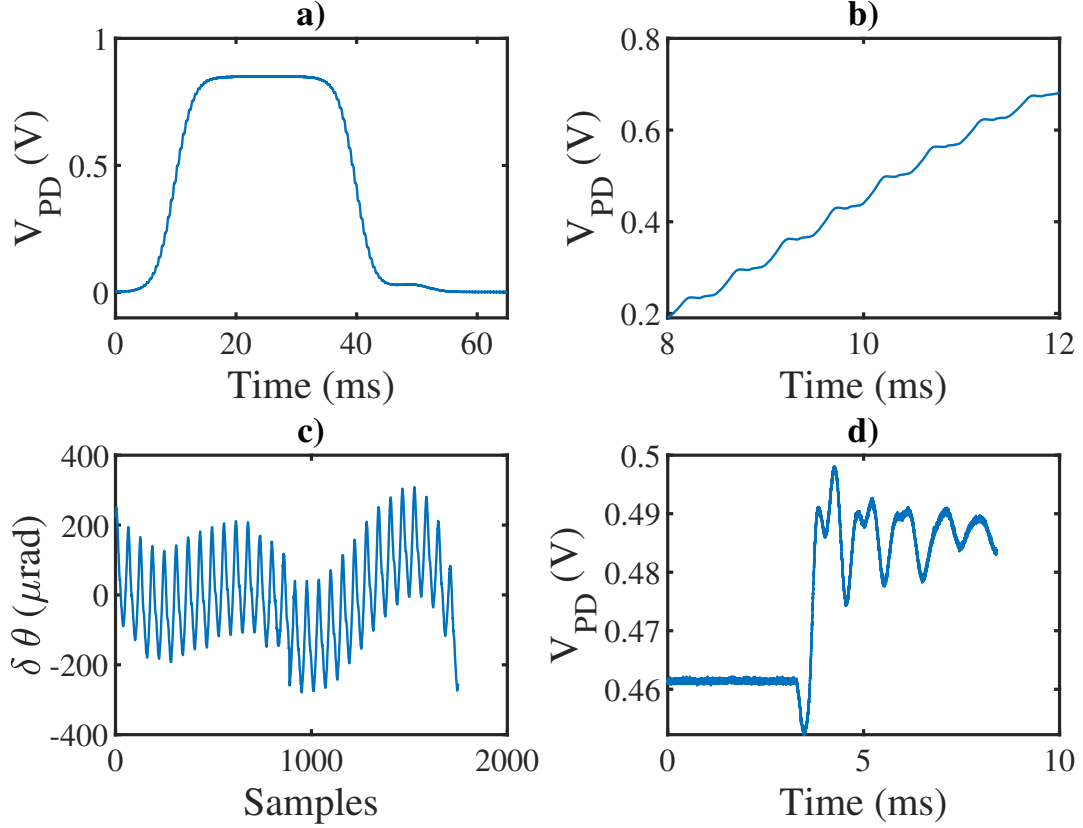


Figure 3.13: Evolution of the response of a photo-diode swept by a laser beam reflected by a mirror directly mounted on the New Focus motor. a) Photo-diode response while a laser beam is swept linearly across the detector according to Method 1 (described Fig. 3.12). b) Zoom on the left slope with the same data set. We resolve each steps and can see some overshoot and oscillating pattern between each click. c) Reconstructed angle variation computed using Eq. 3.43. d) Stopping behavior : measurements after doing only one step. The oscillation pattern is different, presenting an initial small rotation in the reverse direction then a slight overshoot with damped oscillations. The oscillation structure is more complex and present different frequency components. Damping rate in of the order of a few ms.

are shown in Fig. 3.13. The detector pixel size is 3.6 mm. For these data, a gold mirror held in a fixed mount<sup>6</sup> is directly attached to the motor. In Fig.3.13 a), we can see the entire PD being swept, with a top-hat part in the middle where all the light is integrated by the detector. We can also see on the right part of the signal, near 50 ms, spurious effects possibly due to a reflection on the metallic casing of the silicon pixel. We resolve the oscillating motion during the sweep in b) at the expected 2 kHz rate. We see in c) that typical oscillations amplitude is

<sup>6</sup>As we will see in 3.1.5.2, the mounting of the mirror on the motor had a noticeable impact on the surface movement. The case we treat here, with a fixed mount give the most faithful response of the motor movement itself.

on the order of 0.2 mrad. Extracting usable data using the sensitivity criterion ( $SNR > 25$ ) established when presenting the measurement method leads to a spurious discontinuity in the signal that would affect the spectrum so we further trim the edges to have a smooth transitions between the sweep of the left and right side of the detector. We reconstruct correctly the angular fluctuations since the amplitude is constant in time and does not depend on the position on the PD. However, the mean value of the oscillation at 2 kHz oscillate on a longer time scale indicating an error on one of the fit parameters of the theoretical response of the PD or residual edges effects. The stopping behavior presented in d) presents a different pattern. It is composed of multiple oscillation frequencies with a low damping rate. Reducing the motor repetition rate would then add spectral components that would possibly be a further source of heating.

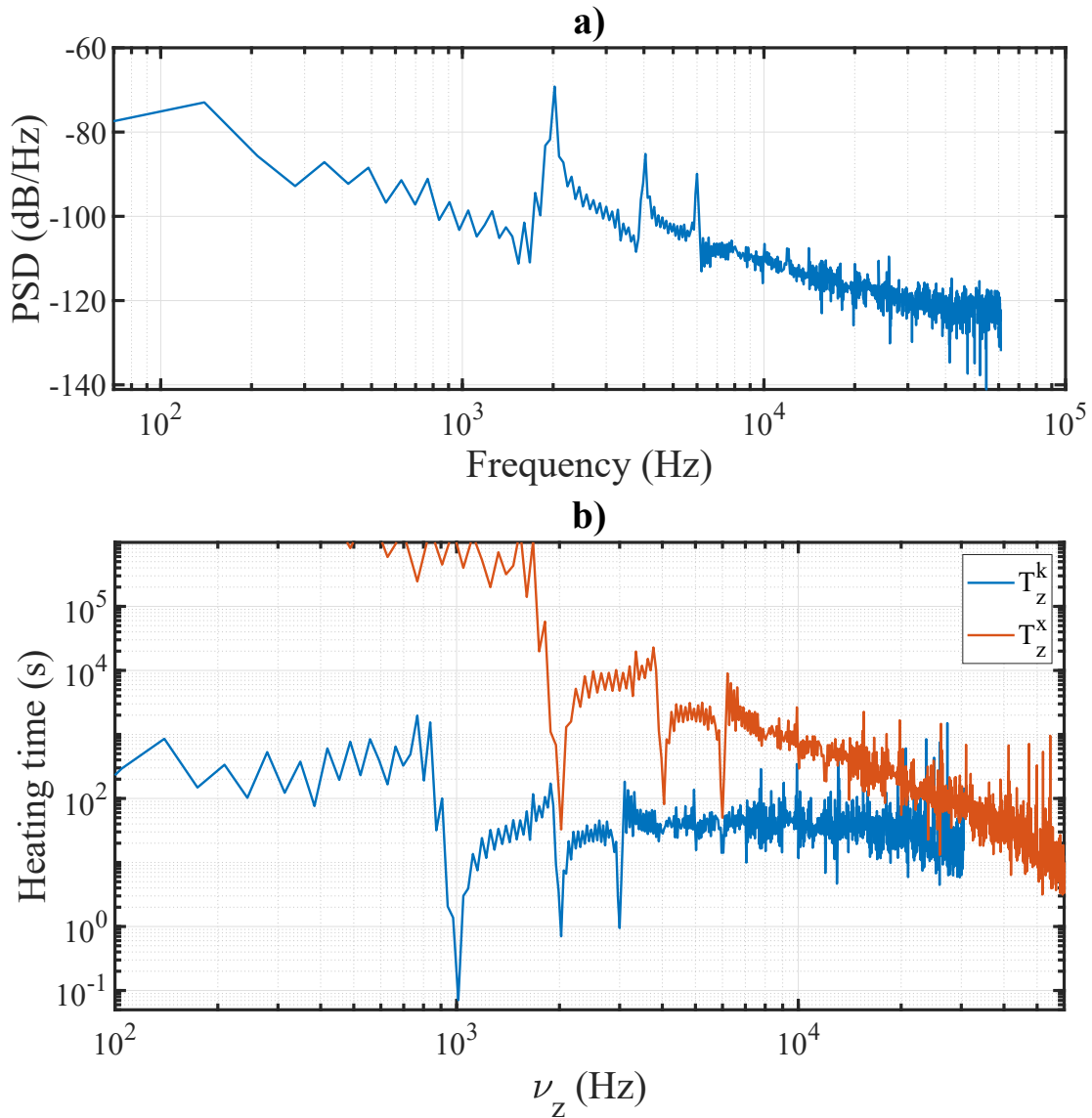


Figure 3.14: a) Power Spectral Density of the angle fluctuations reconstructed following Eq. 3.43. We see peaks at the motor drive frequency of 2 kHz and further harmonics. b) Associated heating time as a function of the longitudinal trapping frequency. The motor driving frequency at 2 kHz will cause heating on the time scale of 70 ms. Parameters used to compute these time are given in the text.

Using Eq. 3.43, the associated power spectral density of the oscillations presented in Fig. 3.13 c) is plotted as a function of the frequency in Fig. 3.14 a). Eq. 3.9 shows that only the  $x$  and  $z$  direction depend on the angle. Using Eq. 3.41 and 3.42, we extract the heating times  $T_z^k$  and  $T_z^x$  which are plotted in Fig. 3.14 b) as a function of the trapping frequency  $\nu_z$ . We see that because of the short time of sensitivity, the lowest usable frequency in the Fourier domain is 350 Hz thus the low trapping frequency along  $x$  are not well resolved and we focus on the longitudinal direction. We took the worst case scenario, at the maximum incidence angle and 3.42) and  $\langle E_0 \rangle / N = 70$  nK, corresponding to the total energy of a 1D-QHO at  $\nu = 2.5$  kHz with  $N = 10^5$  particles in the ground state without interaction. For higher frequency, the ground-state energy increase and the energy per particles computed by solving the 3D-GPE is around  $0.70 \mu\text{K}$ . Even in these conditions, heating due to fluctuation of the trap center position can be neglected as  $T_z^x > 3$  s. Heating due to trap frequency noise could be problematic for trapping frequency near 1, 2, and 3 kHz.

Thus, the trapping scheme should avoid crossing these frequencies, which impose for simplicity that the loading starts at  $\nu_z > 4$  kHz. To refine the characterization, we define a Figure of Merit (FoM) based on the integration of the heating rate on the whole rotation. We introduced in 3.17 an averaging time  $T$  over which the mean frequency of the QHO needs to be constant. Thus, starting at one end of the rotation<sup>7</sup>, we consider blocks of time  $\tau = 10 T_{\text{spectrum}}$  ( $T_{\text{spectrum}} = 1/2\nu_{\text{trap}}$ ) over which the trap frequency will be considered constant. Over these time blocks, we average the power spectral density to compute the heating rate given in Eq. 3.22 or 3.27. The figure of merit is then built by summing the heating rate multiplied by the corresponding time spent at this trap configuration :  $FoM = \sum \Gamma \tau$ . We consider that the rotation will not induce heating if  $FoM \ll 1$ . Using an adapted sequence using a constant rotation at 2 kHz but otherwise analogous to the one defined in part 3.1.3, the associated FoM is computed for both heating terms. The mean energy is taken as one third of the stationary ground state energy computed numerically by solving the 3D-GPE. We find  $FoM_z^k = 10^{-6}$  and  $FoM_z^x = 10^{-5}$ , both very small compared to unity. This particular sequence should therefore enable transport without significant heating. We however recall that we only treated here the longitudinal direction.

### Motor induced vibration

In addition to the residual vibration on the trap we studied above, the stepper motor was also the source of mechanical transmitted vibrations. The motor is rotating with a stick-and-slip movement which produces phonons. We have for example observed that the vibration of the motor were affecting the fiber injections leading to a variation on the output intensity.

On Fig. 3.15, the modulation is clearly visible on the top hat part of the photo-diode sweep where the beam position does not affect the response. As shown in Fig. 3.15, this sensitivity can be reduced by mechanically isolating the fiber injection. This isolation was possible on this test bench but it can hardly be realized on the final setup. This effect is quite complicated to quantify before installing on the main experiment. In the case of the envisioned sequence of Fig. 3.5, the frequency along  $y$  start close to 1 kHz. Vibration causing intensity fluctuations as we observed on the test bench would then lead to heating on this direction at the initial stage,

<sup>7</sup>We can decide to start on either side. Usually we would start to split the time sequence at the beginning. However, for transverse directions, the trap frequency start really low, meaning that this criteria would yield only one step. Starting the splitting at the end, where the trapping frequencies are higher is thus more relevant.

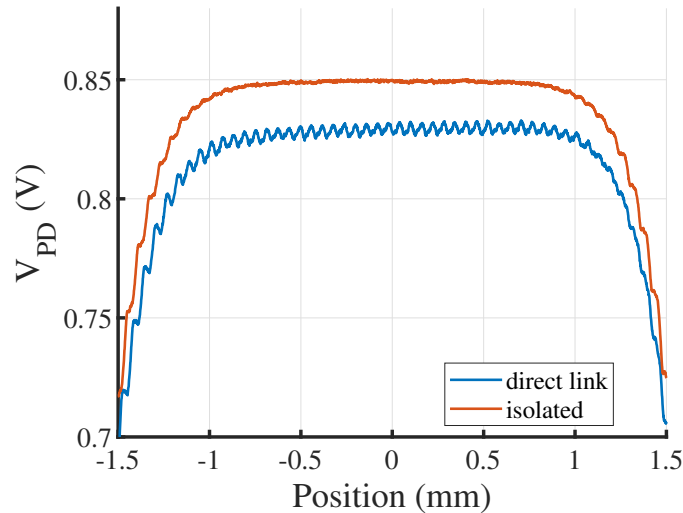


Figure 3.15: Top-Hat part of the photo-diode response during a linear sweep according to Method 1. On this part, the photo-diode is not able to resolve beam displacement and variation in the voltage produced are due to light intensity changes. The plot labeled "direct link" present a situation where the motor is held by a metallic piece, clamped to the same optical table where a laser is injected in a fiber, whose output is used for the measurement. The plot labeled "isolating" present data taken while the motor was held on a separate breadboard. The oscillations on this part are at the same 2 kHz frequency than the motor rotation.

putting one more constraint on the final sequence design.

### Motor general use

Practical considerations on the usage of the motor push to find another solution.

At the maximal rotation speed, imposed by the maximum 2 kHz repetition rate, the whole rotation take almost 1 s. If we reduce the repetition rate, we introduce additional angular oscillations ( Fig. 3.13 d ) and we increase the time to rotate. Both effects are detrimental for the FoM of the transport. This motor also suffer from hysteresis and step uncertainty repeatable only up to 30% precision. To achieve the desired positioning accuracy would require to set a closed loop operation.

#### 3.1.5.2 Tekceleo motor

Previous considerations for the New Focus stepper motor led us to find an alternative to drive the rotation of the chip for our transport scheme : a [Tekceleo WLG-75](#). It is a traveling wave ultrasonic motor (TWUM), based on a different architecture from the stepper-motor. The working principle of a TWUM [108, 109, 110] rely on the friction interaction between a fixed vibrating part (stator or vibrator) and a moving part (rotor) carrying the load. The stator is an annular-shaped plate made of an elastic material pressed on piezoelectric ceramics. An appropriate alternative pattern of polarization of the piezoelectric substrate generate two degenerate flexural vibration modes, spatially orthogonal, producing a flexural traveling wave in the elastic material. When the wave progress along the vibrator, point on each surfaces of the vibrator move elliptically, and the top surface moves in a direction opposed to the one of propagation of the traveling wave. By pressing the rotor on this surface, frictional forces will make it rotate. The movement of the rotor

is then driven by the propagation of the traveling wave, and is therefore continuous. This type of motors is of particular interest for our case because it is non-magnetic, present both a high dynamic (0.75 N.m at 150 rpm) and holding torque (1.5 N.m) and more importantly, it produces a continuous rotation. The motor speed can be adjusted between 5 rotations per minute (rpm) and 175 rpm, and a built-in servo-lock loop allows to make a rotation of a precise given angle. The close loop operation has been tested and allows to reach a precision of 0.273 mrad. This precision is good enough to avoid the cluster of adding another control method and the motor can be driven directly using Matlab, making the integration into Cicero quite straightforward.

To characterize the displacement of this motor, we use a 4-quadrant photo-diode and the data treatment described in section 3.1.4.3 (Method 2). The motor is characterized alone, with a fixed mirror mount directly attached to it. It rotates with a constant driving speed of 6 rpm. Computing the residual fluctuation  $\delta\theta$  presented Fig. 3.16 a) gives multiple components. First, detection noise at 2 MHz has an std  $\sigma = 1.5 \mu\text{rad}$ , which set the minimal detectable fluctuation. Then, there is a triangular oscillations of peak-peak amplitude  $A = 20 \mu\text{rad}$  and period close to  $\tau = 3.6 \text{ ms}$ . Finally there seems to be a sinusoidal oscillation of a few  $\mu\text{rad}$  of amplitude and a frequency close to 1.7 kHz. The overall fluctuations are at least one order of magnitude below the stepper motor.

The PSD of the angular fluctuations plotted in Fig. 3.16 b) is several order of magnitudes below the one of the stepper motor. We can quickly evaluate how to increase the total measuring time to have access to lower values of the spectrum, currently limited to  $\nu_{min} = 1.5 \text{ kHz}$ . By consideration of simple scaling factors, lower frequencies could be obtained by reducing the distance between the detector and the mirror from  $D = 90 \text{ mm}$  to  $D = 22 \text{ mm}$ , giving roughly a factor 4 of the lowest frequency resolved. Also, the waist choice is not optimal, and we have a usable signal only over 2 mm out of the 8 available, giving again a potential factor 4. Implementing data analysis of the beam going out of the detector on each sides (described by method 1) could increase the range of angle we can analyze and give further a factor 4 compared to the current situation (adding-up with the beam size increase and the result multiplying with the detector being closer). With these optimizations, we expect to have meaningful points near 100 Hz, making this method a good candidate to further study the noise in the loose transverse directions.

Analysis of the stopping behavior after a drive at constant speed, presented in Fig. 3.17 shows pronounced damped oscillations. The associated PSD plotted in b) presents the same three main spectral components as seen on the dynamical behavior, with a higher spectral resolution. The first at  $f \approx 300 \text{ Hz}$  has a similar time scale than the triangular modulation mentioned above. The second peak is again at 1.667 kHz. Again, a sharp peak at 20 kHz is present, possibly due to electronic noise. These oscillations are damped with a attenuation factor fitted with  $\tau = 4.63 \pm 0.04 \text{ ms}$ . The impact of these oscillations is evaluated using Eq. 3.41 and 3.42 around  $\theta = 0.3 \text{ mrad}$ . We find heating time values above  $10^{10} \text{ s}$  which compared to the damping time let us conclude that the oscillations when the motor stops will not cause any heating. Given the small amplitude of the oscillations, we didn't try to further investigate their cause<sup>8</sup> or to reduce them.

---

<sup>8</sup>probably internal mechanical vibrations, maybe for instance one peak could be caused by the stator vibration

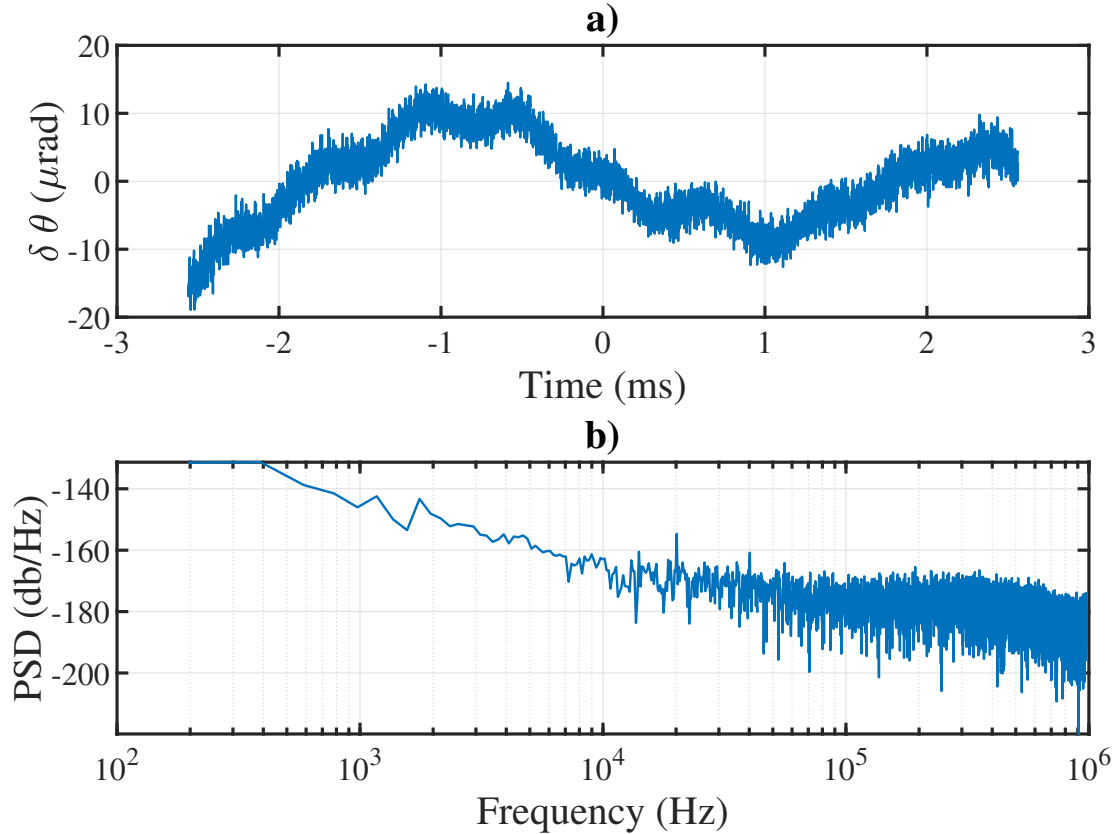


Figure 3.16: a) Deviation of the angle from a linear evolution. The Fourier transform gives the associated PSD in b).

We evaluate the error on the reconstructed angle depending on uncertainty of the experimental parameters such as the beam waist  $w_0 = 1.00(2)$  mm, PD to mirror distance  $D = 95(3)$  mm and the position conversion factor  $c = 0.51(1)$  V/m. We then compute an absolute error of  $160 \mu\text{rad}$  and a relative error of  $20 \mu\text{rad}$ . This error is small enough so we can safely neglect it and consider that the angle we computed is absolute and the considerations above still hold.

The actual dynamic of the motor in the end needs to be characterized while being mounted on the rotating arm since it will surely modify the rotation. Given the scaling arguments presented above, the 4-quadrant method should give access to both the high and low frequency components of the fluctuations to characterize the transverse and longitudinal directions. Given the result we got on the stepper motor and the reduction of the fluctuations by a factor close to 20, we infer that this motor will be able to transport the cloud without significant heating. Moreover, it will be easily integrated on the experiment since it can be controlled with combination of analog voltages.

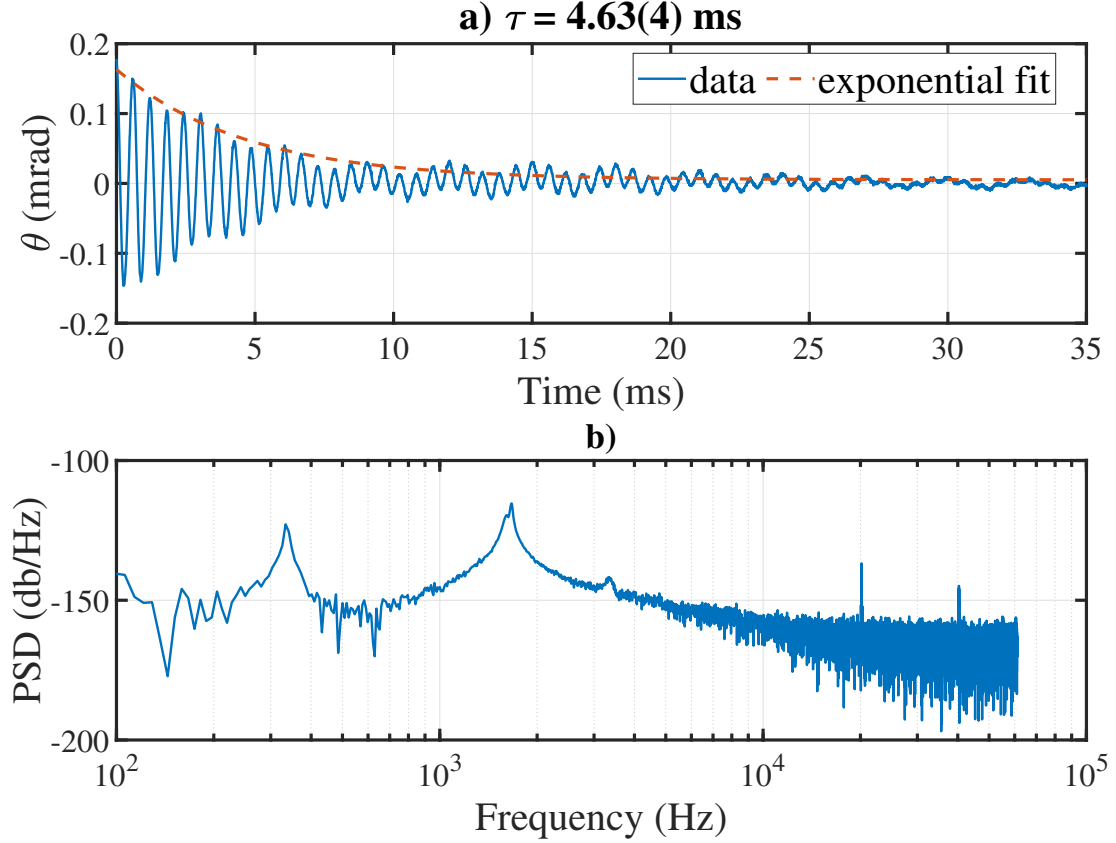


Figure 3.17: Angular evolution after a short driving time at constant speed and an abrupt stop when the motor reached the target angle. a) Damped oscillation of the angle, where we subtracted the mean value for clarity. The angular position has been directly reconstructing using the calibrated 4-quadrant b) Associated PSD.

## 3.2 Design and setup of an atom chip

Atom chip were originally designed to decrease the complexity of cold atoms apparatus, increase the compactness and reduce the electrical power required. In these experiments, usual magnetic coils used to confine the atoms and reach Bose-Einstein condensation are replaced by microscopic lithographic conductors on a chip. Such a lithographic 'chip trap' was first demonstrated in 1999 [111], and significantly simplified the experimental apparatus. Indeed, modest electric currents can produce large magnetic field gradients and curvatures in close proximity to a planar arrangement of wires. Different groups have implemented this configuration to produce BEC in a more compact and robust way [112, 113, 93]. Numerous studies using this type of trapping scheme have flourished notably tackling the issue of ultra-cold atoms transport. Recent experimental realization [42] and theoretical work consider short-cut to adiabaticity [65] or optimal control [114] to improve transport capabilities.

One long term goal of our project is to couple atoms and nano-photonics. It requires to handle both atom trapping capabilities and nano-photonic fabrication. To reduce the constraints to produce the chip and have decided to decouple the two issues by realizing an hybrid micro-chip design. This type of architecture has already been implemented in the group of A. Gauguet in Toulouse, France [94].

We use wires whose diameter is in the millimeter range instead of the regular  $\mu\text{m}$  range [115, 43, 92]. In section 3.2.1, the magnetic field generated by different configuration of wires has been numerically computed using Biot-Savart calculations. Then, we detail in section 3.2.2 the specification followed during the computer assisted design process (CAD). Finally, we elaborate in 3.2.3 on the fabrication process we adopted, putting the emphasis on the possibility of manufacturing such hybrid micro-chip with very simple facilities. We introduce the building-blocks of the atom chip in the schematics ?? for the reader comprehension.

### 3.2.1 Magnetic trap simulation

Numerical simulations allow to evaluate the current required to trap atoms in a Ioffe–Pritchard trap at a given position above the surface and the corresponding heating of the chip. The program has been developed to give a high versatility on the wire management (positioning and number of wires) and to simulate the whole rotation including both the optical and the magnetic potentials. For now, the optical study is done separately and we present here simulation of the magnetic trap including gravity.

For a cylindrical wire, the field outside the conductor is identical to the one of an infinitely thin wire centered on the cylinder axis [44]. The field generated by a wire section along the  $x$  direction, at a position  $(y_0; z_0)$ , in which the current  $I$  flows from  $x_1$  to  $x_2$  is given by :

$$\mathbf{B}(\mathbf{r}) = -\frac{\mu_0 I}{4\pi R^2} \left( \frac{x_2 - x}{\sqrt{(x_2 - x)^2 + R^2}} - \frac{x_1 - x}{\sqrt{(x_1 - x)^2 + R^2}} \right) ((z - z_0) \mathbf{u}_y - (y - y_0) \mathbf{u}_z) \quad (3.47)$$

with  $R = \sqrt{(x - x_0)^2 + (y - y_0)^2}$  the radial distance to the wire. With the expression above, we clearly see that the field can be easily computed in the basis of the wire. The numerical implementation of other potentials, such as gravity or the optical dipole potential derived in 3.1.2 require in general different basis. To implement these different potentials in a single simulation, we derive a general transformation matrix between any given basis and the proper basis of the wire. In this basis, the origin is at one end of the wire. The current run along a single axis  $\mathbf{x}$ . Let's consider a general wire running from  $(x_1, y_1, z_1)$  to  $(x_2, y_2, z_2)$  expressed in the laboratory coordinates. This transformation is composed of a linear translation followed by two rotations. We define an intermediate basis after the translation in which the coordinates are noted  $(x', y', z')$ , and coordinates in the final proper basis are noted  $(x'', y'', z'')$ . The first transformation is a linear translation giving an origin at the beginning of the wire :

$$\begin{pmatrix} x' \\ y' \\ z' \end{pmatrix} = \begin{pmatrix} x \\ y \\ z \end{pmatrix} - \begin{pmatrix} x_1 \\ y_1 \\ z_1 \end{pmatrix} \quad (3.48)$$

Then , we define two successive rotation matrix, the first one around  $\mathbf{x}$  with angle  $\theta_1$  and the second one around  $\mathbf{z}$  of angle  $\theta_2$  such as :

$$\begin{pmatrix} x'' \\ y'' \\ z'' \end{pmatrix} = \begin{pmatrix} \cos(\theta_2) & -\sin(\theta_2) & 0 \\ \sin(\theta_2) & \cos(\theta_2) & 0 \\ 0 & 0 & 1 \end{pmatrix} \begin{pmatrix} 1 & 0 & 0 \\ 0 & \cos(\theta_1) & -\sin(\theta_1) \\ 0 & \sin(\theta_1) & \cos(\theta_1) \end{pmatrix} \begin{pmatrix} x' \\ y' \\ z' \end{pmatrix} \quad (3.49)$$

In the following, we define the origin of angles as  $\theta_2 = 0$  if the wire has no initial components along  $\mathbf{x}$  and  $\theta_1 = 0$  if the wire has no initial components along  $\mathbf{y}$ .

Using this equation at the end of the wire, the system defining the two angles is:

$$\begin{aligned}
 \begin{pmatrix} x'_2 \\ 0 \\ 0 \end{pmatrix} &= \begin{pmatrix} \cos(\theta_2) & -\sin(\theta_2) & 0 \\ \sin(\theta_2) & \cos(\theta_2) & 0 \\ 0 & 0 & 1 \end{pmatrix} \begin{pmatrix} 1 & 0 & 0 \\ 0 & \cos(\theta_1) & -\sin(\theta_1) \\ 0 & \sin(\theta_1) & \cos(\theta_1) \end{pmatrix} \begin{pmatrix} x_2 - x_1 \\ y_2 - y_1 \\ z_2 - z_1 \end{pmatrix} \\
 \Leftrightarrow \begin{cases} x'_2 &= \cos(\theta_2)(x_2 - x_1) - \sin(\theta_2)[\cos(\theta_1)(y_2 - y_1) - \sin(\theta_1)(z_2 - z_1)] \\ 0 &= \sin(\theta_2)(x_2 - x_1) + \cos(\theta_2)[\cos(\theta_1)(y_2 - y_1) - \sin(\theta_1)(z_2 - z_1)] \\ 0 &= \sin(\theta_1)(y_2 - y_1) + \cos(\theta_1)(z_2 - z_1) \end{cases} \\
 \Rightarrow \begin{cases} x'_2 &= \cos(\theta_2)(x_2 - x_1) - \sin(\theta_2)[\cos(\theta_1)(y_2 - y_1) - \sin(\theta_1)(z_2 - z_1)] \\ \theta_2 &= \arctan\left(-\frac{\cos(\theta_1)(y_2 - y_1) - \sin(\theta_1)(z_2 - z_1)}{x_2 - x_1}\right) \\ \theta_1 &= \arctan\left(-\frac{z_2 - z_1}{y_2 - y_1}\right) \end{cases} \quad (3.50)
 \end{aligned}$$

To confirm that the transformation was done correctly, we can verify that the wire coordinates in the new basis are only along one axis and that the total length of the wire has not changed :

$$\begin{aligned}
 |x'_2| &= |\cos(\theta_2)(x_2 - x_1) - \sin(\theta_2)[\cos(\theta_1)(y_2 - y_1) - \sin(\theta_1)(z_2 - z_1)]| \\
 &= \sqrt{(x_2 - x_1)^2 + (y_2 - y_1)^2 + (z_2 - z_1)^2}
 \end{aligned}$$

The code take as inputs the distance from the trap center to the center of the wires along  $\mathbf{z}$ , a minimal value of the magnetic field at the trap bottom to limit Majorana losses, the number of particles, the incidence angle  $\theta$  and the current in the wires. It then finds the magnetic field bias required along each direction and compute different parameters such as the trap frequencies, trap center position, estimations of the two-body elastic collision rate, three-body inelastic collision rate, Majorana losses rate.

Results are presented for a set of wires defined in Fig. 3.18 a) in the chip basis for  $\theta = \pi/2$ , giving the gravity along  $+\mathbf{z}_c = -\mathbf{z}_l$ . This code has been tested by reproducing the result presented in [94]. Changing from a 'U' to an 'I' configuration is done by switching the sign difference of the current flowing in the outer wires defined in Fig. 3.18 a) in green. The central part of the 'Z' wire is symmetric along  $\mathbf{y}_c = \mathbf{y}_l$  and present a positive offset of 1.5 mm along  $\mathbf{x}_c = -\mathbf{x}_l$ . We present in Fig. 3.19 the evolution of the trap parameters and magnetic field bias required as a function of the current  $I_Z$  in the Z wire. Each curves correspond to linearly increasing values of the current in the 'U' wires, from 0 A (darkest curve) to 25 A (lightest curve). We show the case of a trap produced above the chip. The symmetric configuration giving a trap center below the chip can be obtain by inverting the direction of the constant magnetic field bias along  $\mathbf{x}_c$ . Trap center along the three direction are plotted in sub-figure a). A trap center  $z_0$  different from 1 mm indicate that the program didn't converge on the bounded bias fields and we plot only the case where the error is less than  $5 \mu\text{m}$ . The 'U' wires can be used to displace the trap center up to 0.5 mm along  $\mathbf{x}_c$  and 2 mm along  $\mathbf{y}_c$ . Reversing the current inverse the displacement direction.

In this configuration, we can reach trapping frequencies of (1 kHz ; 47 Hz ; 1 kHz) for a trap

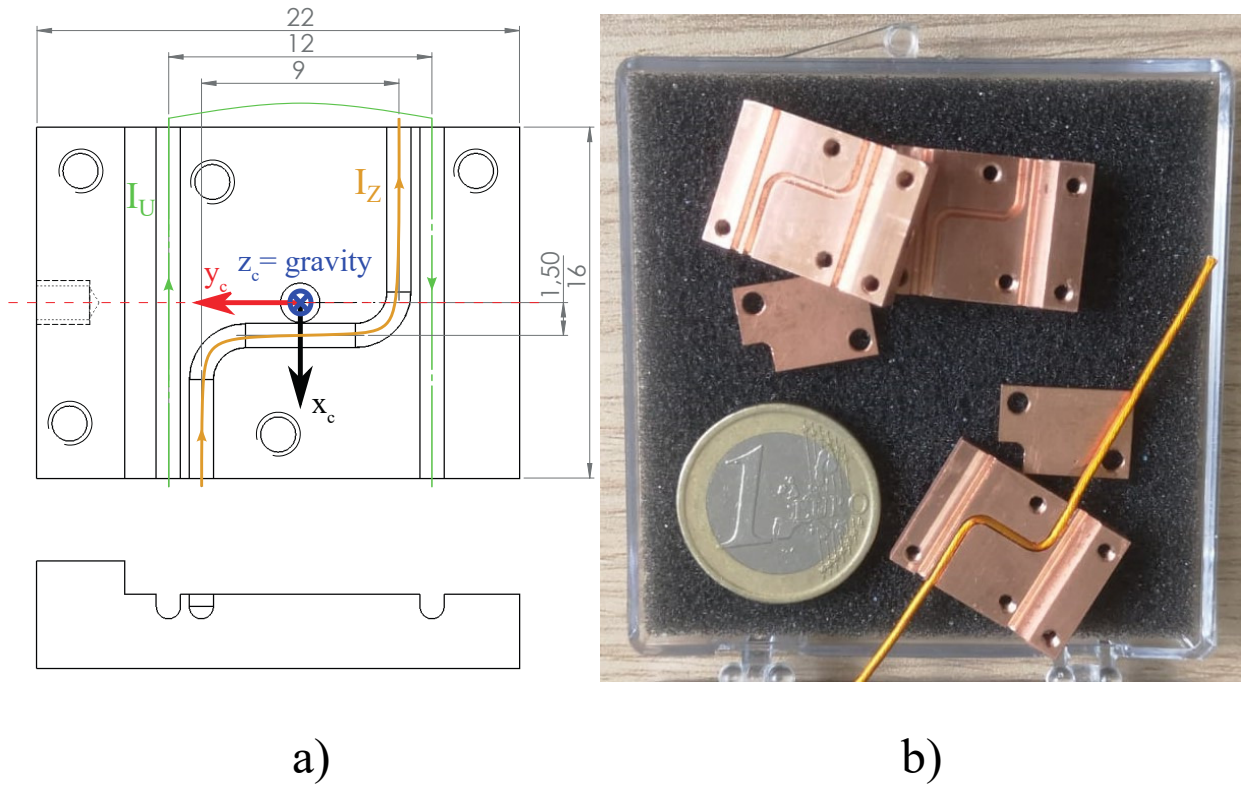


Figure 3.18: a) CAD Schematics of the chip substrate. Wire grooves forming a Z shape (orange) and two parallel I (in green). All the units are in mm. The dashed red curve gives the rotation axis. b) Fabricated chip (see section 3.2.3)

center  $500 \mu\text{m}$  above the top of the wire with 27 A in the Z wire, 0 A in the U and a constant magnetic bias field of 52 G.

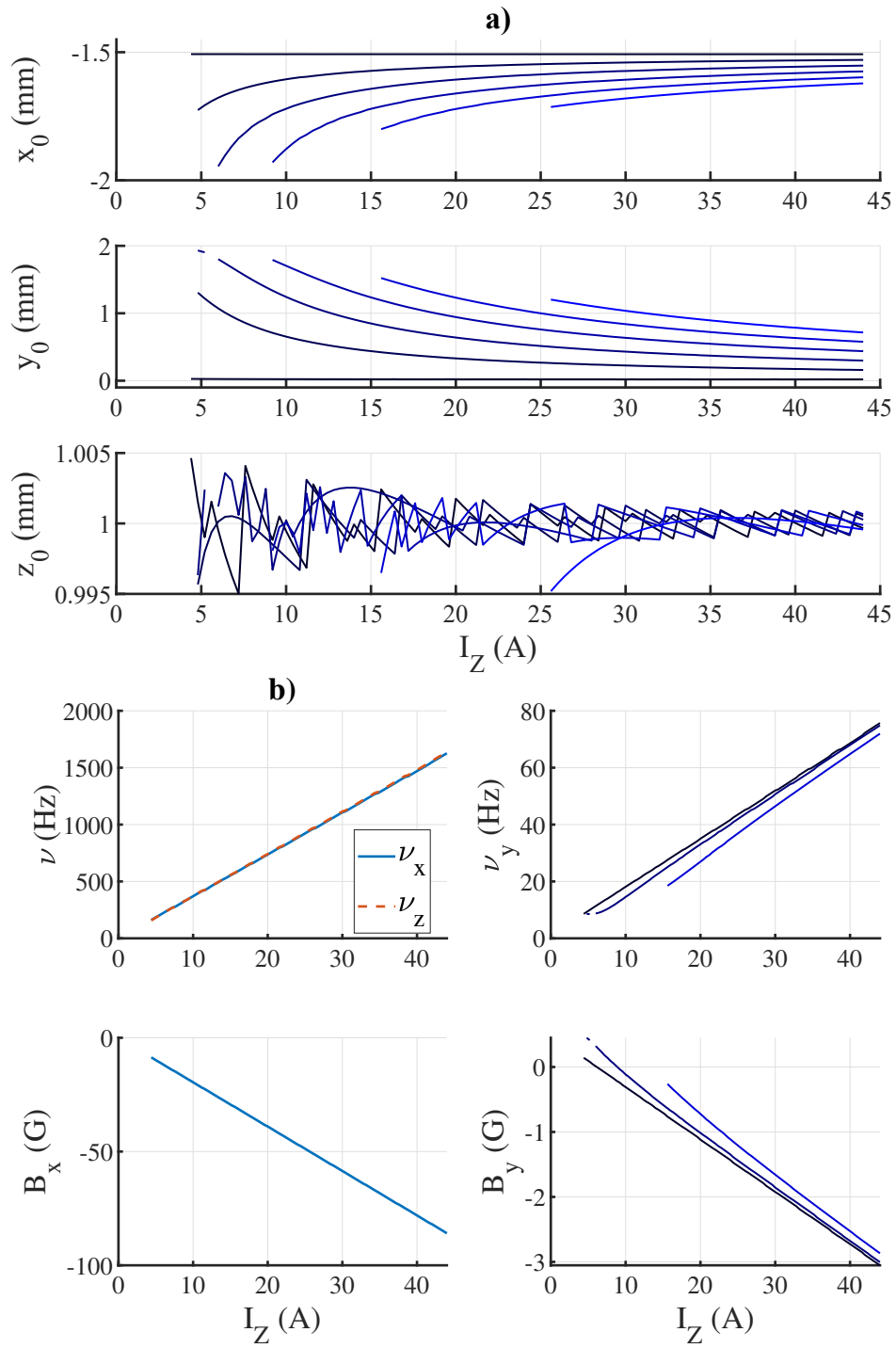


Figure 3.19: Simulated magnetic trap generated by current carrying cylindrical wires. a) Position of the trap center as a function of the current in the 'Z' wire  $I_Z$ . The different curves correspond to current in the 'U' wire  $I_U$  ranging from 0 A (darkest curve) to 25 A (lightest). The wires configuration is given Fig. 3.18. b) Trapping frequencies and required magnetic field bias as a function of  $I_Z$ . Longitudinal trapping frequencies are fairly constant for different  $I_U$  and the curves are plotted only for  $I_U = 0$  A. The transverse trapping frequency  $\nu_y$  is plotted for  $I_U = 0, 10$  and 20 A. Same remark for the static offset field  $B_x$  along  $x$  and bias field  $B_y$  along  $y$ .

### 3.2.2 CAD

We detail below the specifications for the design of the copper substrate, which has been realized using the software SolidWorks (SW).

- Chip size :  
The size is limited by the available size inside the vacuum chamber (re-entrant viewports presented in 1.1.3) to 20 mm vertically. Because the chip will rotate for the transport method, this limit both the height and the depth of the chip.
- Top wire grooves  
In order to reproduce the usual wire pattern shape used in atom chip, millimeter-size straight wires are placed in grooves dug in the copper substrate. A perfect right angle cannot be made for the Z trap. The bend radius need to be large enough so the wire can be safely bent (when trying smaller bend radii, the electrical insulating layer was the first part to degrade, leading to short cuts). The effect of such imperfect 90° angle has been numerically simulated and can be safely neglected. The width of these grooves is adjusted to the wire diameter. The numerical simulations have shown that the absolute positioning of the wire is not critical.
- Rotation axis  
To limit the movement of the cloud, a shoulder is realized on the copper substrate to align the rotation axis and the top of the reflective surface.

### 3.2.3 Fabrication

With design mentioned above, we fabricated the very first version of the atom chip on the AUFRONS experiment. Almost all of the fabrication process was realized at the LP2N laboratory, without high-end and expensive nano-fabrication devices generally used for lithography of the wire pattern. We present below considerations on the chip materials.

- Copper substrate  
Following the SW design, the copper substrate has been machined in the mechanical workshop. We choose copper mostly for its high thermal conductivity and vacuum compatibility.
- Current carrying wires  
For the wires, we choose UHV compatible wires (311-KAP-100-10M) which are made of multiples thin copper wires, twisted to produce a single strand of 1.00 mm diameter, insulated by a layer of Kapton.
- Reflective metallic surface  
Before implementing a chip with a nano-structured top surface, we want to make a proof of principle for the rotation transport using a gold coated reflective surface on the top of the chip to reflect incident laser beams. The near field trap in which atoms will be finally loaded, require a plasmon resonance excitation in a metal, making gold a strong candidate for the surface [53]. Gold<sup>9</sup> provide a high reflectance coefficient over the whole range of

---

<sup>9</sup>a useful website compiling complex refractive index of different materials can be found here

incidence angle ( $R > 0.925$ ) for both wavelength of interest. We used a wafer of silicon,  $275 \mu\text{m}$  thick, coated with a layer of 50 nm of gold, separated by a 5 nm thick adhesion layer of Chromium (10-AU8120 from Micro to Nano company) as a reflective surface. For their [protected gold mirrors](#), Thorlabs give a laser induced damage threshold (LIDT) of  $500 \text{ W / cm}$  for a continuous laser, where thermal effect are the main source of damage. This limit in our case the maximum power to less than 5 W.

This surface has been cut to the proper dimension to fit the copper substrate and the complex refractive index of the mirror at 1064 nm is [101] :  $n = 0.24789 - 7.3057i$ .

- UHV compatible glue

To improve compactness and thermal conductivity, we choose to glue the wire and the surface with epoxy. The choice of the epoxy has been made following the data set produced by the NASA[116], accessible [online](#).

We opted for epoxy with CVCM of 0.00, and WVR below 0.1. Also, we tested different viscosity, the deciding factors on this parameter were the ability (and easiness) to get a bubble-free mixture for 2-components epoxy and to have the thinnest achievable layer. We opted for specific epoxy with high thermal conductivity but electrically insulating properties, filled with silver spheres, small enough to minimize the epoxy layer thickness to  $200 \mu\text{m}$  : [EPO-TEK H77](#), [EPO-TEK H77T](#), [EPO-TEK H77S](#).

We choose the H77S because of its low viscosity, allowing to easily mix the two components without creating air bubbles and to use smaller quantities with a better precision. It also presents a reduced particle size (used for the thermal conductivity) of less than  $20 \mu\text{m}$  allowing a thinner layer.

### 3.2.4 Experimental characterization

Implementation of the atom chip require to break open the vacuum and require, if nothing goes wrong, several weeks during which the experiment will be shut off. Also, because of the complexity of the change, everything needs to be accounted for and characterized before doing the actual implementation. Thus, we tested experimentally in 3.2.4.1 if we could seed the appropriate current in the wire with a controlled heat generation. Also, we study the rotating arm in 3.2.4.2 to decide if it was usable for future implementation.

#### 3.2.4.1 Thermal behavior

Recalling Eq. ??, both the distance between the center of the magnetic trap and the center of the wire, and the normal trapping frequency scale with the seeded current. In [94], 40 A in a wire of diameter  $\phi_{wire} = 1 \text{ mm}$  lead to a temperature increase of  $30 \text{ }^\circ\text{C}$  in the steady state. According to section 3.2.1, our trapping scheme will require current close to 40 A, that requires to test the chip thermal behavior. To reduce the heating of the wires, we should maximize the thermalisation surface of the wire towards the chip and its mount that act as heat-reservoir.

After fabrication of the first chip, we checked the thermal behavior by seeding current up to 37 A. To reduce the strong heating of the 1 mm diameter wire in air, the current is carried towards and outwards the chip by 3 parallel 3 mm diameter wires. The wires are clamped to dedicated dissipating plate attached to the rotating arm, that also help guiding the wires during the rotation.

### Experimental setup for thermal characterization of the chip

We measured the temperature of the chip and the wires using different methods.

- Measuring the resistivity of the wire using a 4-point probe method and using calibration of the temperature dependence of the resistivity [117, 118].
- Using a 10 k $\Omega$  thermistor.
- Using an IR camera (Fluke TiS75+) that gives spatial information on the temperature of the chip. Care should be taken to compare material with different emissivity<sup>10</sup>.

The camera, with adjustable focal plane and emissivity parameter,  $384 \times 288$  pixels, a thermal accuracy of  $\pm 2$  K, resolution of 40 mK, and frequency of 9 Hz is directly imaging the chip. An example of the image generated is found in fig. 3.20. Z-wires are plugged after a passive filter in series to a low-noise diode driver (LDPC laser diode driver), acting as a controllable current-regulated power supply. It deliver up to 37 A, with a rise/fall time of less than 20  $\mu$ s and allow pulsed or continuous operation.

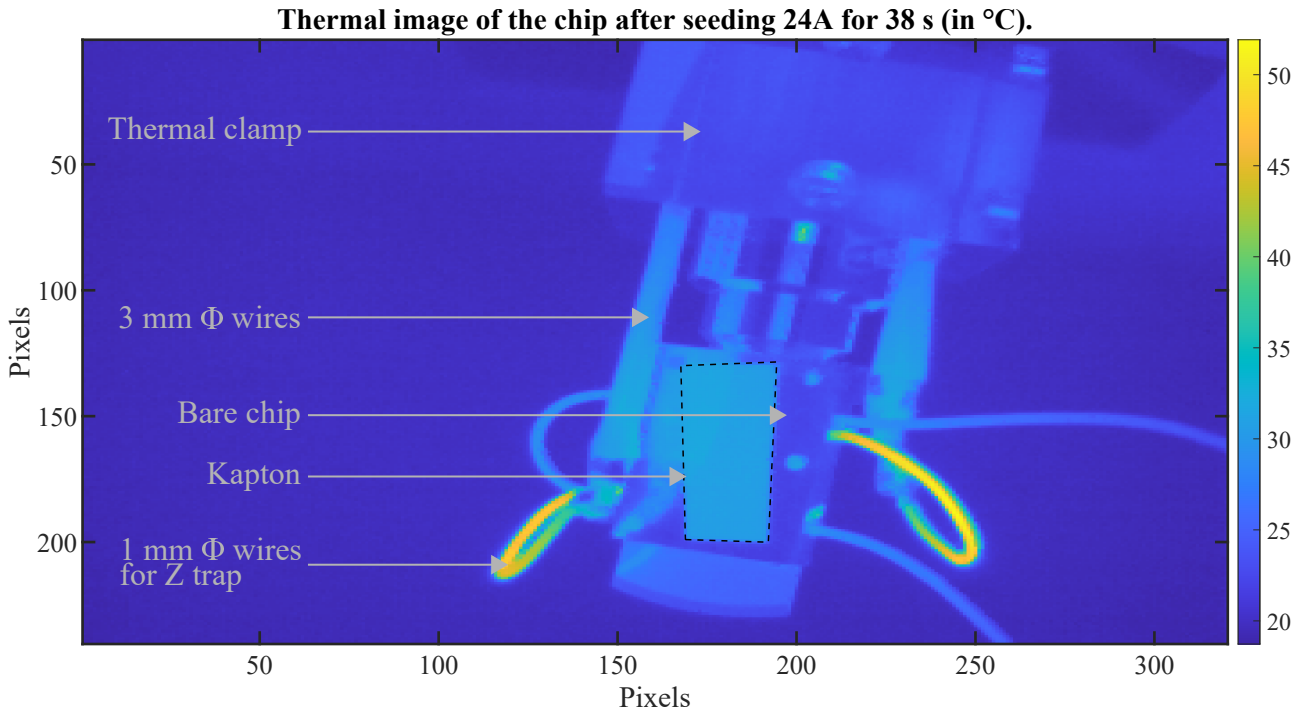


Figure 3.20: Typical image obtained with the thermal camera. We clearly see the temperature difference with and without the Kapton (dashed box) on the copper. Stray reflected field from other heat source are also visible on the aluminum piece holding the chip .

### Result

The chip was attached out of vacuum to the rotating arm with a stainless-steel adaptator. The wires were connected by UHV compatible connectors (FTAIBC094) to bigger wires going to

<sup>10</sup>A more detailed and well illustrated explanation on the [Teledyn FLIR website](#), advise applying on the surface under study a thin material with a well defined and higher emissivity, such as Kapton tape for instance.

a power supply. The supply continuous output is current-regulated at 24 A. We follow the temperature evolution of different point of the chip in Fig. 3.21. With thin wires, the current density is higher, thus leading to more heat being generated by Joule effect. With no heat reservoir to dissipate the energy, we expect an increase of the time gradient of the temperature with the distance to the copper substrate, confirmed experimentally in Fig. 3.21) c). The same experiment is repeated with shorter wire segment being in thin air, showing significantly less heating. Even with short wire segments, the connector was still an important heating point: direct soldering between the wires was required to obtain a contact with a low enough resistivity. We compare the temperature increase after 20 s of continuous operation for different points in table 3.2.4.1.

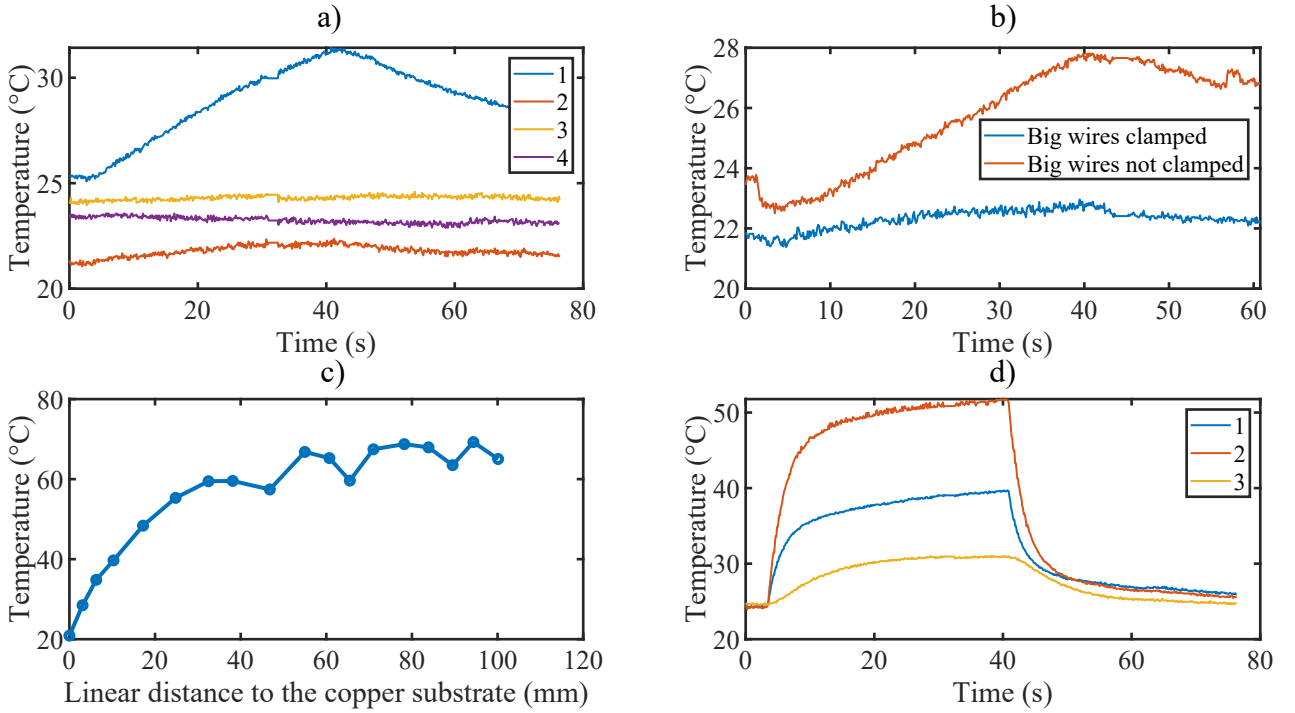


Figure 3.21: Temperature evolution when seeding 24 A for different time. a) Relevance of applying a Kapton film to correctly measure the temperature of metals. 1 : Copper substrate with Kapton; 2 : Bare copper substrate; 3 : Clamping plates with Kapton; 4 : Bare clamping plates). b) Clamping the big wires with the copper piece attached to the rotating arm significantly lower their temperature increase. c) Temperature increase after seeding 24A for 9.5 s as a function of the distance from the substrate. It highlight the importance of having the shortest section of small wire in thin air as possible. d) Temperature evolution of different points in the final configuration. 1 : Small wire close to the substrate; 2 : Small wire far away from the substrate; 3 : Big wire after the soldering point.

With these thermal test, we conclude that the thin wires used for the Z and U-trap, need to be as short as possible after the copper substrate, and soldered to a set of 3 bigger wires clamped to a extra-piece of copper acting as a heat reservoir, rotating with the arm. In this configuration, the resulting heating is less than 10 °C for a continuous usage of 20 s.

Position	Temperature increase ( $^{\circ}\text{C} \pm 0.02$ )
Copper substrate with Kapton	3.76
Bare copper substrate	0.55
Thin wire 1 mm away from the substrate	12.42
Thin wire 20 mm away from the substrate	26.33
Big wires close to the connection point	6.08
Big wire close to the clamping copper plate	3.06
Clamping copper plate	0.29
Big wires clamped, after the copper plate	0.9
Big wires not clamped, after the copper plate	2.88

Table 3.1: Temperature increase at different points of the chip after seeding 24 A for 20 s. The main heating process take place in the thin wires not thermalized with copper, and the clamping copper plates correctly help in dissipating the energy. The temperature increase of the copper substrate indicate a good thermal exchange with the trapped wires.

### 3.2.4.2 Rotating arm

As mentioned in the introduction of the transport method, the atom chip is held under vacuum by the transfer arm that transmit the rotation generated by a motor outside the vacuum chamber. The arm has been characterized at rest by mounting the 4-quadrant PD on it and monitoring the position of a stable incident beam. The resulting stability is presented in Fig. 3.22 for both the longitudinal direction and transverse one. Two cases are studied, one with the arm free of any constraint and one where the arm is mechanically constrained. We also present reference data, acquired when the detector was placed on a fixed mount, giving the stability limit in our measurement. Without stabilization, the transverse direction shows oscillations with peak-peak amplitude of  $20 \mu\text{m}$  at 27 Hz. The constraint reduce the amplitude of the oscillations by at least a factor 10 to a peak-peak value of  $2 \mu\text{m}$ , at the detection limit of our measurement method. Residual oscillations at higher frequencies are probably due to intensity modulation of the incident laser beam. The longitudinal direction (sub-figure b) ), shows a more stable behavior with peak-peak amplitude of only  $4 \mu\text{m}$ . Theses fluctuations can further be reduced down to the detectable limit by placing other constraints. The difference of stability in the two directions can be explained by the fact that flexural modes can be excited more easily than compression modes for an elongated piece of metal. Also, the ball-bearing mechanism used to limit the friction during the rotation, increase the backlash in the transverse direction. Stabilization of the transverse direction at the end of the rotation will be required in the final setup. The ability of the motor to reach the target angle in this configuration still needs to be studied.

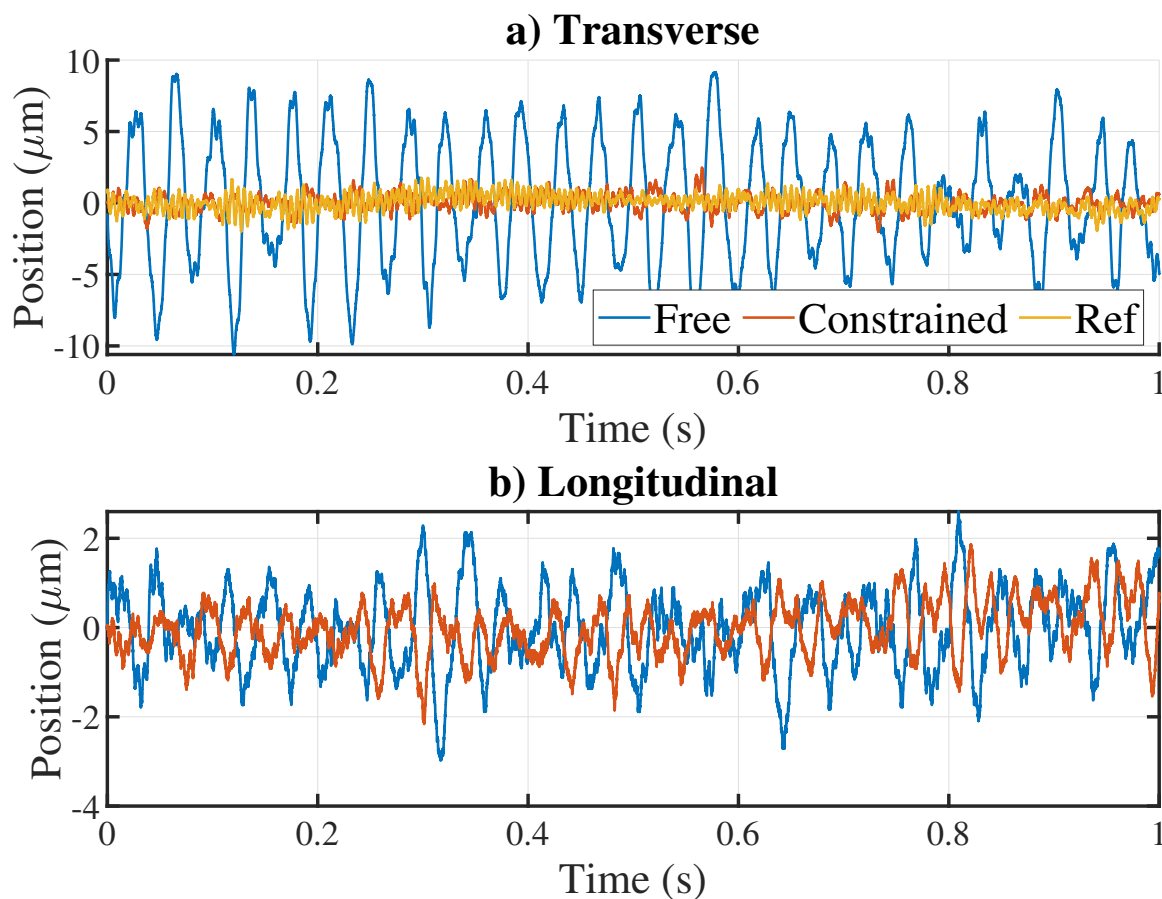


Figure 3.22: Stability of the loaded rotating arm in space. a) Study of the transverse direction compared to the rotation axis, corresponding to the gravity and giving the chip stability along the fringes. b) Longitudinal direction, along the extension direction of the arm. The longitudinal direction present less fluctuations than the transverse one where flexural modes are more easily excitable.

### 3.3 Summary

We report in this chapter our work toward the implementation of an atom-chip system.

First, we elaborate in 3.1 on a new transport method that can be used to transfer atoms trapped in the far field (several microns scale) to near field traps (100 nm distances) using an optical lattice and by rotating the chip. We establish and apply a theoretical framework to study the experimental implementation of our solution. In particular, we have shown that the performance of an ultra-sonic motor should be sufficient to enable heating free transport of the atomic cloud in few hundreds of ms.

Then, we present in 3.2 the design process of the chip including numerical simulations of a magnetic trap based on millimeter-size conducting wires, CAD and fabrication process. Trapping atoms 200  $\mu\text{m}$  above the chip surface require 27 A in the Z wire and a constant magnetic bias of 52 G. This result in trapping frequencies of 1 kHz in the longitudinal directions

and 50 Hz in the transverse direction.

Finally, additional experimental characterization are presented in 3.2.4. We focus on the thermal behavior of the chip while seeding 24 A in the Z wire, and on a rotating transfer arm used to interface the chip in the science chamber with an ultra-sonic motor out of the vacuum.

The implementation of the chip is now becoming a mid-term goal, with the first experimental versions being produced. For the rotation transport scheme, the actual experimental sequence still needs to be decided, with which the numerical application for the different heating terms will be straight-forward. Final test on the rotation transmitted by the arm from the motor will conclude on the feasibility of the rotation transport scheme we proposed. Also, thermal study of the chip should be conducted under vacuum with a higher current to verify that the thermal transfer will indeed be sufficient to limit the temperature increase of the wires. Finally, merging the codes used to simulate the optical and the magnetic traps will makes the design of the whole experimental sequence possible. This will gives access to the theoretical trapping frequencies and trap center position from the MOT to the final doubly-dressed state trap in close vicinity of the surface.

# Conclusion

This PhD thesis was motivated by the development of an hybrid Quantum Simulator platform where ultra-cold atoms are trapped in the near-field of a nano-structured chip. While developing the atom-chip, we also explored a new imaging technique based on doubly dressed states in  $^{87}\text{Rb}$ , attaining resolutions below the standard diffraction limit.

We introduce in Chapter 1 the experimental apparatus used to reach Bose-Einstein condensation of a  $^{87}\text{Rb}$  vapor in an hybrid dipolar and magnetic trap. This chapter contains many technical details on the stabilization of the lasers power and polarization, and of optical alignments. We also present the three absorption imaging axis, with different numerical aperture. We highlight that absorption imaging techniques require to account for a reduction of the scattering-cross section in order to be quantitative on the atom number measured on optically dense cloud. Finally, we presented the optical and atomic characterization of the two-ways accordion lattice, which is used to produce the 1529 nm lattice dressing the excited state in the sub-wavelength imaging method. With this setup, each beams ( $150\ \mu\text{m}$  waist) are stable below  $5\ \mu\text{m}$  over a range of  $5^\circ$ .

In Chapter 2, we present a super-resolution method based on the dressing of the first excited state using a lattice at 1529 nm. We give the theoretical model and the expected resolutions. We experimentally show that sub-wavelength volumes can be transferred in  $|F_g = 2\rangle$  in a few micro-seconds, and imaged using a standard absorption imaging technique. The final spatial resolution directly depend on the 1529 nm lattice spacing and was measured to reach 20 nm. The resolution of this method is not limited by the diffraction but by the modulation amplitude of the excited state which is characterized by a spectroscopy method (BAT-curve). Then, we adiabatically load a BEC in a 1D optical lattice obtained by counter propagating beams at 1064 nm. The lattice depth is characterized using a diffraction method based on Kapitza-Dirac scattering.

We apply our super-resolution method to perform sub-wavelength imaging in this double lattice configuration. The control over the lattice relative phase is a crucial element to image different trapping site. This relative phase is controlled over nano-metric distances using a piezo-stack which was experimentally calibrated.

Scanning the relative phase with such precision also allows with the super-resolution method to measure on-site atomic densities. The method is used to clean specific lattice sites and prepare a single wave-function in a super-lattice configuration (arising from the commensurability of the two lattices). The spatial measurement of this single wave-function is still broadened compared to the expected size, which we infer to be due to the complexity of the cleaning imposed by the

geometry.

Implementing this scheme with a different wavelength is considered, using a 1022 nm laser for the trapping. The commensurability would be 3 for 2. This would increase the SNR by a factor  $13/3 \sim 4$  and simplify greatly the cleaning process.

We also mention that a broadening was measured due to a misalignment of the lattices. A new alignment procedure has been developed and implemented. However, the degradation of the vacuum conditions prevented us to reach a firm conclusion.

Chapter 3 recapitulate progresses on the atom-chip development. We investigated thoroughly the rotation transport method, key point for the future implementation of the DDS trap. After deriving the theoretical model, we experimentally assess the heating induced by the fluctuation of various experimental parameters. Among other things, we show that a supersonic motor could be used to adiabatically transport the cloud from  $5 \mu\text{m}$  to  $250 \text{ nm}$  of the surface. Complementary to the dipole trap used for the transport, a magnetic trap can be generated using conducting wires implemented in the atom-chip. According to our numerical simulation, a longitudinal trapping frequency of 1 kHz could be obtained at 1 mm from the chip with less than 30 A.

The atom-chip we fabricated in the laboratory is composed of a copper substrate holding millimeter size current carrying wires and a metallic reflective surface as needed for the rotation transport scheme. Specific parts intended to dissipate the heat generated by the current in the wire has been produced. A thermal study of the chip while using the Z-wire indicated that 24 A can be seeded for at least 20 s (corresponding to our current MOT loading time) with a temperature increase under  $10 \text{ }^\circ\text{C}$ .

Modifications on the vacuum chamber has recently been made and the implementation of the chip under vacuum is now a mid-term goal. Some final test are still required and the next step will be to test the rotation transport method directly using atoms.

# Appendix A

## Rubidium structure

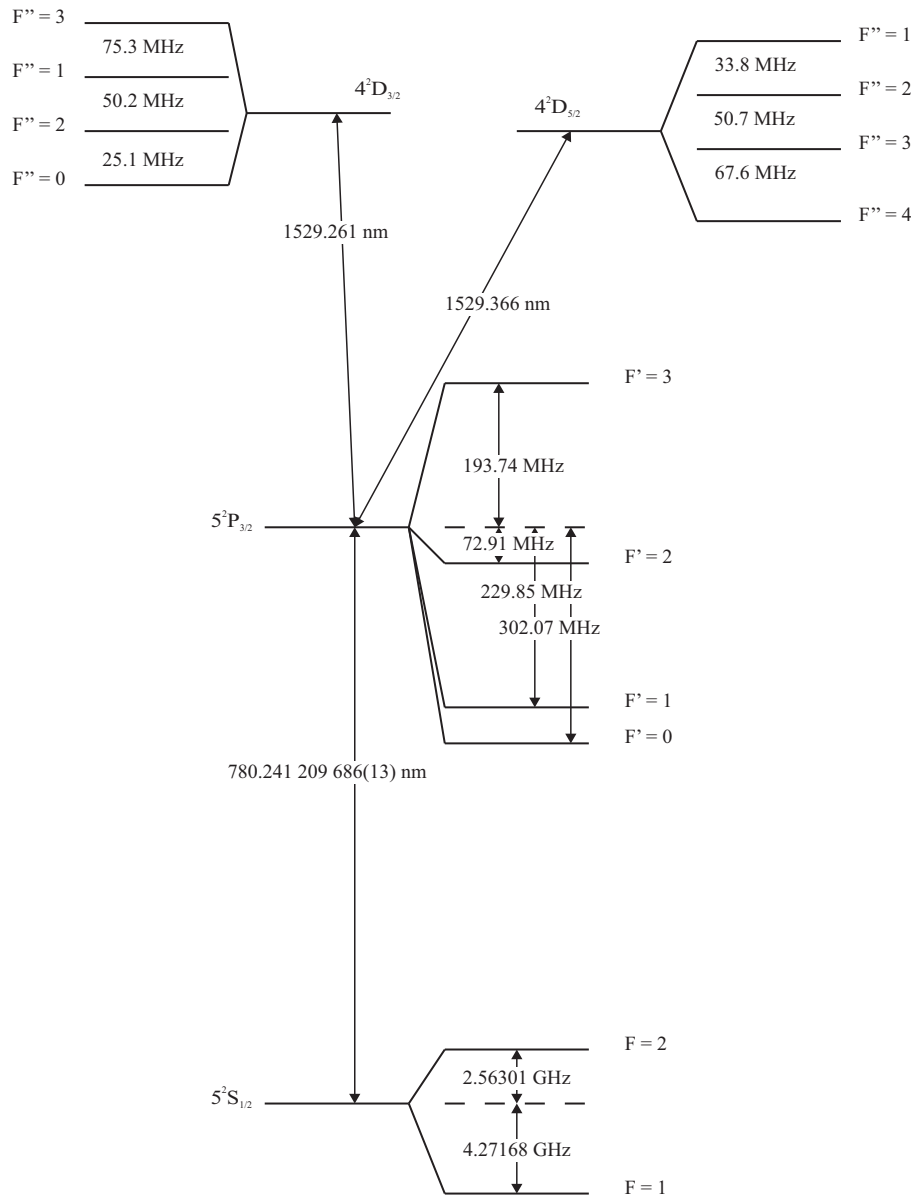


Figure A.1: Detailed energy structure of useful levels for  $^{87}\text{Rb}$  [75, 119]

# Appendix B

## Electric dipole interaction

The interaction of neutral atoms with an electric field can be separated in two components. A dissipative force arises from cycles of absorption and spontaneous emission of photons. This result in a non-zero mean value of the momentum transfer between the light source and the atoms, opposed to the light propagation direction. It is the underlying phenomenon behind laser cooling and magneto optical traps.

The second component is due to the light field inducing and interacting with the dipole moment of the atom. The resulting conservative force shifts the internal energy levels of the atom, called the AC-Stark shift.

### B.1 Far-detuned optical dipole trap

Far of resonance optical trap (FORT) is a well know method used to trap neutral atoms, well understood since 1985 [30] and experimentally reported for the first time in 1986 [120]. Based on the electric dipole interaction, it arise from the dispersive interaction of the induced atomic dipole moment with the intensity gradient of the light field, tuned far away from transitions between the ground state and any excited state. Approximating the atoms by a two-level system (2LS), in the case of large detuning and negligible saturation, the dipole potential can be expressed as [5]:

$$U_{dip}(\mathbf{r}) = -\frac{\hbar\Gamma}{2} \frac{\Gamma}{4\Delta} (\rho_{ee} - \rho_{gg}) s(\mathbf{r}) \quad (\text{B.1})$$

For a two-level atom with the full line strength, the saturation intensity is defined as  $I_{sat} = (\hbar\omega_0^3\Gamma) / (12\pi c^3)$ . In the absence of a driving field near resonance the population is mainly in the ground state ( $\rho_{gg} = 1$ ), so the dipole potential is proportional to the laser intensity :

$$U_{dip}(\mathbf{r}) = \frac{3\pi c^2}{2\omega_0^3} \frac{\Gamma}{\Delta} I(\mathbf{r}) \quad (\text{B.2})$$

The inelastic scattering rate is :

$$\Gamma_{sc} = \frac{\Gamma}{\Delta} \frac{U_{dip}}{\hbar} \quad (\text{B.3})$$

Since the dipole potential scales as  $I/\Delta$ , one should choose the detuning as large as possible for a given available laser power to minimize inelastic scattering process, yielding a conservative potential. In the case of a dipole trap at 1064 nm, a 100 kHz trapping frequency correspond to  $\Gamma_{sc} = 0.01$ , low enough so such trap can be considered as conservative. For red-detuned lasers,  $\delta < 0$  and atoms are attracted to the maximum laser intensity region.

This is the simplest model for dipolar forces exercised on atoms, valid as a first approximation on many cases. However, in our experimental conditions, two correcting terms should be considered.

- Detuning not negligible compared to the transition frequency.

In this case, the rotating-wave approximation is no longer valid and one as to consider both co-rotating and contra-rotating terms [5] :

$$U_{dip}(\mathbf{r}) = \frac{3\pi c^2 \Gamma}{2\omega_0^3} \left( \frac{1}{\omega - \omega_0} + \frac{1}{\omega + \omega_0} \right) I(\mathbf{r}) \quad (\text{B.4})$$

In the FORT scheme of  $^{87}\text{Rb}$  with a 1064 nm laser, the correcting factor is :  $U_{bare}/U_{corrected} = 1.18$ .

- Multi-level atom.

For alkali atoms, considering the  $ns \rightarrow np$  transition, spin-orbit coupling in the excited state leads to the well known  $D$ -line doublet  $^2S_{1/2} \rightarrow ^2P_{1/2}, ^2P_{3/2}$ . See A.1 for definition of the different splitting. Neglecting the excited-state hyperfine splitting  $\Delta'_{HFS}$  compared to the optical detuning  $\Delta$ , the dipolar potential for atoms in their ground state with total angular momentum  $F$  and magnetic quantum number  $m_F$  is for all polarization [5]:

$$U_{dip}(\mathbf{r}) = C_{dip} I(\mathbf{r}) = \frac{\pi c^2 \Gamma_2}{2\omega_{2,F}^3} (2 + \mathcal{P} g_F m_F) \left( \frac{1}{\omega - \omega_{2,F}} + \frac{1}{\omega + \omega_{2,F}} \right) I(\mathbf{r}) \\ + \frac{\pi c^2 \Gamma_1}{2\omega_{1,F}^3} (1 - \mathcal{P} g_F m_F) \left( \frac{1}{\omega - \omega_{1,F}} + \frac{1}{\omega + \omega_{1,F}} \right) I(\mathbf{r}) \quad (\text{B.5})$$

with  $\mathcal{P} = 0, \pm 1$  characterizing resp linearly and circularly  $\sigma^\pm$  polarized light,  $\omega_{1,F}$ , resp.  $\omega_{2,F}$  the frequency between a particular hyperfine state  $F$  of  $5S_{1/2}$  and  $5P_{1/2}$  resp.  $5P_{3/2}$ . The left term of B.5 represent the contribution of the  $D_2$  line and the right term of the  $D_1$  line to the total dipole potential.

For  $\mathcal{P} = 0$  and  $\lambda = 1064\text{nm}$ , the ratio of B.4 over B.5 equals 0.978

Optical lattices are a specific case of FORT in which the radiation has a periodic spatial modulation. The behavior of a cloud of atoms in such trap is considered later in this chapter.

## B.2 Light shift given by second order perturbation theory

For small energy shifts compared to the hyperfine splitting, the energy shifts due to electric-field dipole interaction is accurately obtained using second order perturbation theory. The basis with no perturbation is written  $|n\rangle = |F, m_F\rangle$ , associated to the hyperfine eigen-energy  $E_n^{(0)}$ . Considering an oscillating electric field of frequency  $\omega$ , the total Hamiltonian  $H_{Stark} = -\mathbf{d} \cdot \mathbf{E}$

shift the energy of  $|n\rangle$  by :

$$\Delta E_n = \langle n^{(0)} | H_{Stark} | n^{(0)} \rangle + \sum_{|k \neq n} \frac{|\langle k^{(0)} | H_{Stark} | n^{(0)} \rangle|^2}{E_n^{(0)} - E_k^{(0)}} \quad (\text{B.6})$$

Because of the parity of the dipole operator, the first term in the equation above is zero. In the perturbation approximation and for a linearly polarized field, the energy shift simplify to [107, p.375] :

$$\Delta E_n = -2\mu_0 C \alpha_n I \quad (\text{B.7})$$

expressed using the total polarisability

$$\alpha_n = \alpha_n^{(0)} + \alpha_n^{(2)} \frac{3m_F^2 - F(F+1)}{F(2F-1)} \quad (\text{B.8})$$

where we introduced the scalar and tensor polarisabilities considering the two excited states  $5^2P_{1/2}$  and  $5^2P_{3/2}$  :

$$\begin{aligned} \alpha_n^{(0)} &= \sum_{J', F'} \frac{2\omega_{F'F} |\langle J || \mathbf{d} || J' \rangle|^2}{3\hbar(\omega_{F'F}^2 - \omega^2)} (2F' + 1)(2J + 1) \left\{ \begin{matrix} J & J' & 1 \\ F' & F & I \end{matrix} \right\}^2 \\ \alpha_n^{(2)} &= \sum_{J', F'} (-1)^{F+F'} \sqrt{\frac{40F(2F+1)(2F-1)}{3(F+1)(2F+3)}} \left\{ \begin{matrix} 1 & 1 & 2 \\ F & F & F' \end{matrix} \right\} \frac{\omega_{F'F} |\langle J || \mathbf{d} || J' \rangle|^2}{\hbar(\omega_{F'F}^2 - \omega^2)} \\ &\quad (2F' + 1)(2J + 1) \left\{ \begin{matrix} J & J' & 1 \\ F' & F & I \end{matrix} \right\}^2 \end{aligned} \quad (\text{B.9})$$

This result is very convenient since the energy shift is directly proportional to the intensity but only match experimental data for small displacement. In the case of stronger fields, diagonalisation of the full Hamiltonian is required to correctly compute the energy displacement.



# Appendix C

## Ultra-cold atom trapping

We focus in this section on the trapping of  $^{87}\text{Rb}$  atoms for two specific configurations. After RF evaporation in a magnetic trap, we detail the transfer to an hybrid trap by adding a FORT. This correspond to the last experimental step before the final evaporation and an efficient loading is critical for reaching condensation. We then give the theoretical description of a BEC in a 3D harmonic trap, giving a useful description both for our experimental conditions and for the system under study in 3.1.4.1.

### C.1 Thermal cloud in an hybrid trap

We consider the transfer of a cloud in  $|F_g = 1, mF = -1\rangle$  from a magnetic trap (MT) to an hybrid trap obtain by adding a single beam far-off resonance optical dipole trap on the magnetic trap [63]. We start by and RF evaporation in a quadrupole trap, reducing the phase space density until Majorana spin-flips cause significant loss and heating. To limit Majorana losses during the transfer, the center of the optical trap is offset by at least one beam waist below the field zero of the magnetic trap. This offset quadrupole field also provide harmonic confinement along the beam direction, compensating for the low confinement offered by the small beam divergence along the propagation. The transfer need to be adiabatic to let the trap shape evolve from linear quadrupole to harmonic.

The trapped cloud is described as a thermal gas whose thermodynamic properties are given by the partition function  $\zeta = V_0/\Lambda^3$  where  $\Lambda = \sqrt{\frac{2\pi\hbar^2}{mk_B T}}$  is the thermal de Broglie wavelength and  $V_0 = \int e^{-U(\mathbf{r})/k_B T} d^3\mathbf{r}$  is the cloud effective volume<sup>1</sup>, defined with  $U(\mathbf{r})$  the trapping potential. With  $\zeta$  and  $V_0$ , one can compute the free energy  $A = -Nk_B T \ln(\zeta)$ , the entropy  $S = -\frac{\partial A}{\partial T}$  and the spatial density distribution :

$$n(\mathbf{r}) = \frac{N}{V_0} e^{-\frac{U(\mathbf{r})}{k_B T}} \quad (\text{C.1})$$

---

<sup>1</sup>Here, we neglect the effect of finite trap depth, treated in [121]

We consider in this section, the trapping potential formed by a FORT propagating in the  $\mathbf{y}$  direction and coils in anti-Helmholtz configuration along  $\mathbf{z}$  :

$$U(\mathbf{r}) = \mu B' \sqrt{\left(\frac{x}{2}\right)^2 + \left(\frac{y}{2}\right)^2 + z^2} - U_0 e^{-2(x^2+(z-z_0)^2)/w_0^2} + mgz + E_0 \quad (\text{C.2})$$

where  $\mu = g_F m_F \mu_B$  is the magnetic moment of the cloud,  $m$  the mass of  $^{87}\text{Rb}$  and  $g$  the gravity acceleration. The effective trap volume can be approximated in the two extreme temperature cases. At high temperature, when  $T \gg U_0/k_B$ , the dipole trap influence can be neglected and we have, supposing that gravity is compensated :

$$V_0(T) = \frac{32\pi e^{-E_0/k_B T}}{\left(1 - \left(\frac{mg}{\mu B'}\right)^2\right)^2} \left(\frac{k_B T}{\mu B'}\right)^3 \quad (\text{C.3})$$

where  $E_0 \approx U_0$  for typical offset  $z_0 \approx w_0$ .

At low temperatures, the trap can be approximated as an harmonic trap with pulsations :

$$\begin{aligned} \omega_x = \omega_z &= 2\sqrt{\frac{U_0}{mw_0^2}} \\ \omega_y &= \frac{1}{2}\sqrt{\frac{\mu B'}{m|z_0|}} \end{aligned} \quad (\text{C.4})$$

And the effective volume is :

$$V_0(T) = \frac{(2\pi k_B T/m)^{3/2}}{|\omega_x \omega_y \omega_z|} \quad (\text{C.5})$$

For the intermediate regime, Eq. C.3 gives a better approximation than C.5.

Starting from a cloud at  $T_0$  with a magnetic gradient  $B'_0$ , the evolution of the temperature at constant entropy during the magnetic trap adiabatic decompression is given by :

$$T = T_0 \left(\frac{B'}{B'_0}\right)^{2/3} \left(\frac{1 - (mg/\mu B')^2}{1 - (mg/\mu B'_0)^2}\right)^{4/9} \quad (\text{C.6})$$

The crossover can be considered to happen at  $T_l = 0.1U_0/k_B$ . below this temperature, almost all the atoms will be in the hybrid trap.

Ignoring gravity, Majorana losses rate can be estimated as :

$$\Gamma_m = 1.85 \frac{\hbar}{m} \left(\frac{\mu B'}{k_B T}\right)^2 \quad (\text{C.7})$$

## C.2 Bose Einstein condensate in a 3D harmonic trap

Since it's first experimental observation in the group of Wieman and Cornell at JILA in 1995 [2] Bose-Einstein condensate (BEC) are the corner stone of many experiments. With now almost standard experimental setups, one can routinely produce and manipulate this fourth state of the matter : a system whose quantum properties lies in the macroscopic domain. We recall in

this section the theoretical description of a trapped BEC. Most of the result of this part are obtained following [122, 79].

Interacting spin-less bosonic particles can be described using the Boson field operator  $\hat{\Psi}(\mathbf{r}, t)$ . In the Heisenberg representation, this operator fulfills the equation :

$$i\hbar \frac{\partial \hat{\Psi}}{\partial t}(\mathbf{r}, t) = \left( -\frac{\hbar^2 \nabla^2}{2m} + V_{ext}(\mathbf{r}, t) + \int \hat{\Psi}^\dagger(\mathbf{r}', t) V(\mathbf{r}' - \mathbf{r}) \hat{\Psi}(\mathbf{r}', t) d\mathbf{r}' \right) \hat{\Psi}(\mathbf{r}, t) \quad (\text{C.8})$$

where  $V_{ext}$  is including any external potential and  $V$  is the interaction potential. In the case of a weakly interacting and dilute gas, an effective field theory can be developed to describe the interaction between the particles of the system. Under the Born approximation, the inter-atomic potential  $V$  is replaced by a "soft", short-range potential  $V_{eff}$  to which perturbation theory can be applied. In this description, we keep only the lowest-order component in the momentum decomposition of the potential amplitude, also referred as the coupling constant :

$$\int V_{eff}(\mathbf{r}) d\mathbf{r} = g_{3D} = \frac{4\pi \hbar^2 a_s}{m} \quad (\text{C.9})$$

where  $a_s$  is the s-wave scattering length and  $m$  is the mass of the atom. Following the Bogoliubov ansatz, applicable if the number of particles in the ground state  $N_0$  is high enough, we can replace the operator acting on the ground state by the c-number  $\sqrt{N_0}$ . At low enough temperature (where all the particles are in the ground state) the field operator can thus be replaced by a classical field  $\Psi(\mathbf{r}, t)$ . Assuming that  $\Psi$  is constant on distances of the order of the range of the inter-atomic force, we obtain the many-body, time-dependent Gross-Pitaevskii equation (GPE) for the order parameter [123] :

$$i\hbar \frac{\partial \Psi}{\partial t}(\mathbf{r}, t) = \left( -\frac{\hbar^2 \nabla^2}{2m} + V_{ext}(\mathbf{r}, t) + g_{3D} |\Psi(\mathbf{r}, t)|^2 \right) \Psi(\mathbf{r}, t) \quad (\text{C.10})$$

Considering stationary solutions, we write :

$$\Psi(\mathbf{r}, t) = \Psi_0(\mathbf{r}) e^{-i\mu t/\hbar} \quad (\text{C.11})$$

with  $\mu = \frac{\partial E}{\partial N}$  the chemical potential.

Assuming that the external potential does not depend on time, we write the reduced time independent Gross-Pitaevskii equation [124] :

$$\left( -\frac{\hbar^2 \nabla^2}{2m} + V_{ext}(\mathbf{r}) + g_{3D} |\Psi_0(\mathbf{r})|^2 \right) \Psi_0(\mathbf{r}) = \mu \Psi_0(\mathbf{r}) \quad (\text{C.12})$$

Ignoring correlation among particles (same diluteness criteria), we write the many-body wavefunction of the system in the factorized form according to the Hartree-Fock approximation :

$$\Phi_a(\mathbf{r}_1, \dots, \mathbf{r}_N) = \prod_{i=1}^N \frac{1}{\sqrt{N}} \Psi_a(\mathbf{r}_i) \quad (\text{C.13})$$

The confining potential will often be approximated as a simple harmonic trap and defined as :

$$V_{ext}(\mathbf{r}) = \frac{m}{2} (\omega_x^2 x^2 + \omega_y^2 y^2 + \omega_z^2 z^2) \quad (\text{C.14})$$

We introduce the geometric average of the oscillator pulsations:

$$\omega_{ho} = (\omega_x \omega_y \omega_z)^{1/3} \quad (\text{C.15})$$

With this definition, we also introduce the harmonic oscillator length :

$$a_{ho} = \left( \frac{\hbar}{m\omega_{ho}} \right)^{1/2} \quad (\text{C.16})$$

Depending on the relative strength of the interaction compared to the external trapping potential, we consider the two extreme cases of solutions for the GPE : weak and strong interaction regime.

### Weak interaction regime

In this regime, the interaction energy is negligible compared to the kinetic one. The solution of the GPE then give a Gaussian function for the atomic density :

$$n(\mathbf{r}) = N \prod_{i=1}^3 \frac{1}{r_{i,ho} \sqrt{\pi}} e^{-r_i^2 / r_{i,ho}^2} \quad (\text{C.17})$$

with  $r_{i,ho}$  the radius of the Gaussian distribution in the direction  $i$ , reading :

$$r_{i,ho} = \sqrt{\hbar / m\omega_i} \quad (\text{C.18})$$

The total energy of the system is then given for each direction  $i$  by :

$$E_i(N) = \frac{N\hbar\omega_i}{2} \quad (\text{C.19})$$

### Strong interaction regime

In the case of atoms with repulsive interaction ( $a_s > 0$ ) and neglecting the quantum pressure term in the GPE due to variation of the atomic density over space, the limit  $\frac{N|a_s|}{a_{ho}} \gg 1$  is particularly interesting. In this case, where the dominant term is the interaction potential, the atomic density profile is given by a simple inverted parabola :

$$n(\mathbf{r}) = \begin{cases} \frac{\mu - V_{ext}(\mathbf{r})}{g} & \text{if } \mu \geq V_{ext} \\ 0 & \text{otherwise} \end{cases} \quad (\text{C.20})$$

This is often refereed as the Thomas-Fermi approximation, with the chemical potential being :

$$\mu = n(0)g = \frac{\hbar\omega_{ho}}{2} \left( \frac{15Na_s}{a_{ho}} \right)^{2/5} \quad (\text{C.21})$$

The radii of the parabola is :

$$r_{i,TF} = \sqrt{\frac{2\mu}{m\omega_i^2}} \quad (\text{C.22})$$

In the Thomas-Fermi approximation, the energy of a condensate of  $N$  atoms confined in an harmonic trap is given by :

$$E(N) = \frac{5N\mu(N)}{7} \quad (\text{C.23})$$

where  $\mu(N)$  is the chemical potential defined Eq. C.21.

## C.3 Doubly-dressed state formalism

### C.3.1 Total trapping potential

We consider a cloud of  $^{87}\text{Rb}$  atoms at rest in the ground state  $5^2S_{1/2}$ , interacting with a laser at 1064 nm and one at 1529 nm. In the dressed state picture [30] and neglecting the population in the second excited state  $4^2D_{5/2}$ , the total dipole force on the atoms is :

$$f_{dip}(\mathbf{r}) = -\nabla U_{5S}(\mathbf{r})\rho_{5S} - \nabla U_{5P}(\mathbf{r})\rho_{5P} \quad (\text{C.24})$$

The generated potential by both these far-off resonance lasers is given by Eq. B.5 and atomic coherence can be considered at equilibrium with respect to the populations evolution.

A spatially homogeneous 780 nm laser ( $\omega_{780}$ ) drive the dressed atomic transition ( $\omega_{5S,5P}(\mathbf{r})$ ) and gives the Optical Bloch Equation (OBE) driving the excited state population dynamic ( $\rho_{5P}(\Delta(\mathbf{r}))$ ).

Using the conservation of population, we can re-write the total dipole potential as :

$$f_{dip}(\mathbf{r}) = -\nabla U_{5S}(\mathbf{r}) + \hbar\Gamma\nabla\left(\frac{\Delta(\mathbf{r})}{\Gamma}\right)\rho_{5P}(\Delta(\mathbf{r})) \quad (\text{C.25})$$

where  $\Delta(\mathbf{r}) = \omega_{780} - \omega_{5S,5P}(\mathbf{r}) = \Delta_{780} - \frac{U_{5P}(\mathbf{r}) - U_{5S}(\mathbf{r})}{\hbar}$  is the detuning.

The potential is obtained by integrating the dipole force :

$$U_{dip}(\mathbf{r}) = \int_{-\infty}^{\mathbf{r}} [\nabla U_{5S}(\mathbf{r}') - \hbar\Gamma\nabla(\Delta(\mathbf{r}'))\rho_{5P}(\Delta(\mathbf{r}'))] d\mathbf{r}' \quad (\text{C.26})$$

### 1D DDS potential

We consider the 1D case in the  $\mathbf{x}$  direction. Far from the atoms, the potential energy is zero  $U_{5S}(-\infty) = U_{5P}(-\infty) = 0$  and the resulting potential is :

$$U_{dip}(x) = U_{5S}(x) - \frac{\hbar\Gamma}{4} \frac{s}{\sqrt{1+s}} \left( \text{atan}\left(\frac{2\Delta(x)}{\Gamma\sqrt{1+s}}\right) - \text{atan}\left(\frac{2\Delta_{780}}{\Gamma\sqrt{1+s}}\right) \right) \quad (\text{C.27})$$

We write the energy shift of the excited state due to the 1529 nm radiation as :

$$U_{5P}(x) = \hbar\Gamma\Delta_{ee} \exp\left(-\frac{2x^2}{w_0^2}\right) \quad (\text{C.28})$$

where  $\Delta_{ee}$  is a normalized shift.

It is convenient to define the detuning of the 780 nm radiation depending on the position of the resonance within the excited state modulation :  $\Delta_{780} = r\Gamma (U_{5P} - U_{5S})$ , with  $r \in [0, 1]$ .

Without 1064, the total potential can be written as :

$$U_{dip}(x) = -\frac{\hbar\Gamma}{4} \frac{s}{\sqrt{1+s}} \left( \text{atan} \left( \frac{2\Delta_{ee}}{\Gamma\sqrt{1+s}} \left( r - \exp^{-\frac{2x^2}{w_0^2}} \right) \right) - \text{atan} \left( \frac{2r\Delta_{ee}}{\Gamma\sqrt{1+s}} \right) \right) \quad (\text{C.29})$$

The expression above establish that in this configuration, a cloud of atoms in their ground state can be trapped by dressing the excited state. The 780 nm laser power tunes the trap depth and the 780 frequency detuning tunes the resonant positions.

### C.3.2 Presentation of the near-field trap

In this section, we recall the near-field trapping method previously developed in the team [29]. It relies on the DDS trapping method presented above and Casimir-Polder forces.

#### Casimir-Polder forces

An atom in vacuum interact with a macroscopic body because of quantum charge and field fluctuations, known as Casimir-Polder (CP) interaction [27]. The atom, assimilated to a fluctuating induced dipole with moment  $\mathbf{d}$ , generate an electromagnetic field which is reflected by the surface and interact back with the dipole. The CP interaction is characterized by an energy  $U$  proportional to the the atomic polarizability  $\alpha$  and the scattering Gree tensor  $G^{(1)}(\mathbf{r}, \mathbf{r}, \omega)$  describing the round-trip propagation of the electric field at  $\omega$  from the atom at  $\mathbf{r}$  to the surface. For an atom in the ground state interacting with an electric or paramagnetic surface, the resulting force is attractive, shifting all the energy level accordingly. The exact energy shifts are computed using a non-perturbative approach [125] combining the initial QED description and the linear response theory [126]. For more details, see [31, Chap.4].

#### Doubly-dressed states

A laser radiation close 1529 nm dress the excited state  $5^2P_{3/2}$  of  $^{87}\text{Rb}$  . Exciting a surface plasmon resonance in a thin, well chosen,metallic layer will create an exponentially decaying intensity profile. For a field tuned on the blue of the  $5^2P_{3/2} \leftarrow 4^2D_{5/2}$  transition, the AC Stark shift effect (see Eq. B.7) induces a strongly repulsive potential on the first excited state  $5^2P_{3/2}$  while barely affecting the ground state  $5^2S_{1/2}$ . Thus, the  $5^2S_{1/2} \leftarrow 5^2P_{3/2}$  resonant transition frequency  $\omega_0$  depend on the distance to the surface. Adding a 780 nm laser close to resonance then produces an AC Stark shift on the ground state with a spacial dependency because of the spatially-dependent detuning. We refer to this double dressing of the atomic cloud with light fields as Doubly-Dressed States (DDS).

Using both effects cited above, the attractive CP force and repulsive DDS force can cancel each other at a given distance from a surface, where neutral atoms can be trapped. Implementing such scheme with a nano-structured surface produces in the transverse directions a lattice potential, by modulating the CP forces. The frequency and trapping position along

the longitudinal direction can be adjusted with the two dressing lasers powers and detunings, while the transverse lattices periods depend only on the grating itself.



# Appendix D

## Experimental setup details

### D.1 Vacuum quality

During my PhD, we observed two vacuum related issues: rare gas instability and a leaking viewport.

The leaking viewport has been partially sealed with Torr Seal epoxy (TS10) in 2018. Also, we observed at multiple occasions a phenomena know as 'Argon' or 'rare gas' instability [127]. Rare gas are not very well pumped by ionic pumps that periodically outburst these accumulated gas, degrading the vacuum. The burst period, ranging from days to months, depends on the vacuum quality. It present cycles, where the pressure exponentially increase in time up to the burst, before rapidly falling back to the lowest initial point. Previously, we measured in the team (see Fig. B.5 of [54]) an expected decrease of our MOT life time during these event. Heating both ions pumps while having a turbo-molecular pump connected to the chamber effectively improved the vacuum by pumping out these atoms. After that, we had 11 months spike-free but it is now returning to cycles of 8 months. In fact, we see Fig. D.1 that this phenomenon can happen on both of our two ion pumps. Sub-figure a) present an Argon instability happening for the 'Down' pump, which is pumping the science chamber. Recently two consecutive rare gas instability on the 'Up' pump, which is on a cross between the 2DMOT chamber and the science chamber, led to an increase of the vacuum pressure in the science chamber as we can see with the leakage current of the 'Up' pump being higher after the second spike presented sub-figure b). Instabilities on each pump are distinguishable because of the higher gradient of the leakage current with time of the pump out-bursting compared to the other one and the final pressure reaching zero only for the pump out-bursting. The pressure floor is limited by the ion pump current detection, giving an equivalent pressure of  $10^{-11}$  mbar. As a complementary measurement, we assessed in 02/2023 the 3DMOT lifetime to be 7 s (see Fig. D.6), enough to load further traps but quite short for the evaporation steps. Following [57], this yield an estimated pressure of  $3.7 \times 10^{-9}$  mbar, in good agreement with the  $3.4(3) \times 10^{-9}$  mbar given by the leakage current of the UP Pump. Our latest measurement (03/2023) of the lifetime is 3.8 s for the MT, which is really at the limit given the RF evaporation and transfer to the hybrid trap takes 2.6 s. The degradation of the vacuum conditions had been compensated for the five past years by continuously optimizing all other parameters and we managed to keep reaching a pure BEC with enough atoms to perform the experiment detailed in Chapter 2. My PhD

finishing, the leaking viewport will be changed and we expect that better vacuum conditions will ease to produce a pure BEC with high atom number. Data presented in Chapter 2 were taken between the end of 2021 and July 2022, when the MOT lifetime was longer and BEC threshold was routinely achieved.

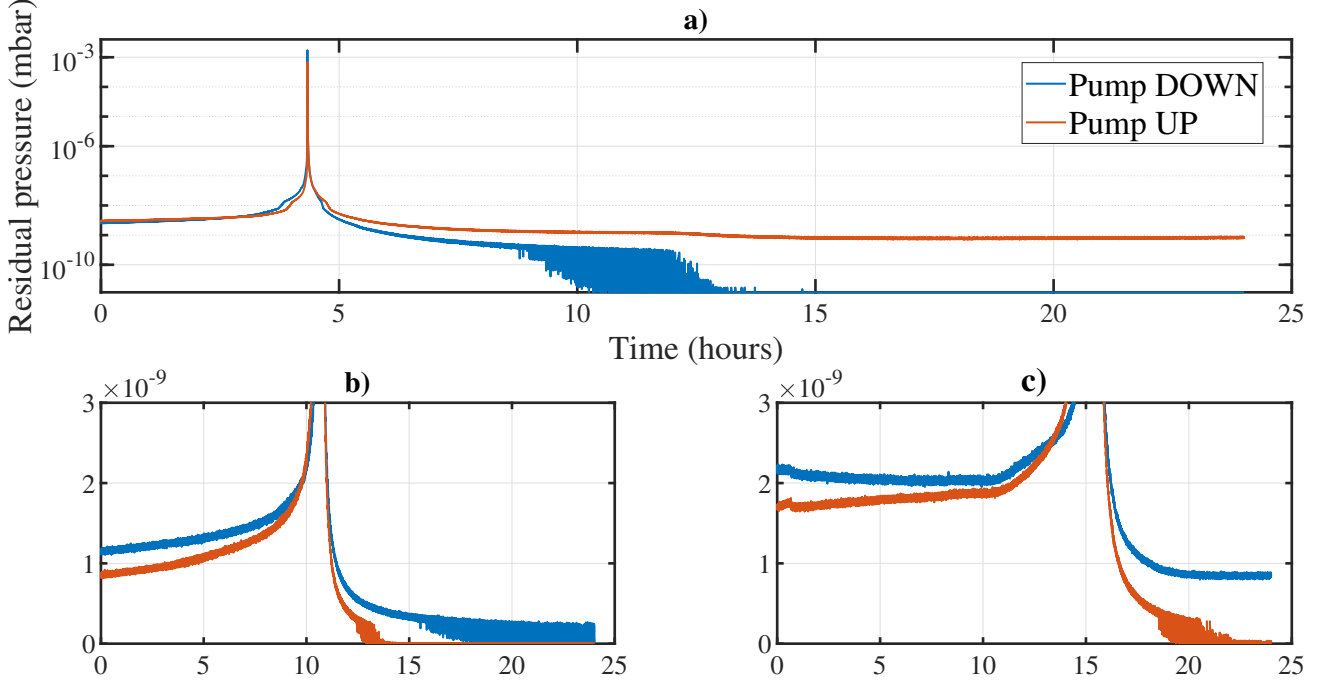


Figure D.1: Leakage current of both our ion pumps. The pump labeled DOWN is close to the science chamber, on a four-way cross near DT2 entering viewport. The pump labeled UP is on a T-cross between the 2DMOT and 3DMOT chamber. All y-axis are the residual pressure computed with the leakage current of each pump as :  $I_{leak}(\text{nA}) = 3.8 \times 10^9 \times P(\text{mbar})$ . The y-axis of a) is in log-scale while being in linear scale for b) and c). a) Pressure evolution during an Argon instability on the DOWNS pump (24/12/2021). b) Rare gas instability on the UPS pump (16/01/2022). c) Second consecutive spike on the UPS pump a few months later (19/10/2022). Notice how the current in the DOWNS pump after the event is higher compared to b).

## D.2 MOT and RF evaporation

We now present the early stage preparation of our cold cloud of  $^{87}\text{Rb}$  starting from a 2DMOT, transferred to a 3DMOT, up to spin polarization steps for loading a magnetic trap.

The 2DMOT purchased from Syrte cools from room temperature a Rubidium vapor to a transverse temperature of  $400 \mu\text{K}$  and was initially loading the 3DMOT with a flux of  $10^{10}$  atoms/s at a speed of 13 m/s. This MOT2D+ is a vacuum chamber integrating a 2 L/s ionic pump and a reserve of  $^{87}\text{Rb}$ . Three successive 2D optical traps are aligned with a hole of 1.5 mm diameter giving a differential vacuum between the 2DMOT chamber and science chamber. Sets of  $2 \times 2$  coils in anti-Helmholtz configuration generate a bi-dimensional magnetic trap



Direction	$x$	$y$	$z$
$I_{max}$ (A)	0.2	0.2	2.5
Monitor pin (mA to V) $I =$	$49.47 V_{mon}^x - 0.110$	$200.2 V_{mon}^y - 0.435$	$\emptyset$
Current conversion (mA to V) $I =$	$-98.9 V_{in}^x - 0.091$	$-164 V_{in}^y - 0.303$	$502 V_{in}^z + 14.9$
Tunability (G/A)	3.66	4.67	2.05

Table D.1: Compensation coils parameters.

**Magnetic trap coils :** The magnetic gradient trapping the atoms is generated by a set of  $2 \times 2$  coils in anti-Helmholtz configuration, details can be found in [50]. A home made electronic circuit<sup>1</sup> lock the current flowing in the coils connected in series to produce the magnetic trapping potential. Throughout the sequence, the compliance voltage is adapted so it is not limiting the current while not being too high to minimize the voltage drop across the MOSFET of the circuit. Because of the slow response time ( $\approx 50$  ms) of the supply, fast switching ON and OFF of the current is accomplished by an IGBT (IXFN200N10P) in  $80 \mu s$ . Nevertheless, due to Eddy current, the magnetic field is only effectively canceled 6 ms later.

The total maximum magnetic gradient ( $B'$  in G/cm) onto the atoms is given by:

$$B' = 2.94 I_{MT} \quad (\text{D.1})$$

Gradients at different stages of the experiment are given table D.2. These coils, sustaining

Sequence step	$B'$ (G/cm)	$I_{meas}$ (A)	$I_{MT}$ (A)
MOT	10.67	3.76	3.6275
CMOT	22.43	7.78	7.6303
Molasses	0	0.0	0
MT abrupt	49.13	18.8	16.7126
MT final	161.6	53.9	54.9542
DT loading	28.18	10.4/9.98	9.5836
DT exp evap	24.48	$\emptyset$	8.3270

Table D.2: Value of the MT gradient during the experiment.  $I_{meas}$  has been measured with an ampere-meter clamp

up to 55 A during the RF-evaporation stages, are thermalized on water-cooled copper blocks. However, the plate temperature is monitored and we see that its temperature increase by several degrees under usage, which is the main limiting factor on the experimental cycling rate. The general monitoring system prevent coil overheating by directly disabling the power supply above  $30^\circ C$ .

**MW antenna :** For all the work presented in this thesis, MW transitions were almost only used for precise compensation of the magnetic field. Description of the complete MW apparatus and previous experiment using it is described in depth in [54, p.62].

Let's consider the two hyperfine ground state manifolds of  $5^2S_{1/2}$ ,  $|F_g = 1\rangle$  and  $|F_g = 2\rangle$ . We

<sup>1</sup>See [54, p.58].

note the bare transition (under no magnetic field) frequency  $\nu_0 = 6.834682$  GHz. Under a constant magnetic field  $\mathbf{B}_0$ , Zeeman effect give an energy splitting of the manifolds and the resulting transition  $|F_g = 1, m_F = m_i\rangle \rightarrow |F_g = 2, m_F = m_j\rangle$  resonance frequency will be at :

$$\nu_{i,j} = \nu_0 + \frac{\mu_B |\mathbf{B}_0|}{2\pi\hbar} (g_{F=2} m_j - g_{F=1} m_i) \quad (\text{D.2})$$

where  $g_{F=1} = -1/2$  and  $g_{F=2} = 1/2$  are the hyperfine Landé  $g$ -factor, and  $\mu_B$  the Bohr Magneton. For numeric, we recall that  $\frac{\mu_B |\mathbf{B}_0|}{2\pi\hbar} g_{F=2} = 700$  kHz/G.

Reducing the system to a two-level system, the probability of transferring atoms from  $|F_g = 1, m_F = m_i\rangle$  to  $|F_g = 2, m_F = m_j\rangle$  is given by a Rabi oscillation process [128] :

$$P(t) = \left( \frac{\Omega_{i,j}}{\tilde{\Omega}} \right)^2 \sin^2 \left( \frac{\tilde{\Omega} t}{2} \right) \quad (\text{D.3})$$

with  $\tilde{\Omega} = \sqrt{\Omega_{i,j}^2 + \delta^2}$  the generalized Rabi frequency,  $\Omega_{i,j}$  the resonant Rabi frequency and  $\delta = 2\pi(\nu_{i,j} - \nu_{MW})$  the detuning between the MW field and the transition frequency.

On resonance, we define a time  $\tau_\pi$  corresponding to a  $\pi$  pulse to transfer all the atoms from  $|F_g = 1\rangle$  to  $|F_g = 2\rangle$ . Starting with a spin polarized cloud in  $|F_g = 1, m_F = -1\rangle$  in a constant magnetic field  $\mathbf{B}_0$ , driving the MW Rabi oscillation at a frequency  $\nu_{MW}$  for a time  $\tau_\pi$  will give a maximum number of atoms transferred in  $|F_g = 2, m_F = -2\rangle$  when the transition is driven on resonance, so  $\nu = \nu_{MW}$ .

Experimentally, the MW signal is generated by mixing a 7 GHz PLDRO with a frequency doubled DDS output at 3.659 MHz. This signal is amplified up to 40.7 dBm and broadcast a horn antenna at 67 cm of the atom cloud. The polarization is linear along the OP direction and for a magnetic field along  $\mathbf{z}$ , the radiated field has equal  $\sigma^+$  and  $\sigma^-$  powers.

**Magnetic field zero :** Using MW transitions described in the section above, the magnetic field generated by the compensation coils can be precisely calibrated [52, 31]. Our calibration of magnetic field compensation is performed using two 1D scans per directions.

The calibration is realized using a cold cloud initially polarized in  $|F_g = 1, m_F = -1\rangle$  and all the compensating coils are driven according a rough field compensation. We send on the cloud a MW pulse of duration  $\tau_\pi$  (defined above) and measure the resulting number of atom in  $|F_g = 2\rangle$ . The initial resonant MW frequency  $\nu_{init}$  is obtained by fitting the transferred atom number while scanning the DDS output frequency  $f = 1/2(7 \text{ GHz} - \nu_{MW})$ . At the cloud position, the residual field is  $\mathbf{B}_0 = (B_{0,x}; B_{0,y}; B_{0,z})$ . On a given axis,  $\mathbf{x}$  for example, a fixed magnetic bias is applied around 500 mG such that  $B_{0,x} \gg B_{0,y}, B_{0,z}$ . The relative Zeeman shift conversion factor of  $|F_g = 1, m_F = -1\rangle \rightarrow |F_g = 2, m_F = -2\rangle$  is 2.1 MHz / G. Initially, we don't know the sign of the initial  $\mathbf{x}$  component of the field so we check the value of the shifted resonance  $\tilde{\nu}$  around both  $\nu_{init} \pm \frac{dB_x}{dV_x} \Delta V$ . This give an estimation at first order on the limited development of  $|\mathbf{B}| = |B_x| + \frac{B_{0,y}^2 + B_{0,z}^2}{B_x}$ . The same way we determined the initial resonance frequency, we scan the MW frequency around  $\tilde{\nu}$  to precisely know the associated resonant frequency  $\nu_{reso}$ . At this frequency, the magnetic field with an opposite component along  $\mathbf{x}$  is also resonant. Scanning the driving voltage of the compensating coils while having

the MW frequency constant at  $\nu_{reso}$ , give two peaks at  $V_{comp,x}^+$  and  $V_{comp,x}^-$  corresponding to a field  $\mathbf{B}^\pm = (\pm B_x; B_{0,y}; B_{0,z})$ . Because of the linearity of  $\frac{dB_x}{dV_x}$ , the average of this two voltages  $V_{comp,x} = (V_{comp,x}^+ + V_{comp,x}^-) / 2$  will produce a field on the atoms being :  $\mathbf{B} = (0; B_{0,y}; B_{0,z})$  no matter what the other components of the magnetic field are. By repeating this method for the three axis, the compensation can be adjusted to get a correct zero of magnetic field on the atomic position. With the updated driving voltages, we scan one last time the MW frequency to be sure that we are at the bare transition resonance.

In the  $x$  and  $y$  directions, the current is adjusted so the residual magnetic field on the atom is zero. For the  $z$  direction, an offset of 500 mG set the quantisation axis matching a  $\sigma^-$  imaging beam. The last calibration and final parameters are given table ???. Fine adjustment of the optical alignment can be further checked by looking at the expansion of the molasses with an holding time. Indeed, during this step, any optical miss-alignment will give a non-zero resulting force along one direction and thus the cloud will quickly expand. An optimal alignment gives more atoms initially and a better lifetime in the MOT, while reducing the heating during the molasses and OP stages.

## D.2.2 OP

After the molasses stage, we usually have  $3 \times 10^9$  atoms at  $30 \mu\text{K}$ , in both  $|F = 1\rangle$  and  $|F = 2\rangle$ . Following an Optical Pumping (OP) configuration, atoms are prepared toward  $|F_g = 1, m_F = -1\rangle$  which is trapped in the quadrupole magnetic trap (MT). First, atoms are de-pumped towards  $|F = 1\rangle$  using only cooler  $\sigma_-$  polarized 780 light. Then, adding a  $\sigma_-$  polarized beam tuned on the repumper transition, atoms are transferred in  $|F_g = 2, m_F = -2\rangle$  where  $|F_g = 1, m_F = -1\rangle$  is a dark state. Keeping only the cooler will then de-pump the atoms in  $|F_g = 1, m_F = -1\rangle$ . Dedicated coils ('OP coils') produce a bias field  $B_{OP}$  setting the quantization axis during these steps. With this scheme, we increase the number of atoms loaded in MT by a factor 1.6.

## D.3 Alignment of the 1529 nm accordion

In this section, we detail how the initial alignment of the accordion lattice setup has been made on the experimental apparatus. The two part of the accordion (forward and RR blocks) are installed on each side of the vacuum chamber. The forward block was installed on the upper breadboard on top of the 1064 where the beams free-space preparations are realized. The RR block was put on a dedicated breadboard (later referred to as prism breadboard) on the other side of the chamber, above the sub-wavelength imaging telescope. We first detail the alignment procedure before presenting the second characterization made on the atoms.

We first describe the optical alignment of the beams at 1064 and 1529 nm. We aim at having 'DT1' perpendicular to gravity, 500  $\mu\text{m}$  below the zero of MT and all lattices beams overlapping with 'DT1' on the atoms at better than a few microns. For that purpose we developed the alignment procedure detailed below.

- Cross dipole trap in 'DT1' and 'DT2'  
Before installing the setup, we aligned 'DT1' optical axis to be purely along  $\mathbf{y}$ , taking

into account a  $0.04^\circ$  tilt of the optical table with respect to gravity. The in-situ atom cloud position in a cross-dipole trap with 'DT1' and 'DT2' is measured using the different imaging axis, giving the reference for further alignments.

- '1064 Lattice'  
Directly measuring the beam centroid position, we geometrically align '1064 lattice' on 'DT1'.
- Lenses mounts  
Dedicated pinholes, made at the exact lens diameters, are used for the initial positioning of the lens mounts in the  $(\mathbf{x}, \mathbf{z})$  plane. For the focal direction, along  $\mathbf{y}$ , the mounts are mechanically placed so the distance between the atoms and the back of the mount match the back-focal length. Coarse adjustment of the mounts tilts are made by placing a mirror in it and retro-reflecting '1064 lattice'. For this step, we add a quarter wave-plate in front of the optical collimator so a PBS placed before the fiber injection will act as a free-space circulator, used to optimize the retro-reflection.
- 1529 forward beams  
'1529 R' is aligned on '1064 lattice' by sliding both PBS along  $-\mathbf{x}$  so the two beams overlap on PBS-R. For this step, we previously measured a deviation of the 1064 beam by the PBS cube of  $16 \mu\text{rad}$ , which is negligible because the corresponding misalignment on the atoms is of  $2 \mu\text{m}$  equals to the repeatability on the cloud position generally obtained using the imaging axis along DT1. Using a fiber optic circulator placed between the 1529 AOM and the free space collimator, M1 is aligned to retro-reflect '1529 R' and to re-inject the fiber. The PBS are slid back so '1529 R' and '1529 L' are symmetrical compared to '1064 lattice'.
- Lenses mounts fine tuning  
Fine tuning of the lens mounts positions in  $(\mathbf{x}, \mathbf{z})$  is made so that '1064 lattice' and 'DT1' optical axis are not deviated when placing the lenses in the mounts.
- Forward lens focus on the atoms  
The focus of the forward lens is adjusted such that '1529 R' will overlap with the cross dipole trap position both when it is close ( $\alpha_{small}$ ) and far from the horizontal optical axis of the lens ( $\alpha_{big}$ ). Using '1529 R' only, we move the incident 1529 beams on the PBS with translation T1 and adjust the lens position along  $\mathbf{y}$  to keep the beam aligned on the cross dipole trap.  
This alignment presented in Fig. D.3, is made by repumping atoms trapped in an homogeneous and large cloud (obtained generally by letting the MT expand) at the top of the modulation with a 1529 beam. Imaging this repumped cloud directly gives the spatial position of the beam. '1529 L' position is finally adjusted on the atoms<sup>2</sup> using the actuator of the '1529 forward RR mirror'. With this, the forward accordion setup is aligned.
- Prism alignment  
The prism is first aligned (translation and rotation along  $\mathbf{x}$  and rotation along  $\mathbf{y}$ ) by

---

<sup>2</sup>The two PBS reflecting surface are not exactly parallel so a perfect RR of '1529 R' on itself would lead to '1529 L' not aligned on the cross-dipole trap.

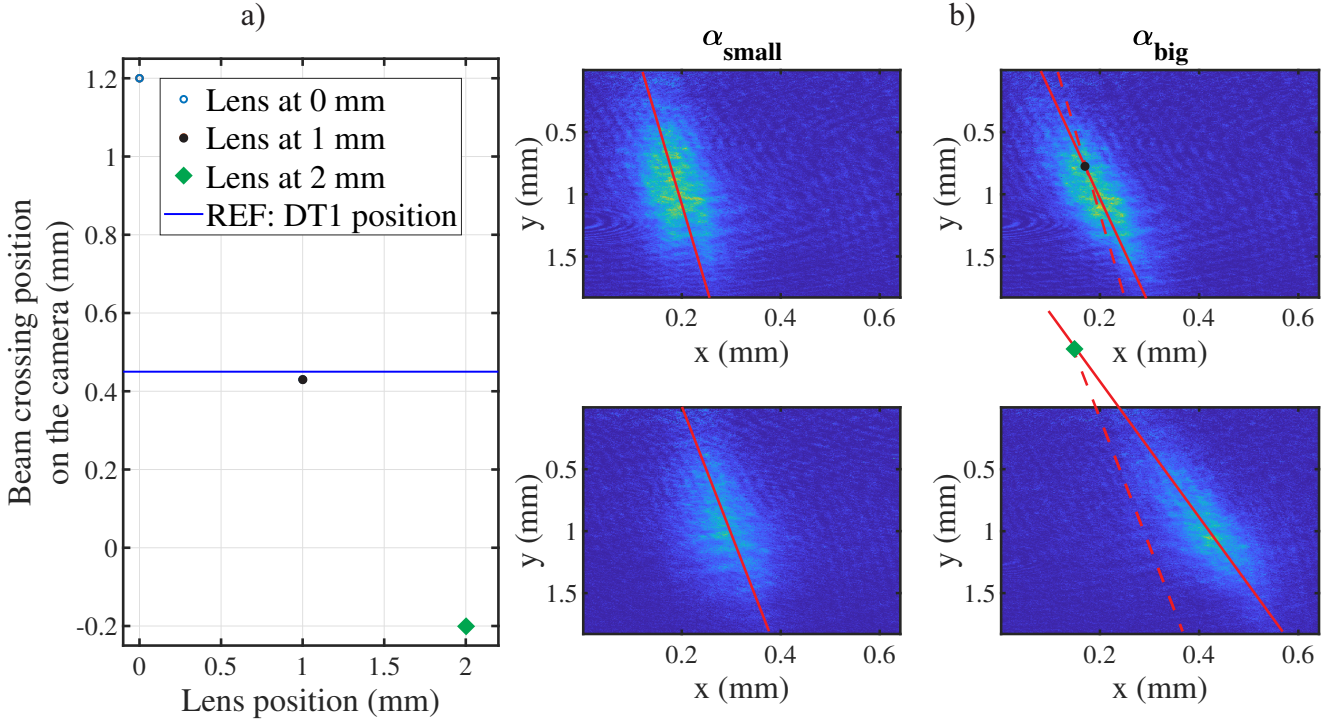


Figure D.3: Alignment of the focal position of the forward lens on the atoms using the imaging axis along DT1. a) Fitted position of the crossing of '1529 R' imaged at a small half-angle  $\alpha_{small}$  and for a bigger half-angle  $\alpha_{big}$  as a function of the lens displacement along  $\mathbf{y}$ . The focal is set such that the crossing is the position of atoms trapped in the cross-dipole trap with DT1 as a reference. b) 2D images corresponding to four of the six data used to plot the left curve. Plains lines indicate the cloud direction for  $\alpha_{big}$ . Dashed lines gives the cloud direction for  $\alpha_{small}$  and are reported on the high angle images.

retro-injecting the optical circulator. With a prism, the beam is always parallel to the incident beam, thus the position of the backward lens can be adjusted along  $\mathbf{y}$  so the focal point will be again on the trap center. This step is done for high incidence angle for a higher precision, which will automatically work for other angles. The prism is then aligned again using the previous method.

- 'Lattice RR'

Using the free-space circulator scheme mentioned above, '1064 lattice' is also retro-reflected by adjusting the piezo-actuated mirror mount holding the reflecting mirror. The 1064 RR mirror is glued to a piezo-electric stack in close-loop operation so the relative position of the two optical lattices can be controlled.

This conclude the backward setup alignment.

## D.4 Lab and coils temperature

### D.4.1 Hybrid trap loading dependency on the MT coils parameters

Even while being water-cooled, the temperature of the copper plate holding the magnetic gradient coils increase when cycling the experiment. This result in an atom number loss during the loading of the hybrid trap. We typically loose up to 60% of the atoms in 150 shots before reaching a steady state where fluctuations are down to a relative standard deviation of 8%. This effect is detrimental as it prevents Bose-Einstein condensation when the conditions are not optimal and reduce the SNR of the sub-wavelength imaging.

The number of atoms loaded in the hybrid trap dependency with the coils temperature and current is presented in Fig. D.4. We use the theoretical section C.1 to explain the decrease in the number of atoms loaded in the hybrid trap for lower gradient during the trap transfer. The Majorana loss rate  $\Gamma_m$  can be estimated following Eq. C.7. At  $B'_0 = 160 \text{ G/cm}$  and  $T_0 = 30 \mu\text{K}$ , we have  $\Gamma_m = 0.4 \text{ s}^{-1}$ . Lowering the magnetic gradient give a higher lifetime limited by Majorana, and given that all the RF evaporation and loading of the hybrid trap are made in less than 2 s in total, this shouldn't be a limiting factor and doesn't explain the difference. However, starting with the same atom number, lowering down the magnetic gradient during the RF evaporation steps give a less confined trap with a reduced collision rate. This impact further evaporation and make them less efficient. Also, according to Eq. C.6, starting from a higher magnetic gradient at the loading stage gives a lower temperature when reaching the same gradient, meaning reaching the crossover temperature  $T_l$  sooner. In our case, it seems like we are really limited by the two-body collision rate, allowing the cloud to thermalise and have an efficient evaporation, which is decreased for lower magnetic gradient.

For information, we need at least  $1.5 \times 10^7$  at the loading of the hybrid trap to reach a pure BEC with  $10^5$  atoms. We detail below the different test that were realized in order to understand the link between the atom number and the coils temperature.

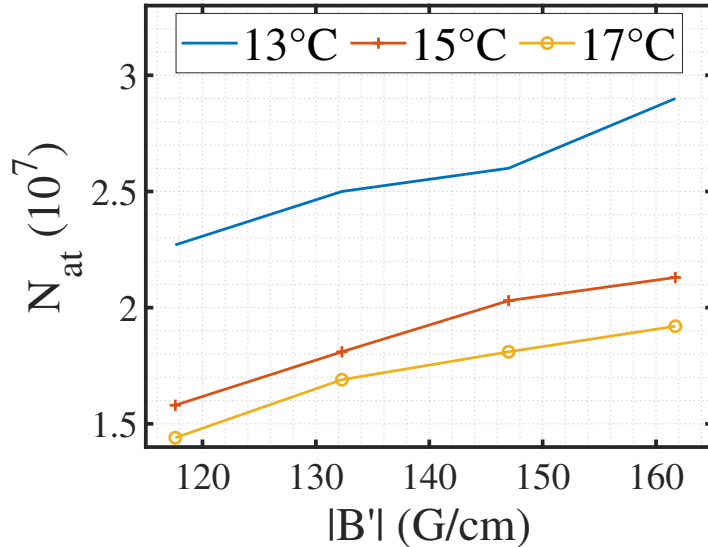


Figure D.4: Atom number loaded in the hybrid trap depending on the current in the magnetic gradient coils during the loading of DT1. The legend gives the chiller temperature setpoint of each curves.

### Investigation on the link parameter

- The current going in the MT coils is locked via the measurement of a voltage drop across a reference resistance in the lock-circuit. We cycled the experiment over 120 shots, with a break time of 45 s between each runs and with the MT current at 56 A during all the evap. Monitoring this resistance showed an slight increase in the measured voltage drop due to thermal effect modifying the resistivity. Monitoring of the actual current flowing through the coils with an amp-meter clamp shows a gradual increase of 0.06 A (0.13 %), which is too little to explain the atom number drift.
- Evolution of the center of MT could lead to a decrease in the number of atoms loaded. To rule out this hypothesis the alignment procedure has been carried while continuously cycling the experiment, keeping it 'hot'. The next day, after leaving it to rest for the night and thermalisation during cycling again, the same initial atom number decrease effect has been observed.
- A clear correlation can be seen in Fig. D.5 between the current in both ion pumps installed on the experiment and the temperature of the copper plate holding the MT coils. The decrease of the 3DMOT lifetime with the coils temperature, presented in Fig. D.6, seems to corroborate this hypothesis [55, 56].

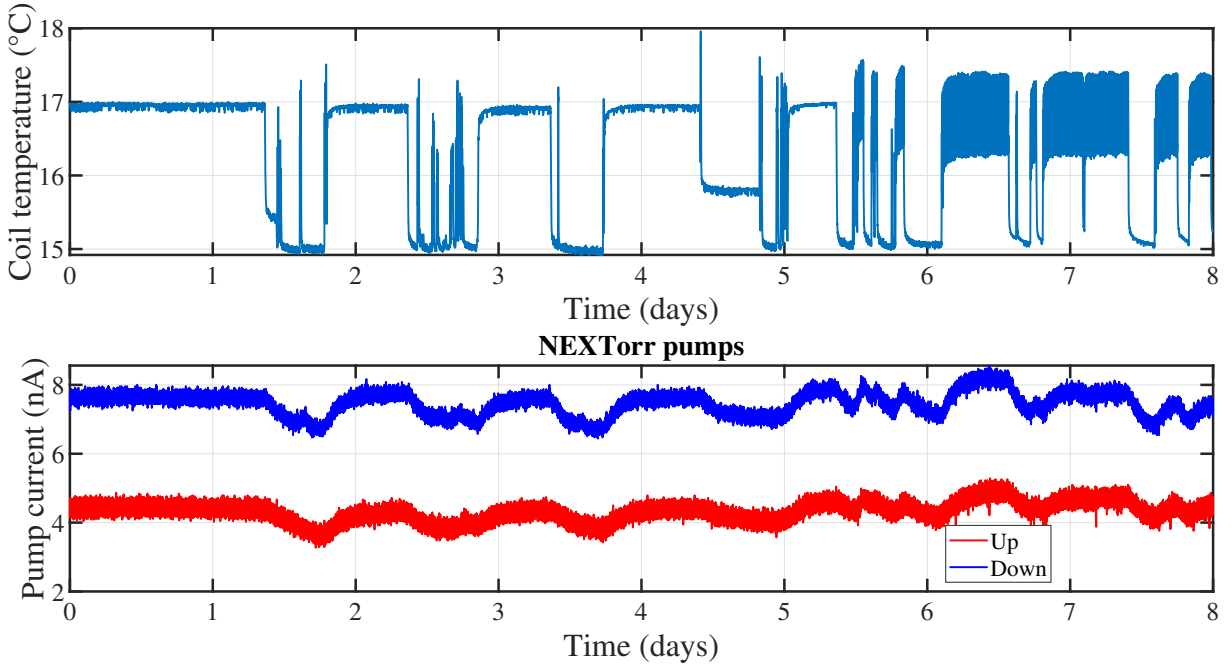


Figure D.5: Correlation between ion pump monitoring current and temperature of the copper plate holding the magnetic gradient coils. The NEX Torr pump labeled Up (lower level) is pumping the 2DMOT chamber. The pump labeled Down pump the science chamber.

In conclusion, we can say that the number of atom loaded in the Hybrid trap depend on the vacuum quality, which is affected by the temperature setpoint of the coils, through reducing the cloud lifetime in both the MOT and MT. Having a high magnetic gradient when loading the

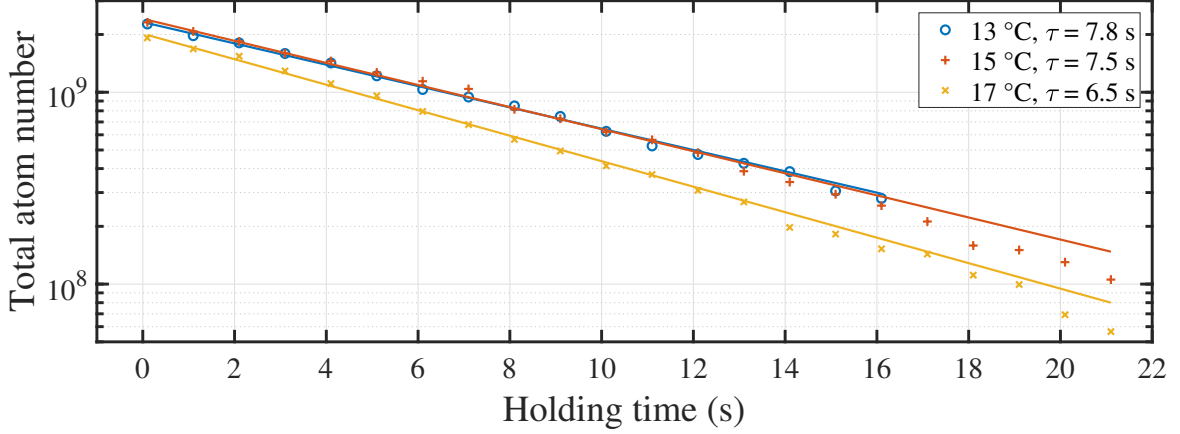


Figure D.6: Life-time scan in the 3DMOT for different temperature set-point of the magnetic gradient coils chiller. The data points (markers) are fitted by each straight lines as  $A \exp(-t/\tau)$ . At  $15^\circ\text{C}$ , a discrepancy can be observed for long holding time and a fit with  $\tau = 7.1 \text{ s}$  is closer to the last data points.

dipole trap is beneficial but also lead to a temperature increase when cycling the experiment so a balance between the two have to be found. Below, we present the solutions we have implemented to reduce this effect and still be quantitative on the atom number with no error on the first 50 to 100 experimental runs.

### Work-around solutions

- Chiller setpoint adjustment when launching a scan.

A first solution is to decrease the setpoint of the coils chiller just after launching a scan. We found that a temperature equilibrium could be conserved leading to a stable atom number. In Fig. D.7, the setpoint temperature is adjusted to have an constant average temperature of the copper plate holding the coils. This effectively balance the coils heating and give a constant atom number (in the shot-to-shot fluctuations).

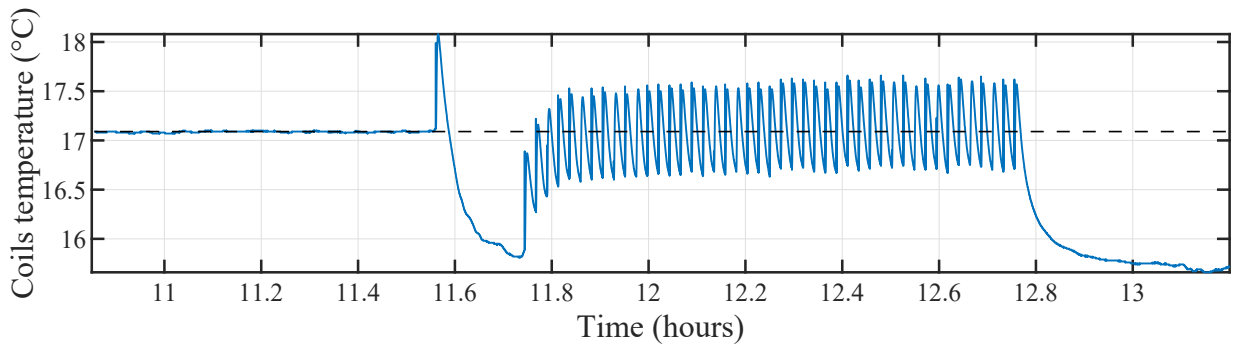


Figure D.7: Temperature evolution of the magnetic gradient coils. Just before launching a scan, the chiller setpoint is reduced by  $2^\circ\text{C}$ . The average temperature before the scan and during the scan are equals.

- Lowering the setpoint and decreasing the magnetic gradient during MTevap2. We see in Fig. D.4 that a decrease in the magnetic gradient from 160 G/cm (55 A) to 120 G/cm (40 A) can be compensating by lowering the chiller setpoint by 4 °C. At this current, the temperature increase while cycling the experiment is low enough not to impact the atom number significantly.

With such change, we load  $1.5 \times 10^7$  atoms in the hybrid trap. With optimization, we can reach  $N = 2.0 \times 10^7$ , value for which the BEC production is straightforward and very stable.

## D.4.2 Room temperature stabilization

The stability of the 1064 and 1529 nm lattices is critical and sensitive to temperature fluctuations of the lab. As monitored by a thermistance hanging around the chamber, we observe a correlation of the temperature with the AC cycles of 40 minutes (see Fig. D.8 a). The dissipation of the 1064 laser and the presence of people also affects the room temperature and the stability of the experimental conditions.

To improve the stability of the experiment we have limited the direct air-flow, and isolated the area around the science chamber by boxing the experiment, increasing the thermal inertia. This process is also referred to as 'boxing' the experiment. The prism breadboard is also independently boxed to further limit direct air-flows and temperature fluctuations.

The change has been done in two step, the first in April 2022 for which gaps were still remaining, and the second in February 2023 with improved isolation. On Fig. D.8 b), we see the thermal behavior when the curtains are closed. Initially at thermal equilibrium, we decrease at the beginning of the day the set-point of the coils chiller of 2 degrees, which also decrease the temperature inside the box. Toward the end of the day, we turned ON our dipole trap laser (the power supplies are out of the curtains but not the laser itself) so it can thermalise during the night, increasing the temperature around the science chamber. This long thermalisation step takes approximately 12 hours and is significant compared to the temperature stability reached afterwards. At equilibrium, we observe reduced fluctuations due to experimental runs, AC cycles and people going in and out of the experimental room.

In a second time, we moved away all the electronics from being on top of the experiment. This way, the curtains were straight with almost no gaps, surrounding nicely the science chamber and the different free-space optics around it. The resulting air temperature stability while having the curtains open or closed in this second configuration is presented Fig. D.9.

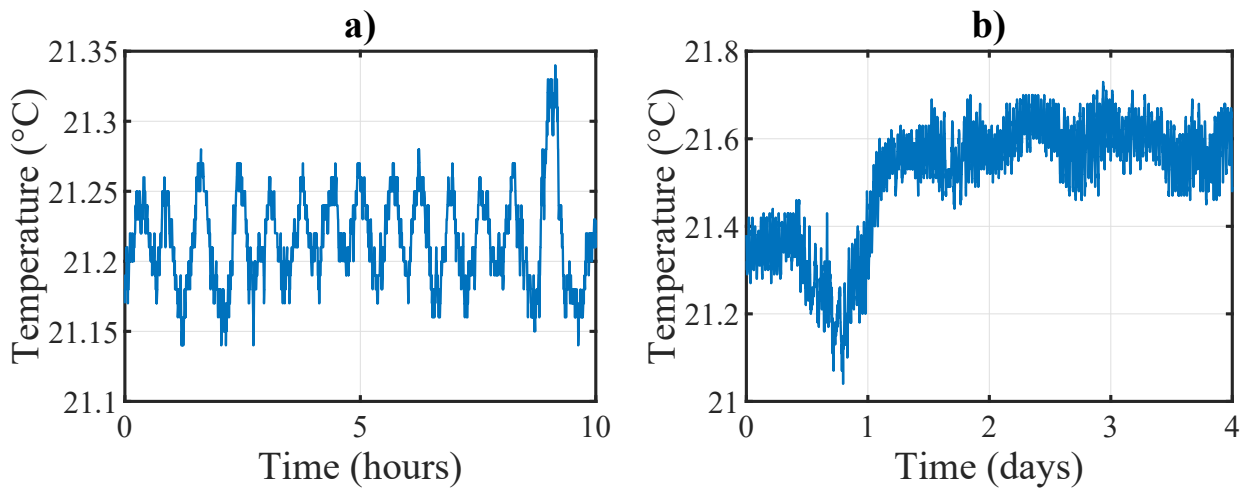


Figure D.8: Temperature of the air around the science chamber. a) When the thermal load is constant inside the room, temperature cycles due to the air conditioning are vivid. b) Typical thermalisation process when all the curtains are closed. After a little bit more than a day, a new thermal equilibrium is reached, giving a stability close to the one presented sub-figure a). Data were taken with the first version of the curtain box.

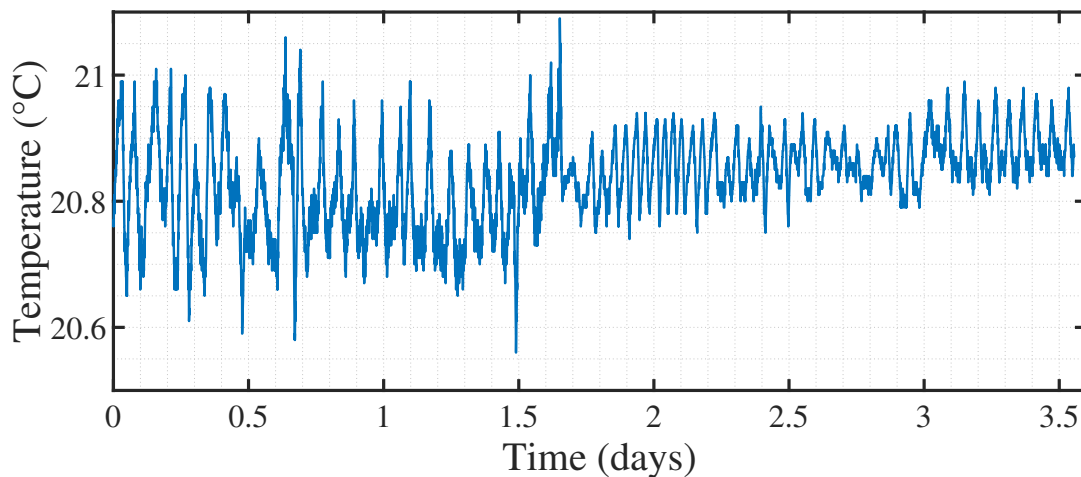


Figure D.9: Temperature stability reached when closing the curtains around the chamber. The curtains are closed a bit after day 1.5, reducing the peak-peak fluctuations from 0.4 K to 0.15 K.

## D.5 General monitoring

Running the experiment on a daily basis has its fair share of technical difficulties and in order to work as efficiently as possible, one should reduce the number of variables that has to be independently checked all the time. For that purpose, we implemented a general monitoring system of various elements. This allows to quickly check them at once and also verify specific parameters while doing data-analysis if needed.

An Arduino DUE, with 12 analog inputs, is equipped with an ethernet shield 2 and stream data via an ethernet cable to the main computer. A dedicated Matlab program is continuously running to read the received packets and storing them in a .txt log file. Two extra commands are implemented. The first is if the channel monitoring the room air temperature exceed a threshold value, the program send an automatic e-mail to specified addresses. This allows to detect quickly AC failure to solve the issue, limiting the maximum temperature increase. The second one is to disable the magnetic gradient coils power supply if the coils exceed a given temperature, to prevent overheating. Previously, the Arduino was streaming to the computer via USB but this often generated bug, and the Arduino had to be manually relaunched. Table D.3

Analog channel	Monitoring
0	Magnetic gradient coils temperature
1	Room temperature
2 - 3	Ion pump UP current (close to 2DMOT)
4 - 5	Ion pump DOWN current (close to DT2)
6	Accordion RR breadboard temperature
7	PDH Cavity transmission
8	S2 power-lock actual value
9	S1 power-lock actual value
10	Master power-lock actual value
11	∅

Table D.3: List of the analog input channel of the Arduino used for general monitoring .

# Appendix E

## Beam position measurement on a photo-diode edge

In this section, we detail the derivation of the calculus giving angular fluctuations of a reflective surface from the photo-diode signal according to method 1 presented in Fig. ?? a).

Assuming a Gaussian beam, the power collected in a rectangular opening is analytical. As shown in figure ??, we consider a laser beam centered on  $(x_0; y_0)$ , of waist  $w_0$ , illuminating a captor extending from  $y_1$  to  $y_2$  in one direction and from  $x_1$  to  $x_2$  in the other. The measured power is :

$$P_{det} = \int_{x_1}^{x_2} \int_{y_1}^{y_2} I(x, y) dx dy = \frac{P_0}{4} [erf(X_2) - erf(X_1)] [erf(Y_2) - erf(Y_1)] \quad (\text{E.1})$$

with  $erf(x) = \frac{2}{\sqrt{\pi}} \int_0^x e^{-t^2} dt$ , the error function,  $P_0$  the total power of the beam in Watt,  $X_2 = \frac{\sqrt{2}(x_2-x_0)}{w_0}$ ,  $X_1 = \frac{\sqrt{2}(x_1-x_0)}{w_0}$ ,  $Y_2 = \frac{\sqrt{2}(y_2-y_0)}{w_0}$ ,  $Y_1 = \frac{\sqrt{2}(y_1-y_0)}{w_0}$ . The derivative of the error function being maximum around zero, the highest sensitivity is reached for  $x_2 = x_0$ . Hence our choice to center the beam on one edge of the detector. The photo-diode response in  $V$  can be written as :

$$V_{PD} = \eta P_{det} G \quad (\text{E.2})$$

with  $\eta$  the quantum efficiency of the detector,  $P_{det}$  the optical power in W captured on the detector and  $G$  the conversion factor (or gain) of the amplification stage at a given wavelength in V/W.

We assume that the beam is centered on the detector in the  $y$  direction and that there is no instability in this direction. We have then  $erf(Y_2) - erf(Y_1) = c_y$ . We set the detector at a distance  $D$  of the rotation axis, as illustrated in Fig. ?. The relation between the beam position  $x(t)$  and the angle of the surface  $\theta(t)$  is given by :

$$\tan(2(\theta(t) - \theta_0)) = \frac{x(t) - x_0}{D} \quad (\text{E.3})$$

where  $\theta_0$  is the reference angle for which the reflected beam is at  $x_0$ .

Assuming a constant rotation speed  $\Omega_m$ , the angular evolution starting from  $\theta_0$  at  $t_0$  is :

$$\theta(t) = \bar{\theta}(t) + \delta\theta(t) = \theta_0 + \Omega_m (t - t_0) + \delta\theta(t) \quad (\text{E.4})$$

In the following, we take  $t_0 = 0$ .

Since  $\delta\theta(t)$  describes angular fluctuations, we perform a first order Taylor expansion and using Eq. E.1 and E.2, we have :

$$\begin{aligned} V_{PD}(t) &= V_{PD}(\bar{\theta}(t) + \delta\theta(t)) = V(\bar{\theta}(t)) + \frac{dV}{d\theta}(\bar{\theta}(t))\delta\theta(t) \\ &= \alpha_{PD} \left\{ \text{erf} \left[ \frac{-\sqrt{2}}{w_0} D \tan(2(\theta(t) - \theta_0)) \right] - \text{erf} \left[ \frac{-\sqrt{2}}{w_0} (p_x + D \tan(2(\theta(t) - \theta_0))) \right] \right\} \end{aligned} \quad (\text{E.5})$$

with  $p_x = x_2 - x_1$  the pixel size in the  $x$  direction,  $\alpha_{PD} = \eta G \frac{P_0}{4} c_y$  and  $V(\theta)$  the analytic function giving the voltage measured by the detector in the absence of fluctuations.

Taking the derivative of  $V$  give :

$$\frac{dV}{d\theta}(\theta) = \alpha_{PD} \frac{\sqrt{2}}{w_0} \frac{2}{\cos^2(2(\theta - \theta_0))} \frac{2D}{\sqrt{\pi}} \left( e^{-\frac{2}{w_0^2}(p_x + D \tan(2(\theta - \theta_0)))^2} - e^{-\frac{2}{w_0^2}(D \tan(2(\theta - \theta_0)))^2} \right)$$

The angular fluctuations are then given by

$$\delta\theta(t) = \frac{V_{PD}(t) - V(\bar{\theta}(t))}{\frac{dV}{d\theta}(\bar{\theta}(t))} \quad (\text{E.6})$$

We evaluate the precision of this first order approximation with numerical simulations. Normalized white noises of different amplitude ( $A$ ) are generated for  $\delta\theta$  and we compute the error made with our approximations. We note  $\delta\theta_{comp}$  the angle fluctuations retrieved with formula 3.43. These simulations confirm some intuitive ideas :

- For a fixed angle scan, the accumulated error  $(\delta\theta_{th} - \delta\theta_{comp})/A$  increases with the amplitude of the noise because the truncated higher order terms in the limited development in  $\delta\theta$  have increasing importance.
- The error on  $\delta\theta$  increases with the average angle : the further we are from one edge of the detector, the lower the sensitivity and the higher the error. This setup is quite simple and gave interesting results on the single step or stopping behavior. Nevertheless, it is not very suited for studying the dynamic of the motor over a significant range of angles as illustrated with the numerical simulations. Indeed, a usable signal can only be obtained for a displacement of roughly two waist, that can be chosen up to the pixel size. In the experiment, we used an amplified photo-diode [PDA36A2](#) with a pixel size of 3.6 mm, and at a distance  $D = 0.3$  m of the surface you have sensitivity over an angle of 6 mrad. For

---

reference, the first motor we used has a step of 0.78 mrad. We expect on one edge of the photo-diode to resolve a few 14 steps (more or less the case, see Fig. 3.13 a) ). This signal can be taken on both edges of the photo-diode, for the beam sweeping through the all detector, doubling the total acquisition time for extracting fluctuations.



# Bibliography

- [1] Einstein, A. (ed.) *Albert Einstein: Akademie-Vorträge: Sitzungsberichte der Preußischen Akademie der Wissenschaften 1914-1932* (Wiley-VCH, Weinheim, 2006).
- [2] Anderson, M. H., Ensher, J. R., Matthews, M. R., Wieman, C. E. & Cornell, E. A. Observation of bose-einstein condensation in a dilute atomic vapor. *Science (New York, N. Y.)* **269**, 198–201 (1995).
- [3] MAIMAN, T. H. Stimulated optical radiation in ruby. *Nature* **187**, 493–494 (1960). URL <https://www.nature.com/articles/187493a0>.
- [4] Frisch, R. Experimenteller nachweis des einsteinschen strahlungsrekts. *Zeitschrift für Physik* **86**, 42–48 (1933). URL <https://link.springer.com/article/10.1007/BF01340182>.
- [5] Grimm, R., Weidemüller, M. & Ovchinnikov, Y. B. Optical dipole traps for neutral atoms. In *ScienceDirect*, vol. 42, 95–170. URL [https://doi.org/10.1016/S1049-250X\(08\)60186-X](https://doi.org/10.1016/S1049-250X(08)60186-X).
- [6] Metcalf, H. J. & van der Straten, P. Laser cooling and trapping of atoms. *Journal of the Optical Society of America B* **20**, 887 (2003).
- [7] Leggett, A. J. What do we know about high  $t_c$ ? *Nature Physics* **2**, 134–136 (2006). URL <https://www.nature.com/articles/nphys254>.
- [8] Haldane, F. D. Model for a quantum hall effect without landau levels: Condensed-matter realization of the "parity anomaly". *Physical review letters* **61**, 2015–2018 (1988).
- [9] Billy, J. *et al.* Direct observation of anderson localization of matter waves in a controlled disorder. URL <https://arxiv.org/pdf/0804.1621>.
- [10] Lahini, Y. *et al.* Observation of a localization transition in quasi-periodic photonic lattices. *Frontiers in Optics FThJ2* (2008).
- [11] Schwartz, T., Bartal, G., Fishman, S. & Segev, M. Transport and anderson localization in disordered two-dimensional photonic lattices. *Nature* **446**, 52–55 (2007). URL <https://www.nature.com/articles/nature05623>.
- [12] Feynman, R. P. Simulating physics with computers. *International Journal of Theoreti-*

- cal Physics* **21**, 467–488 (1982). URL <https://link.springer.com/article/10.1007/BF02650179>.
- [13] Daley, A. J. *et al.* Practical quantum advantage in quantum simulation. *Nature* **607**, 667–676 (2022). URL <https://www.nature.com/articles/s41586-022-04940-6>.
- [14] Arute, F. *et al.* Quantum supremacy using a programmable superconducting processor. *Nature* **574**, 505–510 (2019). URL <https://www.nature.com/articles/s41586-019-1666-5>.
- [15] You, J. Q. & Nori, F. Atomic physics and quantum optics using superconducting circuits. *Nature* **474**, 589–597 (2011). URL <https://www.nature.com/articles/nature10122>.
- [16] Ku, L.-C. & Yu, C. C. Decoherence of a josephson qubit due to coupling to two-level systems. *Physical Review B* **72**, 024526 (2005).
- [17] Aspuru-Guzik, A. & Walther, P. Photonic quantum simulators. *Nature Physics* **8**, 285–291 (2012). URL <https://www.nature.com/articles/nphys2253>.
- [18] Trisnadi, J., Zhang, M., Weiss, L. & Chin, C. Design and construction of a quantum matter synthesizer. *Review of Scientific Instruments* **93**, 083203 (2022). URL <http://arxiv.org/pdf/2205.10389v1>.
- [19] Browaeys, A. & Lahaye, T. Many-body physics with individually controlled rydberg atoms. *Nature Physics* **16**, 132–142 (2020). URL <https://www.nature.com/articles/s41567-019-0733-z>.
- [20] Antoni-Micollier, L. *et al.* Detecting volcano-related underground mass changes with a quantum gravimeter. *Geophysical Research Letters* **49** (2022).
- [21] Scholl, P. *et al.* Quantum simulation of 2d antiferromagnets with hundreds of rydberg atoms. *Nature* **595**, 233–238 (2021). URL <https://www.nature.com/articles/s41586-021-03585-1>.
- [22] Schymik, K.-N. *et al.* In situ equalization of single-atom loading in large-scale optical tweezer arrays. *Physical Review A* **106** (2022).
- [23] Farkas, D. M., Salim, E. A. & Ramirez-Serrano, J. Production of rubidium bose-einstein condensates at a 1 hz rate. URL <https://arxiv.org/pdf/1403.4641>.
- [24] Straatsma, C. J. E. *et al.* On-chip optical lattice for cold atom experiments. *Optics Letters* **40**, 3368–3371 (2015).
- [25] Zwerger, W. Mott hubbard transition of cold atoms in optical lattices. *Journal of Optics B: Quantum and Semiclassical Optics* **5**, S9–S16 (2003). URL <https://iopscience.iop.org/article/10.1088/1464-4266/5/2/352>.
- [26] M. Greiner. *Ultracold quantum gases in three-dimensional optical lattice potentials*. Ph.D. thesis.

- 
- [27] Casimir, H. B. G. & Polder, D. The influence of retardation on the london-van der waals forces. *Physical Review* **73**, 360–372 (1948).
- [28] Chang, D. E., Sinha, K., Taylor, J. M. & Kimble, H. J. Trapping atoms using nanoscale quantum vacuum forces. *Nature Communications* **5**, 4343 (2014). URL <https://www.nature.com/articles/ncomms5343>.
- [29] Maxime Bellouvet *et al.* Doubly dressed states for near-field trapping and subwavelength lattice structuring .
- [30] Dalibard, J. & Cohen-Tannoudji, C. Dressed-atom approach to atomic motion in laser light: the dipole force revisited. *JOSA B* **2**, 1707 (1985).
- [31] Bellouvet, M. *Condensation de Bose-Einstein et simulation d’une méthode de piégeage d’atomes froids dans des potentiels sublongueur d’onde en champ proche d’une surface nanostructurée*. Ph.D. thesis.
- [32] Heintzmann, R. & Huser, T. Super-resolution structured illumination microscopy. *Chemical reviews* **117**, 13890–13908 (2017).
- [33] Vicidomini, G., Bianchini, P. & Diaspro, A. Sted super-resolved microscopy. *Nature Methods* **15**, 173–182 (2018). URL <https://www.nature.com/articles/nmeth.4593>.
- [34] Bakr, W. S., Gillen, J. I., Peng, A., Fölling, S. & Greiner, M. A quantum gas microscope for detecting single atoms in a hubbard-regime optical lattice. *Nature* **462**, 74–77 (2009). URL <https://www.nature.com/articles/nature08482>.
- [35] McDonald, M., Trisnadi, J., Yao, K.-X. & Chin, C. Superresolution microscopy of cold atoms in an optical lattice. *Physical Review X* **9** (2019).
- [36] Subhankar, S., Wang, Y., Tsui, T.-C., Rolston, S. L. & Porto, J. V. Nanoscale atomic density microscopy. *Physical review. X* **9** (2019).
- [37] Weitenberg, C. *et al.* Single-spin addressing in an atomic mott insulator. *Nature* **471**, 319–324 (2011). URL <https://www.nature.com/articles/nature09827>.
- [38] Händel, S., Marchant, A. L., Wiles, T. P., Hopkins, S. A. & Cornish, S. L. Magnetic transport apparatus for the production of ultracold atomic gases in the vicinity of a dielectric surface. *The Review of scientific instruments* **83**, 013105 (2012).
- [39] Nakagawa, K., Suzuki, Y., Horikoshi, M. & Kim, J. B. Simple and efficient magnetic transport of cold atoms using moving coils for the production of bose–einstein condensation. *Applied Physics B* **81**, 791–794 (2005). URL <https://link.springer.com/article/10.1007/s00340-005-1953-8>.
- [40] Lahaye, T., Reinaudi, G., Wang, Z., Couvert, A. & Guéry-Odelin, D. Transport of atom packets in a train of ioffe-pritchard traps. *Physical Review A* **74**, 033622 (2006).
- [41] Minniberger, S. *et al.* Magnetic conveyor belt transport of ultracold atoms to a su-

- perconducting atomchip. *Applied Physics B* **116**, 1017–1021 (2014). URL <http://arxiv.org/pdf/1311.3155v2>.
- [42] Roy, R., Condylis, P. C., Prakash, V., Sahagun, D. & Hessmo, B. A minimalistic and optimized conveyor belt for neutral atoms. *Scientific Reports* **7**, 13660 (2017). URL <https://www.nature.com/articles/s41598-017-13959-z>.
- [43] Folman *et al.* Controlling cold atoms using nanofabricated surfaces: atom chips. *Physical review letters* **84**, 4749–4752 (2000).
- [44] Reichel, J. Microchip traps and bose–einstein condensation. *Applied Physics B* **74**, 469–487 (2002).
- [45] Gustavson, T. L. *et al.* Transport of bose-einstein condensates with optical tweezers. *Physical review letters* **88**, 020401 (2002).
- [46] Schrader, D. *et al.* An optical conveyor belt for single neutral atoms. *Applied Physics B* **73**, 819–824 (2001). URL <https://link.springer.com/article/10.1007/s003400100722>.
- [47] Schmid, S., Thalhammer, G., Winkler, K., Lang, F. & Denschlag, J. H. Long distance transport of ultracold atoms using a 1d optical lattice. *New Journal of Physics* **8**, 159 (2006). URL <https://iopscience.iop.org/article/10.1088/1367-2630/8/8/159>.
- [48] Dimova, E. *et al.* Continuous transfer and laser guiding between two cold atom traps. *The European Physical Journal D* **42**, 299–308 (2007). URL <https://link.springer.com/article/10.1140/epjd/e2007-00022-0>.
- [49] Pritchard, M. J. *et al.* Transport of launched cold atoms with a laser guide and pulsed magnetic fields. *New Journal of Physics* **8**, 309 (2006). URL <https://iopscience.iop.org/article/10.1088/1367-2630/8/12/309>.
- [50] Busquet, C. *Développement d’un système d’imagerie superrésolue d’un gaz d’atomes ultrafroids piégés dans des réseaux*. Ph.D. thesis, Bordeaux. URL <https://www.theses.fr/2017BORD0749>.
- [51] Vasquez Bullon, H. S. *Construction d’une nouvelle expérience pour l’étude de gaz quantiques dégénérés des réseaux optiques, et étude d’un système d’imagerie super-résolution*. Ph.D. thesis, Bordeaux and Bordeaux. URL <https://www.theses.fr/2016BORD0035>.
- [52] Caroline Busquet. *Busquet\_V3\_SB*. Ph.D. thesis.
- [53] Bellouvet, M. Condensation de bose-einstein et simulation d’une méthode de piégeage d’atomes froids dans des potentiels sublongueur d’onde en champ proche d’une surface nanostructurée (2018).
- [54] Romain Veyron. *Subwavelength imaging of optically dense atomic clouds in a quantum gas microscope*. Ph.D. thesis (2021).
- [55] Arpornthip, T., Sackett, C. A. & Hughes, K. J. Vacuum-pressure measurement using a

- magneto-optical trap. *Physical Review A* **85** (2012).
- [56] Moore, R. W. G. *et al.* Measurement of vacuum pressure with a magneto-optical trap: A pressure-rise method. *The Review of scientific instruments* **86**, 093108 (2015).
- [57] Prentiss, M. *et al.* Atomic-density-dependent losses in an optical trap. *Optics letters* **13**, 452–454 (1988).
- [58] Scherschligt, J. *et al.* Development of a new uhv/xhv pressure standard (cold atom vacuum standard). *Metrologia* **54**, S125–S132 (2017).
- [59] Ness, G., Vainbaum, A., Shkedrov, C., Florshaim, Y. & Sagi, Y. Single-exposure absorption imaging of ultracold atoms using deep learning. *Physical Review Applied* **14** (2020).
- [60] Veyron, R. *et al.* Effective two-level approximation of a multilevel system driven by coherent and incoherent fields. *Physical Review A* **105**, 043105 (2022).
- [61] Veyron, R. *et al.* Quantitative absorption imaging: The role of incoherent multiple scattering in the saturating regime. *Physical Review Research* **4** (2022).
- [62] Romain Veyron. *Subwavelength imaging of optically dense atomic clouds in a quantum gas microscope*. Ph.D. thesis, Université de Bordeaux and Université de Bordeaux (02/06/2022). URL <https://theses.hal.science/tel-03685203>.
- [63] Lin, Y. J., Perry, A. R., Compton, R. L., Spielman, I. B. & Porto, J. V. Rapid production of  $^{87}\text{Rb}$  becs in a combined magnetic and optical potential. *Physical Review A* **79**, 181 (2009). URL <http://arxiv.org/pdf/0904.3314v1>.
- [64] Pitaevskii, L. P. Dynamics of collapse of a confined bose gas. *Physics Letters A* **221**, 14–18 (1996). URL <https://www.sciencedirect.com/science/article/pii/0375960196005385>.
- [65] Corgier, R. *et al.* Fast manipulation of bose–einstein condensates with an atom chip. *New Journal of Physics* **20**, 055002 (2018).
- [66] Bernon, S. *Piégeage et mesure non-destructive d’atomes froids dans une cavité en anneau de haute finesse*. Ph.D. thesis, Palaiseau, Ecole polytechnique. URL <https://www.theses.fr/2011EPXX0034>.
- [67] W. Ketterle. Making, probing and understanding bose–einstein condensates .
- [68] Li, T. C., Kelkar, H., Medellin, D. & Raizen, M. G. Real-time control of the periodicity of a standing wave: an optical accordion. *Optics express* **16**, 5465–5470 (2008).
- [69] Ville, J. L. *et al.* Loading and compression of a single two-dimensional bose gas in an optical accordion. *Physical Review A* **95**, 013632 (2017).
- [70] Bertoldi, A., Bernon, S., Vanderbruggen, T., Landragin, A. & Bouyer, P. In situ characterization of an optical cavity using atomic light shift. *Optics Letters* **35**, 3769–3771

- (2010).
- [71] Black, E. D. An introduction to pound–drever–hall laser frequency stabilization. *American Journal of Physics* **69**, 79–87 (2001).
- [72] Rudenberg, H. G. & Rudenberg, P. G. Origin and background of the invention of the electron microscope **160**, 207–286.
- [73] Erni, R. P. Atomic resolution imaging with a sub-50 pm electron probe .
- [74] Yue, L. *et al.* Image super-resolution: The techniques, applications, and future. *Signal Processing* **128**, 389–408 (2016). URL <https://www.sciencedirect.com/science/article/pii/S0165168416300536>.
- [75] Steck, D. A. Alkali d line data .
- [76] Wen, J., Zhang, Y. & Xiao, M. The talbot effect: recent advances in classical optics, nonlinear optics, and quantum optics. *Advances in Optics and Photonics* **5**, 83 (2013).
- [77] Ashcroft, N. W. & Mermin, N. D. *Solid state physics* (Brooks / Cole Cengage Learning, Belmont (Calif.), 1976).
- [78] Wannier, G. H. The structure of electronic excitation levels in insulating crystals. *Physical Review* **52**, 191–197 (1937).
- [79] Gardiner, C. W. & Zoller, P. *The quantum world of ultra-cold atoms and light*, vol. vol. 5 of *Cold atoms* (World Scientific, New Jersey etc., 2017).
- [80] Kohn, W. Analytic properties of bloch waves and wannier functions. *Physical Review* **115**, 809–821 (1959).
- [81] D. Jaksch, C. Bruder, J. I. Cirac, C. W. Gardiner, and P. Zoller. Cold bosonic atoms in optical lattices (1998).
- [82] Saint-Jalm, R. *et al.* Dynamical symmetry and breathers in a two-dimensional bose gas. *Physical review. X* **9** (2019).
- [83] Cataliotti, F. S. *et al.* Josephson junction arrays with bose-einstein condensates. *Science (New York, N.Y.)* **293**, 843–846 (2001).
- [84] Ben, D. M., Peik, E., Reichel, J., Castin, Y. & Salomon, C. Bloch oscillations of atoms in an optical potential. *Physical review letters* **76**, 4508–4511 (1996).
- [85] Denschlag, J. H. *et al.* A bose-einstein condensate in an optical lattice. *Journal of Physics B: Atomic, Molecular and Optical Physics* **35**, 3095–3110 (2002).
- [86] Band, Y. B., Malomed, B. & Trippenbach, M. Adiabaticity in nonlinear quantum dynamics: Bose-einstein condensate in a temporally-varying box. URL <https://arxiv.org/pdf/cond-mat/0108114>.

- [87] Gericke, T. *et al.* Adiabatic loading of a bose–einstein condensate in a 3d optical lattice. *Journal of Modern Optics* **54**, 735–743 (2007).
- [88] Trippenbach, M., Band, Y. B. & Julienne, P. S. Theory of four-wave mixing of matter waves from a bose-einstein condensate. *Physical Review A* **62** (2000).
- [89] H. K. Andersen. Bose-einstein condensates in optical lattices (2008). URL <https://www.semanticscholar.org/paper/Bose-Einstein-condensates-in-optical-lattices-Andersen/92e8eaced5a1cc5dd338e012aee4537e8d3cbe80>.
- [90] Davis, J. R. *Metals handbook* (ASM International, Materials Park, 1998), 2nd ed. edn.
- [91] Amico, L. *et al.* Roadmap on atomtronics: State of the art and perspective. *AVS Quantum Science* **3**, 039201 (2021).
- [92] Reichel, J., Hänsel, W., Hommelhoff, P. & Hänsch, T. W. Applications of integrated magnetic microtraps. *Applied Physics B* **72**, 81–89 (2001).
- [93] Schneider, S. *et al.* Bose-einstein condensation in a simple microtrap. *Physical Review A* **67** (2003).
- [94] Alibert, J., Décamps, B., Bordoux, M., Allard, B. & Gauguier, A. A millimeter magnetic trap for a dual (85rb and 87rb) species atom interferometer. *The Review of scientific instruments* **88**, 113115 (2017).
- [95] Rowe, M. A. *et al.* Transport of quantum states and separation of ions in a dual rf ion trap (2002). URL <https://arxiv.org/pdf/quant-ph/0205094>.
- [96] Reichle, R. *et al.* Transport dynamics of single ions in segmented microstructured paul trap arrays. *Fortschritte der Physik* **54**, 666–685 (2006).
- [97] Lewandowski, H. J., Harber, D. M., Whitaker, D. L. & Cornell, E. A. Simplified system for creating a bose–einstein condensate. *Journal of Low Temperature Physics* **132**, 309–367 (2003). URL <https://link.springer.com/article/10.1023/A:1024800600621>.
- [98] Kuhr, S. *et al.* Deterministic delivery of a single atom. *Science (New York, N.Y.)* **293**, 278–280 (2001).
- [99] Schmidt, S., Muga, J. G. & Ruschhaupt, A. Stopping particles of arbitrary velocities with an accelerated wall. *Physical Review A* **80**, 023406 (2009).
- [100] Sophocles J. Orfanidis. *Electromagnetic Waves and Antennas* (1999-2016). URL [www.ece.rutgers.edu/~orfanidi/ewa](http://www.ece.rutgers.edu/~orfanidi/ewa).
- [101] Yakubovsky, D. I., Arsenin, A. V., Stebunov, Y. V., Fedyanin, D. Y. & Volkov, V. S. Optical constants and structural properties of thin gold films. *Optics express* **25**, 25574–25587 (2017).

- [102] P. B. Johnson and R. W. Christy. Optical constants of the noble metals .
- [103] Ness, G., Shkedrov, C., Florshaim, Y. & Sagi, Y. Realistic shortcuts to adiabaticity in optical transfer. *New Journal of Physics* **20**, 1 (2018).
- [104] Savard, T. A., O'Hara, K. M. & Thomas, J. E. Laser-noise-induced heating in far-off resonance optical traps. *Physical Review A* **56**, R1095–R1098 (1997).
- [105] Pippard, A. B. (ed.) *The physics of vibration - Vol.2* (Cambridge University press, Cambridge and New York and Melbourne, 1983).
- [106] Gehm, M. E., O'Hara, K. M., Savard, T. A. & Thomas, J. E. Dynamics of noise-induced heating in atom traps. *Physical Review A* **58**, 3914–3921 (1998).
- [107] Steck, D. A. Quantum and atom optics (2019).
- [108] P. Gaudenzi, A. Meschini & A. Scipioni. Design and analysis of a travelling wave ultrasonic motor for space applications .
- [109] Hiroshi Hirata and Sadayuki Ueha. Design of a traveling wave type ultrasonic motor .
- [110] Hagedorn, P. & Wallaschek, J. Travelling wave ultrasonic motors, part i: Working principle and mathematical modelling of the stator. *Journal of Sound and Vibration* **155**, 31–46 (1992).
- [111] Reichel, J., Hänsel, W. & Hänsch, T. W. Atomic micromanipulation with magnetic surface traps. *Physical review letters* **83**, 3398–3401 (1999).
- [112] Hänsel, W., Hommelhoff, P., Hänsch, T. W. & Reichel, J. Bose–einstein condensation on a microelectronic chip. *Nature* **413**, 498–501 (2001).
- [113] Ott, H., Fortagh, J., Schlotterbeck, G., Grossmann, A. & Zimmermann, C. Bose-einstein condensation in a surface microtrap. *Physical review letters* **87**, 230401 (2001).
- [114] Amri, S. *et al.* Optimal control of the transport of bose-einstein condensates with atom chips. *Scientific reports* **9**, 5346 (2019).
- [115] Brugger, K. *et al.* Nanofabricated atom optics: Atom chips. *Journal of Modern Optics* **47**, 2789–2809 (2000).
- [116] Astm e595\_\_07 .
- [117] D. B. Poker and C. E. Klabunde. Temperature dependence of electrical resistivity of vanadium, platinum, and copper .
- [118] Matula, R. A. Electrical resistivity of copper, gold, palladium, and silver. *Journal of Physical and Chemical Reference Data* **8**, 1147–1298 (1979).
- [119] Moon, H. S., Lee, L. & Kim, J. B. Double-resonance optical pumping of rb atoms. *JOSA B* **24**, 2157 (2007).

- 
- [120] Steven Chu, J. E. Bjorkholm, A. Ashkin & and A. Cable. Experimental observation of optically trapped atoms .
- [121] Luiten, O. J., Reynolds, M. W. & Walraven, J. T. Kinetic theory of the evaporative cooling of a trapped gas. *Physical Review A* **53**, 381–389 (1996).
- [122] Pitaevskii, L. P. & Stringari, S. *Bose-Einstein condensation and superfluidity*, vol. 164 of *International series of monographs on physics* (Oxford University Press, Oxford, United Kingdom, 2016), first edition edn. URL <https://ebookcentral.proquest.com/lib/kxp/detail.action?docID=4413979>.
- [123] Erdős, L., Schlein, B. & Yau, H.-T. Derivation of the gross-pitaevskii equation for the dynamics of bose-einstein condensate. *Annals of Mathematics* **172**, 291–370 (2010).
- [124] Lieb, E. H., Seiringer, R. & Yngvason, J. Bosons in a trap: A rigorous derivation of the gross-pitaevskii energy functional. *Physical Review A* **61** (2000).
- [125] Buhmann, S. Y., Knöll, L., Welsch, D.-G. & Dung, H. T. Casimir-polder forces: A nonperturbative approach. *Physical Review A* **70**, 052117 (2004).
- [126] A.D. McLachlan. Retarded dispersion forces between molecules. *Proceedings of the Royal Society of London. Series A. Mathematical and Physical Sciences* **271**, 387–401 (1963).
- [127] Vaumoron, J. A. & de Biasio, M. P. Argon and rare gas instability with heavy metal cathode penning pumps. *Vacuum* **20**, 109–111 (1970).
- [128] Mordini, C., Trypogeorgos, D., Wolswijk, L., Lamporesi, G. & Ferrari, G. Single-shot reconstruction of the density profile of a dense atomic gas. *Optics express* **28**, 29408–29418 (2020).